NTNU

Date

Faculty of Engineering
Department of Marine Technology

MASTER'S THESIS 2022
for
Master Student HANS CHRISTIAN HØYLAND

Comparing measured loads and responses on a riser system to results from computer modeling

Sammenligning av målt last og respons for et stigerørsystem med resultat fra numeriske beregninger

The wellhead is the connection point between the lower section of the drilling riser and the oil well. It will therefore be the component of the well which experiences the most significant environmental loads. In particular, oscillatory environmental loads are of concern since they may lead to fatigue on the wellhead. Unfortunately, due to its location on the bottom of the sea, it is difficult to check and maintain the integrity of the wellhead. All the same, damage to the wellhead can have catastrophic environmental and social consequences, as a collapse of the wellhead could lead to a blowout which circumvents the BOP.

The objectives of the present thesis are accordingly to address the following topics:

1. Give a general description of the main components of typical top tensioned riser systems.

2. For a specific riser system, static and dynamic response analyses are to be performed. The type of system to be considered is decided based on discussion with the supervisor. The computer program SIMA/Riflex should be applied for the purpose of these analyses. The focus of the dynamic analysis should be related to wellhead fatigue. A discussion on eigenvalues of the system should also be included.

3. The loads which act on the top tensioned riser system are to be described, and the methods used in SIMA/ Riflex for computation of load-effects along the riser shall be summarized. The discussion of the loads should focus on the loads in relation to wellhead fatigue.

4. Wellhead fatigue should be discussed and a discussion of how to measure it should be included.

5. For the selected riser system, it is intended that full-scale measurement records and weather data are also available. Descriptions of the instrumentation system and available datasets are to be given.

6. A convergence study with respect to mesh refinement is subsequently performed. A base case mesh that satisfies a good balance between accuracy and computation time is to be identified.

7. A Parametric variation study should be performed for the selected riser system. A matrix of cases to be analyzed is to be agreed upon prior to commencing the analyses themselves.

Address:
NO-7491 TRONDHEIM
Norway

Org.nr. 974 767 880
Email:
kontakt@marin.ntnu.no
https://www.ntnu.edu/imt

The work scope may prove to be larger than initially anticipated. Subject to approval from the supervisor, topics may be deleted from the list above or reduced in extent.

In the thesis, the candidate shall present his personal contribution to the resolution of problems within the scope of the thesis work. Theories and conclusions should be based on mathematical derivations and/or logic reasoning identifying the various steps in the deduction.

The candidate should utilise the existing possibilities for obtaining relevant literature.

The thesis should be organised in a rational manner to give a clear exposition of results, assessments, and conclusions. The text should be brief and to the point, with a clear language. Telegraphic language should be avoided.

The thesis shall contain the following elements: A text defining the scope, preface, list of contents, summary, main body of thesis, conclusions with recommendations for further work, list of symbols and acronyms, references and (optional) appendices. All figures, tables and equations shall be numbered.

The supervisor may require that the candidate, in an early stage of the work, presents a written plan for the completion of the work. The original contribution of the candidate and material taken from other sources shall be clearly defined. Work from other sources shall be properly referenced using an acknowledged referencing system.

NTNU supervisor: Prof. Bernt J. Leira
Co-supervisor from Equinor: Guttorm Grytøyr

Signatures: Bernt J. Leira

Start-up: January 15th, 2022
Deadline: June 10th, 2022

Address:
NO-7491 TRONDHEIM
Norway

Org.nr. 974 767 880
Email:
kontakt@marin.ntnu.no
https://www.ntnu.edu/imt

Preface

This report is the result of my thesis work, within the field of marine structures, at the department for Marine technology at the Norwegian University of Science and Technology, NTNU. The work has been conducted during the spring of 2022.

The topic of the report is modeling of wellhead fatigue on a top tensioned riser system. In the report, results from models are compared with full scale measurements provided by Equinor. This report presents an extension of the authors work during the project thesis conducted during the autumn of 2021.

I would like to thank Equinor in general, and Guttorm Grytøyr in particular, for providing the measurement data and descriptions of the riser system used in this report, as well as guidance in relation to modeling in RIFLEX. I would also like to thank Bernt J. Leira for being my supervisor and providing support in regards to writing this report.

I would also like to thank my girlfriend Vilde for helping me by proofreading the report.

Abstract

This report considers loads on a subsea wellhead, with a focus on wellhead fatigue. The basis of the report is a drilling campaign committed by Equinor, from which Equinor has provided measurements of wellhead moment and related parameters throughout the campaign. The drilling campaign was operated by a top tensioned riser system. A detailed model of the riser system has been made in SIMA/RIFLEX. Time domain dynamic analysis has been utilized on the model, as well as eigenvalue analysis.

The wellhead moment calculated in the SIMA/RIFLEX model has been compared with the direct measurements of wellhead moment. The results shows that the eigenmodes are highly important in relation to the moment experienced on the wellhead. They also show that the RIFLEX model were conservative in relation to predicting the oscillating wellhead moment, and it was highly accurate in relation to predicting the oscillatory periods that excited the riser system. The model was however too conservative in regards to damping.

Indirect measures of wellhead moment has also been investigated. A quasi-static model has been presented, and the resulting wellhead moment has also been compared to the direct measurement of wellhead fatigue. The initial quasi-static model was non-conservative, but using higher than originally anticipated values for top tension on the wellhead, gave results with very high accuracy. It was also shown, as previous papers have indicated, that rotational angles on the BOP is a better indirect measure of wellhead moment than displacement on the top of the BOP.

Table of Contents

List of Figures

List of Tables

1 Introduction

Up until the oil price crash in 2014, E&P activities in the North Sea was drastically increasing, at current oil prices the activity in the North Sea is expected to restart that trend. This activity leads to a large number of wells to be drilled and a large number of well interventions. In harsh environments like the North Sea fatigue damage on the wellhead is of concern as the loads on the riser system causes major oscillating forces on the wellhead. Fatigue damage on the wellhead is also difficult to asses due to its limited accessibility.

Today wellhead fatigue is mostly calculated based on analytical methods, combining global load analysis with local response analysis. This report will investigate the the validity of global load analysis by comparing it to measured load data and look into alternative ways of calculating global loads on the wellhead.

1.1 Report Structure

The second section gives a general description of top tensioned drilling risers.

The third section describes the concept of wellhead fatigue and gives a brief overview of how it is usually modeled and measured.

The fourth section describes how the program RIFLEX works, and describes some choces made in regards to the modeling in RIFLEX.

The fifth section describes in detail how the top tensioned riser considered in this report has been modeled in RIFLEX.

The sixth section describes the eigenvalues of the riser system considered in this report.

The seventh section describes the environmental data used in this report.

The eighth section describes the measurement systems that have provided the data used in this report.

The ninth section describes a convergence study conducted on the RIFLEX model.

The tenth section goes into how the environmental data, found in section seven, can be used to expose the RIFLEX model to similar environments, so that they can be compared.

The eleventh section describes a large sensitivity study, which considers the effect on the model of changing a large range of parameters.

The twelfth section describes a simple quasi-static model for measuring wellhead moment and compares it with directly measured data.

The thirteenth section has the conclusion of the report.

1.2 Abbreviations

WH	Wellhead
SRSS	Square Root of Sum of Squares
LFJ	Lower flex joint
FEM	Final Element Method
DOF	Degrees Of Freedom
BOP	Blowout Preventer
TTR	Top Tensioned Riser
LMRP	Lower Marine Riser Section
STD	Standard Deviation

1.3 Symbols

i	integer
D_H	Hydrodynamic diameter
u	Particle speed of water
$\dot{u}$	Particle acceleration of water
u_x	Particle speed of water in global x-direction
$\dot{u}_x$	Particle acceleration of water in global x-direction
u_z	Particle speed of water in global z-direction
$\dot{u}_z$	Particle acceleration of water in global z-direction
$\Delta\sigma$	Change in stress
a	Fatigue exponent
ΔM	Change in wellhead moment
N	Number of cycles before fracture
EI	Material bending stiffness
EA	Material axial stiffness
C_a	Added mass coefficient
$A_{external}$	External area of a cross-section
$A_{internal}$	Internal area of cross-section
ρ	Density of sea water, equal to 1025 kg/m^3
C_d	Drag coefficient
η	Displacement vector for the system
$\dot{\eta}$	Movement vector for the system
$\ddot{\eta}$	Acceleration vector for the system
T_e	Effective tension
T_{tw}	True wall tension
p_i	internal pressure
p_e	external pressure
σ_e	effective stress
σ_p	hydrostatic stress
σ_{tw}	true wall stress
σ_{vm}	von Mises stress
g	gravitational constant, equal to 9.81 m/s^2
w_e	effective weight
ϕ	Velocity potential function
ζ	Wave elevation function
ζ_a	Wave amplitude
h	Depth of sea bed
ω	Angular wave frequency
$\Delta\omega$	Angular wave frequency increment
k	wave number
p_d	Dynamic pressure
β^{phase}	Phase angle
$S(\omega)$	Wave spectrum
$D(\omega, \theta)$	Directional spectrum
r^{Vessel}	Rigid body movement of vessel
$H_r(\beta^{phase}, \omega)$	Relationship function between rigid body motion and waves
$R^S(\eta)$	Internal structural reaction force vector
$R^E(\eta)$	External force vector
$R(\eta)$	Force imbalance vector
$\Delta\eta$	Incremental displacement vector
Q	Loads vector

M	Mass matrix
C	Damping matrix
K	Stiffness matrix
γ	Newmark gamma parameter
β	Newmark beta parameter
Hs	Significant wave height
Tp	Spectral peak period
$E(\epsilon)$	Expected value
α_1	Stiffness proportional damping parameter
α_2	Mass proportional damping parameter
TT'	Top tension on top of BOP
θ_{BOP}	Rotational angle of BOP
θ_{LFJ}	Rotational angle of lower flex joint

2 Top Tensioned Risers and their Components

A top tensioned riser is a riser that connects a platform to a subsea oil well through a straight, slender, thin walled pipe, as can be seen in Figure 1. The pipe itself will generally be made of steel, which is heavier than water. This weight in water, combined with relatively low bending stiffness and environmental loads, would lead the pipe to buckle under its own weight. To avoid this buckling, the platform adds a significant vertical tensile force on the top of the riser, so that the effective tension (explained more in detail in Section 4.2.1) is positive throughout the riser. Another way to avoid effective compression in the riser is by utilizing buoyancy modules, a buoyancy module is a lighter-than-water-material, often plastic, which is attached along the riser to reduce its weight in water. Adding tensile forces and utilizing buoyancy modules, are used in combination in most top tensioned risers.

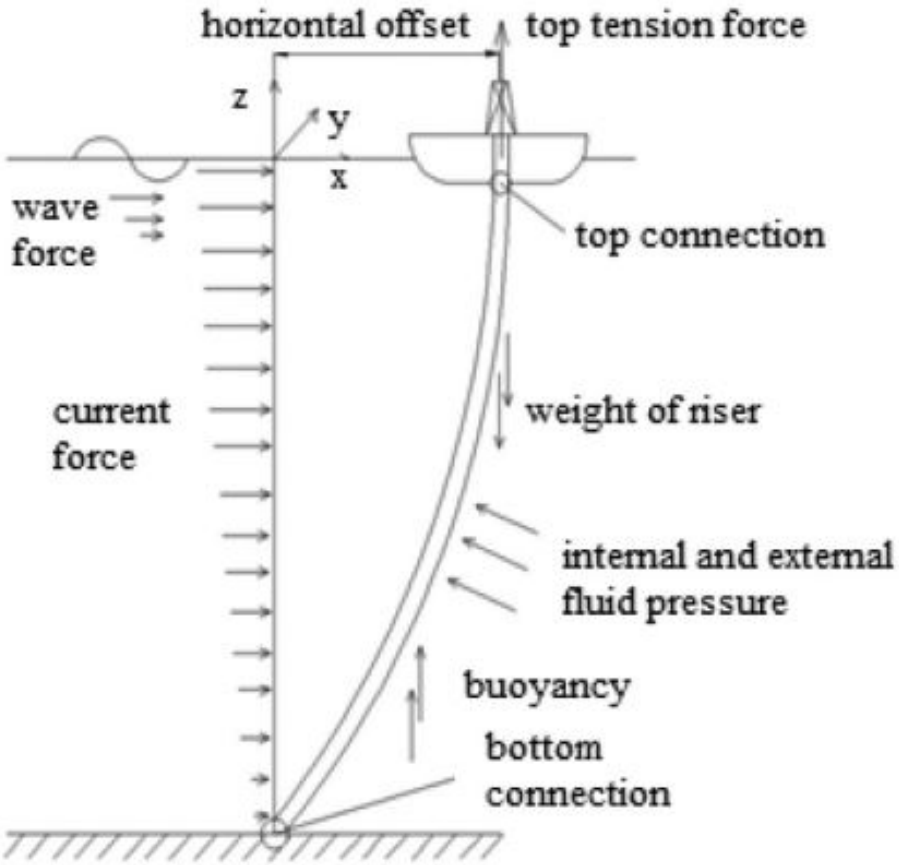

Figure 1: Schematic of a top tensioned riser and the main loads it is exposed to [17]

The top tension will generally need to be larger than the riser's weight in water, with some extra margin to ensure that the forces in the riser never become compressive, as even relatively small compressive forces could lead to buckling. It should, however, be noted that for specific parts with short length, high weight and high bending stiffness, like a subsea BOP, it is possible to have effective compressive forces without experiencing buckling. This is the case for the TTR which will be explored in this report (ref Figure 27).

A TTR necessitates small motions from the platform it is connected to. Especially heave motions are critical, as heave motions would lead to major oscillations in the top tension the riser experiences. This is achieved by utilizing platforms which have low heave motions in general, like tension leg platforms (TLP), spar platforms or semi-submersibles, often in combination with a heave compensation system.

2.1 The Basics of Drilling Equipment

During a offshore drilling operation, a drilling riser is needed to connect the drilling rig on the surface to the oil well on the sea bed. The drilling riser serves as a conduit for the drill string, it moves drilling fluid into the annulus and moves drilling mud out of the annulus.

The heart of a drilling operation is the drilling bit. A typical drilling bit consists of rotating cones, which break up the rock underneath into small chips called "cuttings". The cones may consist of either hardened metal teeth or industrial diamond cutters, depending on the composition and hardness of the formation to be drilled. The cutting action is also supported by powerful jets of drilling fluid, which cool the bit and help remove the "cuttings" out of the hole. The combination of "cuttings" and drilling fluid is called drilling mud and will be transported to the rig through the riser for disposal.

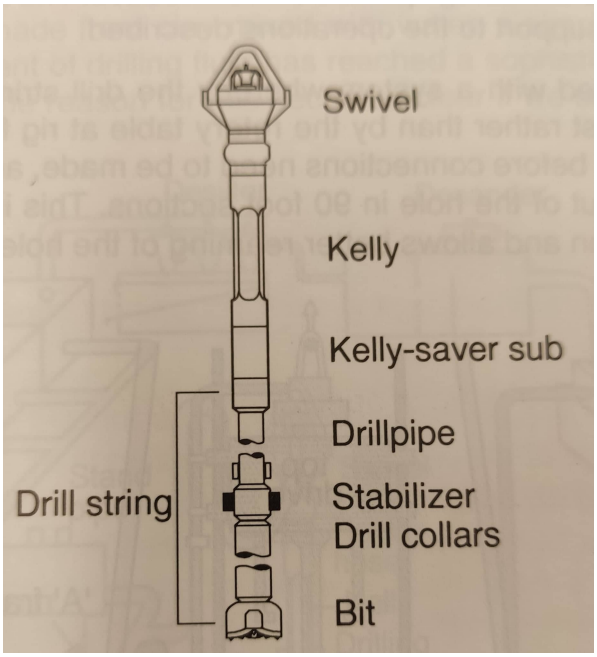

Figure 2: Illustration of the drill string [9]

The drilling string is located above the drilling bit. The drilling string transmits torque generated at the surface to the drilling bit. It also adds the required weight for the drilling bit to be able to drill, and controls direction angle of the drilling bit, but that is beyond the scope of this report [9].

2.2 Well

When drilling a well it is necessary to strengthen the walls of the borehole as the operation progresses. The consequence of foregoing such strengthening would be collapse of the well, or in the worst case scenario, uncontrolled oil and gas under high pressure from the reservoir would break open the rock formations in the well, causing blowout. The walls of the well are strengthened by inserting steel pipes into the borehole, called casings. Then a layer of cement is cemented on the outside of the casing to fasten it to the soil. As the well becomes deeper, new cas-

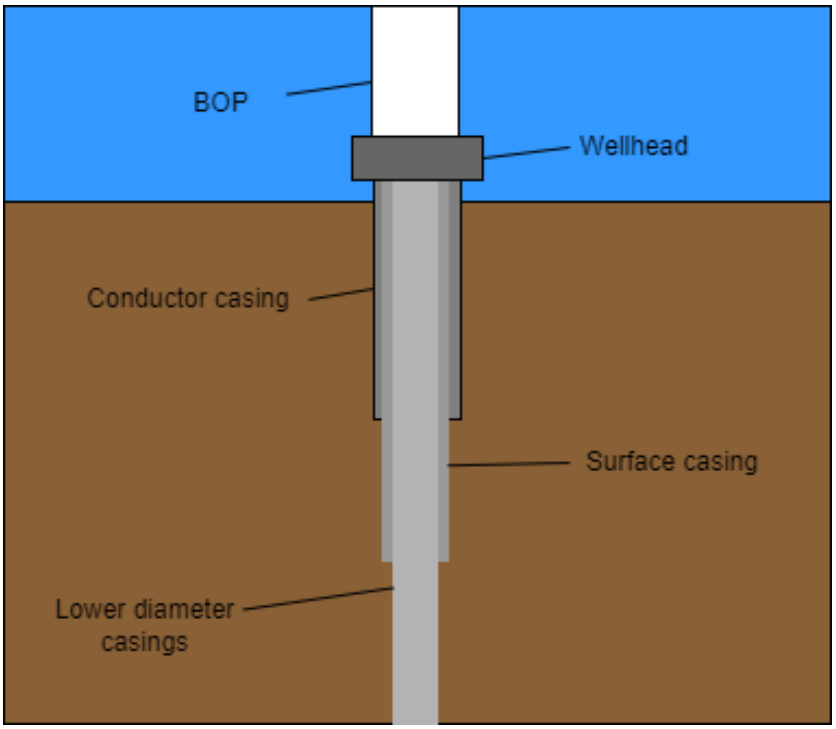

Figure 3: Main components of a subsea oil well

ings have to be inserted so that the well stays reinforced. Each new casing must have a lower diameter than the previous casing, so that it can fit through the inside of the previous casing, as illustrated in Figure 3.

The wellhead is the component of the oil and gas well that stands on the sea bed. It is the connection point between the lower section of the drilling riser and the oil well. Therefore, it is the component of the well which experiences the most environmental loads. Especially oscillatory environmental loads are concerning, as they may lead to fatigue on the wellhead. Due to its location on the bottom of the sea, it is difficult to check and maintain the wellhead, as one would normally check and maintain fatigue-exposed marine components. Damage to the wellhead can have catastrophic environmental and social consequences, as a collapse of the wellhead could lead to a blowout that bypasses the BOP.

2.3 Blowout Preventer (BOP)

As the name suggests, this component exists for the purpose of preventing blowouts. It is a complicated structure that consists of valves and sensors, which monitor and control the pressure and flow of the fluid that flows into the riser. When needed it will completely stop the flow of fluid going through it. This may be in case of a controlled disconnect, or in case of an emergency.

The BOP will often stand on the sea bed, right above the wellhead, as seen in Figure 3. This is the safest as it makes it so that the well can be shut down, in the event something happens that may damage the riser, and it makes it possible to control the internal pressure in the riser. If the well is in relatively shallow waters and the structure on the surface is fastened to the sea bed (meaning the riser will experience very minor environmental loads) like with a jack-up workover riser, the BOP might be on the platform itself as the likelihood of damage to the riser is low.

2.4 Lower Marine Riser Package (LMRP)

Not all riser systems have an LMRP, but for drilling risers they are very common. An LMRP sits on top of the BOP, and will disconnect the riser from the BOP when abnormally harsh weather is experienced. This is to prevent damage to the BOP and wellhead. This makes it necessary to have positive effective tension between the LMRP and the BOP, so that this disconnection is possible.

2.5 Riser Joints

From the top of the BOP to the tensioner system, the riser consists of riser joints. This section is the longest component of the riser system, it is the actual pipes moving drilling equipment and drilling mud between the rig on the surface and the well on the sea bed. To lessen the effective tension needed from the structure on the surface, and the stresses in the riser, one often tries to make the riser joints close to naturally buoyant. As the main pipe is made of steel, this is done by adding buoyancy through fastening polymers to the riser. As depth increases, heavier and more complicated

Figure 4: Picture of some riser joints with buoyancy modules [1]

polymers are needed to withstand the large hydrostatic pressures. These polymers will often be fairly bulky and add considerable drag forces to the riser. Consequently, they are often not in use close to the surface, as they would increase the wave loads on the structure.

Each individual riser joint is typically $50ft = 15.24m$ long, with some shorter riser joints called pup joints. The riser joints are assembled in different combinations to adapt the length of the riser to varying ocean depths, the shorter pup joints are used to fine tune this total length.

2.6 Tensioner System and Telescopic Joint

A riser is a long and slender thin-walled pipe, and it will therefore have a strong natural tendency to buckle. To prevent this, tension is added to the top of the structure, giving the riser a positive effective tension. The effective tension should stay positive throughout the riser joints, and as stated in Section 2.4, it should be large enough to lift the LMRP off the BOP in case of an emergency or simply in case of a controlled disconnect.

The tensioner system functions by having multiple wires from different directions attached to a ring on the riser called a tension ring (see Figure 5). The wires all have close to constant tension, resulting in their force on the tension ring being a tensile force directed straight upwards.

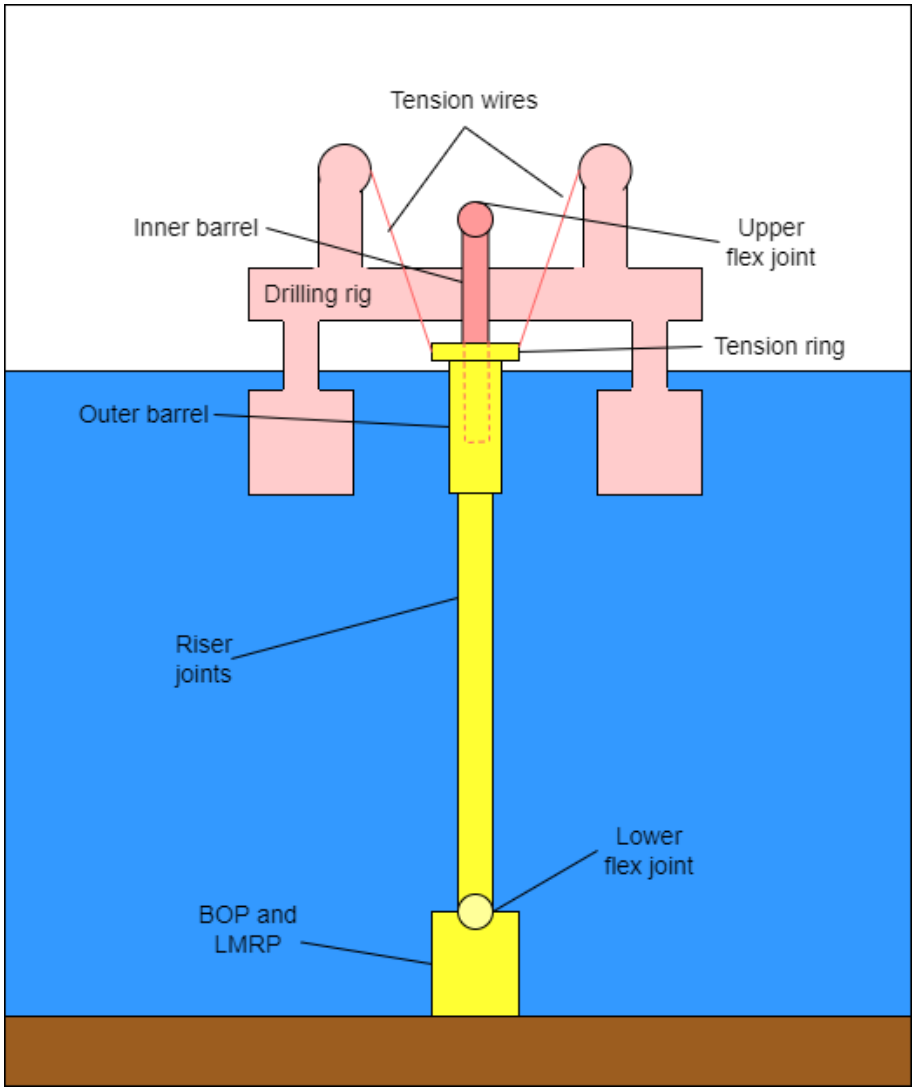

Figure 5: Sketch showing how the tensioner system interacts with the slip joint

The telescopic joint consists of two connected pipes, called the outer and inner barrel, as illustrated in Figure 5. The outer barrel is directly connected to the riser joints. The inner barrel is directly connected to the drilling rig, through the upper flex joint. The inner barrel fits inside the outer barrel, and is free to move in and out of the outer barrel as the drilling rig moves in heave. The aforementioned tensioner ring is connected to the outer barrel, resulting in constant tension from the platform to the riser system almost independent of the platform's heave movements.

2.7 Flex Joints

Typically a top tension riser system has two flex joints, one between the riser joints and the LMRP/BOP (called lower flex joint in Figure 5), and one on the top of the telescopic joint (called upper flex joint in Figure 5). A flex joint is a joint that allows the riser to rotate with limited restriction, resulting in only limited amounts of moment getting transferred trough the flex joint. The upper flex joint is mostly there to limit the transfer of moment from the platform on the surface to the riser, as this would cause a lot of stress at the connection point. The lower flex joint reduces the bending moment in the lower sections of the riser, to avoid plastic deformations of the pipe. In addition, it reduces moment on the wellhead, and consequently it reduces wellhead fatigue.

3 Wellhead Fatigue

Fatigue damage is a progressive and localized structural damage that occurs when a material is subjected to cyclic loading. Fatigue damage is generally characterized as having two phases: crack initiation and subsequent crack propagation, which may lead to an unstable fracture. During all riser-connected operations, the well system is subjected to fatigue loading induced by environmental conditions. Interactions between the rig, riser system, wellhead system, casing system and soils should be adequately modeled to assess the fatigue life of the wellhead.[5]

3.1 SN-Curve

The fatigue capacity of welded joints and base materials are defined by SN curves, which are obtained from fatigue tests. Fatigue tests consist of exposing structures to oscillating loads until they fracture, and then measuring the number of cycles until fracture. The design SN curves are based on the mean-minus-two-standard-deviation curves, which are associated with a 97.5% probability of survival in fatigue tests. Equation 1 describes the relationship between the oscillating stress $\Delta\sigma$ and the number of cycles before fracture N. [4]

$$log(N) = log(K_2) - a \cdot log(\Delta\sigma) \tag{1}$$

K_2 is simply a constant which has been found empirically and it will differ based on:

1. The geometry of the detail
2. The direction of the fluctuating stress relative to the detail
3. The method of fabrication (misalignment/defects and surface condition) and inspection of the detail

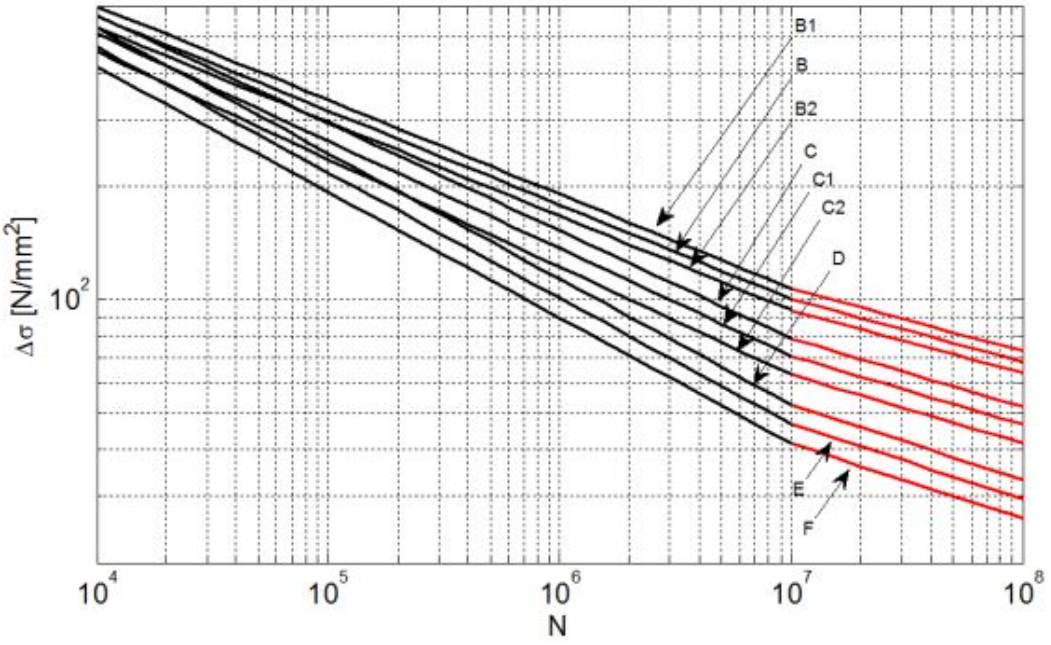

Figure 6: SN-curves for different load cases [4]

Most fatigue damage occurs for fairly large $\Delta\sigma$, for such stresses a (often referred to as fatigue exponent) in Equation 1 is normally in the range $3 - 4$. Solving Equation 1 for N yields:

$$N = \frac{K_2}{\Delta\sigma^a} \tag{2}$$

Equation 2 shows that the fatigue life of a structure is extremely sensitive to $\Delta\sigma$, a safety factor of 2.0 in the calculation of $\Delta\sigma$ would cut the fatigue life by 8-16. This makes it productive to calculate $\Delta\sigma$ as accurately as possible, so that uncertainties can be reduced and safety margins can be decreased.

3.2 Local Load Analysis

When calculating wellhead fatigue, one starts by conducting a detailed local analysis of the wellhead. In the detailed analysis it is possible to see how stresses is propagating throughout the wellhead as it is exposed to differing moments. For all hot spots in question, like grooves, transitions and contact points, the relationship between stress and total wellhead moment is investigated. As this relationship is established, it can be combined with the SN-curve (Equation 1) to develop a MN-curve, which establish the fatigue capacity of the wellhead in relationship to the wellhead moment rather than the local stresses [3].

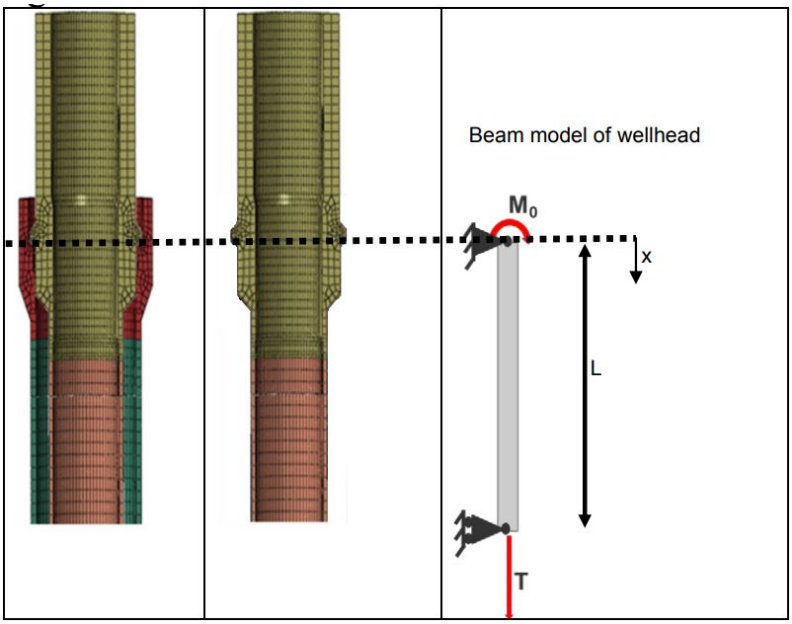

Figure 7: Illustration of local analysis of the wellhead, showing how a complicated FEM analysis can be handled as a simple beam [3]

3.2.1 Wellhead Moment

$$\Delta\sigma = \frac{\Delta M}{EI_{wellhead}} y \tag{3}$$

Equation 3 shows a simplified version of how oscillating stresses propagate throughout the cross-section of the wellhead, without accounting for hot spots. In reality this relationship should be investigated more detailed, as described above. But by using Equation 3 it possible to show, in a simplified way, how the MN-curve can be developed in combination with Equation 1:

$$log(N) = log(K_2) - a \cdot log(\frac{\Delta M}{EI_{wellhead}} y_{max}) \tag{4}$$
$$log(N) = log(K_2) - a \cdot log(\frac{y_{max}}{EI_{wellhead}}) \cdot log(\Delta M)$$

Fatigue damage close to the wellhead is almost completely resulting from oscillating moments on the wellhead. Most of the uncertainty related to wellhead fatigue comes from the calculation of $\Delta\sigma$, and $\Delta\sigma$ is mostly a result of ΔM. This report will therefore not consider fatigue life directly, but rather focus on oscillating moments at the wellhead as a proxy for how well fatigue damage is calculated from the model compared to measurements.

3.3 Global Load Analysis

Global load analysis is a less detailed analysis, which is finding the oscillating moments acting on the wellhead. It analyses the entire riser system which is considered, and it is dependent on a large number of parameters. Global load analysis is the focus of this report and Section 5 goes into the details of how it has been modeled in this report.

3.4 Direct and Indirect Measurement of Wellhead moment

It has been suggested that one may try to measure the wellhead moment , rather than analyzing the global loads on the wellhead based on time domain analysis. This makes it possible to avoid some of the uncertainties related to FEM global load analysis. It can however only be used to verify results from global analysis as the measurements can only be calculated after the operation has started, it may however allow fatigue life to be extended beyond the estimates from global load analysis. As the fatigue life is highly sensitive to the the wellhead moment, substantial fatigue life extensions is possible.

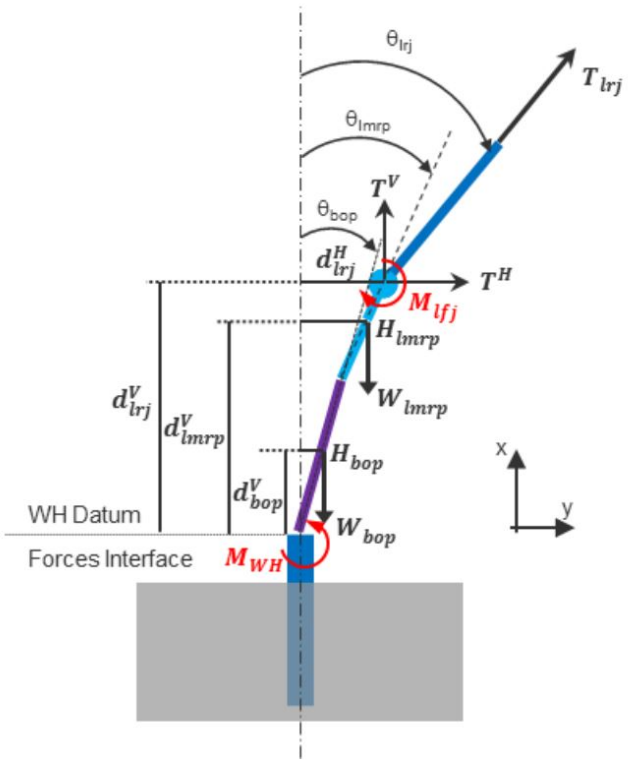

Figure 8: Illustration of how wellhead moment can been calculated based on angular rotations in a quasi-static approach [7]

Direct measurements, like strain gauges, is one possible way to measure wellhead moment. Combining strain gauge readings close to the wellhead, with local FEM analysis, gives good measurements of the moment the wellhead is exposed to. [13] Such measurements exist for the operations described in this report, and are described in Section 8. Direct measurements are however expensive and impractical to implement on a general basis, so other types of measurements are generally preferred.

It has also been proposed to measure wellhead moment indirectly. By indirect measurements, one refers to measurement systems which are easier to implement, like accelerometers or angular rate sensors. Horizontal displacement on top of the BOP, based on accelerometers, have been proposed as a method of calculating wellhead moment. The method consisted of using local FEM analysis to calculate the moment needed to displace the top of the BOP equal to the measured displacements [10]. Later papers has disputed this method. The problem has been identified as being that the conductor beam may exhibit more than one mode of deflection, so that different wellhead moments

may be related to the same deflection on the top of the BOP . Angular rate has been proposed as an alternative and better basis for calculating wellhead moment, and it has been shown that such measurements combined with a quasi-static approach yields good estimates for wellhead moments. Adding a dynamic component improves the results further [7].

4 Modeling in RIFLEX

The following is the purpose of RIFLEX according to its user guide [15]. RIFLEX was developed as a tool for analysis of flexible marine riser systems, but is suited for any type of slender structure, such as mooring lines, umbilicals, steel pipelines and conventional risers. These slender structures are characterized by:

- Low bending stiffness
- Deflection
- Large upper end motion excitation
- Nonlinear cross section properties
- Complex cross section structure

The program allows for an array of different analyses, which can be divided into two types: static and dynamic. Static analyses can again be split into equlibrium configuration and parameter variations, while dynamic analyses can be divided into eigenvalue analyses and harmonic- and irregular wave- and motion excitation.

4.1 System Specification in RIFLEX

A system in RIFLEX is described as lines going between supernodes, as is illustrated in Figure 9. Each line can be divided into segments with given cross-section properties, and each segment is again divided into small elements, allowing for normal FEM analysis to be performed.

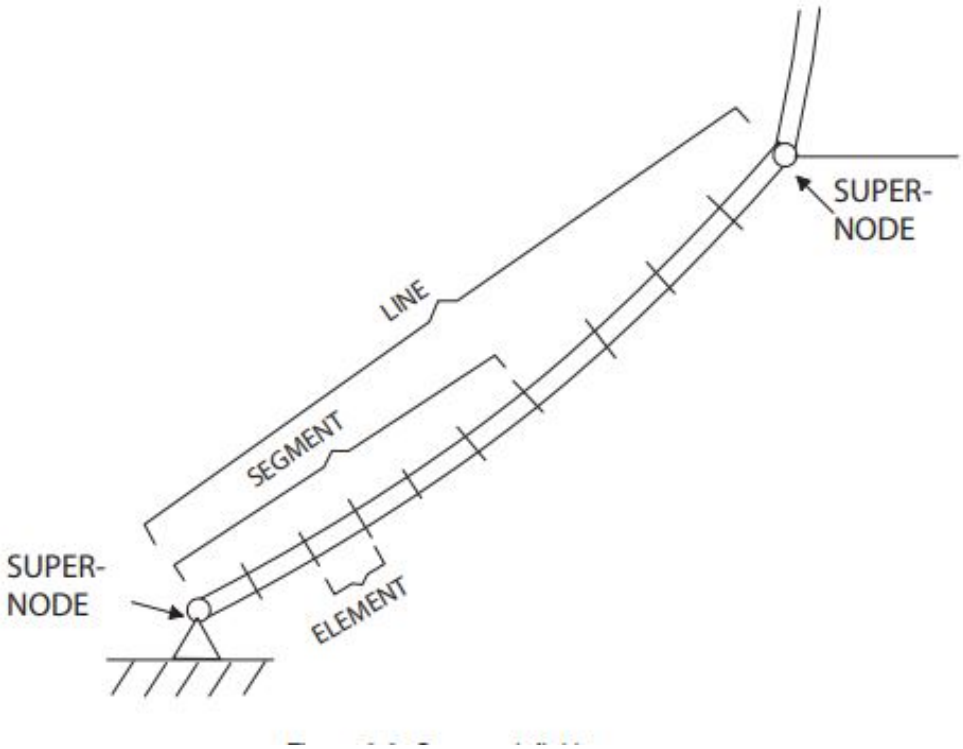

Figure 9: Illustration of the components of system specification in RIFLEX [15]

4.1.1 Supernodes

The first component needed for describing a system in RIFLEX is supernodes. Supernodes have an initial position given in x-y-z-coordinates, and they have different forms of boundary conditions. Supernodes are denoted as slave, free, fixed or prescribed, based on their boundary conditions. A supernode denoted as free will have free boundary conditions in all DOFs, and only its initial position needs to be set. A supernode denoted as a slave will move in tandem with another supernode, called the master, so that its position in relation to the master is consistent with the initial position throughout the analysis. A fixed or prescribed supernode has some or all of its DOFs fixed in relation to its initial position. A slave may also be fixed in relation to a support vessel, so that the supernode can simulate the movements of an end in a riser system which is connected to a floating vessel.

4.1.2 Lines and Segments

A line goes between two supernodes, and describes the actual slender structures that are to be analyzed. A line is divided into segments, which set the properties of the cross-section of the line. There are multiple types of cross sections which can be used: , but in this report only Axi-symmetric cross-sections are used.

As the name suggests, axi-symmetric cross sections exhibit circular symmetry in the local y-z plane. In an axi-symmetric cross section, a wide array of parameters may be set to allow for an accurate model of the real system. The mass of the segments is given as a mass coefficient indicating mass per unit length. The buoyancy of the segment is handled by giving the segment an external area ($A_{external}$). The properties of a fluid in a riser is handled by giving the segments of the riser an internal area ($A_{internal}$), and filling it with a fluid which is given properties like density. Gyration radius can also be set, but as rotations around the local x-axis is irrelevant for the model behavior considered in this report, gyration radius is set equal to one meter so that the model runs without problems.

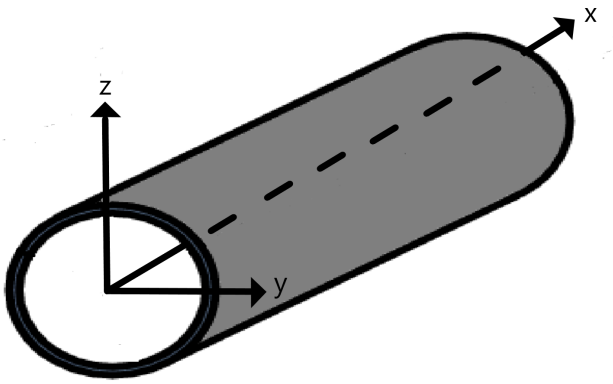

Figure 10: Local coordinate system for slender structures

The stiffness properties of the cross sections should also be set. It is possible to model the segments as both bars and beams, but in this report beams are used if not otherwise specified. Bending stiffness (EI) and axial stiffness (EA) also need to be set for each cross section. RIFLEX allows for both of these values to be non-linear, but if nothing else is specified, constant stiffness is assumed. Torsion stiffness can also be set, but as with gyration radius, this value has negligible effect on the wellhead moment, hence it is generally set to a fairly stiff value.

Hydrodynamic force coefficients can also be set for the cross section of the segments. RIFLEX allows for multiple types of load formulation, but only Morison is used in this report. When Morison is selected, the hydrodynamic forces on the segment per unit length is calculated by the generalized Morison's equation given in Equation 5. This means that the added mass coefficient C_a, the drag coefficient C_d, and the hydrodynamic diameter D_H have to be selected. The hydrodynamic force coefficients is only relevant for segments which are submerged in water.

Equation 5 is a somewhat simplified version of the equation used in the theory manual, as Froude-Krylov scaling has not been utilized in this report, linear drag forces has also been neglected[14].

$$dF = A_{external} \cdot \rho \cdot \dot{u} + C_a \cdot \rho \cdot \frac{\pi \cdot D_H^2}{4}(\dot{u} - \ddot{\eta}) + \frac{1}{2}\rho \cdot C_d \cdot D_H(u - \dot{\eta})|u - \dot{\eta}| \tag{5}$$

The segments may also be given Rayleigh damping ratios.

4.1.3 Nodal Components

RIFLEX also allows for multiple types of nodal components, which are components that give properties to specific nodes on the slender structure. The types used in this report are as follows:

- Flex Joints, these components allow for rotational stiffness and rotational damping between two segments.
- Nodal bodies, these components add mass, displaced volume, and hydrodynamic coefficients in one node between two segments.
- Global springs, these components act as springs in the way that they give a counteracting force to a displacement in the slender structure. Global springs may counteract both displacements in one global axis and in one global plane, they may also counteract rotations around a global axis.

4.2 Load Models

The following physical effects contribute to system loads [14]:

- Weight and inertia, governed by line mass, including pipe contents and external wrapping
- Hydrostatic forces, dependent on pressure gradients
- Hydrodynamic forces dependent on wave, current and structure motions
- Forced motion on line, dependent on vessel motions
- Aerodynamic forces dependent on wind and structure motions. As these forces has limited effect on wellhead fatigue and the relevant data for the drilling rig is not available, this effect has been neglected in this report.

4.2.1 Hydrostatic Forces

When considering long slender risers in water, the effect of hydrostatic pressure combined with the internal pressure in the riser is obviously important, and a major cause for confusion. As buckling is a major cause for concern, one needs to find a way to calculate an effective tension T_e for buckling analysis which takes into account the effect of the hydrostatic pressure. This results in Equation 6 .

$$T_e = T_{tw} + (-p_i A_{internal}) - (-p_e A_{external}) \tag{6}$$

The rationale for using this equation comes from the fact that the hydrostatic pressure is equal in all directions, so that the resulting stress σ_p, creates no distortion in the structure, leading the true wall stress σ_{tw} to be higher than the effective stress when the compressive stress from hydrostatic pressure to be taken into account [16].

$$\sigma_e = \frac{T_e}{A_{external} - A_{internal}} \tag{7}$$

$$\sigma_e = \sigma_{tw} + \sigma_p \tag{8}$$

If the von Mises stress σ_{vm} in a riser under hydrostatic pressure is to be calculated, the hydrostatic effect on shear stress τ needs to be taken into account. It is done as in Equation 9, where r is the distance from the center of the riser to the point one want to calculate τ.

$$\tau = \frac{(p_i - p_e)A_{internal} \cdot A_{external}}{(A_{external} - A_{internal}) \cdot \pi r^2} \tag{9}$$

$$\sigma_{vm}^2 = \sigma_e^2 + 3\tau^2 \tag{10}$$

When bending stresses (σ_b) are to be included, Equation 10 needs to be expanded:

$$\sigma_{vm}^2 = (\sigma_e + \sigma_b)^2 + 3\tau^2 \tag{11}$$

Hydrostatic forces also have an effect on the effective weight per unit length w_e of the riser sections. It is found by calculating the weight in water of the structure, as seen in Equation 12

$$w_e = m \cdot g + A_{internal} \cdot \rho_{internal} \cdot g - A_{external} \cdot \rho \cdot g \tag{12}$$

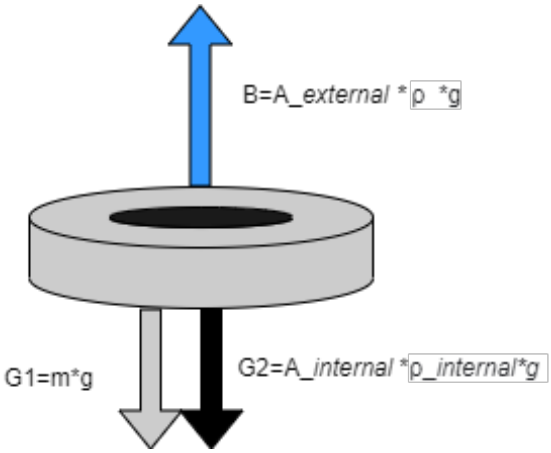

Figure 11: An illustration showing how the effective weight is calculated by combining the gravity forces and the buoyancy forces on a riser section

RIFLEX allows for two models to account for these effects:

1. Volume force model
   Use of vertical, conservative forces to represent hydrostatic effects. These forces will be in equilibrium with the effective tension, which means that axial stresses need not necessarily be calculated during an iteration for equilibrium.

2. Pressure force model
   Calculation of non-conservative hydrostatic forces by considering pressure on the deformed pipe geometry. These forces are in equilibrium with the axial stress resultants. Effective tension needed for calculation of the stiffness matrix must, however, be found by introducing artificial pressure forces in the axial direction.

As the riser system considered in this report is assumed to not be deformed by hydrostatic pressure, the volume force model is used.

4.2.2 Airy Linear Wave Theory

RIFLEX allows for the use of both Airy linear wave theory and Stoke's 5th order wave theory when calculating wave potential. Airy linear wave theory is used in this report, as minor effects in the wave zone have limited effect on wellhead moment. This wave theory also allows for linear superposition of multiple Airy-waves into an irregular sea state, as described in the next section.

The basic assumptions of linear wave theory are as follows [6]:

- Horizontal sea bed, Equation 13
- Free surface condition, which linearized becomes Equation 14 and Equation 15
- Harmonically oscillating velocity potential in time with a circular frequency ω. Combined with Equation 14 and Equation 15, this leads to Equation 16.
- The incompressibility of water, leading to the Laplace equation: Equation 17
- The velocity potential can be represented as a product of functions, each of which are dependent on just one independent variable

$$\frac{\delta\phi}{\delta z} = 0 \qquad for \quad z = -h \tag{13}$$

$$\frac{\delta\zeta}{\delta t} = \frac{\delta\phi}{\delta z} \qquad on \quad z = 0 \tag{14}$$

$$g\zeta + \frac{\delta\phi}{\delta t} = 0 \qquad on \quad z = 0 \tag{15}$$

$$-\omega^2\phi + g\frac{\delta\phi}{\delta z} = 0 \qquad on \quad z = 0 \tag{16}$$

$$\frac{\delta^2\phi}{\delta x^2} + \frac{\delta^2\phi}{\delta y^2} + \frac{\delta^2\phi}{\delta x^2} = 0 \tag{17}$$

The end result of all of these assumptions is the velocity potential presented in Equation 18, with $k = \frac{2\pi}{\lambda}$ and $\omega = \frac{2\pi}{T}$. For simplicity only calculations for the 2D-version in the xz-plane is shown here.

$$\phi = \frac{g\zeta_a}{\omega}\frac{cosh(k(z+h))}{cosh(kh)}cos(\omega t - kx) \tag{18}$$

The velocity potential can be used further to find dynamic pressure (Equation 19), x-component of velocity (Equation 20), x-component of acceleration (Equation 21), z-component of velocity (Equation 22) and z-component of acceleration (Equation 23), all of which are essential for calculating the dynamic forces like the Morrison's equation on a riser.

$$p_d = \rho_w g\zeta_a\frac{cosh(k(z+h))}{cosh(kh)}sin(\omega t - kx) \tag{19}$$

$$u_x = \omega\zeta_a\frac{cosh(k(z+h))}{sinh(kh)}sin(\omega t - kx) \tag{20}$$

$$\dot{u}_x = \omega^2\zeta_a\frac{cosh(k(z+h))}{sinh(kh)}cos(\omega t - kx) \tag{21}$$

$$u_z = \omega\zeta_a \frac{sinh(k(z+h))}{sinh(kh)} cos(\omega t - kx) \tag{22}$$

$$\dot{u}_z = -\omega^2\zeta_a \frac{sinh(k(z+h))}{sinh(kh)} sin(\omega t - kx) \tag{23}$$

Wave Potential Close to Surface

Airy wave theory is based on an assumption of infinitesimal wave height; Equation 14 assumes that the wave potential exists for all coordinates with $z = 0$. In reality the surface of waves in the ocean will move up and down, so that the wave potential should not exist for $z = 0$ in a wave valley, and it should exist above this level in the wave peak. This causes some issues related to how one should handle this effect numerically along the riser.

RIFLEX gives five options for particle motion modeling close to the surface, a description of four of these can be found in Figure 12. The fifth option is called "Second order wave integration" and is the most accurate, but also the most computationally heavy option. The first option, integration to mean water level, has been chosen in this report. This option simply uses Airy wave theory directly, without mitigating the errors caused by this theory close to the surface. As the focus of this report is modeling of wellhead moment, effects in the wave zone are assumed to not be that important, and this choice allows for shorter computational time.

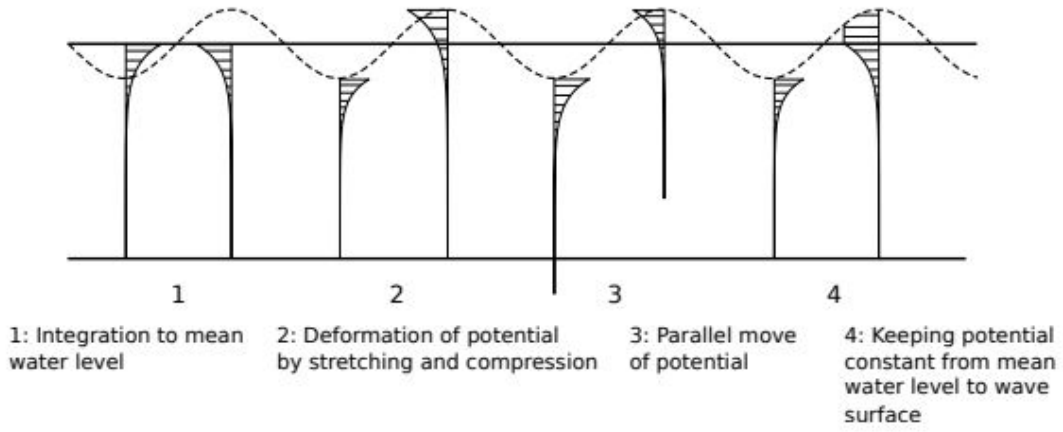

Figure 12: Illustrations of different ways to handle the wave potential at the surface [14]

4.2.3 Irregular Waves

Linear wave theory describes how sea state with one single wave amplitude, one single wave frequency and one single wave length will behave. But such waves are only able to exist in laboratory conditions. In real marine environments irregular waves will be found, and wave elevation may be described as N linear waves as in Equation 24.

$$\zeta = \sum_{i=1}^{N} \zeta_{a,i}\, sin(\omega_i t - k_i x + \beta_i^{phase}) \tag{24}$$

The random phase angle β_i^{phase} is, as the name suggests, a uniformly distributed value between 0 and 2π. The wave amplitude $\zeta_{a,i}$ can be described by a hypothetical wave spectra $S(\omega)$ as in Equation 25.

$$\frac{1}{2}\zeta_{a,i}^2 = S(\omega_i)\,\Delta\omega \tag{25}$$

Combined with the dispersion relationship between ω_i and k_i (Equation 26), the entire irregular sea state described by Equation 24 can be found from a simple wave spectrum.

$$\frac{\omega^2}{g} = k\,tanh(k\,h) \tag{26}$$

Directional Spectra

Until now only unidirectional wave spectra have been considered, but actual sea waves will often come from multiple directions. The standardized way of introducing directions is by multiplying the wave spectra found, with some kind of directional function like in Equation 27.

$$S(\omega,\theta) = S(\omega)\cdot D(\omega,\theta) \tag{27}$$

With Equation 28 being the needed criteria for $S(\omega,\theta)$ to still be valid.

$$\int_{-\pi}^{\pi} D(\omega,\theta)d\theta = 1 \qquad\qquad for\ all\ \omega \tag{28}$$

Different functions may be used for $D(\omega,\theta)$, but the function used in RIFLEX is a cosine function on the form of Equation 29, with K_n being defined such that Equation 28 is satisfied.

$$D(\theta) = \begin{cases} K_n\,cos^n(\theta) & \text{for } -\frac{\pi}{2} < \theta < \frac{\pi}{2} \\ 0 & \text{else} \end{cases} \tag{29}$$

4.2.4 Vessel Motions

The riser system considered in this report is connected to a drilling rig at the surface. The motions of this vessel must therefore be included in the model. This necessitates the first order motion functions for the vessel, which can be found in Appendix A.

A first order motion function gives the relationship between wave elevation and the six rigid body motions (surge, sway, heave, roll, pitch and yaw) of the vessel, as seen in Equation 30. This relationship is dependent both on the wave frequency ω and phase angle β^{phase}. In this section this relationship will be described generally, so r^{Vessel} is representative for any of the six rigid body motions.

$$H_r(\beta^{phase},\omega) = \frac{r^{Vessel}(\beta^{phase},\omega)}{\zeta_a(\beta^{phase},\omega)} \tag{30}$$

RIFLEX calculates the motions of the vessel by combining $H_x(\beta^{phase},\omega)$ with Equation 24. The motions of the vessel can be expressed accordingly as:

$$r^{Vessel} = \sum_{i=1}^{N} H_r(\beta_i^{phase},\omega_i)\,sin(\omega_i t - k_i x + \beta_i^{phase}) \tag{31}$$

As described in Section 4.1.1, the supernodes in the riser system that are connected to the rig can have the rig as its reference system, meaning it will move rigidly, as described in Equation 31.

4.3 Static Analysis: Finite Element Method

Each segment is as seen in Figure 9, divided into elements. For beam elements, each element has three degrees of rotation and three degrees of displacement at each end. These DOFs have to match from one element to the next. These displacements and rotations also give rise to internal forces in each element. Then, all of these internal forces are combined into one large vector called the internal structural reaction force vector $R^S(\eta)$. Each element also experiences external forces like rigid body forces for representation of support vessels, clump weights etc; and contribution from distributed loading, i.e. weight, buoyancy. These external forces are combined into a vector called external force vector $R^E(\eta)$. The finite element method finds the DOFs in the structure in question, which satisfies the equilibrium between the internal and external forces as in Equation 32.

$$R^S(\eta) = R^E(\eta) \tag{32}$$

4.3.1 Incremental Equilibrium Iterations

To find η, one needs to start with an initial guess for η, then the force imbalance vector $R(\eta)$ is calculated according to Equation 33.

$$R(\eta) = R^S(\eta) - R^E(\eta) \tag{33}$$

For each iteration k, the tangential stiffness matrix $\frac{\delta R_{k-1}}{\delta \eta}$ from the previous load step is calculated. Then, the incremental displacement vector $\Delta\eta_k^0$ can be calculated according to Equation 34, and the next load step η_k can be found using Equation 35

$$\Delta\eta_k^0 = -[\frac{\delta R_{k-1}}{\delta \eta}]^{-1}(R_{k-1}^S - R_k^E) \tag{34}$$

$$\eta_k^0 = \eta_{k-1} + \Delta\eta_k^0 \tag{35}$$

Finding $\frac{\delta R_{k-1}}{\delta \eta}$ is fairly computationally heavy, so the η_k^0 can be improved further through a modified Newton-Raphson iteration. For each iteration j, $\Delta\eta_k^j$ and η_k^j is found through Equation 36 and Equation 37. This iteration cycle is continued until η_k^j converges. When it has converged, a new load step can be found until $\Delta\eta_k^0$ converges towards zero.

$$\Delta\eta_k^j = -[\frac{\delta R_{k-1}}{\delta \eta}]^{-1}(R_k^{j-1}) \tag{36}$$

$$\eta_k^j = \eta_k^{j-1} + \Delta\eta_k^j \tag{37}$$

4.4 Dynamic Analysis: Time Integration

Time integration is a way to calculate the dynamic responses of a FEM structure, where the loads are known, and perhaps even a function of the dynamic responses themselves. If the loads Q_i are a function the dynamic responses, it will need to be continuously updated.

General procedure:

1. η_i, $\dot{\eta}_i$, $\ddot{\eta}_i$, Q_i and Q_{i+1} are know at step i
2. Also know that $M\ddot{\eta}_i + C\dot{\eta}_i + K\eta_i = Q_i$
3. An assumption about $\ddot{\eta}$ in the time between t_i and t_{i+1} is made

4. η_{i+1}, $\dot{\eta}_{i+1}$ and $\ddot{\eta}_{i+1}$ can be found based on the assumptions and dynamic equilibrium

The equation of motion will always be valid:

$$M\ddot{\eta} + C\dot{\eta} + K\eta = Q(t) \tag{38}$$

In time integration, dynamic equilibrium is found at discrete points between t_i and t_{i+1}. There is no exact representation of $\eta(t)$ or dynamic equilibrium. Based on the assumptions made about $\ddot{\eta}$ from t_i to t_{i+1}, $\dot{\eta}_{i+1}$ and η_{i+1} can be found through Equation 39 and Equation 40 for each element in the FEM.

$$\dot{\eta}_{i+1} = \dot{\eta}_i + \int_{t_i}^{t_{i+1}} \ddot{\eta}(t)dt \tag{39}$$

$$\eta_{i+1} = \eta_i + \int_{t_i}^{t_{i+1}} \dot{\eta}(t)dt \tag{40}$$

Now, dynamic equilibrium means that $\ddot{\eta}_{i+1}$ can be found:

$$\ddot{\eta}_{i+1} = M^{-1}(Q_{i+1} - C\dot{\eta}_{i+1} - K\eta_{i+1}) \tag{41}$$

To calculate Equation 39 and Equation 40, these equations needs to be rewritten into something which can be calculated numerically based on how one assumes $\ddot{\eta}(t)$ behaves over the time interval. The standardized way to calculate this relationship is by utilizing Newmark's procedure, meaning Equation 39 and Equation 40 is rewritten to Equation 42 and Equation 43, and then choosing values for γ and β to emulate the assumptions made.

$$\dot{\eta}_{i+1} = \dot{\eta}_i + \gamma \cdot \Delta t \cdot (\ddot{\eta}_i + \ddot{\eta}_{i+1}) \tag{42}$$

$$\eta_{i+1} = \eta_i + \Delta t \cdot \dot{\eta}_i + \beta \cdot \Delta t^2 \cdot (\ddot{\eta}_i + \ddot{\eta}_{i+1}) \tag{43}$$

4.4.1 Constant Average Acceleration Method

The default way for RIFLEX to do these calculations is through Newmark's procedure, and the default parameters used ($\gamma = \frac{1}{2}$) and ($\beta = \frac{1}{4}$), makes it a special case called the constant average acceleration method. The assumption is simply that the acceleration is constant on the interval t_i to t_{i+1}:

$$\ddot{\eta}(t) = \frac{1}{2}(\ddot{\eta}_i + \ddot{\eta}_{i+1}) \tag{44}$$

This makes it possible to write out Equation 39 and Equation 40 to Equation 45 and Equation 46 respectively.

$$\dot{\eta}_{i+1} = \dot{\eta}_i + \frac{\Delta t}{2}(\ddot{\eta}_i + \ddot{\eta}_{i+1}) \tag{45}$$

$$\eta_{i+1} = \eta_i + \Delta t \cdot \dot{\eta}_i + \frac{\Delta t^2}{4}(\ddot{\eta}_i + \ddot{\eta}_{i+1}) \tag{46}$$

By inserting Equation 41 into Equation 46 and Equation 45, one end up with the following two equations with two unknowns, $\dot{\eta}_{i+1}$ and $\ddot{\eta}_{i+1}$, meaning they are solvable through some algebra.

$$\eta_{i+1} = \eta_i + \Delta t \cdot \dot{\eta}_i + \frac{\Delta t^2}{4}(\ddot{\eta}_i + M^{-1}(Q_{i+1} - C\dot{\eta}_{i+1} - K\eta_{i+1}) \tag{47}$$

$$\dot{\eta}_{i+1} = \dot{\eta}_i + \frac{\Delta t}{2}(\ddot{\eta}_i + M^{-1}(Q_{i+1} - C\dot{\eta}_{i+1} - K\eta_{i+1})) \tag{48}$$

4.4.2 Non-linear Analysis

In the start of this section, the equation of motion Equation 38 was presented. There the mass matrix M, the damping matrix C, the stiffness matrix K and the load vector $Q(t)$ was presented as independent of η. That is not the case in reality, so in this report non-linear dynamic analysis is used to account for these effects.

Here these are replaced by displacement dependent force vectors as seen in Equation 49.

$$R^I(\eta, \ddot{\eta}, t) + R^D(\eta, \dot{\eta}, t) + R^S(\eta, t) = R^E(\eta, \dot{\eta}, t) \tag{49}$$

- $R^I(\eta, \ddot{\eta}, t)$ is the inertia force vector, described in Equation 50
- $R^D(\eta, \dot{\eta}, t)$ is the damping force vector, described in Equation 51
- $R^S(\eta, t)$ is the internal structural reaction force vector, as described in Section 4.3
- $R^E(\eta, \dot{\eta}, t)$ is the external force vector

External force vector

$R^E(\eta, \dot{\eta}, t)$ is largely defined as it was in Section 4.3, it includes specified nodal forces, weight and buoyancy, but now it also includes dynamic forces like forced displacement from support vessel motions in waves and wave related forces like the forces resulting from the Morison's equation.

Inertia force vector

The inertia force vector is defined as in Equation 50.

$$R^I(\eta, \ddot{\eta}, t) = [M^S + M^H(\eta)] \cdot \ddot{\eta} \tag{50}$$

M^S is defined as the structural mass matrix, simply the mass in each element distributed on the element's nodes. $M^H(\eta)$ is defined as the displacement-dependent hydrodynamic mass matrix accounting for the structural acceleration terms in the Morison equation as added mass contributions in local directions.

Damping force vector

The damping force vector is defined as in Equation 51.

$$R^D(\eta, \dot{\eta}, t) = [C^S(\eta) + C^H(\eta) + C^D(\eta, \dot{\eta})] \cdot \dot{\eta} \tag{51}$$

$C^S(\eta)$ is defined as the internal structural damping matrix, accunting for Rayleigh damping. $C^H(\eta)$ is defined as hydrodynamic damping matrix accounting for diffraction effects for floating, partly submerged elements (irrelevant in other situations). $C^D(\eta, \dot{\eta})$ matrix of specified discrete dashpot dampers which may be displacement- and velocity- dependent, for example flexible joints or global springs.

The analysis

The incremental form of the equation of motion, Equation 49, is obtained by considering this equation in two time steps a short time interval Δt apart:

$$(R^I_{t+\Delta t} - R^I_t) + (R^D_{t+\Delta t} - R^D_t) + (R^S_{t+\Delta t} - R^S_t) = (R^E_{t+\Delta t} - R^E_t) \tag{52}$$

The nonlinear incremental equation of motion is linearized by introducing the tangential mass-, damping- and stiffness matrices at the start of the increment. The linearized incremental equation of motion can be expressed as Equation 53 where M_t, C_t and K_t denote the tangential mass-, damping- and stiffness matrices computed at time t.

$$M_t \Delta\ddot{\eta} + C_t \Delta\dot{\eta} + K_t \Delta\eta = \Delta R^E_t \tag{53}$$

As the incremental equation of motion now is linearized η may now be calculated as shown earlier in this section, but for each time iteration, new matrices for M_t, C_t and K_t needs to be calculated.

4.5 Autospectrum of a Time Series

An autospectrum is a function that transforms a time series function into a frequency dependent function. This makes it possible to clearly see what frequencies (or periods) are the most prevalent in the time series. It is, for example, hard to see the periods of the load graphed in the time series shown in Figure 13, but when looking at the autospectrum, it becomes apparent that most of the loads have a period of 9s-13s.

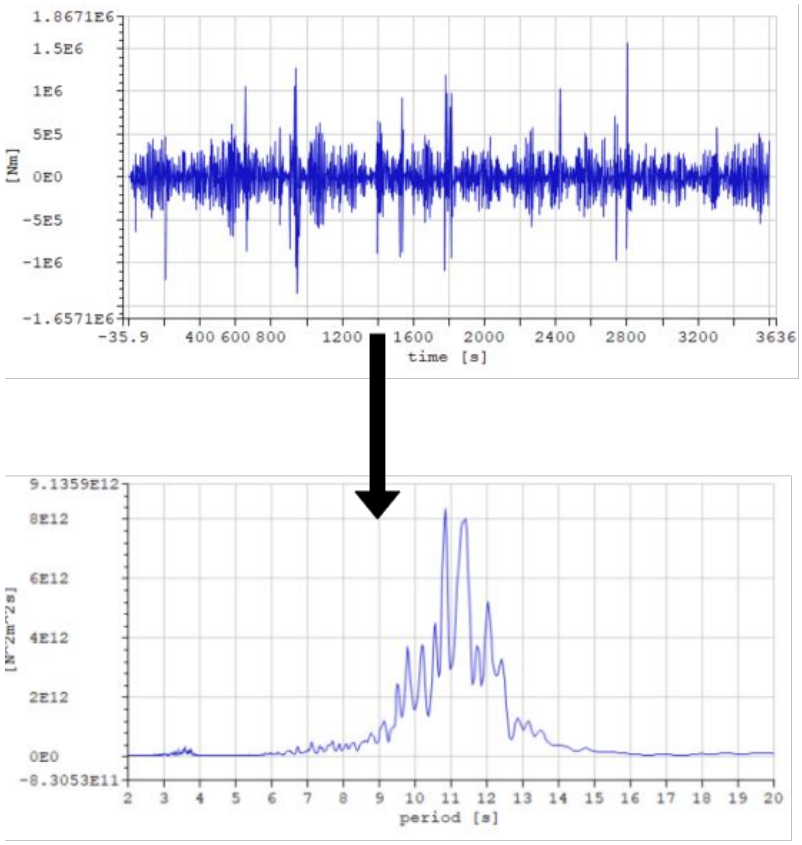

Figure 13: An example of an autospectrum of a time series

The autospectrum in the frequency domain $S_{xx}(f)$ of a time series $x(t)$ is found from the Fourier transform of the time series Equation 54. In this report all autospectrum functions are shown in the period domain.

$$S_{xx}(f) = \int |x(t) \cdot exp(-2\pi i \cdot f \cdot t)| dt \tag{54}$$

Autospectrum smoothing

There is a high level of randomness in many time series data, which causes the autospectrum to vary a lot for neighboring periods. To make the autospectra easier to read, a weighing function is introduced Equation 55. The default weight parameter in SIMA is m=3, but in this report m=20 is used as it gives smoother functions that are easier to discuss.

$$f_{weight\ function} = 1 - cos(\frac{\pi k}{m+1}), \qquad k = 1, 2, ..., 2m+1 \tag{55}$$

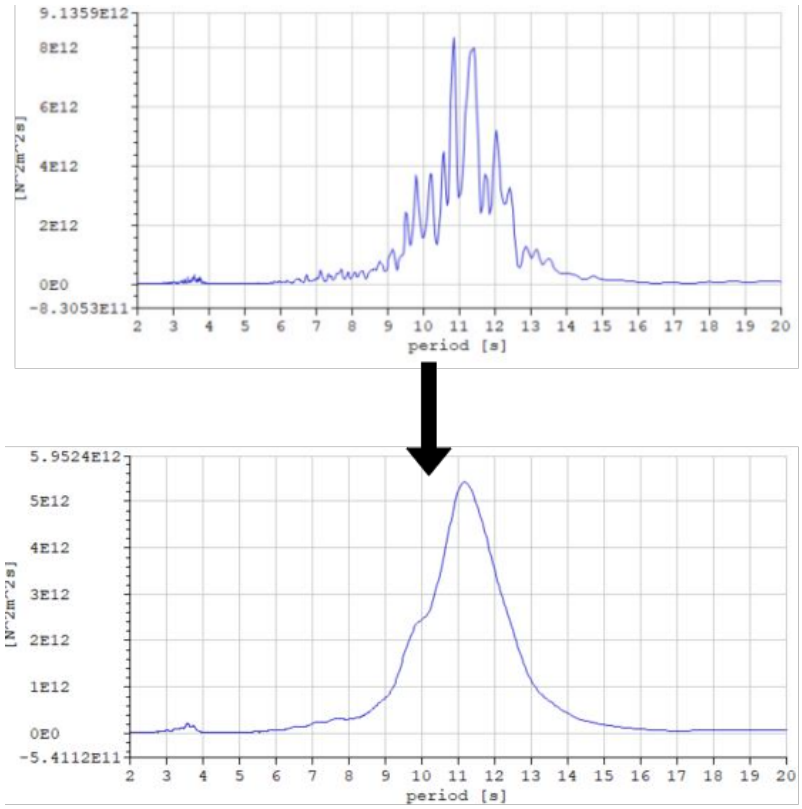

Figure 14: The effect of going from using smoothing parameter m=3 to using m=20

Combining autospectra

In this report the orientation of the coordinate system of the model in relation to the measurements are not known. This makes in necessary to combine autospectra of a load in x- and y-direction so that this combined autospectrum can be compared between the model and the measurements. This is done by calculating the autospectrum in both x- and y- direction individually, and then combining them through SRSS of the individually calculated autospectra.

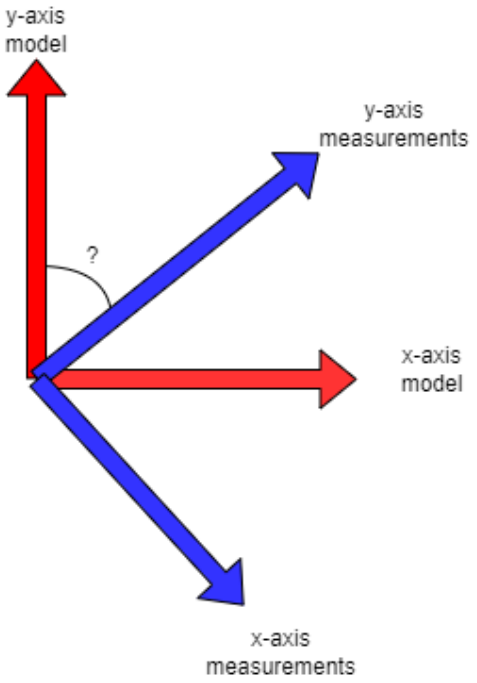

Figure 15: Illustration of the different coordinate systems

5 Modeling of a Top Tensioned Riser System

In this report, the riser system of a semi-submersible, mobile drilling rig operating at a depth of 112 meters shall be modeled, and the results from the numerical modeling shall be compared with real life measurements from a drilling campaign. In this section, the main components of the system will be described and a description of how they have been modeled in SIMA/RIFLEX will be presented.

For shallow waters, the rig's riser system looks, in principle, as shown in Figure 17. In the SIMA model, the rig itself is treated as a Support Vessel, with first order motion transfer functions provided from Equinor, a subset of which can be found in Appendix A.

The riser system is modeled as three connected lines: the well, the riser, and the tensioner system. Additional lines are used to model the tensioner wires in the tensioner system. Each of these lines are described in the following sections.

5.1 Well

The interaction between the riser and the well is highly important and complex. In the real system, the well goes from the sea bed and down hundreds of meters. However as the well gets deeper, it becomes statically fixed in the soil. Below 60 meters, there will be negligible movements in the well, so it is unnecessary to model the parts of the well below this point. The well is modeled as a line going from the WH 3.2 meters above the sea bed (a supernode called well_head, which is free in translation and rotation) to 60 meters down in the soil (a supernode called soilNode, which is fixed in translation and z-rotation). The interaction between this line and the soil is modeled as multiple non-linear global springs, with the stiffness depending both on displacement and depth, as the different compositions of the soil give different stiffness.

The supernode called soilNode is fixed in z-rotation. This is non-physical, but it is necessary to make the system statically determined, the soil stiffness at these depths will be so stiff that there would not be any significant rotation in soilNode.

5.1.1 Composition of Well Line

The well line itself is not hard to model, but it will experience minor changes throughout the drilling operation, as can be seen in Table 3. Hence for operations before 04.12.2012, only the conductor and surface casing will be a part of the well, but for operations after this date, the well will also consist of a 13 3/8" casing. For operations after 10.12.2012 a 9 5/8" casing (the liner) will also be a part of the well. For simplicity, the effect of these extra components will be neglected, while EI, EA and mass of the well will be calculated based on the conductor casing and the surface casing as given in Table 4.

Casing	Weight [tons]	Date of landing
13 3/8" casing	approx. 90	04.12
9 5/8" casing	approx. 100	10.12

Table 3: Components of the well and the time intervals they are added to the well

	Cross sectional area $[m^2]$	Outer Radius $[m]$	I $[m^4]$	E [GPa]
Conductor casing	0.086647	0.318	0.0056914	202
Surface casing upper section	0.044743	0.254	0.001284	202

Table 4: Important characteristics of the largest components of the well, given by Equinor

With these assumptions, EA, EI and mass per unit length are as follows:

$$EA = 0.086647m^2 \cdot 202GPa + 0.044743m^2 \cdot 202GPa = 26.54 \cdot 10^9 \frac{Nm^2}{m^2}$$

$$EI = 0.0056914m^4 \cdot 202GPa + 0.001284 \cdot 202GPa = 1.409 \cdot 10^9 Nm^2$$

$$w = 7750kg/m^3 \cdot (0.086647m^2 + 0.044743m^2) = 1018kg/m$$

5.1.2 Soil Springs

As recommended by DNV GL, the soil is modeled as a series of non-linear springs along the well [5], as illustrated in Figure 16. The stiffness of the soil springs has been determined by taking samples of the soil close to where this operation was executed and then setting the stiffness based on the contents of the soil. The samples were only collected down to 9.2 meters. The samples consisted of clay and sand. Below the point where samples were taken, the soil has been assumed to consist of sand, as most movements of the well is in the upper layers of the soil, this assumption should not give rise to major errors. Appendix B shows the non-linear stiffness of each spring along the riser.

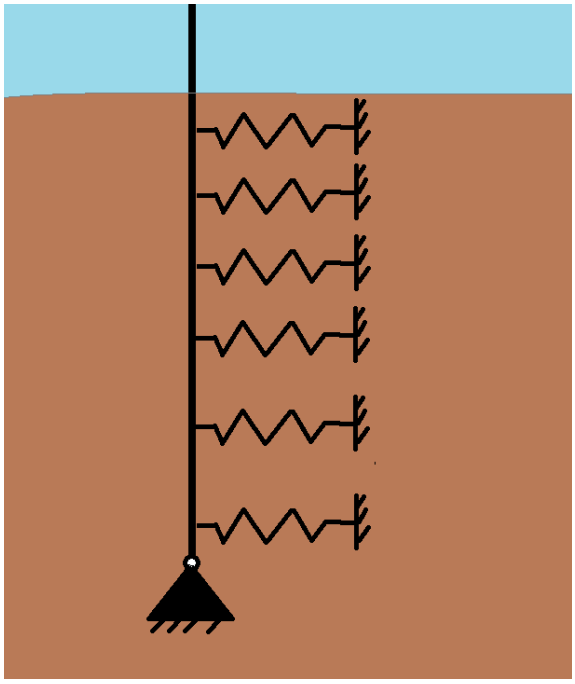

Figure 16: Sketch showing how the soil is modeled as multiple non-linear springs along the well

The soil spring's stiffness in Appendix B has been calculated based on the recommendations in API RP2 GEO "Geotechnical and Foundation Design considerations" [8]. The entire calculations are fairly complicated, and most of the work in procuring these soil springs were done by Equinor, but the main steps are as follows:

1. The ultimate resistance force per unit length for sand and clay are calculated based on empirical models, which depends on depth in the soil, composition of the soil, and the outer diameter of the well. It should be noted that the ultimate resistance force is calculated with an assumption that low ultimate resistance force is conservative.

2. The soil is divided into sections with small changes in ultimate resistance force per unit length over the section (parts of the soil with similar composition and relatively small changes in depth).

3. The resistance force per unit length over the section is multiplied with the length of the section.

4. Lateral soil resistance-displacement curves for each section is made based on empirical models for sand and clay, these models are a function of the resistance force. With the assumption that low ultimate resistance force is conservative from the 1. step, the springs are made so that they are more likely to be too soft than to be too stiff.

5.2 Riser Line

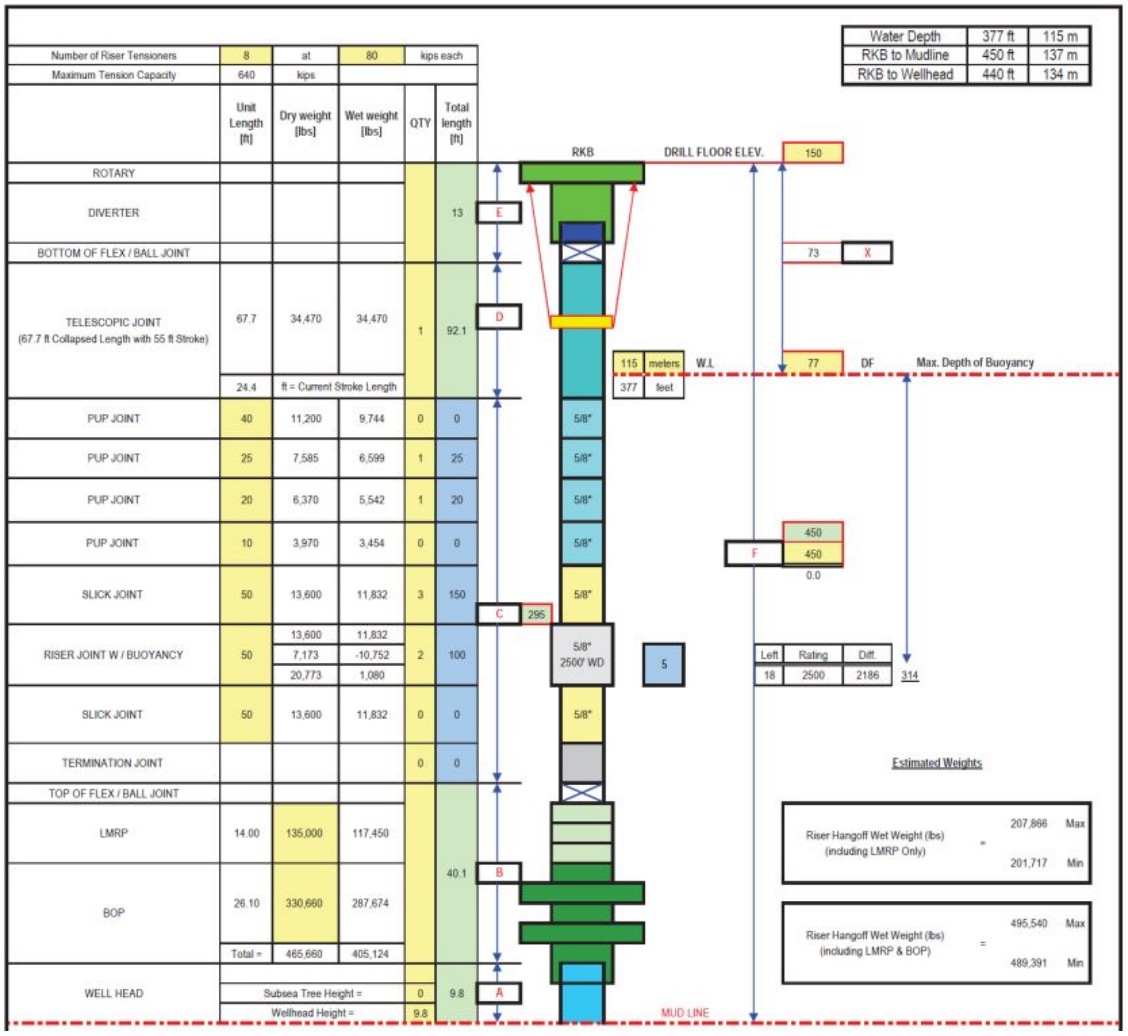

Figure 17: Overview of the riser system on the semi-submersible rig. It should be noted that this is for 115 m, not 112 m, this is handled by using shorter pup joints. This drawing has been provided by Equinor.

The riser line starts in the supernode called well_head, and ends up in a supernode called tensionerRingNode (free in translation and rotation) at 8.858 meters above the surface. The riser line represent the main part of the riser system, and it is modeled as a long line with different cross sections to represent the different components of the riser system. This entire line has an internal area of $0.19765m^2$ corresponding to an internal diameter of 19.75 inches, which is true, for the riser

joints. For the BOP and LMRP the same internal area has been modeled, while the real internal area is a bit more complicated for these components. The internal area for the entire line is filled with a fluid with density of $1600kg/m^3$, this corresponds to recommendations from Equinor.

5.2.1 BOP

The BOP is 7889.4 mm tall, and goes from the wellhead connection to the LMRP connector. Its weight can be found in Figure 17: $330660lbs = 149957.6kg$, giving it a mass coefficient of $19007kg/m$. The wet mass of the BOP can also be found in Figure 17, and it is $287674lbs = 130486.7kg$.

$$A_{external} = \frac{m_{dry} - m_{wet}}{L \cdot \rho_w} + A_{internal} \tag{56}$$

Now $A_{external}$ can be calculated from Equation 56, and the resulting value is $A_{external} = 2.6054m^2$.

$$A_{external} = \frac{149957.6kg - 130486.7kg}{7.8894m \cdot 1025kg/m^3} + 0.19756m^2 = \underline{\underline{2.6054m^2}}$$

As can be seen in Figure 19, the BOP is a complicated component with valves and monitoring systems to control pressure entering the riser. This makes it hard to estimate the drag and added mass forces on this component. However Equinor has tested this in lab conditions, and the results can be found in Figure 18 [2]. Here, buoyancy diameter is used based on the sum of $A_{external}$ as in Equation 57. This gives a buoyancy diameter of $1.82m$, which is set as hydrodynamic diameter. With a proper hydrodynamic diameter set, the drag coefficient can be set at $C_d = 4.5$ and the added mass coefficient can be set at $C_a = 1.1$. As the cross-sections are modeled as axi-symmetric, the direction which gives the lowest C_a and C_d in Figure 18 are now considered, this will be discussed further in Section 11.5.

$$D_{buoyancy} = \sqrt{\frac{4A_{external}}{\pi}} \tag{57}$$

BOP category	Added mass coefficient		Drag coefficient		Reference diameter
	C_{ax}	C_{ay}	C_{dx}	C_{dy}	
Medium / Small	1.1	1.4	4.0 - 5.5	5.0 – 10.0	Buoyancy
Large (> 300 metric tonnes mass)	1.5	2.0	8.0 - 13.0	15.0 - 25.0	diameter

Figure 18: BOP drag coefficients used by Equinor. The BOP considered in this report is characterized as a medium/small BOP

The BOP has also been modeled as very stiff: $EA = 1.0 \cdot 10^{13}N$, $EI = 1.0 \cdot 10^{13}N/m^2$, in reality it is probably less stiff, but it will generally have very limited displacements relative to the rest of the riser.

5.2.2 LMRP

The LMRP is 4653.4 mm tall from the LMRP connector hub face to the riser adapter. From Figure 17, its dry weight can be found at $135000lbs = 61235.0kg$ and its wet weight can be found to be $117450lbs = 53274.4kg$. This gives a mass coefficient of $13159kg/m$ and an external area of $1.8665m^2$.

$$A_{external} = \frac{61235.0kg - 53274.4kg}{4.6534m \cdot 1025kg/m^3} + 0.19756m^2 = \underline{\underline{1.8665m^2}}$$

Similar to the BOP, the LMRP is a complicated component. Hence when it comes to stiffness, it has been modeled just as the BOP, meaning $EA = 1.0 \cdot 10^{13}N$ and $EI = 1.0e \cdot 10^{13}N/m^2$. The buoyancy diameter is calculated according to Equation 57 and comes to $D_{buoyancy} = 1.54m$. Setting $D_{buoyancy}$ as hydrodynamic diameter, the same drag and added mass coefficients as in Section 5.2.1 can be used ($C_d = 4.5$ and $C_a = 1.1$).

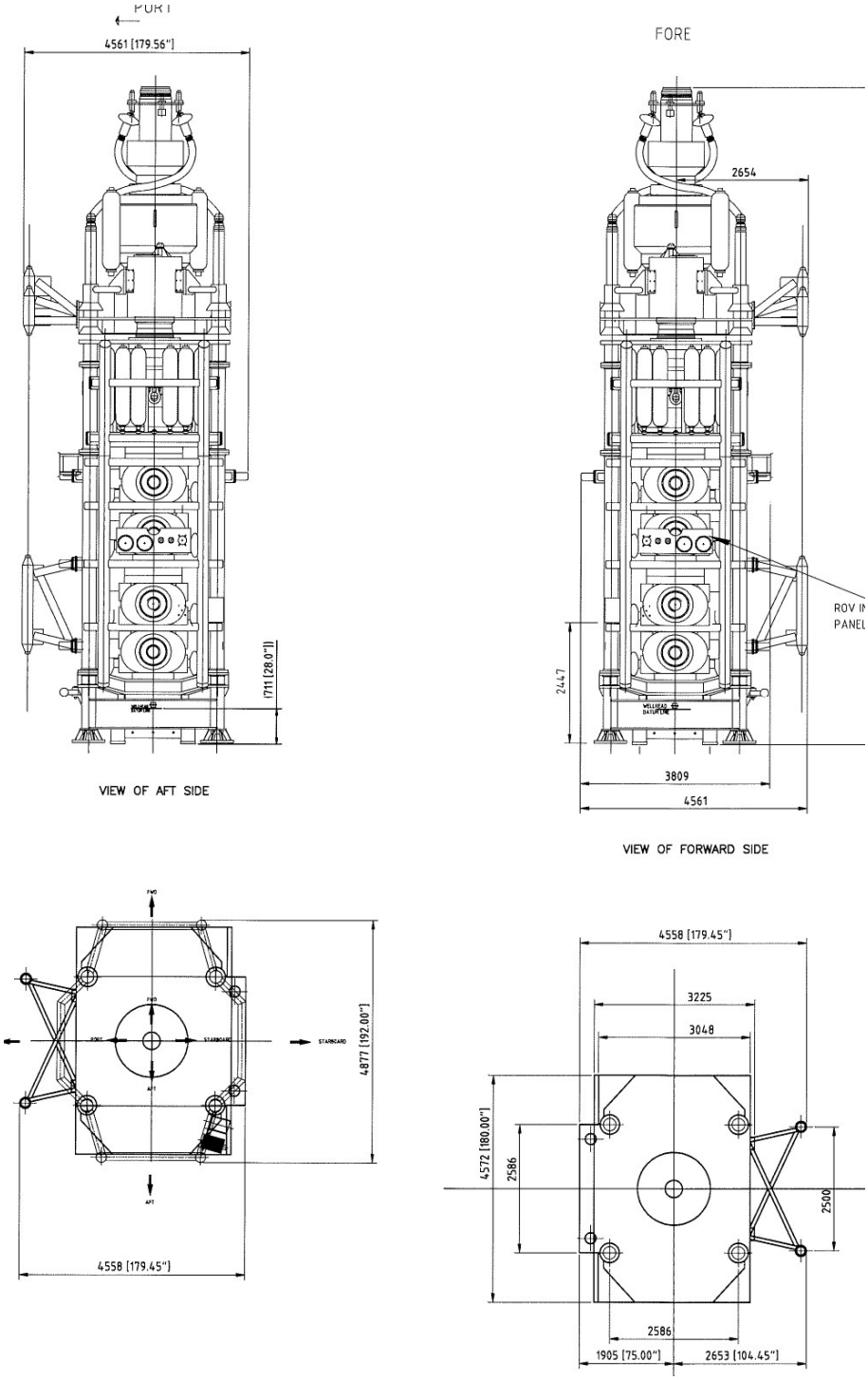

Figure 19: BOP with LMRP illustration, provided by Equinor

5.2.3 Lower Flex Joint (LFJ)

The lower flex joint is a complex component. It allows the lower section of the riser to rotate while causing limited loads on the BOP and wellhead. It is a part of the LMRP, and is modeled as a nodal component 2.8 meters above the connection between LMRP and BOP. The LFJ is modeled as a component with rotational stiffness and damping. The damping is in reality non-linear, being 60kNms/deg up to 0.25 degrees and then getting less damped, lessening to a level just above 44kNms/deg. As non-linear damping in a flex joint is not supported by RIFLEX, linear damping of 60kNms/deg is used. For lower riser rotations below 0.25 degrees, this simplification is valid. For lower riser rotations above 0.25 degrees, this simplification is non-conservative, as the damping in reality should be lower. But as rotational speed is highest in rotations around zero, and the lessening of damping is gradual, this non-conservative simplification should not have a large effect. This assumption is investigated in Section 11.4. The rotational stiffness of the LFJ is simply modeled as a non-linear spring with stiffness as seen in Figure 20.

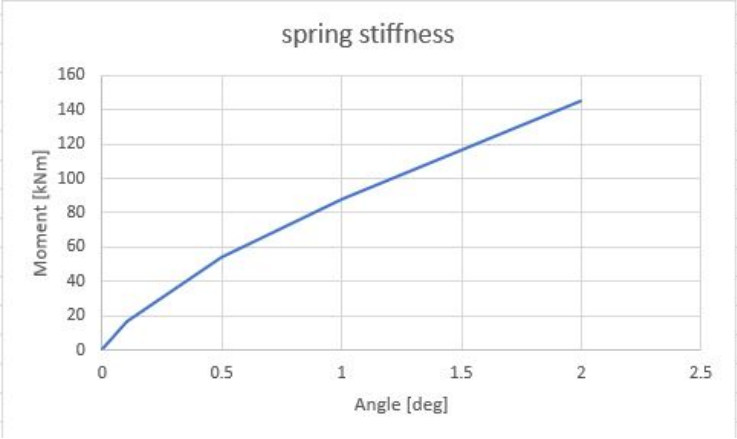

Figure 20: Non-linear stiffness of the LFJ, provided by Equinor

5.2.4 Riser Joints

The riser system considered in this report has three different kinds of riser joints as can be seen in Figure 17. They are called Slick joints, Riser Joints W/ Buoyancy and Pup joints.

Slick Joints

These are normal ,$50ft = 15.24m$ long riser joints. They consist of the main steel pipe and three smaller pipes, one booster line, one kill line and one choke line. The main pipe has an inner diameter of $502mm$ and an outer diameter of $533mm$. The kill and choke lines have inner diameters of $76mm$ and outer diameters of $127mm$. The booster line has an outer diameter of $114mm$ and an inner diameter of $98mm$. Figure 21 illustrates the location of these lines in relation to one another. The kill, choke and booster lines are free to move axially, so they will not contribute to the axial stiffness of the riser joints.

With all the important dimensions known, the axial stiffness can be calculated. The total steel area can be calculated as follows:

$$A_{steel} = \frac{\pi(0.533^2 - 0.502^2)m^2}{4}$$

$$A_{steel} = 0.0252m^2$$

With the knowledge that steel has an elastic Young's modulus of $202GPa$, the axial stiffness is $EA = 5.09 \cdot 10^9 \frac{Nm^2}{m^2}$.

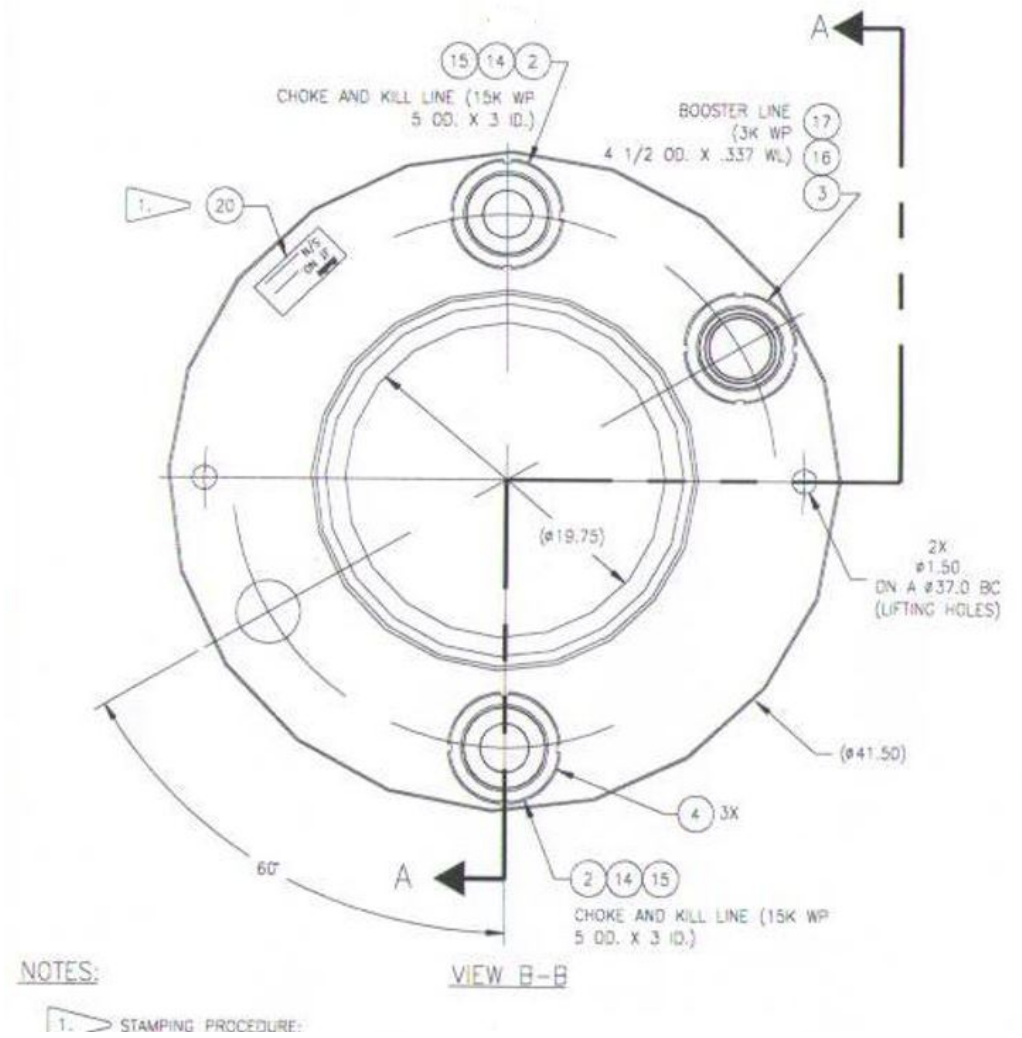

Figure 21: The cross section of a slick joint, provided by Equinor

Next, the bending stiffness needs to be calculated. To do that, the second moment of inertia must be known. The booster line, the choke line and the kill line are, as mentioned, free to move axially. This means that they will experience bending along their local axis and not along the axis of the entire cross-section. Therefore the contribution from the parallel axis theorem is zero, and the second moment of inertia of the riser joint's cross-section can be calculated as follows:

$$I_{steel} = \frac{\pi(0.5334^4 - 0.5016^4)m^4}{64} + 2 \cdot \frac{\pi(0.127^4 - 0.0762^4)m^4}{64} + \frac{\pi(0.1143^4 - 0.098^4)m^4}{64}$$
$$= \underline{8.968 \cdot 10^{-4}\, m^4}$$

This gives a bending stiffness of $EI = 181.5 \cdot 10^6\ Nm^2$, with the assumption that $E = 202GPa$.

The hydrodynamic diameter is complicated for this cross section. To find it conservatively the main pipe can be considered to be in line with the kill and choke lines, as drawn in Figure 22. This gives a hydrodynamic diameter of $787mm$ ($127mm + 533mm + 127mm$). Since there could be some flow interaction between the pipes, combining this hydrodynamic diameter with a drag coefficient of 1.1 will allow the model to accurately reflect the properties of the real slick joints. The added mass components of Morrison's equation is proportional to the hydrodynamic diameter squared, leading the added mass coefficient needs to be calculated as in Equation 58, resulting in $C_a = 0.51$.

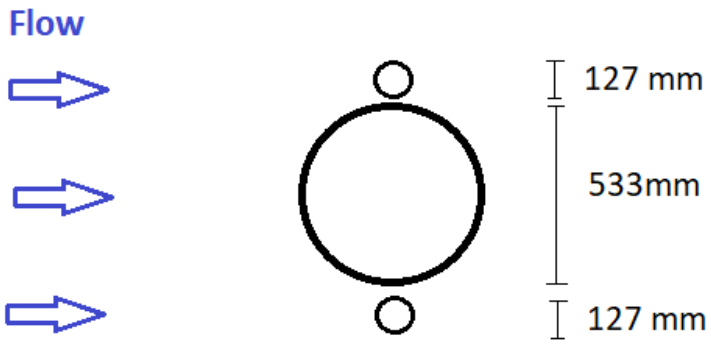

Figure 22: The assumed direction the hydrodynamic diameter for the riser joint is based on

$$C_a{}^*{}_{total} \cdot {D_H}^2 = C_a{}^*{}_{main\ pipe} \cdot {D_{main\ pipe}}^2 + 2 \cdot C_a{}^*{}_{kill/choke\ line} \cdot {D_{kill/choke\ line}}^2 \tag{58}$$

$$C_a{}^*{}_{total} = \frac{C_a{}^*{}_{main\ pipe} \cdot {D_{main\ pipe}}^2 + 2 \cdot C_a{}^*{}_{kill/choke\ line} \cdot {D_{kill/choke\ line}}^2}{{D_H}^2}$$

$$C_{a\,total} = \frac{1 \cdot 0.533^2 + 2 \cdot 1 \cdot 0.127^2}{0.787^2} = 0.51$$

The dry and wet mass of the slick joint can be found in Figure 17, and are $13600lbs = 6168.9kg$ and $11832lbs = 5366.9kg$ respectively. This gives a mass coefficient of $404.8kg/m$ and an external area of $0.2489m^2$

$$A_{external} = \frac{6168.9kg - 5366.9kg}{15.24m \cdot 1025kg/m^3} + 0.19756m^2 = \underline{\underline{0.2489m^2}}$$

In this configuration, three slick joints totaling a length of $45.72m$ is used. These starts at the top of the riser joints with buoyancy, and ends up at the pup joints.

Riser Joints w/ Buoyancy

These riser joints are similar to Slick Joints, but to increase buoyancy, a set of buoyancy modules made of lighter-than-water-polymer are clamped to the riser line, as can be seen in Figure 23. These polymers have far lower Young's modulus than steel, and they are clamped in a way which allows them to have limited contributions to the stiffness of the riser joint. The axial and bending stiffness will therefore be modeled as identical to the slick joint. However, buoyancy modules will increase the hydrodynamic diameter, the mass coefficient, and the external area.

The dry and wet weight can be found in Figure 17, and are $20773lbs = 9422.5kg$ and $1080lbs = 489.9kg$ respectively. This gives a mass coefficient of $618.3kg/m$ and an external area of $0.7694m^2$. This external area is substantially lower than what an outer diameter of $1118mm$ indicates. The reason for this discrepancy is that the buoyancy modules have multiple cavities, for example to give room to the choke, kill, and booster lines; these cavities get filled with seawater, which becomes part of the added mass.

$$A_{external} = \frac{9422.5kg - 489.9kg}{15.24m \cdot 1025kg/m^3} + 0.19756m^2 = \underline{\underline{0.7694m^2}}$$

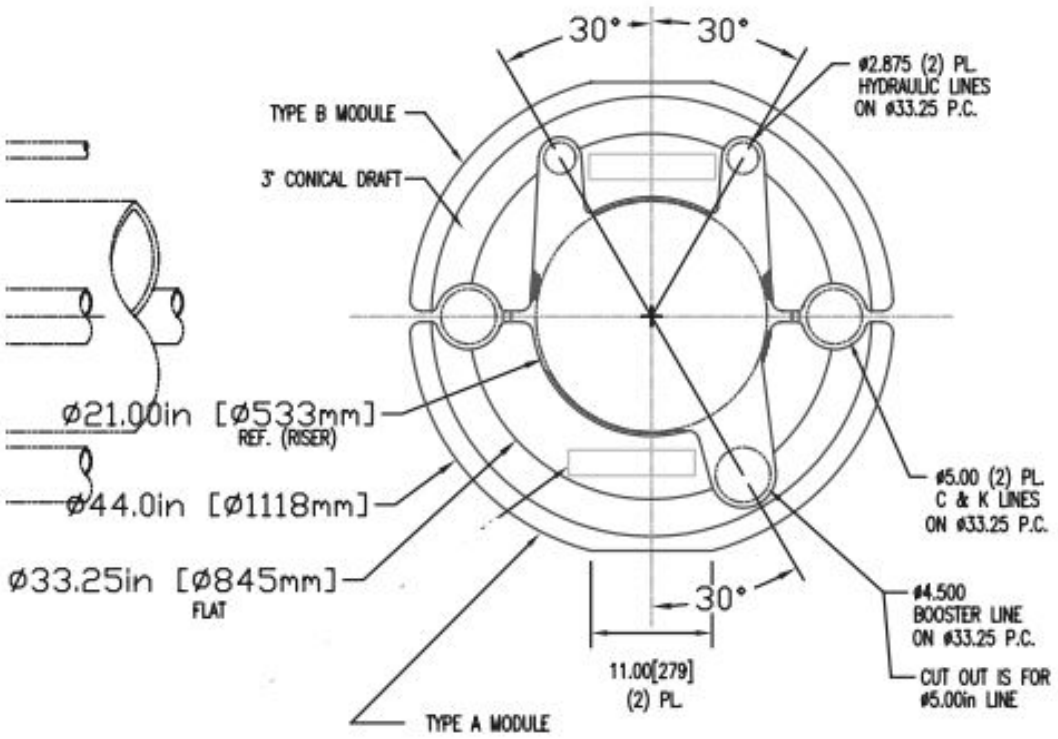

Figure 23: The polymers around riser joints, provided by Equinor

As the riser joints w/ buoyancy has a cylindrical cross-section, the hydrodynamic parameters are fairly straight forward to calculate. The hydrodynamic diameter can be taken directly from the diameter in Figure 23, $D_H = 44in = 1118mm$. Both the drag and mass coefficient simply becomes 1.0, as this is simply a cylinder moving in water.

In this configuration, two riser joints with buoyancy are used. They total $30.48m$ in length, and starts at the top of the LMRP and ends at the bottom of the slick joints.

Pup Joints

Pup joints can be described as shorter slick joints that are used to fine tune the length of the riser system for different water depths. They have the same stiffness as the slick joints: $EA = 5.09 \cdot 10^9 \frac{Nm^2}{m^2}$ and $EI = 181.5 \cdot 10^6\ Nm^2$, and the same hydrodynamic parameters are used. Their mass coefficient and external area are in reality marginally higher, but also these values are considered as the same as in the slick joints.

There has not been spent any time adjusting the right number of the different pup joints, so the model simply uses $10.29m$ of pup joints from the slick joints to the bottom of the telescope joint.

Rayleigh Damping

Equinor has done analyses on the riser joints with the conclusion that the riser joints with buoyancy has a critical damping ratio of 2.5% to 3.0%, and the slick joints have a critical damping ratio of 0.3% to 0.5%. The values depend on several factors, including amplitude and riser length. To be conservative, the lowest of the values are used.

To most accurately set the Rayleigh damping coefficients, one should ideally have the damping ratio for at least two different frequencies, so that both the mass proportional damping coefficient α_1 and the stiffness proportional damping coefficient α_2 can be calculated. Rayleigh damping is by far most important in relation to the main eigenmodes. Hence α_1 can be set to zero, and then α_2 can be found from Equation 59, so that it matches with the eigenfrequency of the first eigenmode. The eigenmodes are discussed in Section 6, and the eigenperiod of the first eigenmode is $T_n = 7.43s$, corresponding to an angular frequency of $\omega = 0.85\, rad/s$.

All this results in $\alpha_2 = 0.058$ for the riser joints with buoyancy and $\alpha_2 = 0.0070$ for the slick joints and pup joints.

$$\lambda_i = \frac{1}{2}(\frac{\alpha_1}{\omega_i} + \alpha_2\omega_i) \tag{59}$$

The rest of the components have zero Rayleigh damping in the model, but the riser joints are the largest components, so the Rayleigh damping is most important in relation to them.

5.3 Telescopic Joint

The telescopic joint consists of one outer barrel and one inner barrel. The inner barrel can move freely in and out of the outer barrel, so that heave motions from the rig does not put tension onto the riser.

This is challenging to model in RIFLEX, but it has been done by modeling the outer barrel as one normally would, while giving the inner barrel an extremely low axial stiffness. That way, the inner barrel will shorten and elongate as the rig moves up and down, mimicking how the real inner barrel moves in and out of the outer barrel. To do this, it is important to only model the inner barrel with one element. If it is modeled with multiple elements, the lower elements will compress until they get zero length, which causes numerical instability, and results in the model crashing.

The total mass of the telescopic joint is $15635kg$, which has been divided into $13409kg$ in the outer barrel and $2229kg$ in the inner barrel to make it possible to model. With a length of $20.63m$, the outer barrel gets a mass coefficient of $650kg/m$ in the model. The outer barrel has an outer diameter of $904.9mm$, which is also its hydrodynamic diameter. As this component is partly submerged, no wet mass is given, and subsequently, the external area can not be calculated according to Equation 56, as has been done for previous components. Additionally, the outer surface of the outer barrel has a simple cylindrical shape, making it sensible to calculate $A_{external}$ as a circle with an outer diameter of $904.9mm$. This results in $A_{external} = 0.6431m^2$. The inner barrel gets a mass coefficient of $300kg/m$ due to its length of $7.43m$. The hydrodynamic diameter and external area of the inner barrel are irrelevant as it is not submerged.

Most of the outer barrel ($18.63m$) is modeled as a part of the riser line, ending in a supernode called tensionerRingNode. The rest of the telescopic joint is modeled as its own line, colored in pink in Figure 25, ending up in the top of the riser system in a supernode called upperFlexJointNode. This node is fixed in the local coordinate system of the drilling rig, rather than the global coordinate system, as this node is the point of connection between the rig and the riser.

5.3.1 Upper Flex Joint (UFJ)

At the top of the riser sits an upper flex joint, it is the small pink ball illustrated in Figure 25. It is modeled as a linear spring on top of the telescopic joint, with a rotational spring-stiffness at $10Nm/deg$ around the local y- and z-axes. This flex joint limits the moments transferred from roll and pitch motions in the rig onto the riser system. This is, in reality, a ball joint that ideally should have close to zero stiffness, but this will functionally be the same, and it is necessary to make the model stable.

5.4 Tensioner System

The tensioner system has been modeled by creating four pre-tensioned lines. All four lines are connected to a slave-node, with tensionerRingNode as its master, in one end and a node at the elevation of the drilling floor in the other end. There is some angle between these supernodes, to mimic the transverse forces from the original system on the riser, but this angle is not equal to that of the real system.

No	Relative Elongation	Axial Force
1	0.0	0.0
2	1.0	2.925e+05
3	13.517	3.25e+05
4	27.035	3.575e+05

Figure 24: Axial stiffness of the tensioners

The tensioner lines are made as bar elements with non-constant axial stiffness, the given axial stiffness can be seen in Figure 24. By then setting the stress free length to be 1 meter, the tensioner lines will be elongated 13.517 times (the distance between the supernodes the tensioner lines are connected to is $13.517m$), so that it will exert a force of $3.25 \cdot 10^5\ N$ (1.3MN divided by 4) to the tensionerRingNode. The axial stiffness in Figure 24 is calculated from a single variable given to the system called Top_tension, which will be the total force from the tensioner lines acting on the tensionerRingNode.

As can be seen in Figure 24, the axial force increases slightly above this level (the Top_tension divided by 4) for higher elongation, and decreases slightly below this level for lower elongation. This is done to make sure that the tensionerRingNode finds a stable balance-point.

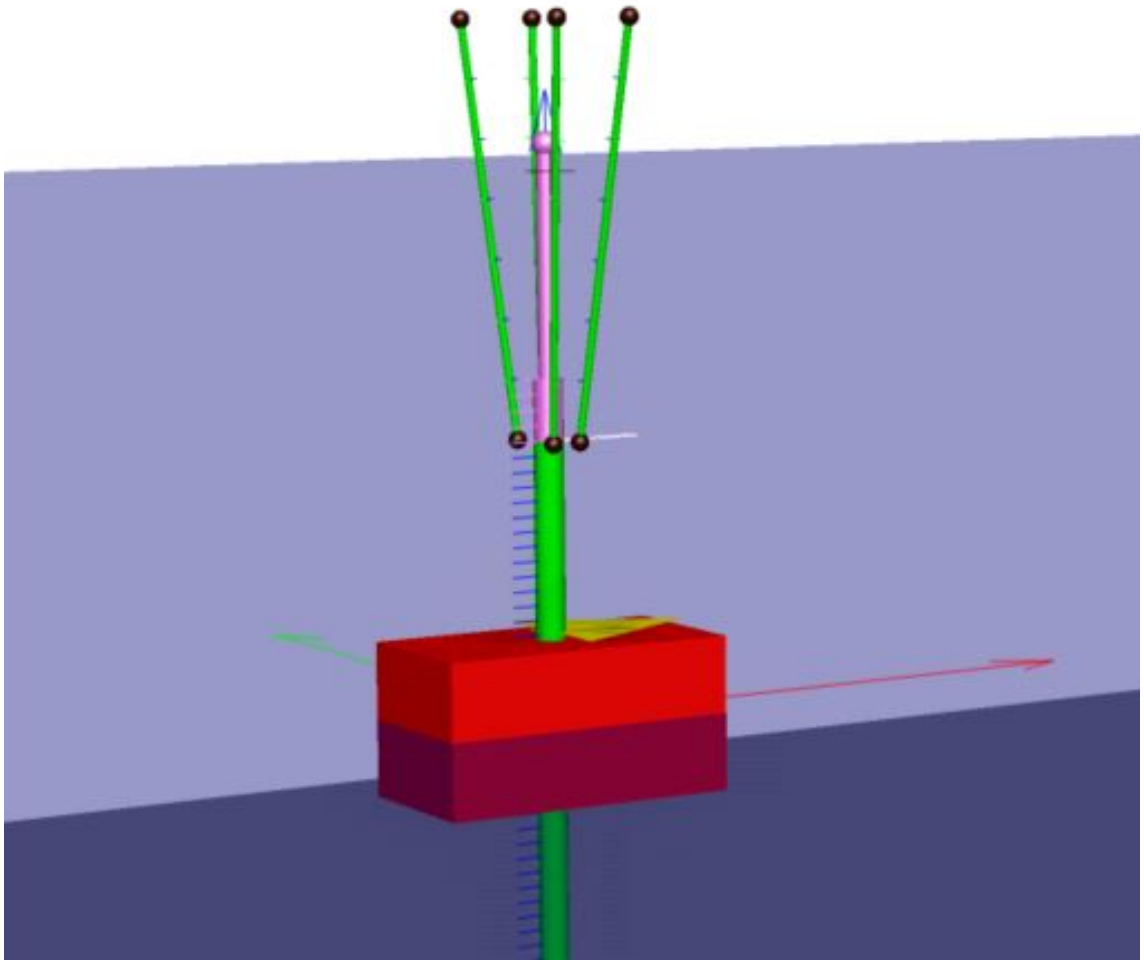

Figure 25: Screenshot of the top part of the riser model, showing the tensioner system

5.4.1 Calibrating the Top Tension

It is necessary to have positive effective tension in the connection point between LMRP and BOP. For this system, that positive effective tension have to be around 20-25 tons, or about 0.20-0.25MN for the LMRP to be able to disconnect in case of an emergency, according to Equinor.

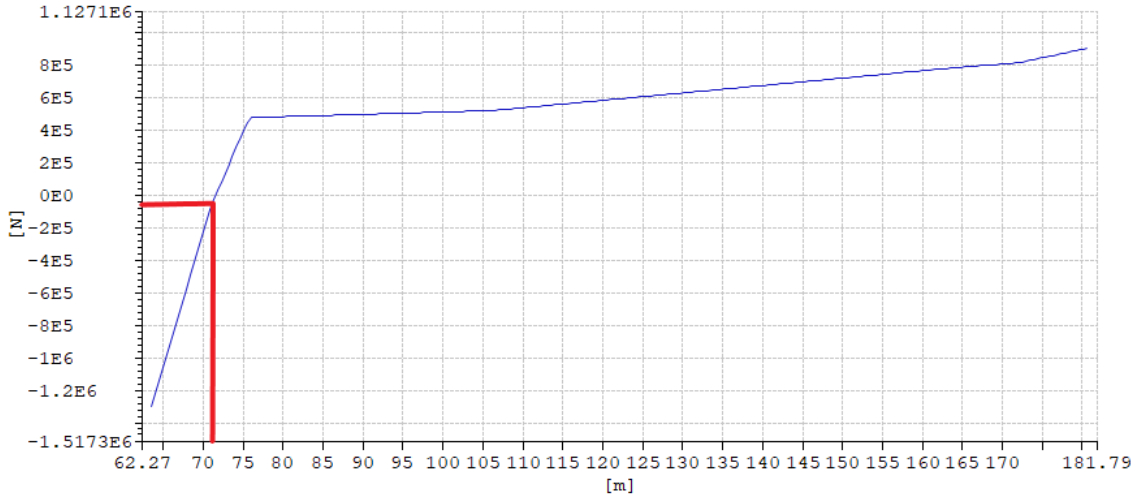

Figure 26: The effective tension throughout the riser line with a top tension of 1.0 MN, the red line indicates the connection point between BOP and LMRP

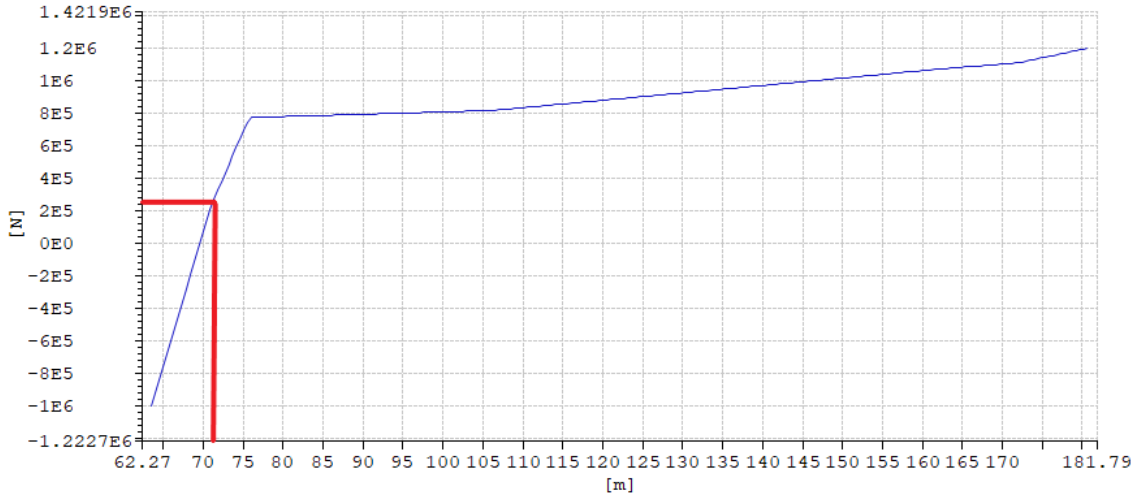

Figure 27: The effective tension throughout the riser line with a top tension of 1.3 MN, the red line indicates the connection point between BOP and LMRP

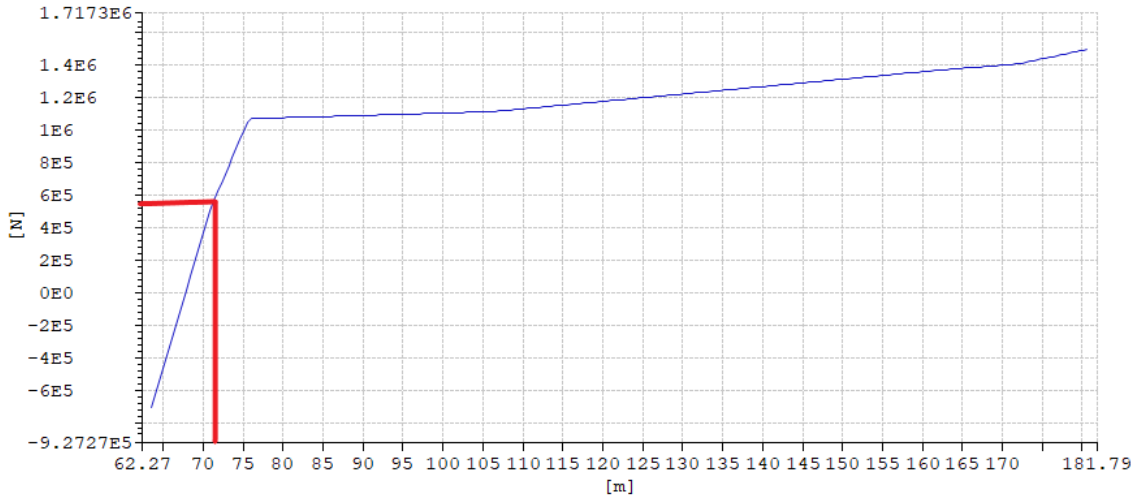

Figure 28: The effective tension throughout the riser line with a top tension of 1.6 MN, the red line indicates the connection point between BOP and LMRP

In the three figures above, the effective tension throughout the riser line is shown for different top tensions, which have been calculated through static analysis. The x-axis shows the length in relation to the lowest point in the model (60 meters below the surface), which means that the riser line starts at 63 meters. In the graphs, the connection point between LMRP and BOP is at around 70.9 meters on the x-axis, this point is found by summing 63m (the height of the supernode well_head) with 7.9m (the height of the BOP).

For the effective tension of 1.0MN, this corresponds to around -0.05MN at the connection point. If the top tension used was this low, the LMRP would not be able to disconnect if needed. By increasing the top tension by 0.3MN to 1.3MN, the effective tension in the point between LMRP and BOP also goes up by about 0.3MN to 0.25MN. This corresponds well with the needed overpull to disconnect the LMRP, hence 1.3MN is the top tension used in the model. The cusp at around 75 meters marks the connection point between the riser joints and the LMRP. Both the LMRP and the BOP are extremely heavy in water compared to the riser joints with buoyancy, which are practically naturally buoyant. As the LMRP weighs about 55 tons in water ($\sim 0.55MN$), the overpull between LMRP and BOP can also be found by looking at the effective tension at this cusp and taking away the weight of the LMRP.

It should also be noted that for some drilling operations, the effective top tension might be substantially higher as a result of tension related to the drill string.

5.5 Summary

This subsection gives a short summary of the components of the model and their properties.

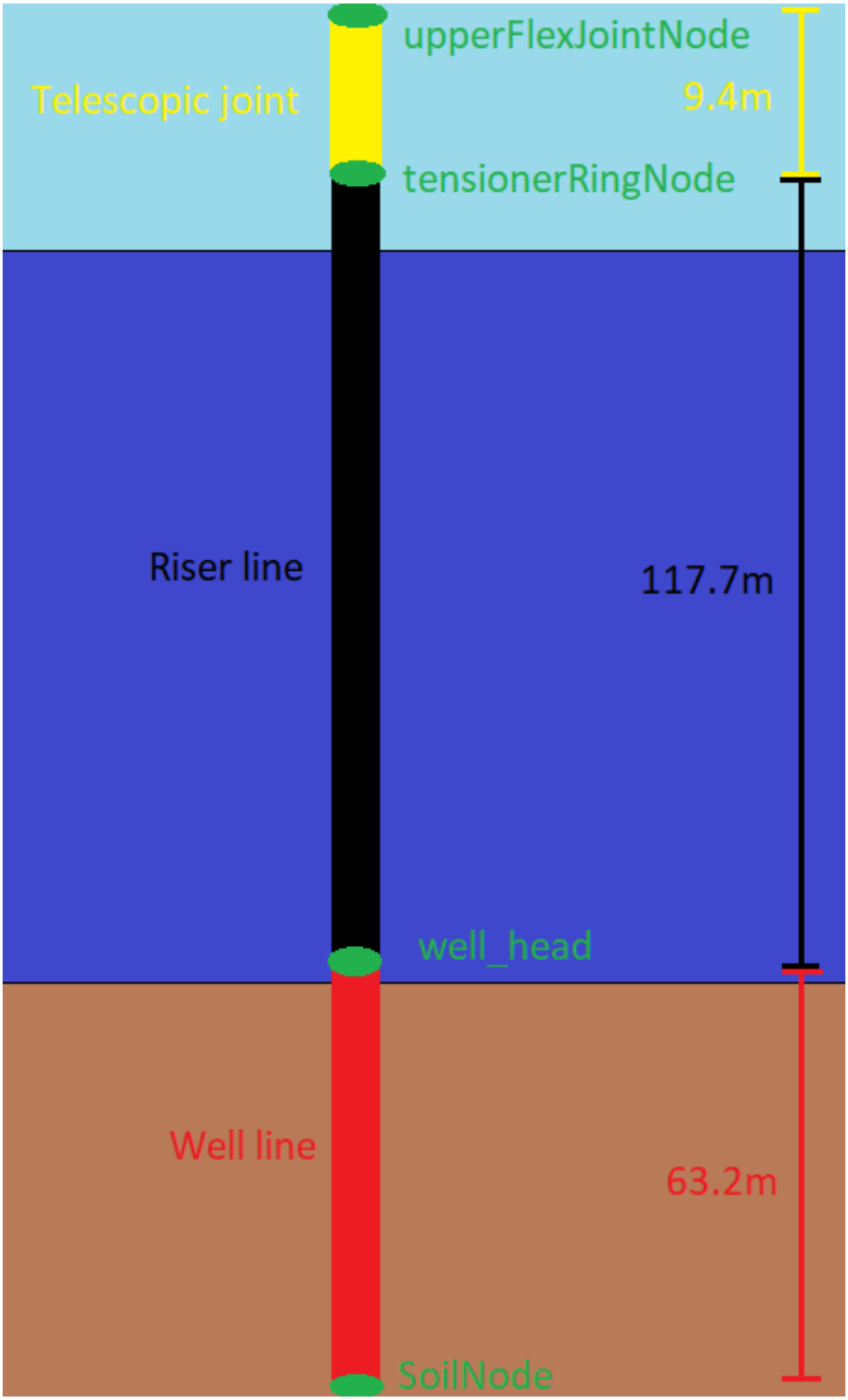

Figure 29: Illustration showing the lines and supernodes used in the RIFLEX model

5.5.1 Well Line

The well line is divided into 16 segments, numbering from 1, starting at soilNode, to number 16 ending at well_head, it has a layout corresponding to Table 6. The entire well have the basic properties, summarized in Table 5. 15 of the 16 segments has a soil spring connected to it, as seen in Table 6.

mass coefficient	EA	EI	Hydrodynamic parameters
1018 kg/m	26.5 GN	1409 MNm^2	NaN

Table 5: Basic properties of the well

Segment	Length $[m]$	Soil spring
1	20	Figure 74
2	10	Figure 73
3	5	Figure 72
4	5	Figure 71
5	4	Figure 70
6	2	Figure 69
7	2	Figure 68
8	2	Figure 67
9	2	Figure 66
10	2	Figure 65
11	2	Figure 64
12	1.5	Figure 63
13	0.5	Figure 62
14	1	Figure 61
15	1	Figure 60
16	3.2	above soil

Table 6: Layout of the well, with reference to the soil spring located in the middle of each component

5.5.2 Riser Line

The riser line starts with the BOP on the supernode called well_head, and ends with the lower part of the outer barrel in the supernode called tensionerRingNode. The properties of the components of the riser line can be found in Table 7.

Name	Length $[m]$	$A_{external}$ $[m^2]$	Mass coeff. $[kg/m]$	EA $[GN]$	EI $[MNm^2]$	D_H $[m]$	Cd	Ca
BOP	7.89	2.605	19007	10^4	10^7	1.82	4.5	1.1
LMRP under LFJ	2.81	1.866	13159	10^4	10^7	1.54	4.5	1.1
LMRP above LFJ	1.84	1.866	13159	10^4	10^7	1.54	4.5	1.1
Riser joints w/ buoyancy	30.48	0.770	618	5.09	182	1.118	1.0	1.0
Slick joints	45.72	0.249	405	5.09	182	0.787	1.1	0.51
Pup joints	10.29	0.249	405	5.09	182	0.787	1.1	0.51
Outer Barrel	18.63	0.642	650	6.22	274	0.905	1.0	1.0

Table 7: Components of the riser line and the properties of the components. The table also indicates the position of the components, with the BOP in the top being closest to the WH and the outer barrel being the farthest from the WH

5.5.3 Upper Section of Telescopic Joint

The upper section of the telescopic joint starts in the supernode tensionerRingNode, and ends in the supernode called upperFlexJointNode, it only consists of two components with properties outlined in Table 8. The properties of the telescopic joint are simulated by giving the inner barrel a very low axial stiffness, so that it will deform as the rig moves in heave.

Name	Length $[m]$	$A_{external}$ $[m^2]$	Mass coeff. $[kg/m]$	EA $[GN]$	EI $[MNm^2]$	D_H $[m]$	Cd	Ca
Outer Barrel	2.00	0.642	650	6.22	274	0.905	1.0	1.0
Inner barrel	7.43	-	300	10^{-8}	182	-	-	-

Table 8: The components and the properties of the upper section of the telescopic joint

6 Eigenvalues

An eigenvalue analysis has been made on the model described in Section 5, and the resulting eigenfrequencies and their associated periods can be seen in Figure 30. It is important to read this data with caution, the system is essentially symmetric along the global XY-axis, so one should expect all eigenvalues in the XY-axis to come in pairs, like the two first eigenvalues (with a period of 7.43s). Eigenvalues that do not come in pairs, like the 11th eigenvalue (with a period of 0.92s), are related to rotation in the riser around the global z-axis, or to axial eigenvalues. Such eigenvalues is not interesting in regards to general riser movements, and has not been a focus in this model. Only eigenvalues that do come in pairs are therefore considered in this report.

Eigenperiods of connected systems are complicated. In this connected system, there are mainly two modal movements, which results in eigenmodes being excited. The first one is a pendulum movement. As the heavy BOP moves from side to side, it will move as an up-side-down pendulum, with the soil springs and tension keeping it in place. The other movement will be a regular sinusoidal movement in the riser between the flex joints.

By considering a very simple model of the riser, as a combination of a tensioned string and a beam, with boundary conditions fixed in displacement, and free in rotation, an estimation for its angular eigenfrequencies can be calculated according to Equation 60.

	Eigenperiod	Eigenfrequencies
1	[s]	[1/s]
2	7.4349	0.1345
3	7.4349	0.1345
4	3.6166	0.2765
5	3.6153	0.2766
6	2.324	0.4303
7	2.324	0.4303
8	1.7409	0.5744
9	1.7406	0.5745
10	1.1013	0.908
11	1.1013	0.908
12	0.92353	1.0828
13	0.76899	1.3004
14	0.76899	1.3004
15	0.56202	1.7793
16	0.56202	1.7793
17	0.47479	2.1062
18	0.42089	2.3759
19	0.42089	2.3759
20	0.33005	3.0298
21	0.33005	3.0298

Figure 30: Table showing the 20 first eigenperiods and their associated eigenfrequencies of the combined system

$$\omega_{bs} = \frac{i\pi}{L}\sqrt{\frac{T}{m_{total}} + \frac{i^2\pi^2}{L^2}\cdot\frac{EI}{m_{total}}} \quad (60)$$

To be able to use Equation 60, some assumptions need to be made. The bending stiffness and the mass can be set according to the riser joints. The bending stiffness is the same for the riser joints at $EI = 182MPa$. The mass coefficient m is slightly more complicated. Firstly, the added mass needs to be calculated according to Equation 61. Using $\rho = 1025[kg/m^3]$ gives an added mass coefficient at $m_{added} = 1795[kg/m]$ for the riser joints with buoyancy, and $m_{added} = 336[kg/m]$ for the slick joints and pup joints. The total mass coefficient then becomes $m_{total} = 2413[kg/m]$ for the riser joints with buoyancy, and $m_{total} = 741[kg/m]$ for the slick joints and pup joints. A weighed average of m_{total} between the different riser joints can then be found to be $1330[kg/m]$. The length between flex joints can be found in the model $L = 115m$, and the tension in the riser can be seen as an average between the top tension at $1.3MN$ and the bottom tension at $0.8MN$, leading to $T = 1.05MN$. The results from these rough calculations can be found in Table 9.

$$m_{added} = \rho \cdot C_a \cdot \frac{\pi \cdot D_H^2}{4} + \rho \cdot A_{external} \tag{61}$$

Mode (i)	1	2	3	4
Angular eigenfrequency [rad/s]	0.86	2.01	3.63	5.80
Eigenperiod [s]	7.33	3.13	1.73	1.08

Table 9: Eigenperiods from simple riser model

If the information in Figure 30 is condensed to only consider the eigenperiods which come in pairs, Table 10 is the result, and this can be compared this to Table 9.

Mode	1	2	3	4	5
Eigenperiod [s]	7.43	3.62	2.32	1.74	1.10

Table 10: Eigenperiods from model (Figure 30)

When comparing Table 9 and Table 10, it seems like the simple calculation was fairly good at predicting the eigenperiod, even with the simplifications that had to be made. One thing to note, which is explained in the next subsection, is that mode 3 in Table 10 corresponds to something in between mode 2 and 3 in Table 9.

6.1 Eigenvectors

Presented below are a few figures of the eigenvectors of the riser system. The figures show the displacements in the x- direction for the modes referred to in Table 10. The figures show the height of the riser on the x-axis, and the displacement on the y-axis. The soil start at a height of 60 meters, and the LFJ is located at about 74 meters. The red line corresponds to the section of the telescopic joint above the tension ring, the blue line corresponds to the riser line and the green line corresponds to the well line.

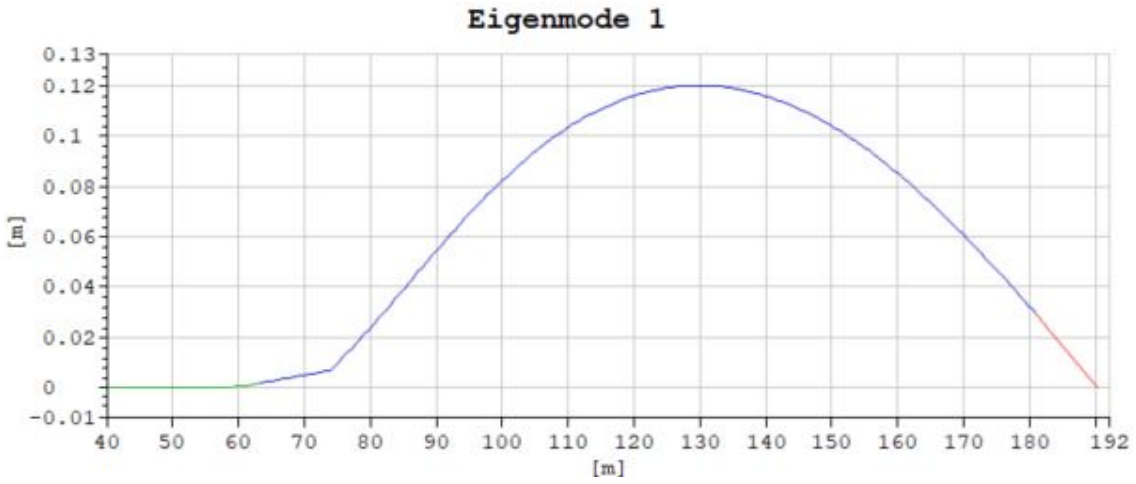

Figure 31: Eigenmode associated with the eigenperiod 7.43s

The first eigenmode of the system corresponds well with the first sinusoidal mode. While the eigenperiod is a bit larger than the one found in Table 9, this can partly be explained by the BOP contributing to the mode of the riser, causing a slightly increased "effective length" (this term is explained in Section 6.1.1).

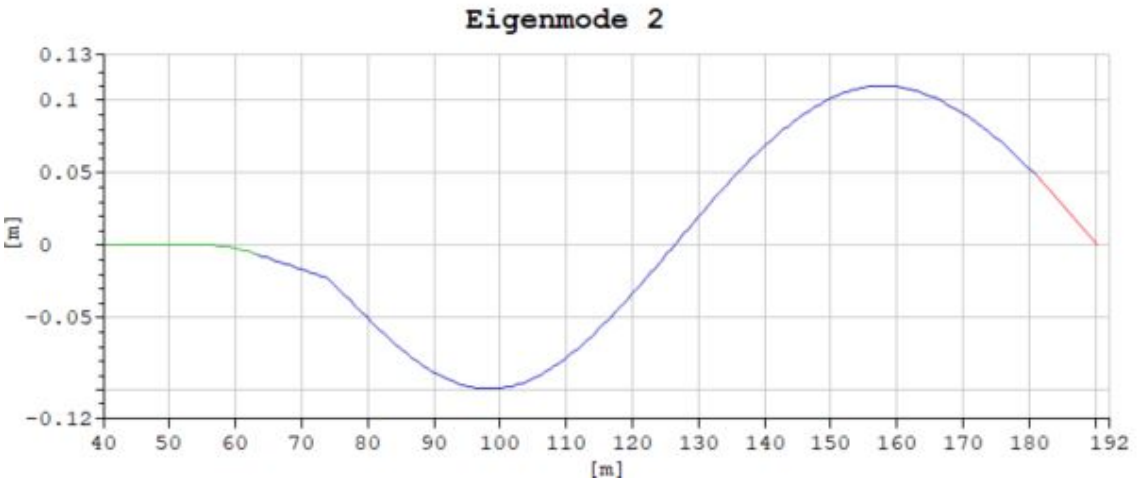

Figure 32: Eigenmode associated with the eigenperiod 3.62s

The second eigenmode of the system corresponds well with the second sinusoidal mode. As with the first mode, the eigenmode of the BOP contributes to the eigenmode, now even more than for the first mode, explaining the larger discrepancy in eigenperiod from the calculated mode in Table 9.

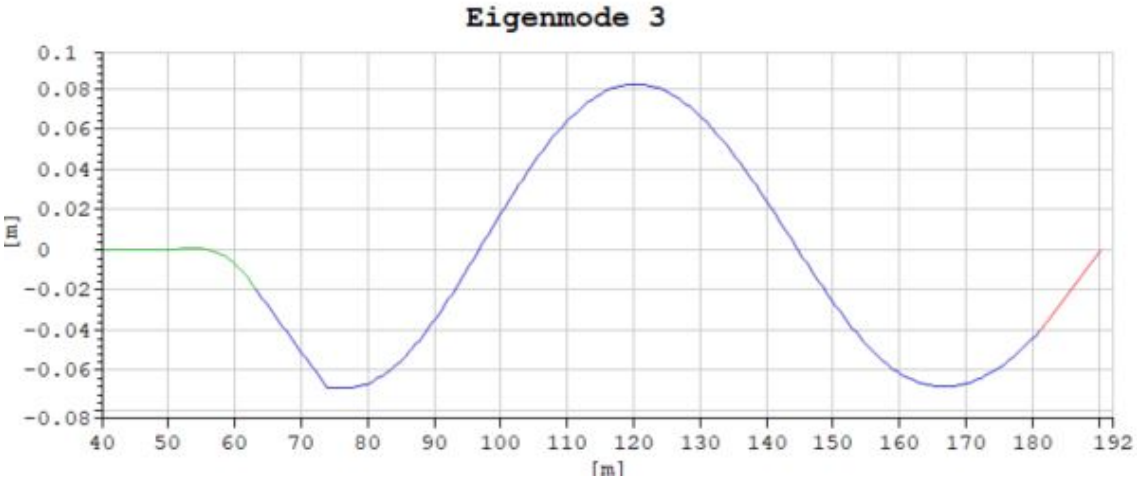

Figure 33: Eigenmode associated with the eigenperiod 2.32s

The third eigenperiod of the system is neither close to the second nor third eigenperiod calculated for the riser in Table 9. This is because this eigenmode seems to be dominated by the eigenmode of the BOP, and the risermode can either be seen as following the second mode with a large increased effective length, or following the third mode with a substantially shortened effective length.

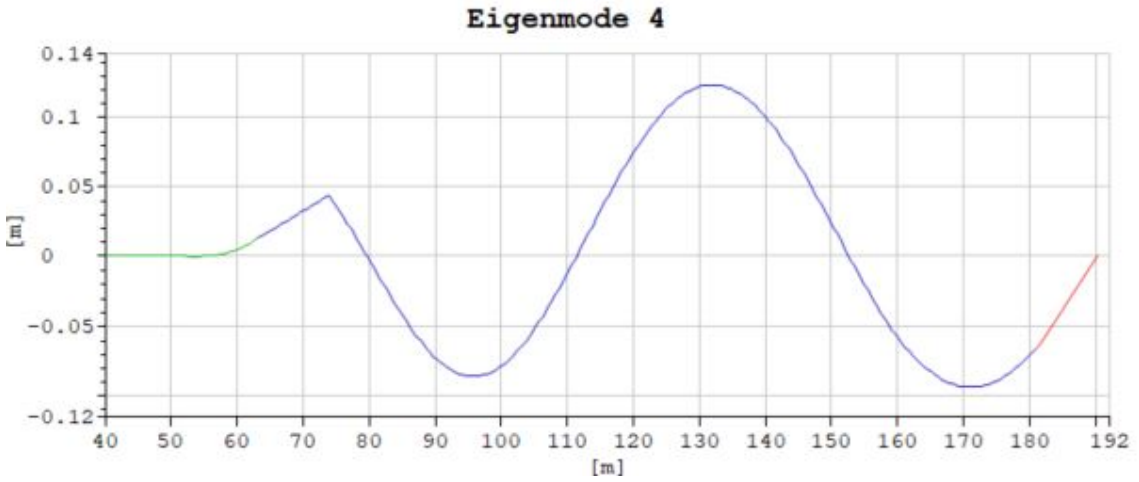

Figure 34: Eigenmode associated with the eigenperiod 1.74s

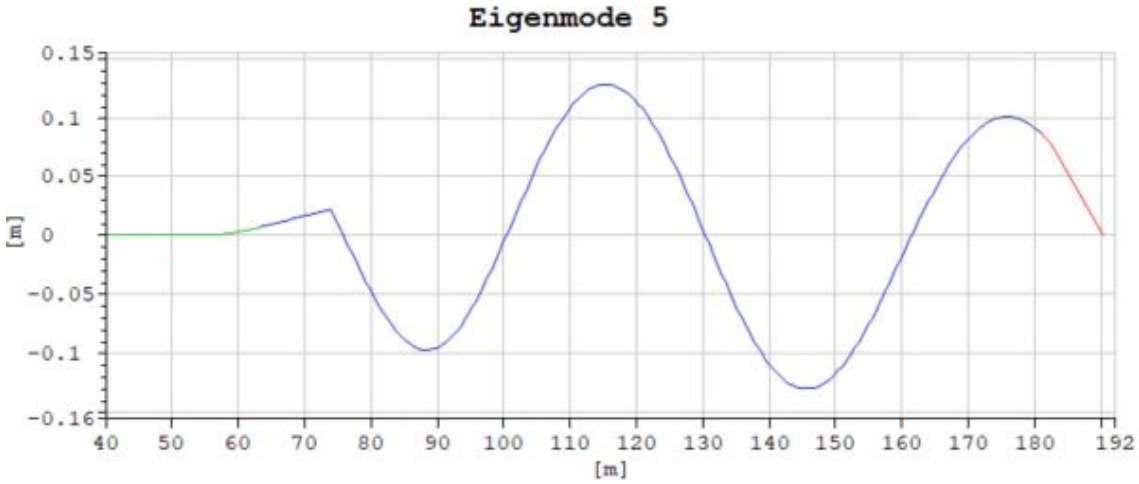

Figure 35: Eigenmode associated with the eigenperiod 1.10s

The fourth and fifth eigenmodes of the system correspond to the third and fourth sinusoidal modes respectively. As their eigenperiods are shorter than the eigenperiod of the BOP, the eigenmode of the BOP counteracts the movement of the riser, causing a decrease in effective length, explaining the fact that these modes have a shorter eigenmode than calculated for the riser alone in Table 9.

6.1.1 Effective Length

This section has introduced the term effective length in relation to sinusoidal eigenvectors. The term has been used to explain the effect the BOP mode has on the riser's boundary conditions in a way which theoretically could be inserted into Equation 60 instead of needing to rewriting the entire equation.

When reference is made to the BOP mode contributing to the effective length, one considers the riser as if it was lengthened from the point above the LFJ so that one would have an almost complete sinusoidal function as seen in Figure 36.

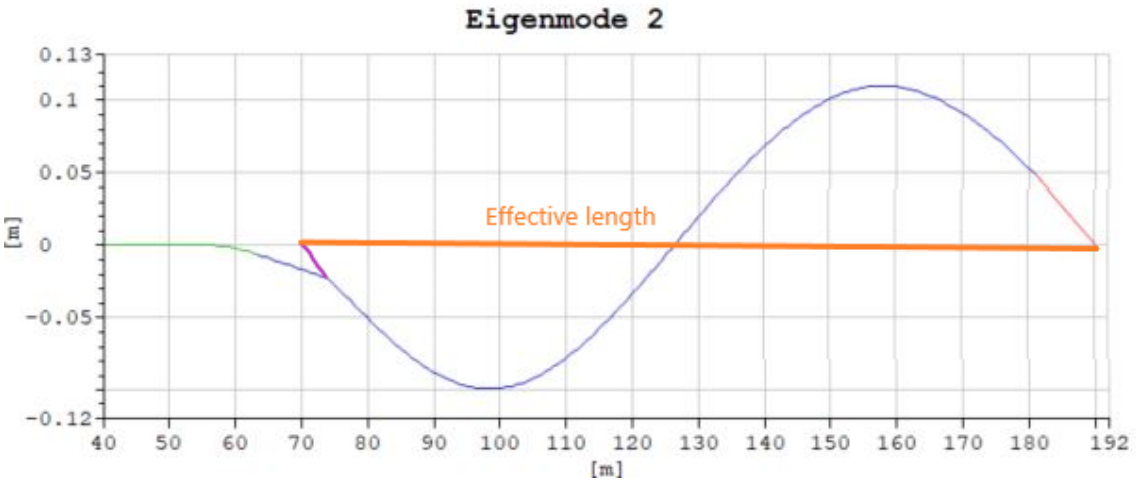

Figure 36: Effective length eigenmode 2

When reference is made to the BOP mode reducing the effective length, one considers the riser as if it was shortened to the point where the displacement is zero, as seen in Figure 37.

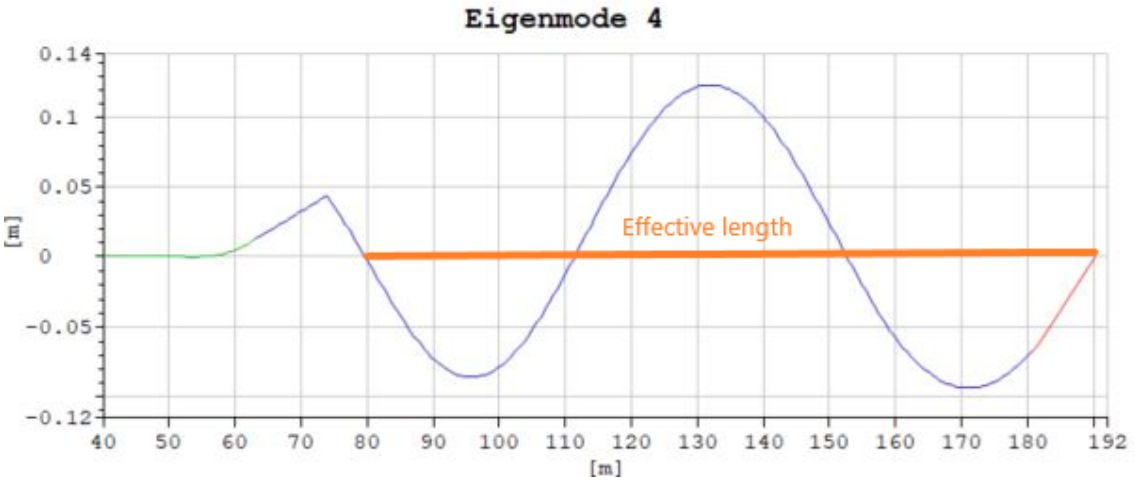

Figure 37: Effective length eigenmode 4

Because the length has a negative relationship with ω_{bs} in Equation 60, it has a positive relationship with the eigenperiod. This means that an increased effective length will lead to a higher eigenperiod, while a shortened effective length will cause a decrease in the eigenperiod.

7 Environmental Data

Six 1-hour events during the drilling campaign have been chosen to be studied more in detail. Choosing these six events allow for more detailed studies on how the model responds to different environmental loads, particularly in regards to specific frequencies. In Table 11, one can find the starting point of each of the six events, combined with a basic description of its associated metaocean data. Comparing the events to the data in Figure 38 shows that the events capture some of the range in different sea states experienced during the operation. It should be noted that the riser was disconnected from the BOP during the peak in "Total HS" at 14.dec-16.dec and in Figure 38.

	Date	Hour	Hs (m) wind	Tp (s) wind	Wind direction	Hs (m) swell	Tp (s) swell	Swell direction
Event 1	30-Nov	12:00	0.1	0.0	39	1.2	7.3	166
Event 2	02-Dec	20:00	1.3	5.0	271	1.9	18.9	106
Event 3	04-Dec	20:00	0.4	3.4	196	1.7	14.2	106
Event 4	06-Dec	09:00	0.2	3.0	91	1.5	12.5	106
Event 5	07-Dec	05:00	4.0	9.4	271	2.0	9.4	271
Event 6	07-Dec	21:00	0.6	4.4	301	2.4	9.4	301

Table 11: Time and date of the six 1-hour periods, combined with Hs and Tp from swell and wind wave from hindcast data

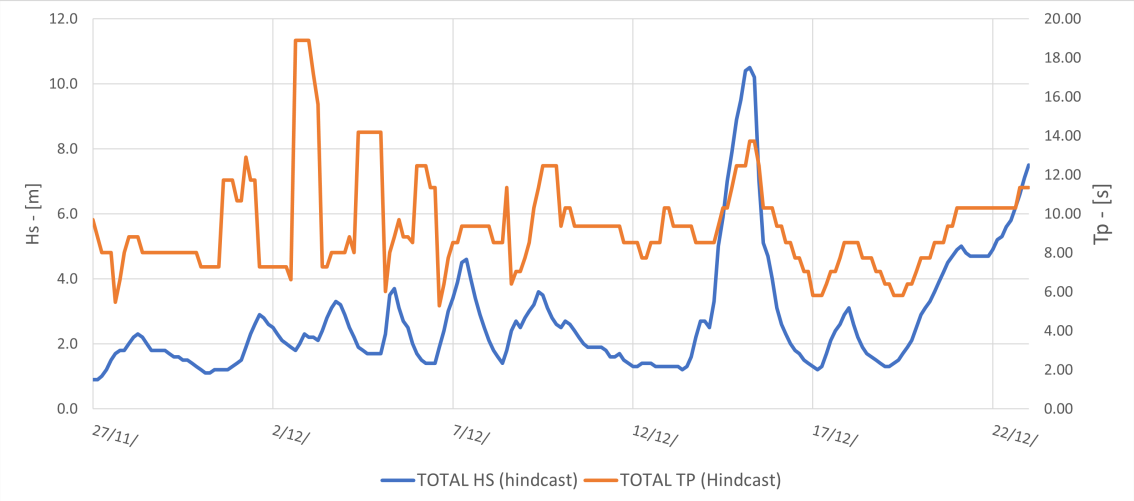

Figure 38: Metaocean data for the entire drilling period

All the sea states are, however, not well represented by a two peaked wave spectrum, as Table 11 suggests. Figure 39 shows the detailed wave spectrum for Event 2, which makes it clear that this wave environment can not be described sufficiently by a two peaked wave spectrum. On the other hand, a sea state like in Event 5 (Figure 40) seems to be easily modeled as a two peaked wave spectrum. The rest of the 2D wave spectra can be found in Appendix C.

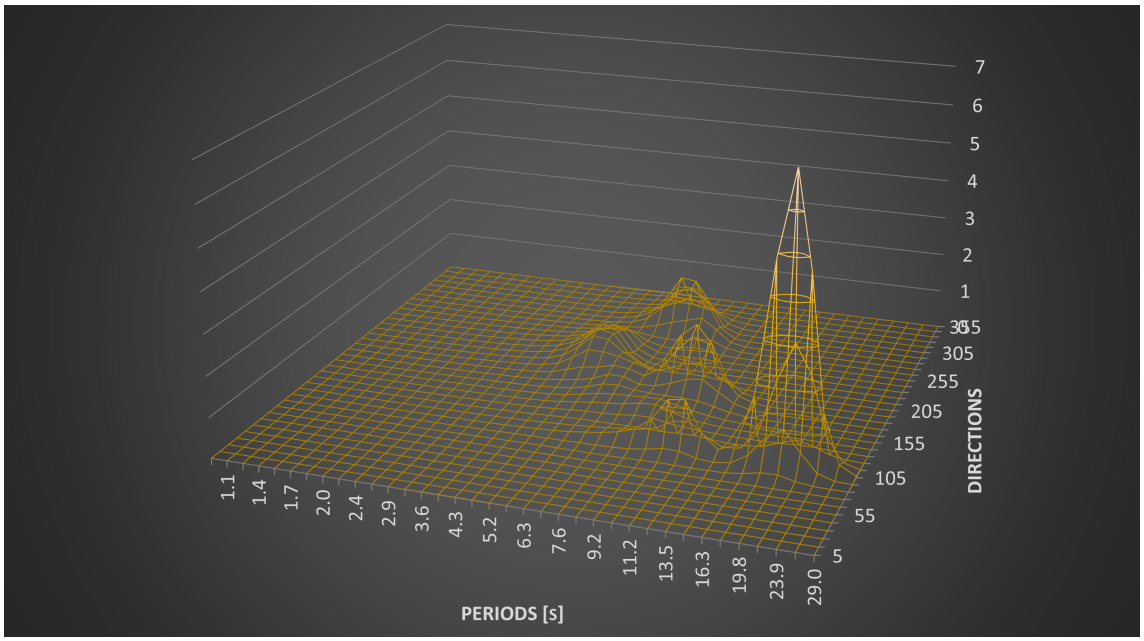

Figure 39: Event 2: 2D-wave spectra

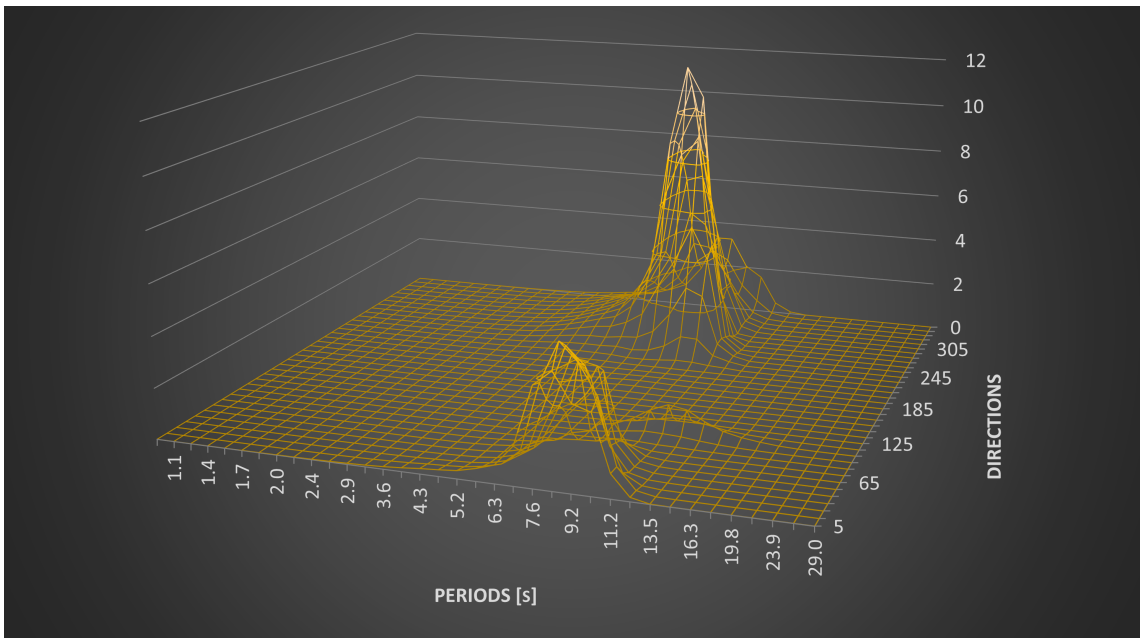

Figure 40: Event 5: 2D-wave spectra

8 Measurement Systems

Equinor has provided a large data set to this report, most of the data has not been investigated in detail, but data for direct measurements of wellhead moment, LRS angle and BOP angle has been used.

8.1 Wellhead Moment Measurements

During the drilling campaign considered in this report, six strain gauges were located on the surface casing as shown in Figure 41. The data from these strain gauges has been provided by Equinor. In addition to the data, Equinor has provided a Matlab script which transforms these strain gauge readings into axial forces and bending moments on the entire wellhead through fitting by least squares. As this report is focused on wellhead fatigue, and therefore ΔM is the most interesting parameter, the mean of the measured wellhead moment has been subtracted so that only the fluctuations in the wellhead moment is considered.

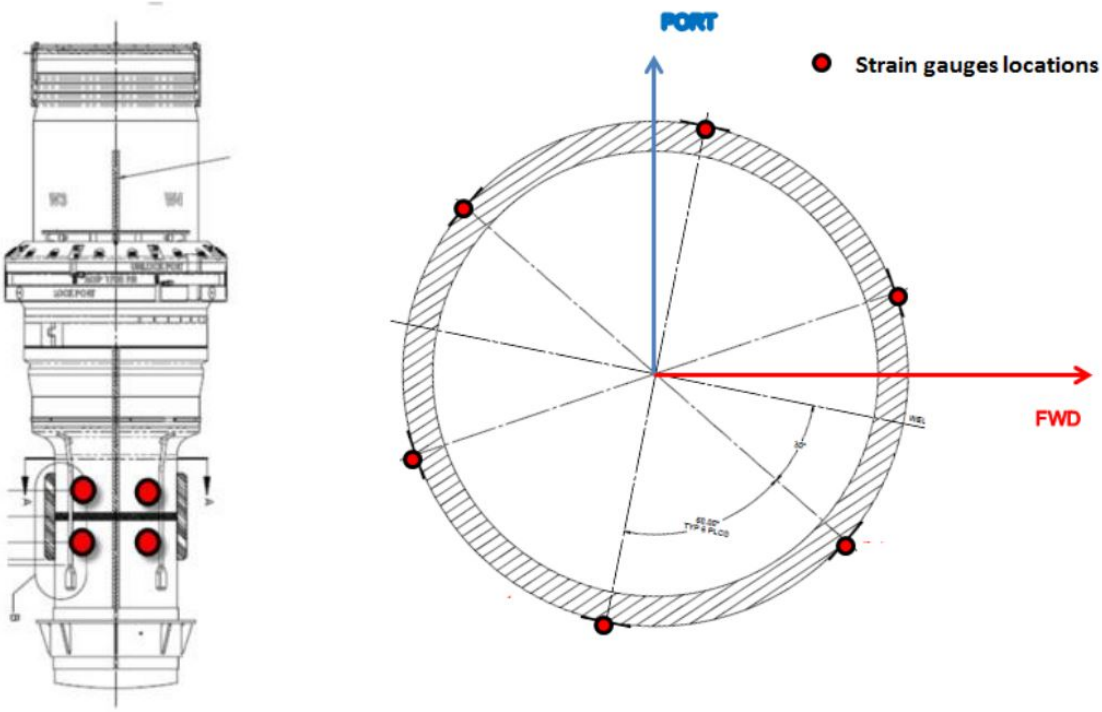

Figure 41: Location of strain gauges on the surface casing close to wellhead [12]

8.2 LRS and BOP Angle Measurements

The rotations around the lower flex joint, called LRS angle, were measured by a motion sensor package right above the lower flex joint, as can be seen in Figure 42. The motion sensor package contained a set of bi-axial pair of angular rate sensors and a bi-axial pair of accelerometers, but only the data from the angular rate sensors are considered in this report.

The rotations of the BOP, called BOP angle, were measured by a sensor package located in the middle of the BOP, as can be seen in Figure 43. This sensor package did also contain a pair of bi-axial angular rate sensors and accelerometers, but only the rotations are used in this report. The coordinate system of the LRS angles and the BOP angles were defined such that they are aligned [11].

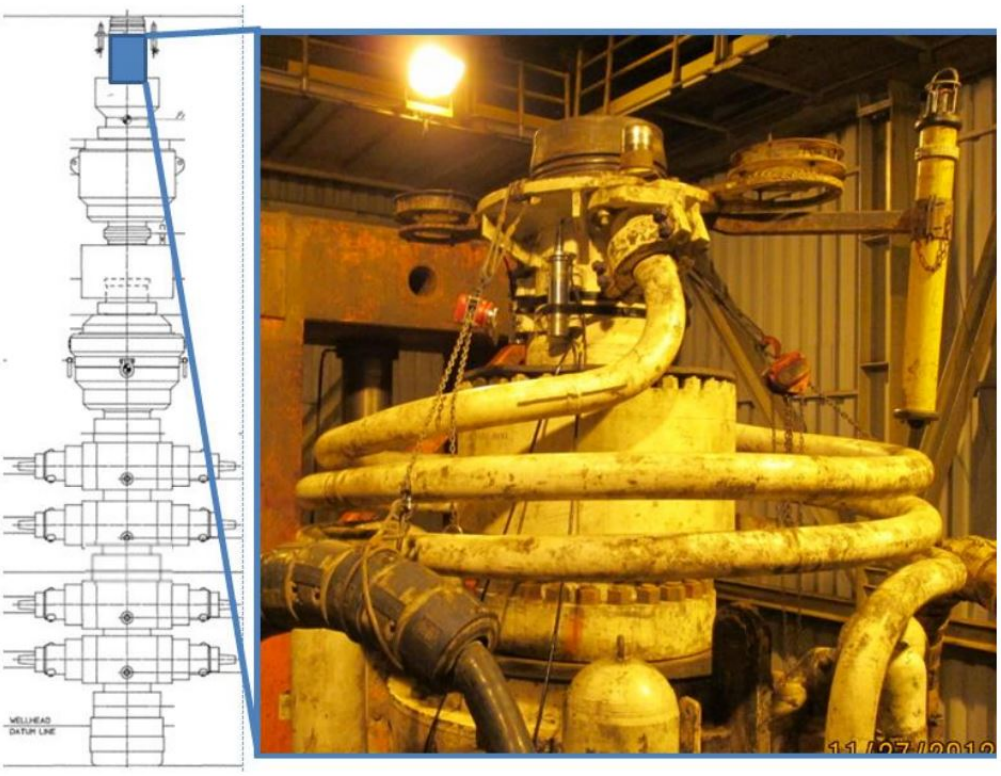

Figure 42: The location of the motion sensor package providing inclination angles right above the LFJ [12]

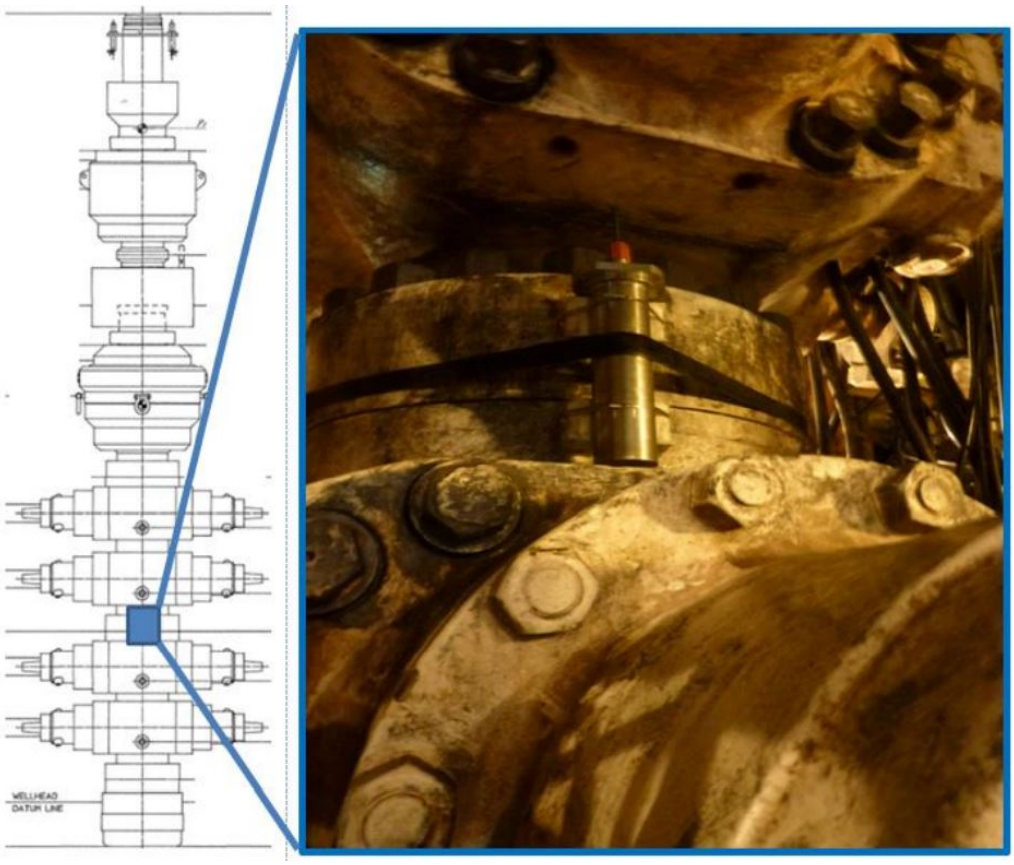

Figure 43: The location of the motion sensor package providing inclination angles of the BOP [12]

9 Convergence Study

Before the model can be considered further, a mesh convergence study needs to be performed to ensure that the beams elements of the numerical model are short enough for the values to converge. This is done by decreasing the element size until some predefined calculated values no longer change substantially with a finer mesh. When this happens, the results have converged.

9.1 SRSS of STD

To be able to compare different models with each other and with measurement data, it is useful to condense the results into one result parameter. Since the most critical parameter in an operation like this is wellhead fatigue, the result parameter should be related to fatigue damage on the wellhead. In addition, directions should be eliminated, as it is not fully known how the coordinate system in the measurement data translates to the coordinate system of the model or the environment.

The choice of result parameter has landed on taking the square root of the sum of the squares of the standard deviation of the moment on wellhead in each direction ($\sqrt{STD(M_x)^2 + STD(M_y)^2}$). The reasoning for this choice begins with the equation for strain energy, Equation 62. Where E is the Young's modulus, ε is the strain, dA is the differential area and dE is the differential energy. All the factors on the right side of Equation 62 are constant except for ε, so if the strain is calculated correctly, the strain energy in the wellhead is also calculated correctly.

$$dE = \frac{1}{2} E \varepsilon^2 dA \tag{62}$$

The strain is proportional to the total moment, and the average strain, or expected value of the strain, will therefore be proportional to the root mean square of the total moment:

$$E(\varepsilon) \propto \sqrt{E(M_T^2)} \tag{63}$$

With M_T defined as in Equation 64

$$M_T = \sqrt{M_x^2 + M_y^2} \tag{64}$$

Equation 63 and Equation 64 can now be combined to show:

$$E(\varepsilon) \propto \sqrt{E(M_T^2)} = \sqrt{E(M_x^2 + M_y^2)} = \sqrt{E(M_x^2) + E(M_y^2)} \tag{65}$$

Knowing that the expected value for both M_x and M_y is zero ($E(M_x) = E(M_y) = 0$), Equation 65, can be expanded to:

$$\begin{aligned} E(\varepsilon) \propto \sqrt{E(M_x^2) + E(M_y^2)} &= \sqrt{E(M_x^2 + E(M_x)) + E(M_y^2 + E(M_y))} \\ &= \sqrt{STD(M_x)^2 + STD(M_y)^2} \end{aligned} \tag{66}$$

Proving that a model that calculates the square root of the sum of squares for the standard deviations for wellhead moment correctly, will also be a model that calculates the strain energy on the wellhead correctly. Essentially making $\sqrt{STD(M_x)^2 + STD(M_y)^2}$ a good parameter for figuring out the accuracy on the model in relation to fatigue damage.

9.2 Environment

When choosing the environment to be used in a convergence study, it is important that the environment captures the range in environments that the model will experience. It is especially important that environments with a lot of energy close to the eigenfrequencies of the model are considered. Based on these considerations, the environments presented in Table 12 have been chosen.

	Hs [m]	Tp [s]
Environment 1	2	4
Environment 2	6	4
Environment 3	2	7
Environment 4	6	7
Environment 5	2	12
Environment 6	6	12

Table 12: Parameters in JONSWAP spectra used in convergence study, all the environments have a cosine squared spreading function

9.3 Results

Mesh length	2.0 m	1.0 m	0.5 m	0.25 m	0.125 m
Environment 1 [kNm]	186.7	182.0	180.5	180.2	180.2
Environment 2 [kNm]	443.4	431.1	427.1	426.2	426.0
Environment 3 [kNm]	164.2	163.2	162.8	162.7	162.7
Environment 4 [kNm]	345.1	350.0	352.9	354.6	355.5
Environment 5 [kNm]	120.2	120.1	120.1	120.0	120.0
Environment 6 [kNm]	245.6	245.1	244.9	244.9	244.9
Largest error	4.1%	1.5%	0.7%	0.3%	-

Table 13: SRSS of STD of wellhead moment for each environment for mesh lengths from 2.0 meters to 0.125 meters

Table 13 shows how the measured parameter converges for decreasing mesh lengths. For a mesh length of 0.5 meters the results seem to have converged fairly well, at most the error is 0.7% compared to using a mesh length of 0.125 meters. For the uses in this report, where far larger sources of error is present, a mesh length of 0.5 meters has been determined to be a sufficient balance between accuracy and computational load. Hence, that is the mesh length which will be used in this report.

10 Testing of Environmental Spectra

RIFLEX does not allow for creating wave environments with numerical short crested wave spectra like the ones seen in Figure 39 and Figure 40. It only allows for long crested numerical wave spectra, or a wave spectra created from a common wave spectrum like JONSWAP. This raises the issue of which kind of metaocean data it is fruitful to expose the model to.

Three different wave spectra have been chosen to determine which gives the most accurate results in regards to wellhead fatigue.

- The first wave spectrum, called "Numerical", is a long crested numerical spectrum made by integrating the energy in the 2D wave spectra over its directions. The actual 2D wave spectra can be found in Appendix D.
- The second wave spectrum, called "Long crested", is made by taking Hs and Tp data from Table 11, and creating two long crested JONSWAP spectra for the wind wave and the swell wave respectively, with both going in the same direction. For the wind wave the gamma-parameter in the JONSWAP wave is at the default 3.3, while the swell wave has the gamma parameter set to 1, since the swell wave is assumed to be fully developed.
- The third wave spectrum, called "Short crested", is made by taking Hs, Tp and directional data from Table 11, and creating one JONSWAP spectrum for the wind wave and another JONSWAP spectrum for the swell wave. Each have their respective main direction and a directional spreading function of $cos^4(x)$. Just as with the "Long crested" wave spectrum, the gamma-parameter is set to 3.3 for the wind wave and 1 for the swell wave.

10.1 Results

	Event 1	Event 2	Event 3	Event 4	Event 5	Event 6
Measurements [kNm]	69	140	73	69	297	134
Numerical [kNm]	112	171	143	117	299	193
Long crested [kNm]	116	111	137	96	275	191
Short crested [kNm]	163	139	112	117	300	201

Table 14: SRSS of STD of wellhead moment when the model has experienced different wave spectra

The results in Table 14 indicate that the RIFLEX-model itself is generally conservative. They also indicate that modeling with numerical long crested waves will give the most consistently conservative results compared to measurements. This is especially true for Event 2, where the wave loads resulting from JONSWAP waves undershoot the real loads on the wellhead. This becomes especially obvious when considering the autospectra in Figure 44. The reason for the large difference in Event 2, can be found in the numerical 2D-wave spectra for Event 2 (Figure 39). There seems to be a few waves in addition to the main wind ($Tp = 18.9s$) and swell waves ($Tp = 5.0s$). These additional waves seem to have periods around the first eigenperiod, so the two-peaked JONSWAP spectra has far less of the wave energy in the periods around the first eigenmode of the system.

The autospectum for all the events exposed to differing wavespectra can be found in Appendix E. As in Table 14, the autospectra shows that the model is generally conservative in relation to the measurements, and especially the second eigenmode (with a period of 3.62s) get excited far more in the model than in the measurements. This suggests that the model is too conservative in relation to damping of both the first and second eigenmode.

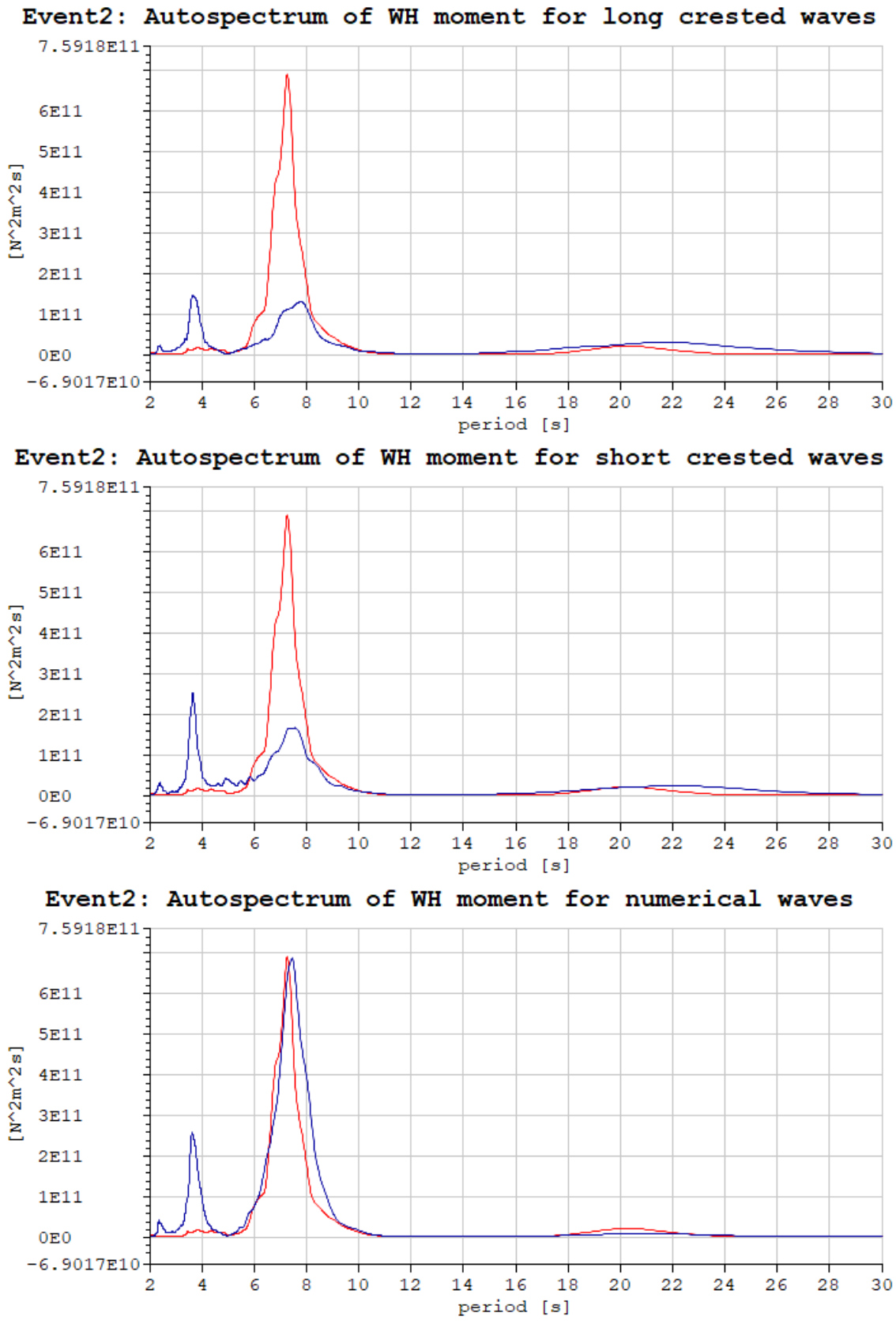

Figure 44: Event 2: Autospectra for different types of environment. The blue graphs is the auto spectra for WH moment in the model for each of the different environments, the red is from measurements

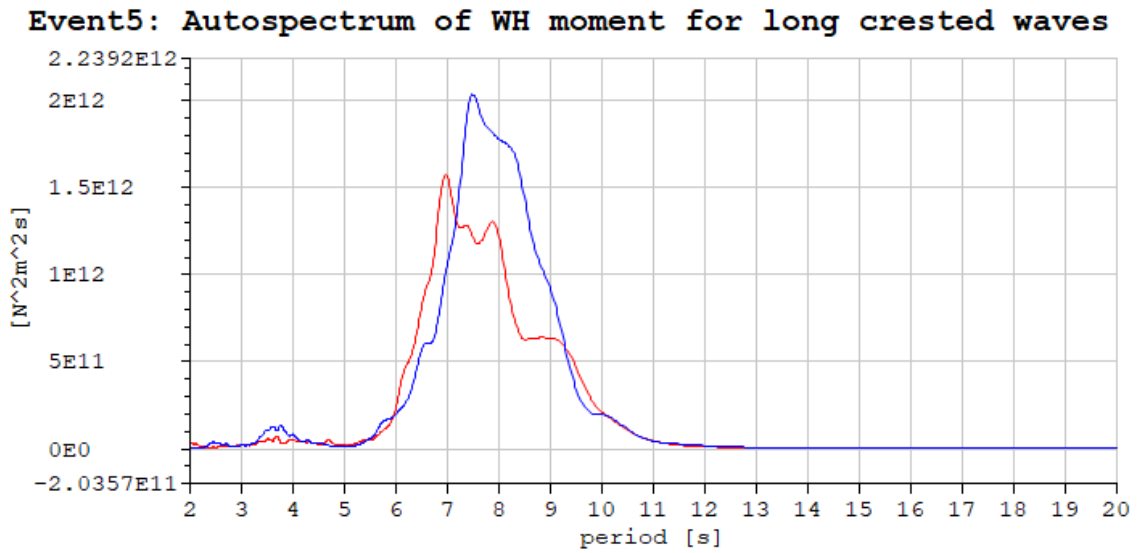

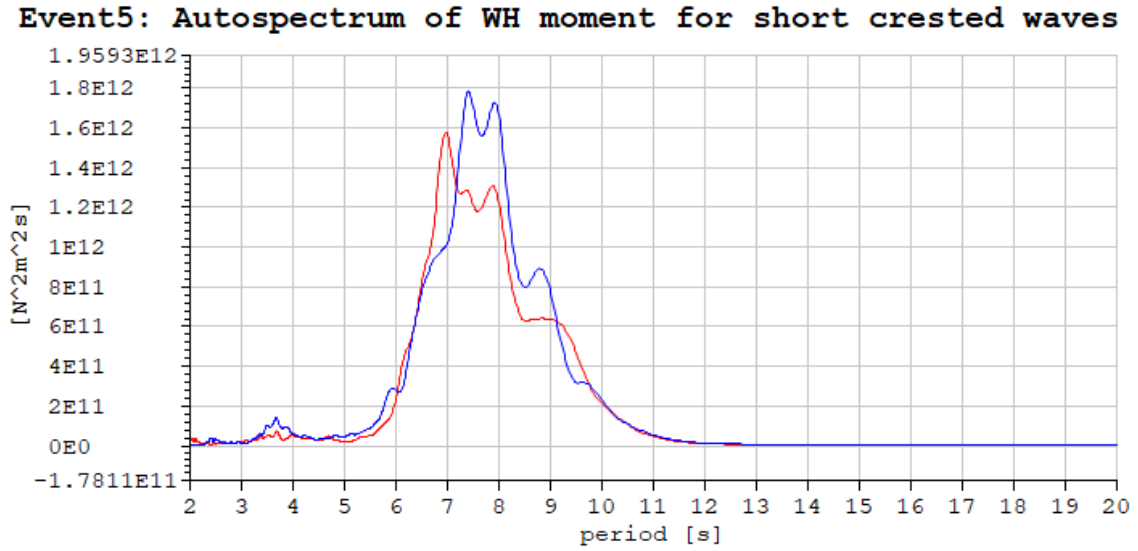

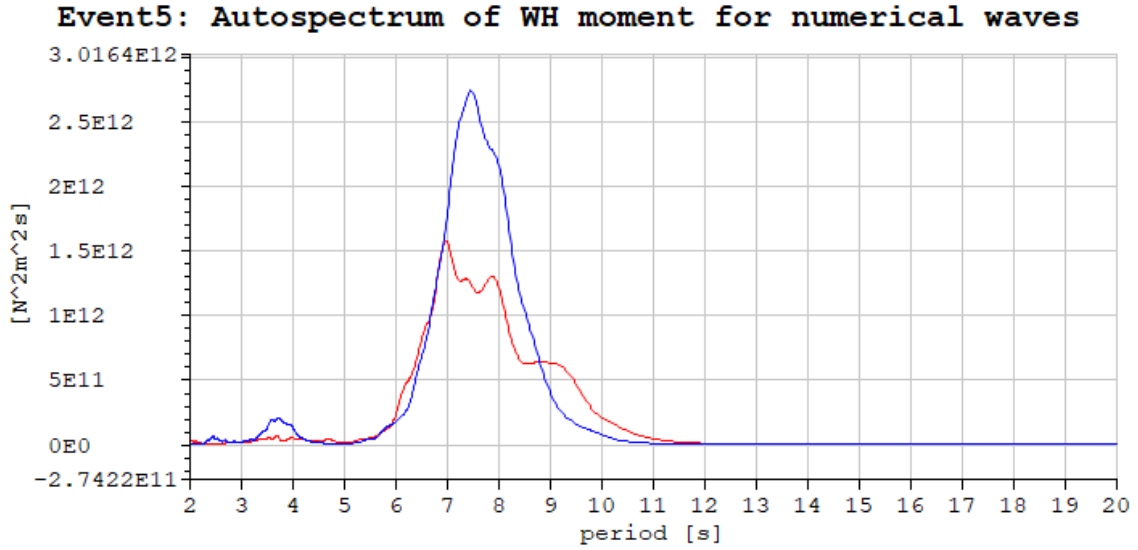

Figure 45: Event 5: Autospectra for different types of environment. The blue graphs is the auto spectra for WH moment in the model for each of the different environments, the red is from measurements

10.2 Low Frequency Loads

The autospectrums of the model and the measurements seem to line up fairly well, at least in shape, for moment oscillations with a period up to 20 seconds. None of the models have much if any moment oscillations with a period above 20 seconds, while such oscillation can be found in the measurements. This is clearest for Event 5 which has its autospectrum pictured in Figure 46, but can also be found in Event 3, 4 and 6 (can be seen in Appendix F).

This explains why the modeled SRSS of STD of the wellhead moment is fairy close to the measurements in Table 14 for Event 5, while the autospectrums only considering periods up to 20s (Figure 45) shows the models as generally being more conservative than the measurements.

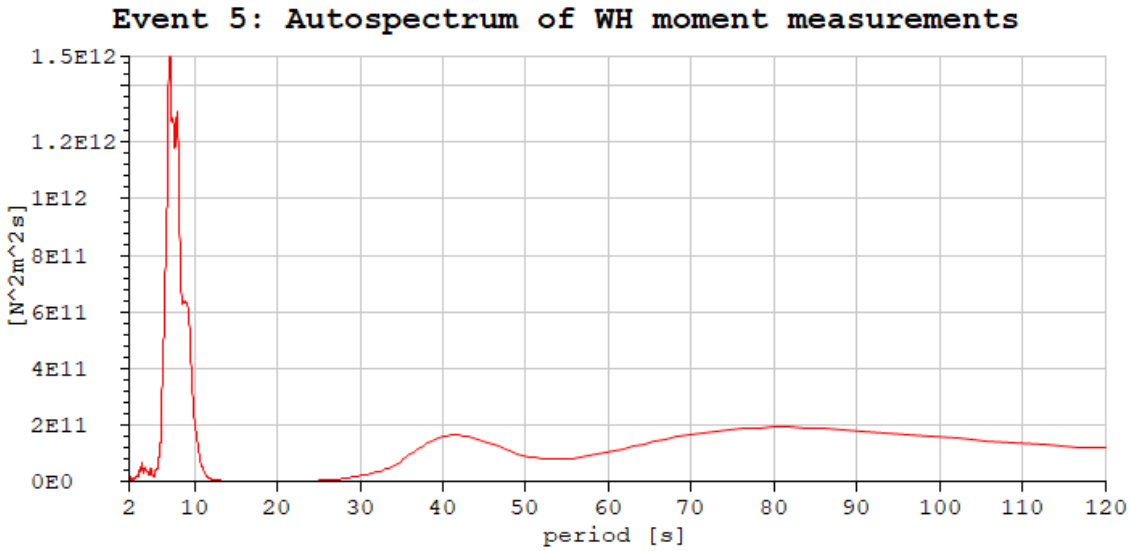

Figure 46: Autospectrum of measured WH moment

11 Sensitivity Study

The model described in Section 5 has a lot of uncertainty related to the modeling of different components. This section will look into a few of these in more detail and explore how a different modeling might change the results. This section uses the wave spectra referred to as Numerical in Section 10 for each of the events.

11.1 Top Tension

The top tension has a large effect on the eigenperiod of the riser mode, and will therefore have a major influence on the moment variations on the wellhead. The model starts to become unstable when top tension falls below 1.0MN, so no lower top tension has been considered. As the top tension has such a large effect on the response of the model, low variations from the original top tension has been selected. As mentioned in Section 5.4.1 there are some uncertainties related to the effective top tension as drilling operations will have an effect on this parameter.

The effect from drilling operations is mainly increasing the effective top tension as the drilling string also needs top tension so that it will avoid buckling.

Top tension [MN]	1.0	1.15	**1.3**	1.45	1.6	1.9	Measurements
Event 1	97.4	106.1	**112.1**	115.6	115.4	106.7	69.0
Event 2	162.5	168.1	**171.0**	172.5	172.1	165.3	139.7
Event 3	132.6	139.5	**142.6**	143.5	141.2	130.9	72.8
Event 4	104.2	111.1	**116.6**	120.6	121.3	115.3	68.9
Event 5	272.4	289.6	**299.1**	301.5	298.0	278.0	297.4
Event 6	178.3	189.8	**192.6**	188.9	180.8	160.0	134.0

Table 15: SRSS of STD of WH moment using different top tension, the values are given in kNm

There is not one choice of top tension that will give the most conservative result, as this parameter affects the eigenperiod, and the most conservative eigenperiod depends on the wavespectrum. Figure 47 and Figure 48 clearly shows the effect of changing top tension in the model. As one could assume based on Equation 60, the eigenperiods becomes shorter as the top tension increases. The eigenmodes also seems to be more dominating as the top tension increases, this can be explained by the fact that a stiffer system is more frequency dependent than a softer system. The autospectra of the WH moment for all events and top tensions may be found in Appendix H.

By looking at the autospectra, one may also conclude that the top tension which gives the best match in eigenperiod between the model and measurements, shifts from one event to another. For example Event 3 (Figure 47) seems to have the best match in eigenperiod for fiarly low top tension. Event 5 on the other hand seems to match better for higher top tension. This substantiates the claim that the drilling operations have an effect on the effective top tension, and that this should be investigated to accurately model the fatigue on the wellhead.

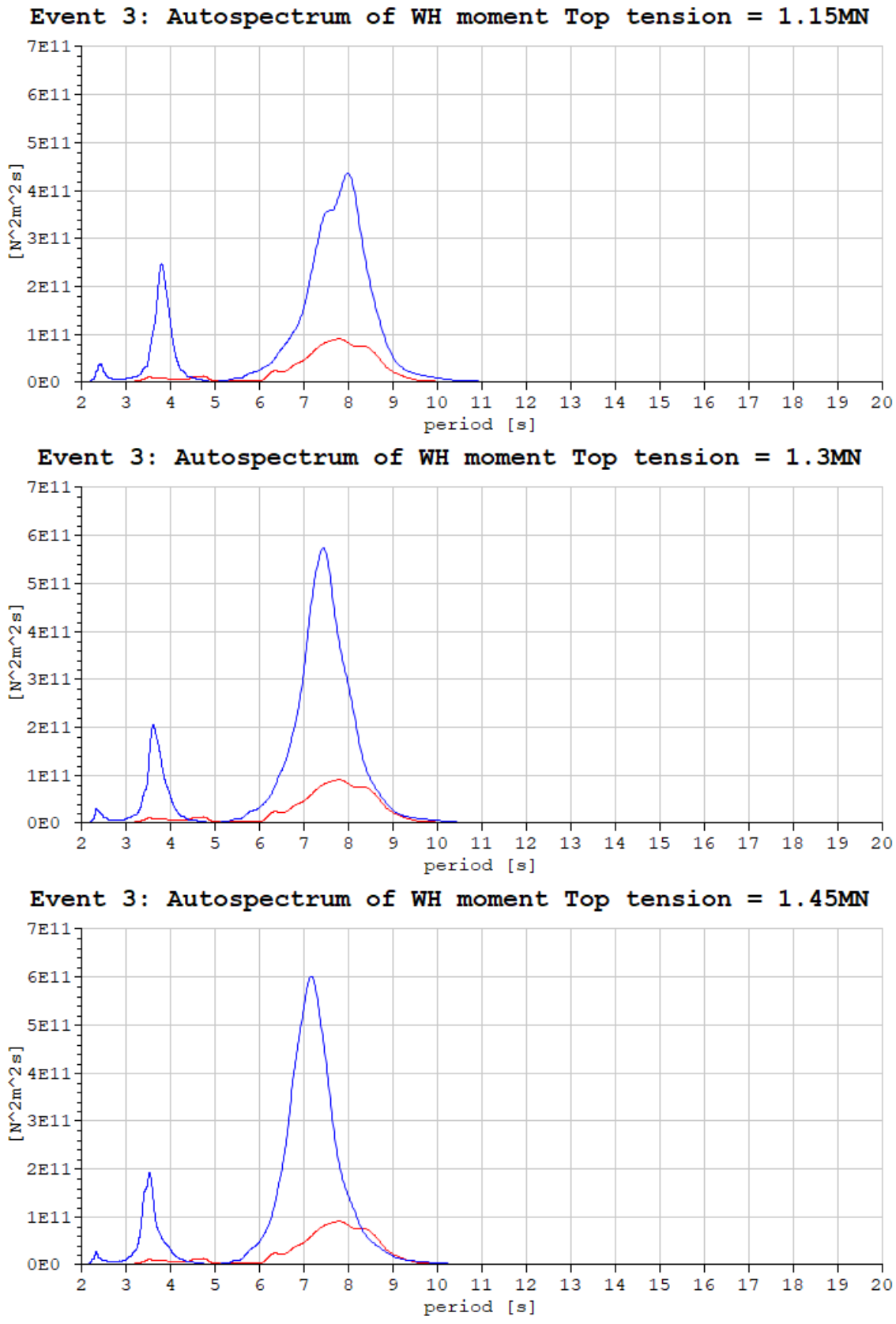

Figure 47: Event 3: The effect of different top tension on WH moment. The blue graphs shows the autospectra for the model with different top tensions, the red graph shows the autospectrum of the measurements. For all top tensions see Figure 100

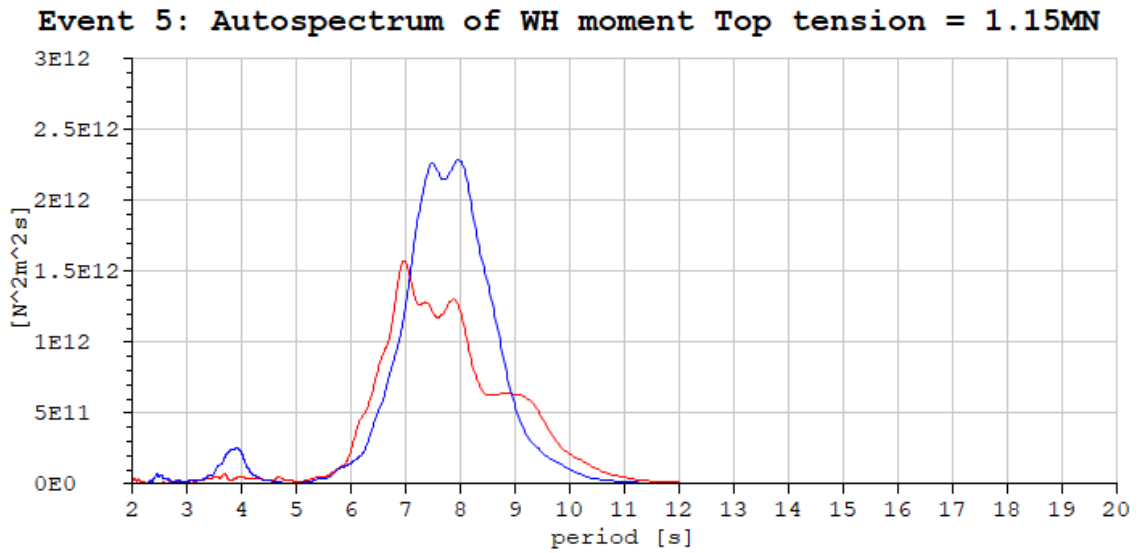

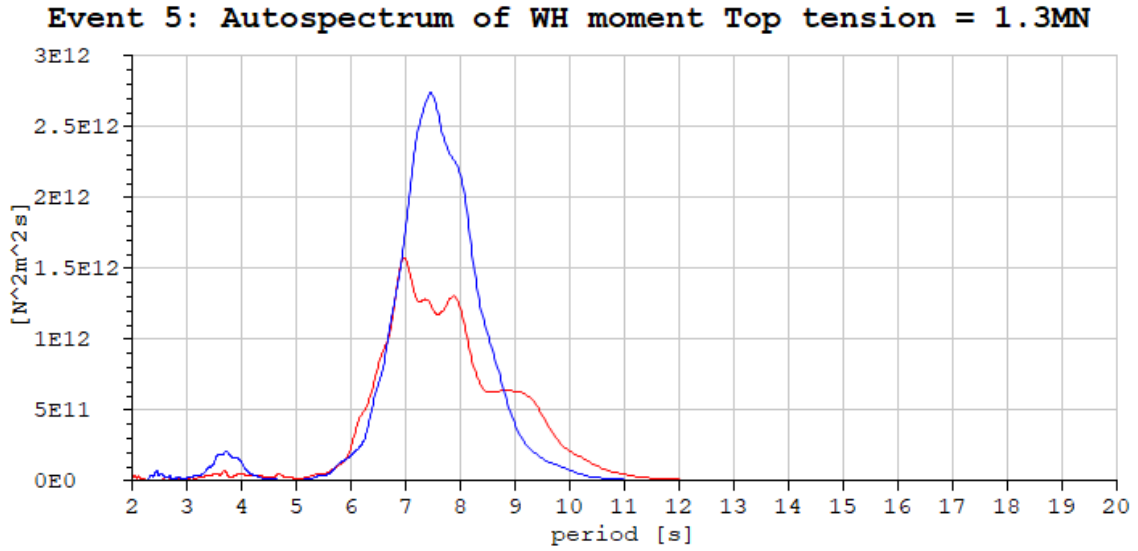

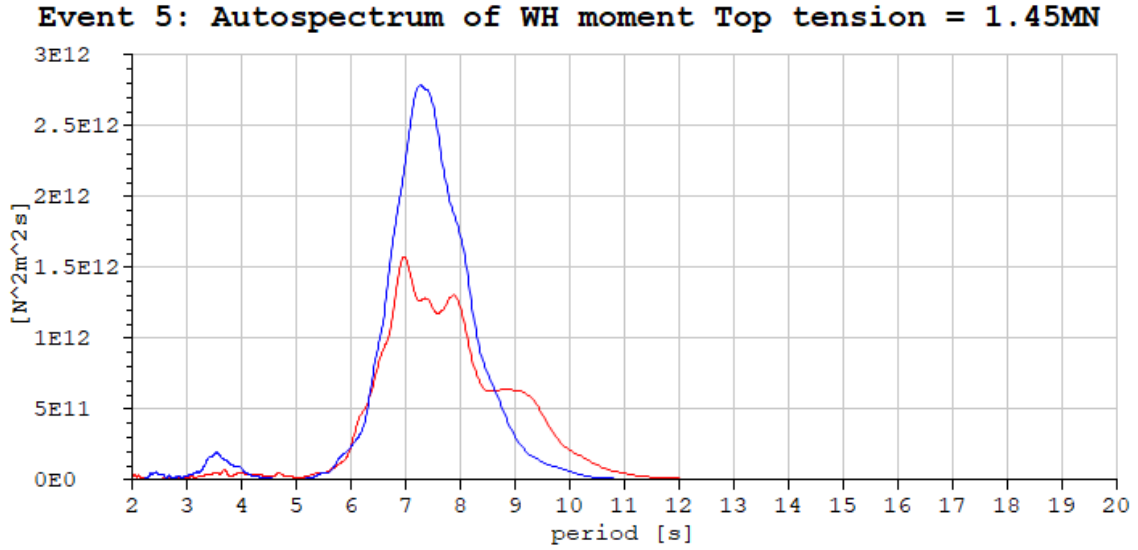

Figure 48: Event 5: The effect of different top tension on WH moment. The blue graphs shows the autospectra for the model with different top tensions, the red graph shows the autospectrum of the measurements. For all top tensions see Figure 102

11.2 Soil Stiffness

There are large uncertainties when choosing the stiffness of the soil spring mentioned in Section 5.1.2, therefore their influence on the end result will be investigated. To investigate this, a factor called soil_factor has been included in the definitions of the soil springs to regulate their stiffness. soil_factor is a factor which is multiplied with the calculated soil stiffness, meaning that a soil_factor equal to 2.0 would mean that the stiffness of all the soil springs is twice that of the original soil springs found in Appendix B .

soil_factor	0.5	0.75	**1.0**	1.25	2.0	10	Measurements
Event 1	116.0	113.4	**112.1**	111.2	109.7	106.1	69.0
Event 2	180.2	173.9	**171.0**	169.2	166.2	159.2	139.7
Event 3	149.6	144.9	**142.6**	141.3	138.9	133.2	72.8
Event 4	120.7	118.0	**116.6**	115.7	114.2	110.3	68.9
Event 5	310.8	303.0	**299.1**	296.5	292.2	283.7	297.4
Event 6	198.4	194.6	**192.6**	191.4	189.2	184.4	134.0

Table 16: SRSS of STD of WH moment using different stiffness in the soil springs, the values are given in kNm

The stiffness of the soil will have an effect on the BOP pendulum mode mentioned in Section 6. As the BOP pendulum mode becomes stiffer, the period becomes shorter, so that it will contribute less to the first and second eigenmode of the system. The effect is largest on the second eigenmode which is clearly visible in the autospectra of the wellhead moment for event 3 Figure 49, this can also be seen for the other events (Appendix G). For the events that have some energy in the third mode, it is also possible to see how this moves towards shorter periods as the stiffness increases. This effect is due to the third system mode being dominated by the BOP mode.

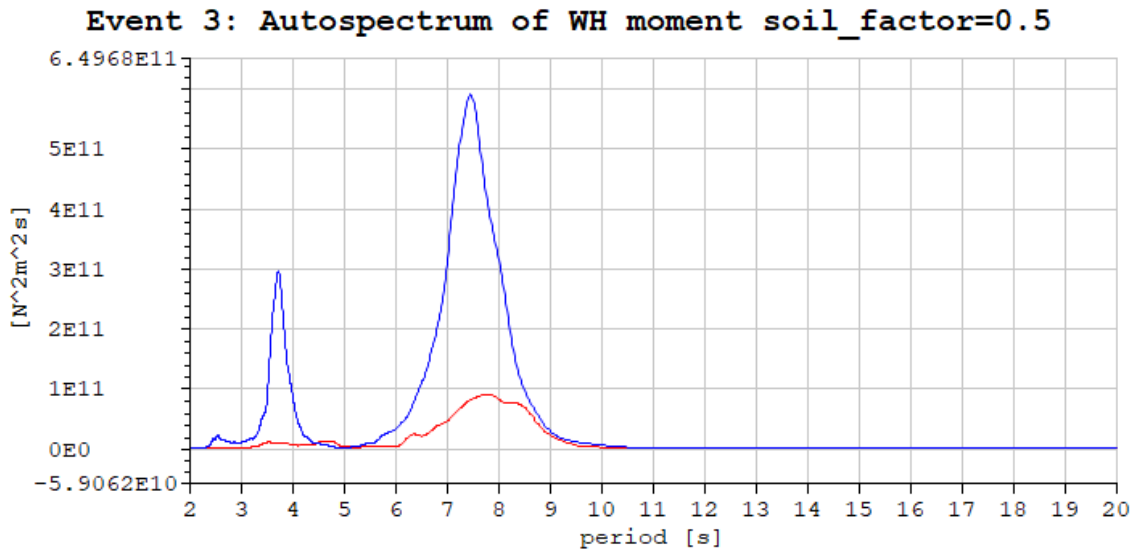

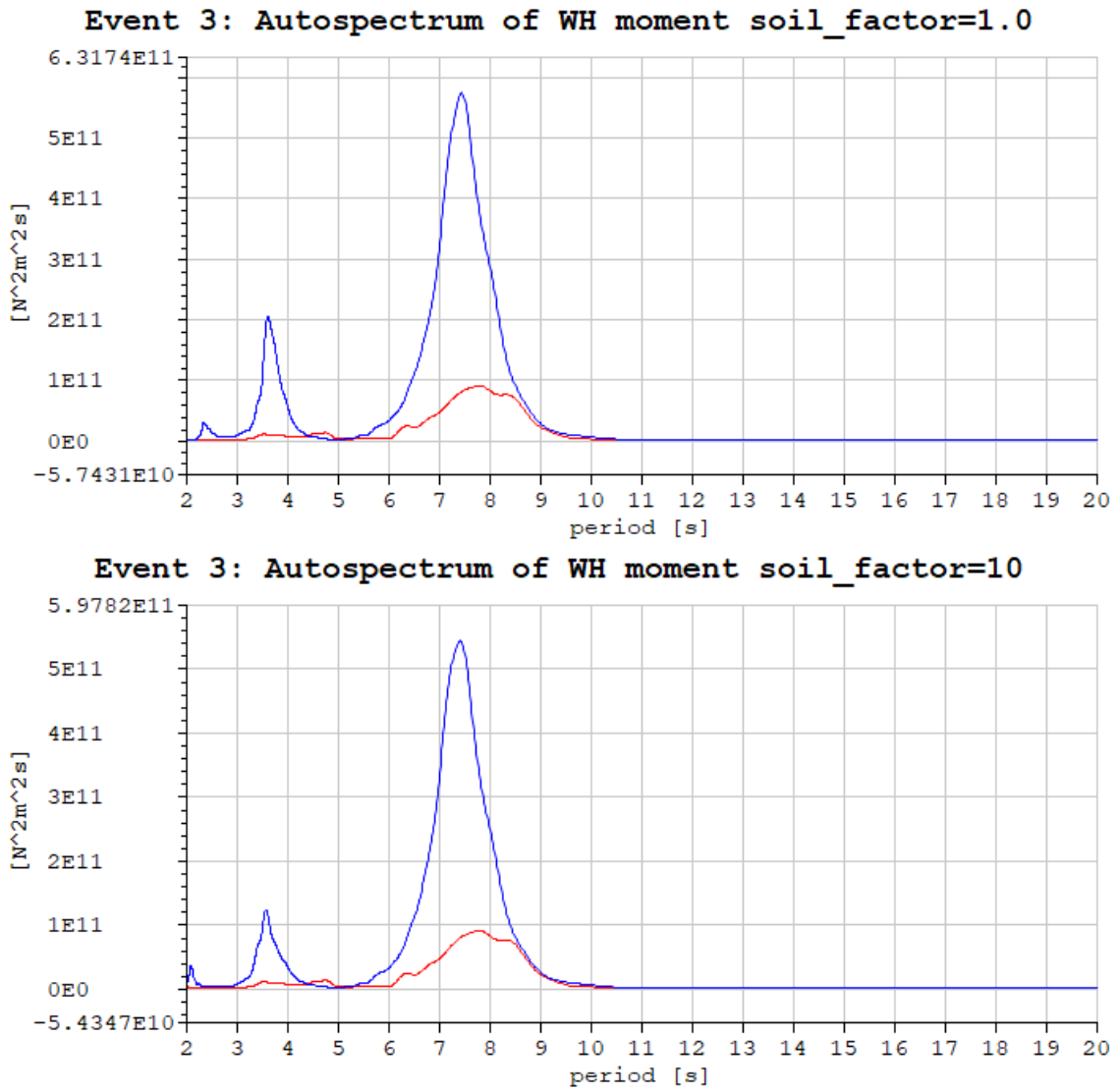

Figure 49: Event 3: The effect of different soil_factor on WH moment. The blue graphs is the auto spectra for WH moment in the model for each of the soil_factor, the red is from measurements. The autospectrums with the rest of the values for soil_facor can be found in Figure 94

11.3 Rayleigh Damping

The modeling of Rayleigh damping can have a major effect on the final result. The model described in Section 5 makes some assumptions about Rayleigh damping, which are investigated in this section. Firstly, as the model assumes no mass proportional damping, only stiffness proportional damping, this assumption will be investigated. Conservatism of critical Rayleigh damping ratio has also been assumed, this must also be tested. The result is that two different tests needs to be performed:

- The effect of moving more of the Rayleigh damping towards mass proportional damping while keeping the original critical damping ratios
- The effect of changing the critical damping ratios

11.3.1 Effect of Stiffness and Mass Proportional Damping

In the model it has been assumed that α_1 is zero so that Equation 59 can be rewritten to Equation 67. This case is called Original. The first alternative case that will be tested is to divide the damping ratio equally between α_1 and α_2, as in Equation 68. This case is called Mixed. The last case to be investigated will assume zero stiffness proportional damping, so that α_1 is calculated according to Equation 69. This case is called Mass.

$$\alpha_2 = \frac{2\lambda}{\omega_n} \tag{67}$$

$$\alpha_1 = \lambda \cdot \omega_n \quad \text{and} \quad \alpha_2 = \frac{\lambda}{\omega_n} \tag{68}$$

$$\alpha_1 = 2\lambda \cdot \omega_n \tag{69}$$

	Original	Mixed	Mass
buoyancy joint α_1	0.058	0.029	0
buoyancy joint α_2	0	0.021	0.043
slick joint α_1	0.007	0.004	0
slick joint α_2	0	0.003	0.005

Table 17: α_1 and α_2 in the different cases

Case	**Original**	Mixed	Mass	Measurements
Event 1	**112.1**	113.0	114.6	69.0
Event 2	**171.0**	173.4	176.7	139.7
Event 3	**142.6**	144.9	148.0	72.8
Event 4	**116.6**	118.3	120.9	68.9
Event 5	**299.1**	300.6	301.7	297.4
Event 6	**192.6**	193.0	193.9	134.0

Table 18: SRSS of STD of WH moment using different types of Rayleigh damping, the values are given in kNm

It seems like choosing different types of Rayleigh damping has little effect on the end result. The stiffness dominated Rayleigh damping will cause a bit more damping in the eigenmodes which have a shorter period than the first eigenmode, so the effect is larger for events like Event 3, where a lot of the energy is in the second eigenmode, than for Event 5, where most energy is in the first eigenmode. The autospectra for the different Rayleigh models for all the events can be found in Appendix I.

11.3.2 The Effect of Critical Damping Ratios

The damping ratio is the most important parameter for calculating the Rayleigh damping. Therefore a test of the different damping ratios outlined in Table 19 will be tested. Zero mass proportional damping is assumed, meaning α_2 is calculated by Equation 67.

Case	Zero	Low	Original	Non-conservative	High	Very high
Buoyancy joints	0	1.25%	2.5%	3.0%	6%	12%
Slick joints	0	0.15%	0.3%	0.5%	1%	2%

Table 19: Damping ratios used in sensitivity study

Case	Zero	Low	**Original**	Non-conservative	High	Very high
Event 1	121.4	116.4	**112.1**	109.8	101.6	89.5
Event 2	185.2	177.6	**171.0**	167.4	154.7	136.7
Event 3	156.2	148.8	**142.6**	139.3	127.6	111.3
Event 4	128.2	121.8	**116.6**	113.8	104.2	91.0
Event 5	311.0	304.8	**299.1**	295.9	283.2	262.2
Event 6	201.5	196.9	**192.6**	190.3	181.0	165.4

Table 20: SRSS of STD of WH moment using different critical damping ratios, the values are given in kNm

Table 20 shows the large effect damping ratio has on wellhead fatigue. Especially when considering the autospectra on the next pages, it is clear that the higher damping ratios give a model which is far more accurate compared to the measurements. For higher damping ratios, the second eigenmode becomes far less pronounced, which lines up well with the data. The first eigenmode is also receiving less energy, which also lines up well with the measurements.

The exception is Event 2 (Figure 51). This event was well described by the original RIFLEX-model and the models with higher damping ratios gives lower loads than the measurements for this event. This is particularly true for the periods around the first eigenmode.

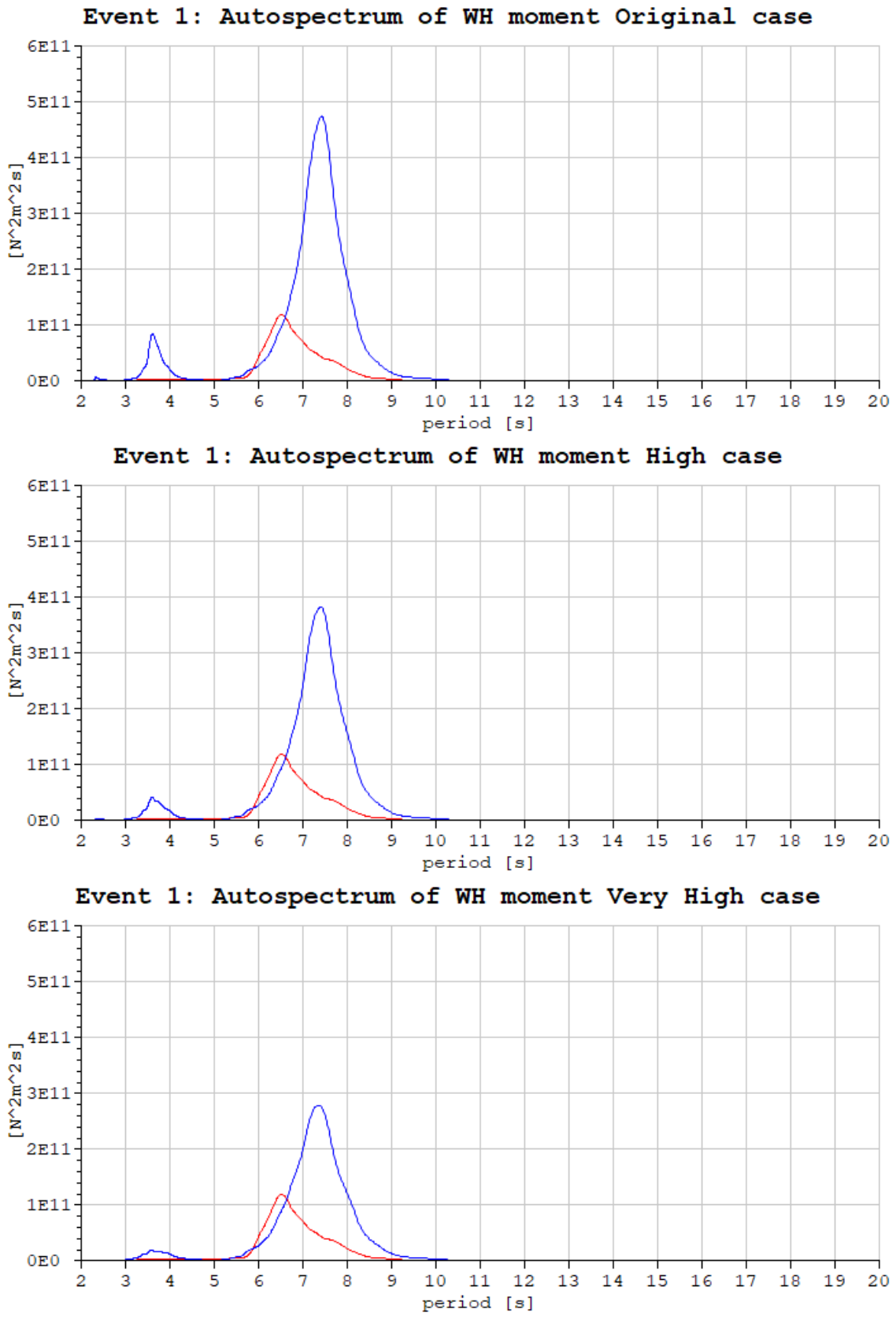

Figure 50: Event 1: The effect of higher critical damping ratio on WH moment autospectrum. The blue graphs are the autospectra for WH moment in the model for some of the damping ratios described in Table 19, the red is from measurements. The autospectrum for all the damping ratios described in Table 19 is found in Figure 110

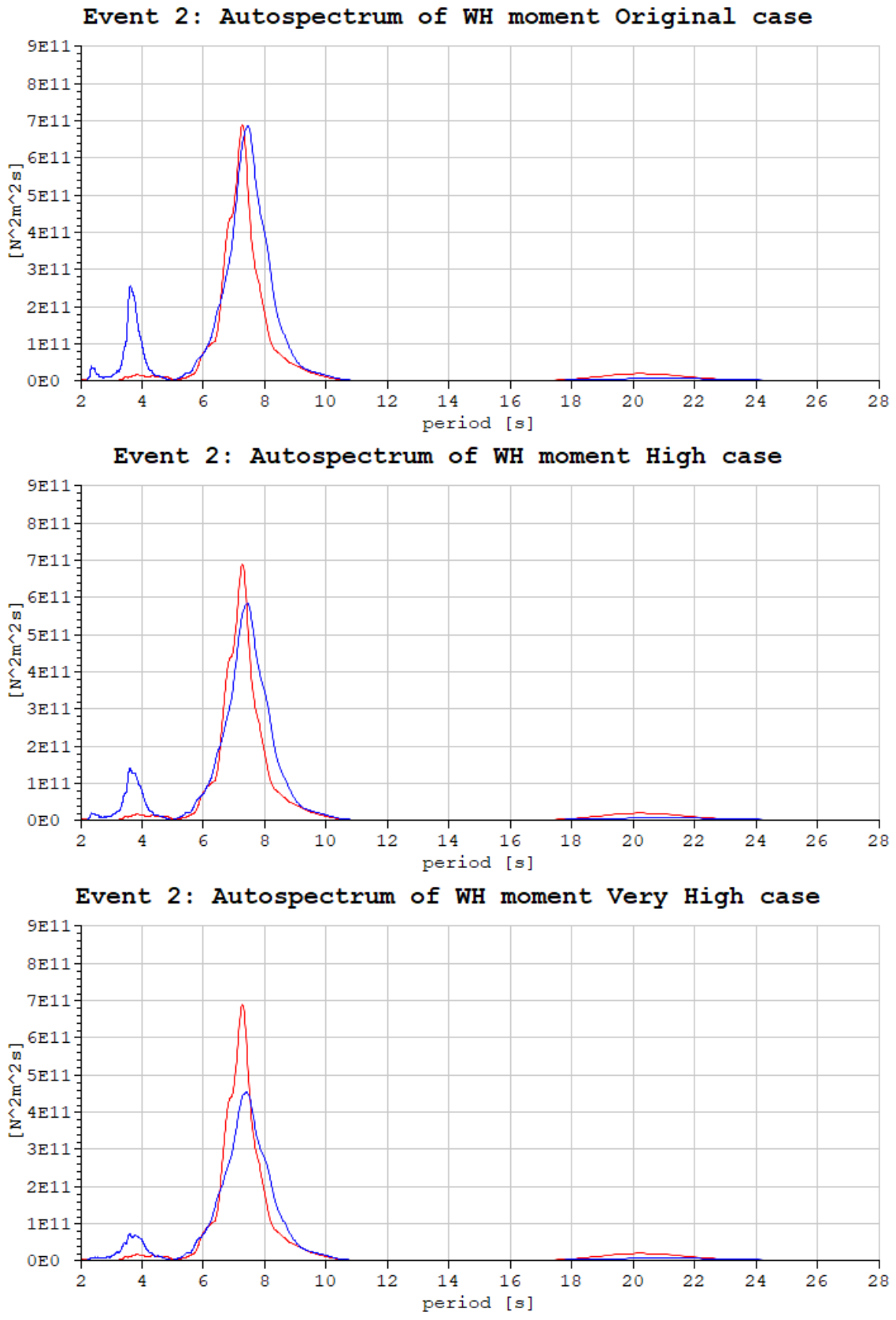

Figure 51: Event 2: The effect of higher critical damping ratio on WH moment autospectrum. The blue graphs are the autospectra for WH moment in the model for some of the damping ratios described in Table 19, the red is from measurements. The autospectrum for all the damping ratios described in Table 19 is found in Figure 111

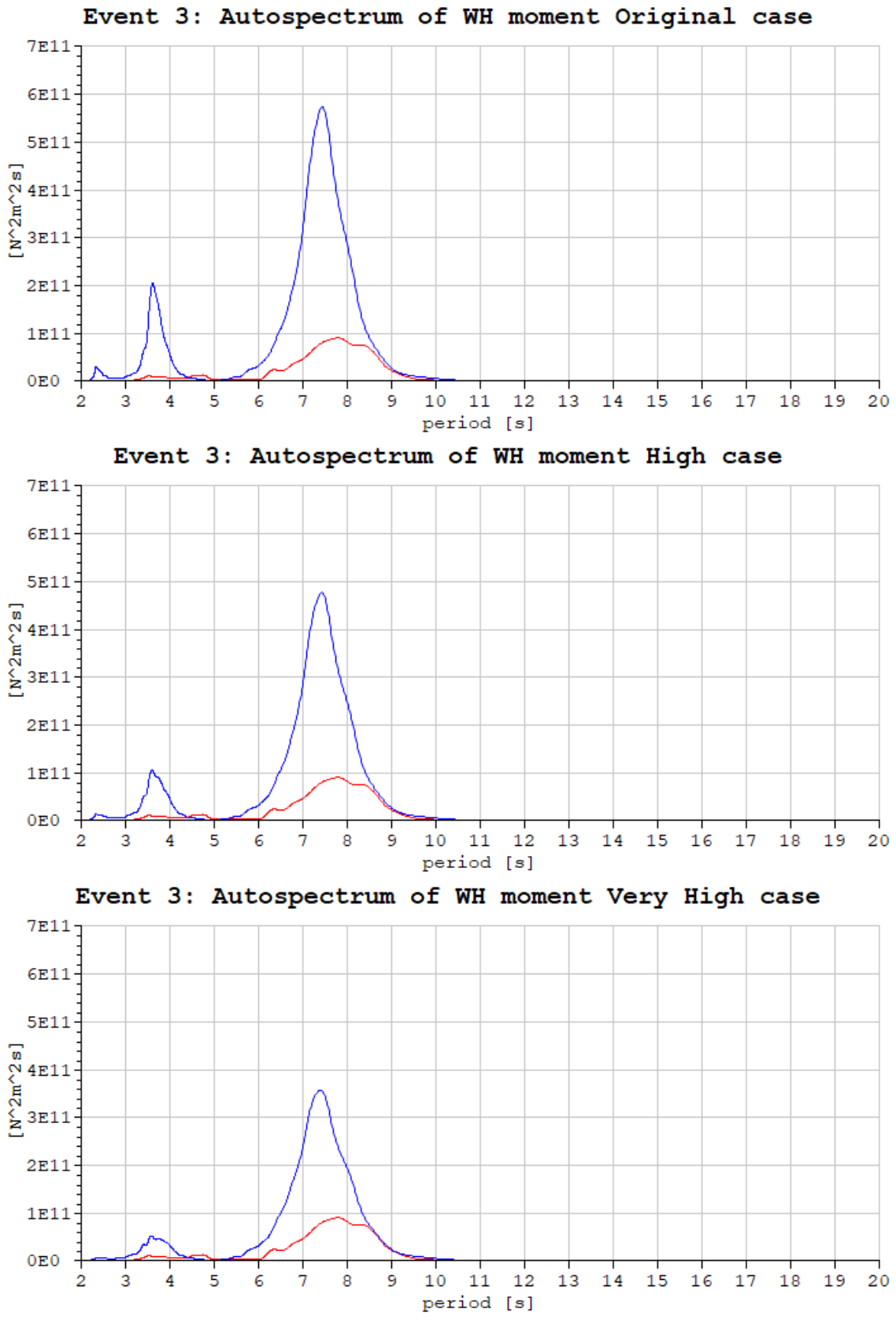

Figure 52: Event 3: The effect of higher critical damping ratio on WH moment autospectrum. The blue graphs are the autospectra for WH moment in the model for some of the damping ratios described in Table 19, the red is from measurements. The autospectrum for all the damping ratios described in Table 19 is found in Figure 112

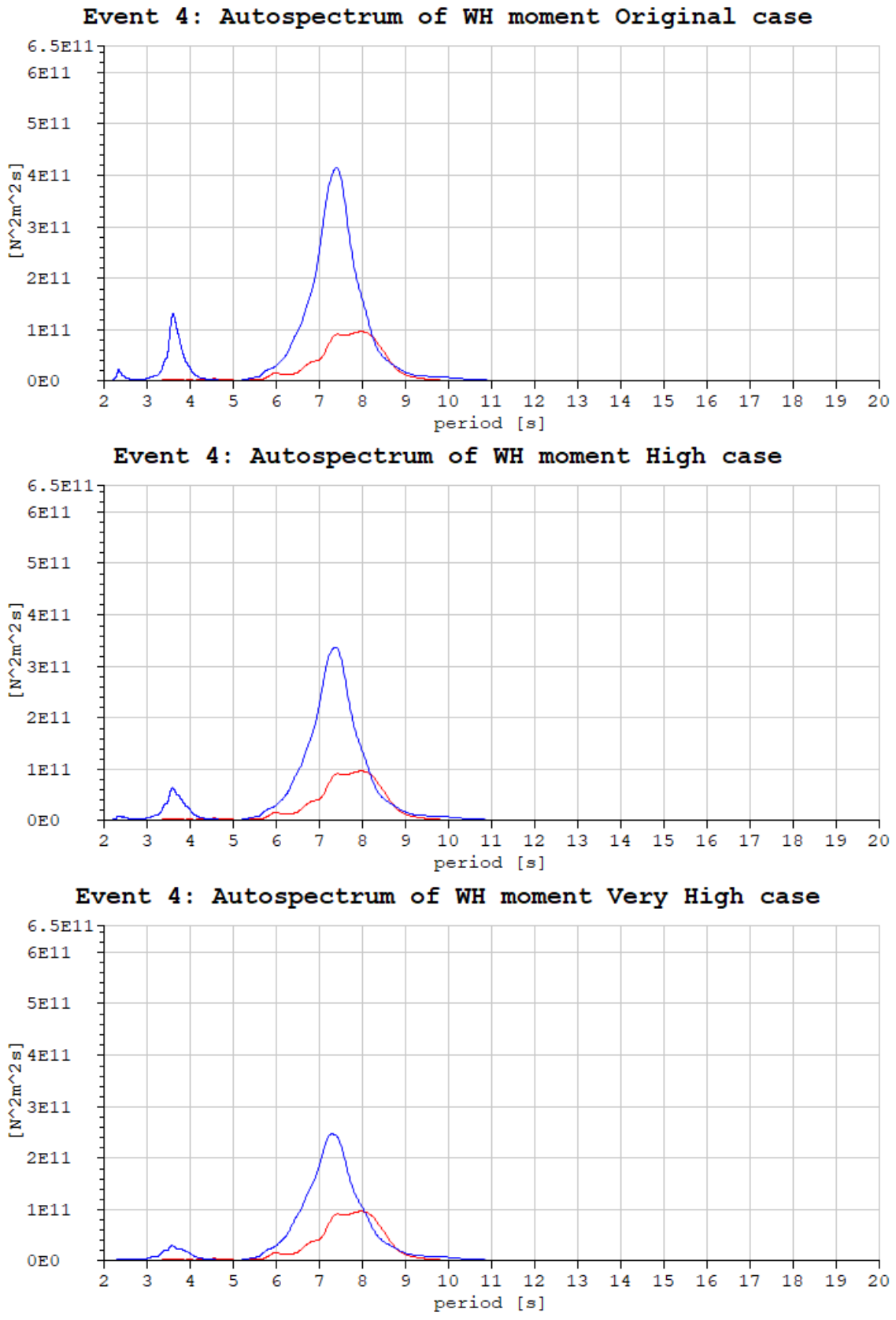

Figure 53: Event 4: The effect of higher critical damping ratio on WH moment autospectrum. The blue graphs are the autospectra for WH moment in the model for some of the damping ratios described in Table 19, the red is from measurements. The autospectrum for all the damping ratios described in Table 19 is found in Figure 113

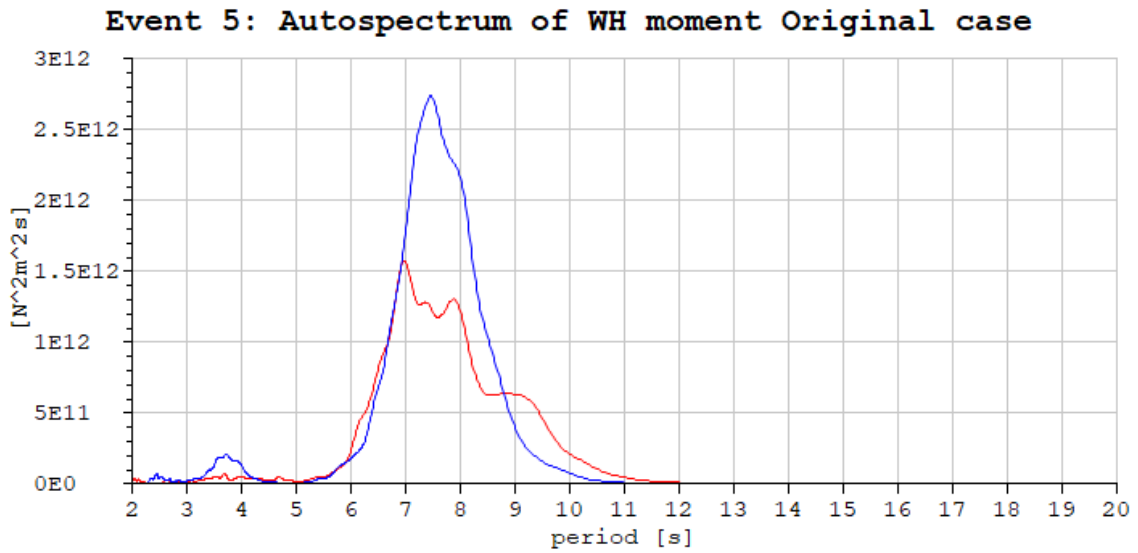

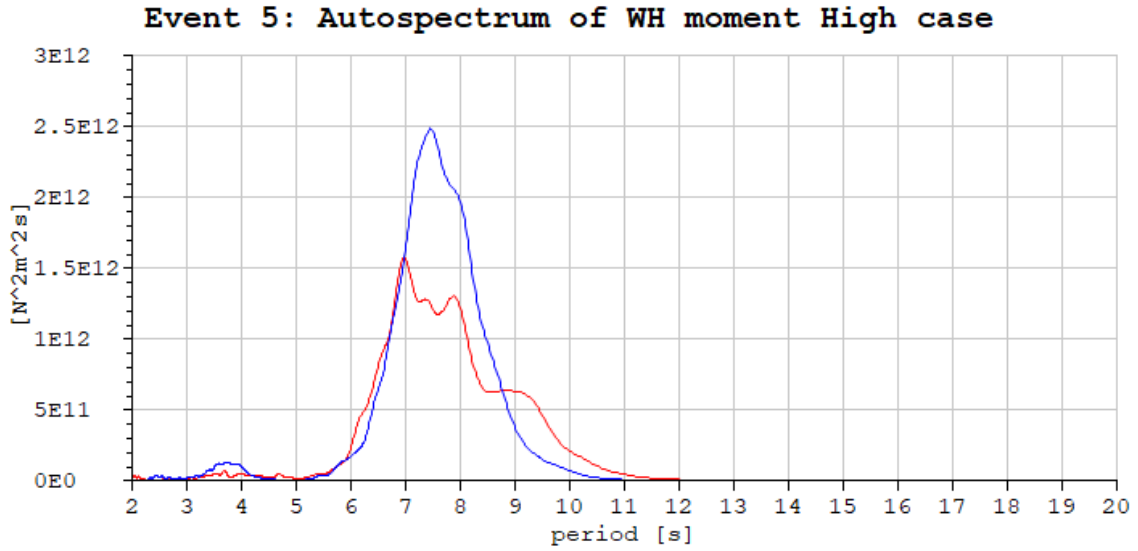

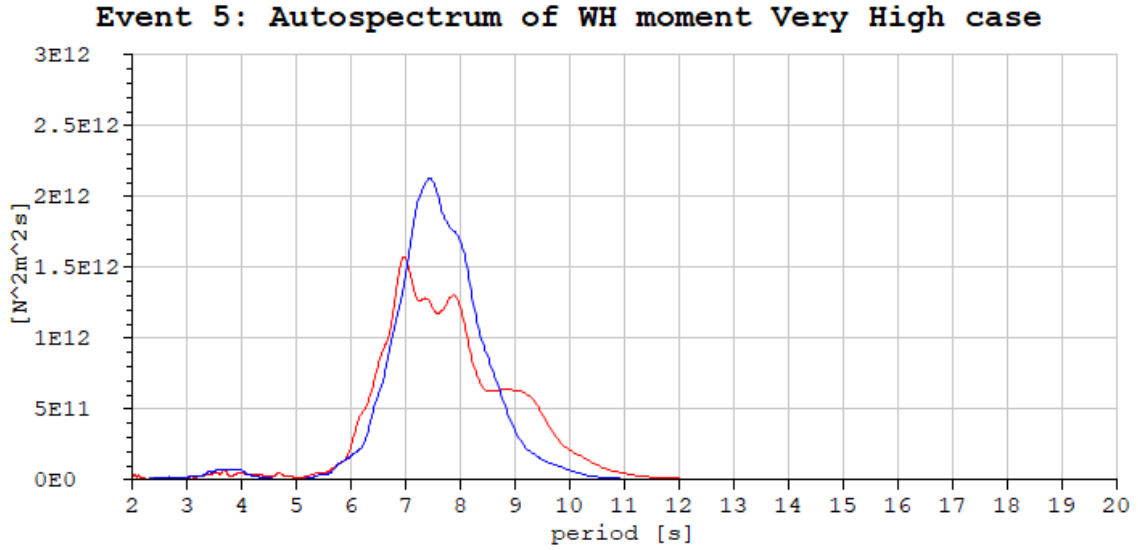

Figure 54: Event 5: The effect of higher critical damping ratio on WH moment autospectrum. The blue graphs are the autospectra for WH moment in the model for some of the damping ratios described in Table 19, the red is from measurements. The autospectrum for all the damping ratios described in Table 19 is found in Figure 114

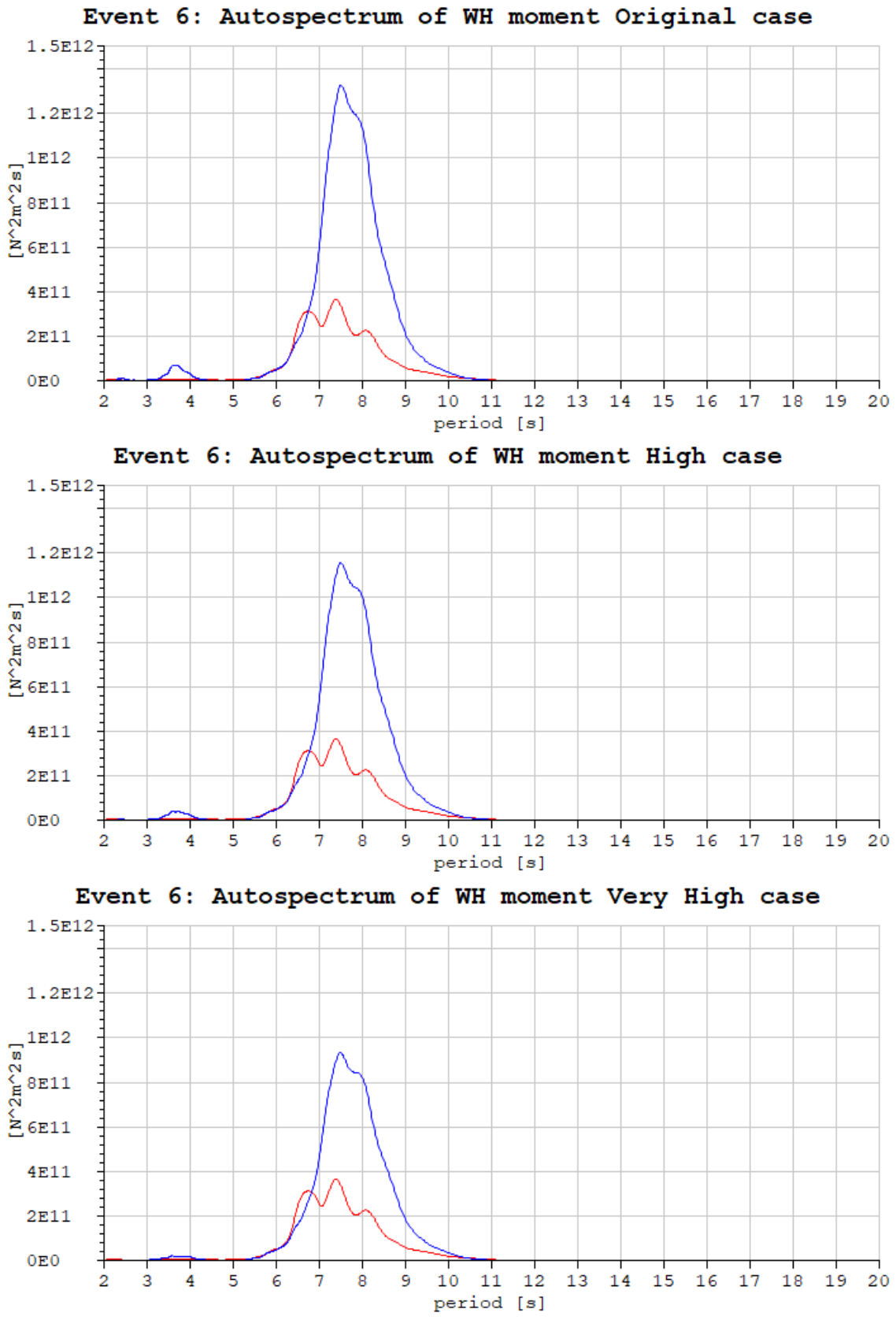

Figure 55: Event 6: The effect of higher critical damping ratio on WH moment autospectrum. The blue graphs are the autospectra for WH moment in the model for some of the damping ratios described in Table 19, the red is from measurements. The autospectrum for all the damping ratios described in Table 19 is found in Figure 115

11.4 LFJ Damping

As mentioned in Section 5.2.3, the choice of linear damping coefficient for the LFJ damping 60 $kNms/deg$ was non-conservative. This makes it important to investigate the contribution of this component on the final result. In this sensitivity study, the possible range for the LFJ damping (44 $kNms/deg$ to 60 $kNms/deg$) has been investigated, in addition to two coefficients well outside this range (20 $kNms/deg$ and 90 $kNms/deg$). This makes it possible see the effect a more conservative choice of damping coefficient might have, and to see the more general effect of this parameter.

LFJ damping [kNms/deg]	90	**60**	52	44	20	Measurements
Event 1	110.5	**112.1**	112.8	113.6	117.0	69.0
Event 2	169.6	**171.0**	171.8	172.8	177.8	139.7
Event 3	140.8	**142.6**	143.5	144.6	149.3	72.8
Event 4	114.9	**116.6**	117.4	118.3	122.4	68.9
Event 5	299.4	**299.1**	299.6	300.6	306.0	297.4
Event 6	191.1	**192.6**	193.3	194.2	198.3	134.0

Table 21: SRSS of STD of WH moment using different damping coefficients in relation to the damping in the LFJ, the values are given in kNm

Table 21 shows the result of this sensitivity study. Within the range of possible damping coefficients, the effect of different choices was relatively minor, in the range 0.5% to 1.5%. As one would expect, the effect of different damping coefficients had a larger effect for the two outlier coefficients, in the range 2.3% to 6.5%. These effects are generally small, and the effect of different damping coefficients seems to diminish as the wellhead moments increase. This phenomenon might be explained by the fact that Rayleigh damping becomes more important as the loads causing movements in the riser become larger. This phenomenon substantiates the use of a damping coefficient that is more accurate for smaller rotations, as this will be the case where the damping coefficient has the largest impact.

11.5 BOP Drag Coefficients

In Section 5.2.1 it was shown that the drag coefficient on the BOP and LMRP could be in the range 4-10. A drag coefficient of 4.5 was chosen. In this sensitivity study, the effect of choosing less conservative drag coefficients will be explored.

C_d	**4.5**	7.0	10	Measurements
Event 1	**112.1**	112.0	112.0	69.0
Event 2	**171.0**	170.7	170.4	139.7
Event 3	**142.6**	142.5	142.3	72.8
Event 4	**116.6**	116.5	116.4	68.9
Event 5	**299.1**	298.9	298.7	297.4
Event 6	**192.6**	192.6	192.5	134.0

Table 22: SRSS of STD of WH moment using different drag coefficients on the BOP and LMRP, the values are given in kNm

As seen in Table 22, the drag coefficient has very limited effect on the variations in wellhead moment. It can be noted that the effect seems to be largest for Event 2 and 3, this is probably because they have the most energy in the third eigenmode, so the effect of viscous damping on the BOP is largest for these events.

11.6 Hydrodynamic Parameters for Slick Joint

In Section 5.2.4, the hydrodynamic parameters for slick and pup joints were based on a conservative assumption of flow in relation to the main pipe and the additional lines, as seen in Figure 22. Now, the non-conservative assumption of flow, rotated 90 degrees in relation to the flow in Figure 22 will be considered. This gives the following parameters:

	"Non-conservative"	Original
D_H	533 mm	787 mm
C_a	1.0	0.51
C_d	1.0	1.1

The results from this study were quite surprising. What was thought to be the more conservative case was in fact less conservative. This can be explained if the hydrodynamic damping of the slick joints is more important than the hydrodynamic excitation from the waves on this part of the riser. This indicates that one could reduce the wellhead fatigue by using more buoyancy modules in this riser set-up.

Case	"Non-conservative"	**Original**
Event 1	121.5	**112.1**
Event 2	184.1	**171.0**
Event 3	153.5	**142.6**
Event 4	125.5	**116.6**
Event 5	333.9	**299.1**
Event 6	212.7	**192.6**

Table 23: SRSS of STD of WH moment with different modeling of slick joints, the values are given in kNm

12 Measuring WH Moment Based on a Quasi-Static Approach

As mentioned in Section 8, Equinor also took measurements of LRS angle and BOP angle during the operation considered in this report. These can also be used to give an approximation of the oscillation wellhead moment during the operation based on indirect measurements. This is useful as it could make it possible to increase the fatigue life of the wellhead continuously as operations are performed.

12.1 Quasi-static Approach

The following assumptions have been made to create a simple model for finding wellhead moment based on θ_{LRS} and θ_{BOP}:

1. rigid body motion as seen in Figure 56
2. equally distributed mass in the BOP
3. top tension on the LFJ of 80kNm, as seen in the cusp in Figure 27
4. height of the BOP equal to $H_{WH} = 12.54$ meters
5. small angles
6. top tension on the BOP TT', flex joint moment in LFJ, and weight in water are the only forces acting on the BOP

With these assumption made the total moment on wellhead can be described by the following equation:

$$\sum M = -M_{WH} + M_{LFJ} + M_{TT} + M_G \quad (70)$$

Where M_{WH} is the moment on the wellhead, M_{LFJ} is the moment due to the rotations in the LFJ, M_{TT} is the moment from the "Top tension" on the BOP and M_G is the moment from the weight in water of the structure.

M_{LFJ} can fairly easily be calculated by finding the rotation in the LFJ, which is simply $\theta_{LRS} - \theta_{BOP}$, and then find the moment based on the non-linear stiffness of the LFJ (Figure 20).

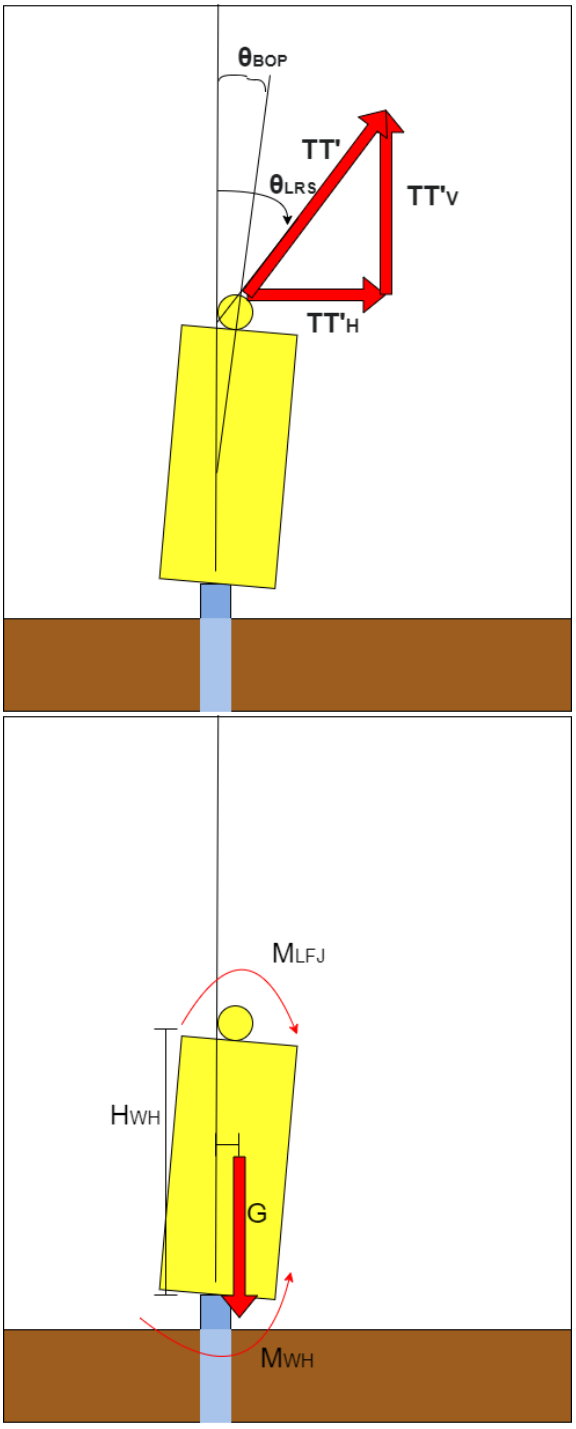

Figure 56: Illustration of the static forces acting on the BOP

To calculate M_{TT}, one has to consider its two contributions to the wellhead moment. This is done by decomposing TT' into its vertical TT'_V and horizontal TT'_H contributions. Due to the assumption of small angles Equation 71 is valid.

$$TT'_H = TT' \cdot \theta_{LRS} \qquad TT'_V = TT' \quad (71)$$

Multiplying the decomposed values for TT' with their respective arms in relation to the wellhead gives M_{TT}:

$$M_{TT} = TT'_H \cdot H_{WH} - TT'_V \cdot H_{WH} \cdot \theta_{BOP} = TT' \cdot \theta_{LRS} \cdot H_{WH} - TT' \cdot H_{WH} \cdot \theta_{BOP} \tag{72}$$

M_G is calculated by assuming that the center of gravity in the BOP is simply $H_{WH}/2$ meters above the wellhead and using the weight in water from Figure 17:

$$M_G = BOP_{WIW} \cdot g \cdot \frac{H_{WH}}{2} \theta_{BOP} \tag{73}$$

Assuming that the total moment in Equation 70 is close to zero, the wellhead moment can now be calculated:

$$M_{WH} = M_{LFJ} + M_{TT} + M_G \tag{74}$$

These calculations have been made into a script which can be seen in Appendix K.

12.2 Results from the Quasi-Static Model

This model is highly sensitive to the value used for top tension, so the results are presented with different values for top tension.

TT'	**800 kN**	1200 kN	1600 kN	Measurements
Event 1	**38**	48	59	70
Event 2	**93**	121	150	140
Event 3	**44**	57	69	73
Event 4	**44**	56	69	69
Event 5	**190**	252	315	297
Event 6	**91**	121	150	134

Table 24: SRSS of STD of WH moment from quasi static approach, the values are given in kNm

The quasi-static method of calculating WH moment from θ_{LRS} and θ_{BOP} gave far better results if one considered the top tension on wellhead to be 1600kNm. This might be due to the top tension in reality being higher than what has been assumed in this report, but it can also be explained by the fact that the quasi-static model is a very simple model that does not take into account all the forces acting on the BOP. The placement of the BOP angle measurement is also a bit problematic, in Section 8 it is clear that the motion sensor on the BOP sits fairly low on the BOP. This may cause the measured BOP angle to be lower than the actual the rotations of the entire BOP, resulting in lower contributions on wellhead moment from the BOP angle. Equation 74 is based on an assumption of zero dynamic contribution on the wellhead moment, that may also cause some of the errors.

The quasi-static approach does however give extremely similar shapes in the autospectra of the WH moments. This indicates a very strong correlation between the moment the wellhead experiences and the angles considered. The autospectra for Event 3 have been added here to highlight how well the shapes matches up, but the same can be seen in all the autosprectra found in Appendix L.

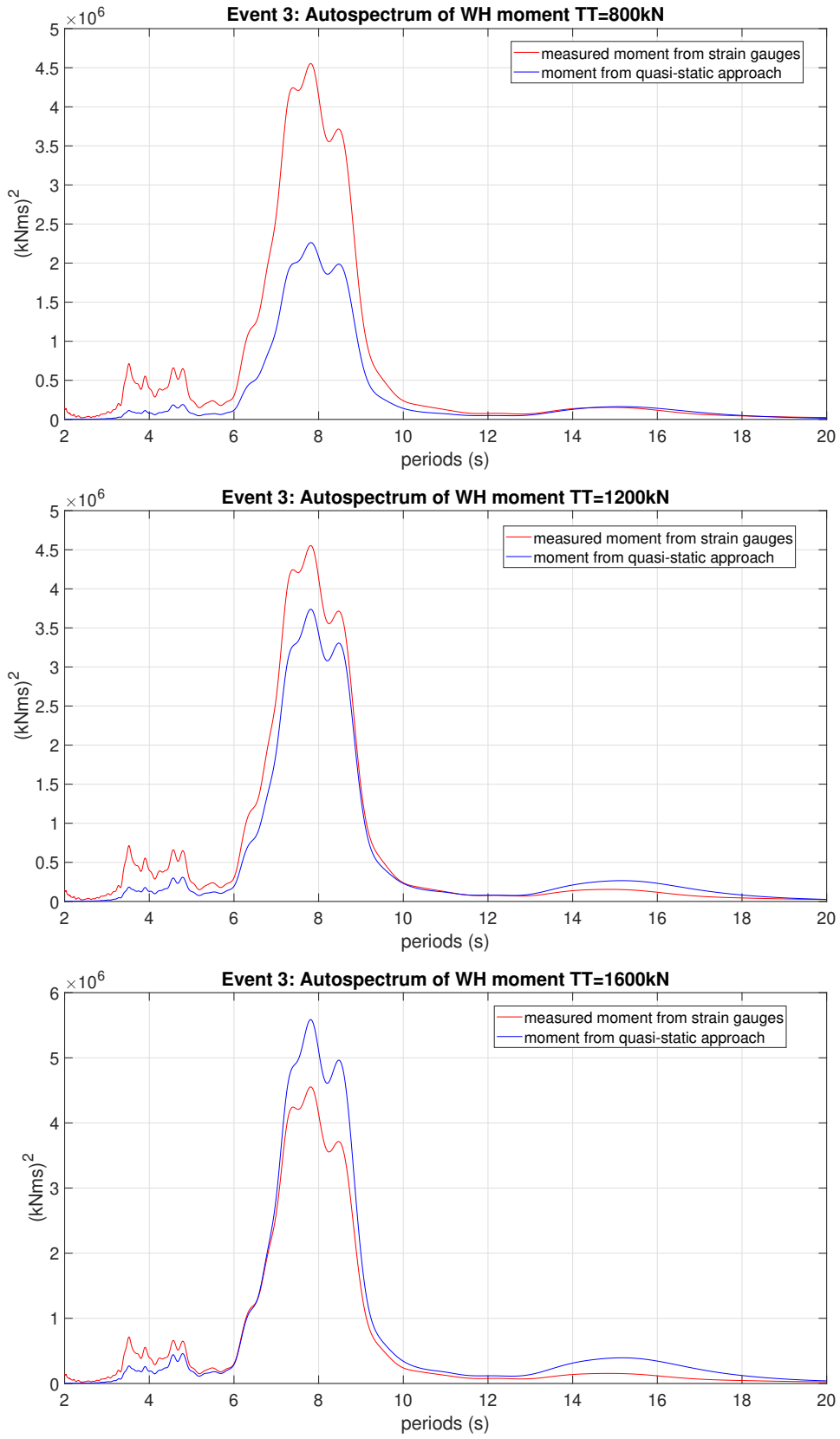

Figure 57: Event 3: Autospectra from quasi-static approach with differing top tension on BOP

12.3 Correlations between Wellhead Moment and other Measurements Parameters

In this section, a model for finding wellhead moment based on LRS angle and BOP angle has been presented. It has earlier been mentioned that some papers have indicated that displacement on the top of the wellhead may also be a good indirect measure to find the wellhead moment. This will now be investigated.

For all the events, the SRSS of the wellhead moment has been plotted against the SRSS of the BOP angle, against the SRSS of the LRS angle, and against the SRSS of the displacement of the top of the BOP. These plots can be seen in Appendix M, but the general trend follows what can be found for event 2 in Figure 58. The displacement has a weak correlation with the wellhead moment, while the LRS angle and especially the BOP angle, shows good correlation with the wellhead moment. This indicates that an indirect model based on the mentioned rotational angles will yield better results than an indirect model based on displacement of the top of the BOP.

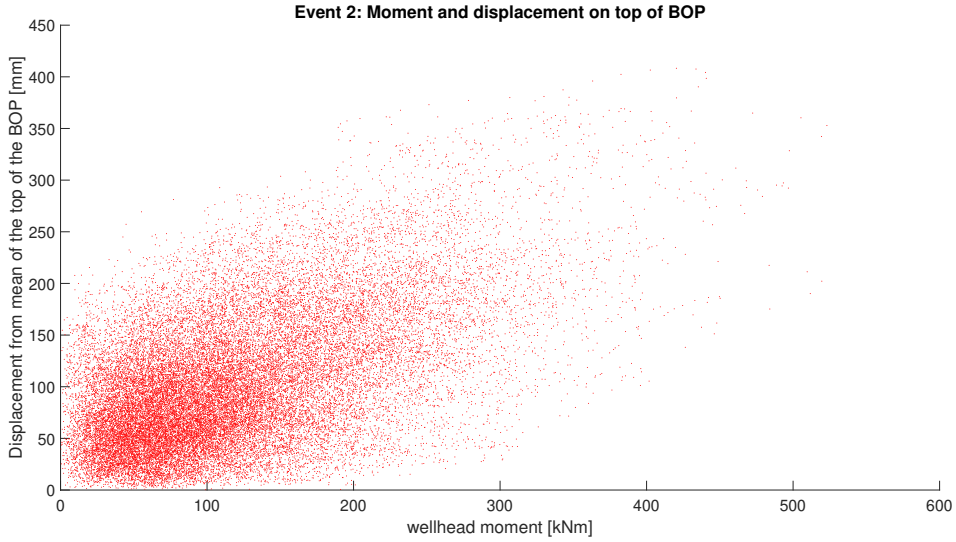

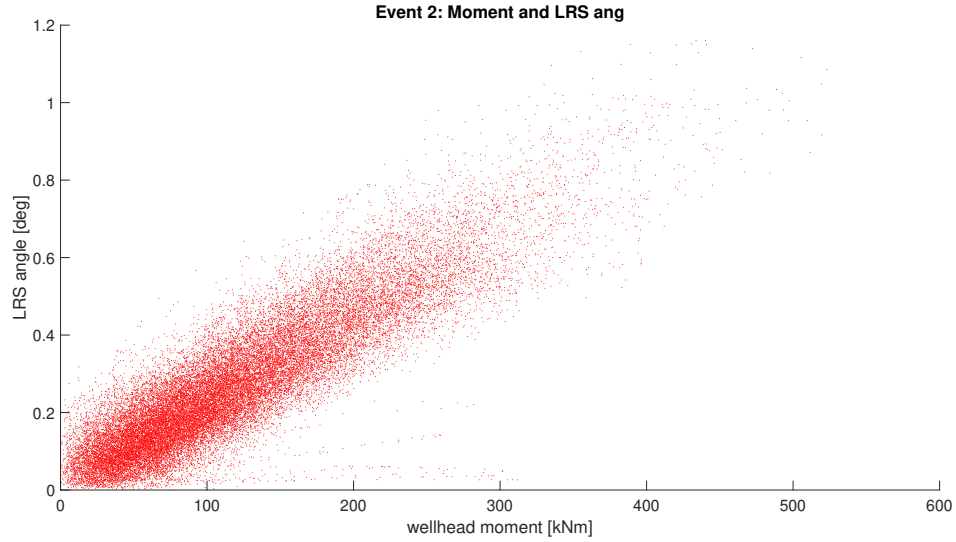

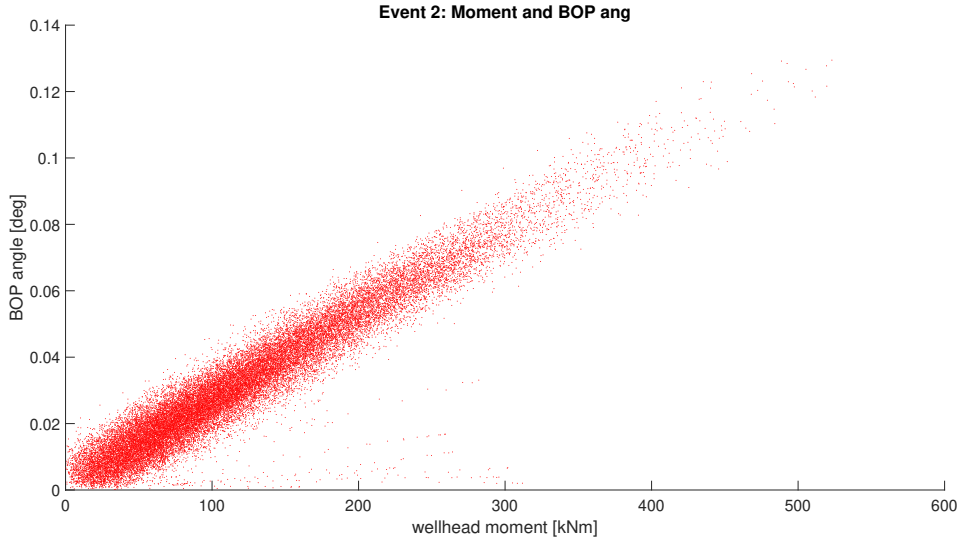

Figure 58: Event 2: Correlation between WH moment and other measurement parameters

13 Conclusion

In this report, wellhead fatigue has been investigated. A brief overview of how WH fatigue is predicted has been presented, and a detailed model for conducting global load analysis on a top tensioned riser has been presented. The model has been created in RIFLEX. The results from this model has been presented and the effect of a large number of model parameters has been investigated thoroughly. The results from the global load analysis, has been compared with measured data from an actual campaign in the North Sea. The RIFLEX model also made it possible to analyze the eigenvalues of the riser system.

The results showed that the global load model was generally conservative, and this conservatism persisted for most reasonable parameter adjustments. It was concluded that the model performed well against the measurements, but that the damping seemed to be substantially higher in the measurements than in the original riser model. This report highlights the importance of damping in top tensioned risers, especially when they have eigenperiods close to typical wave periods. The report clearly shows the importance of eigenvalues in global load analysis of top tensioned risers, as most fatigue damage is related to the eigenmodes of the system.

The possibility of measuring wellhead moment based on indirect methods has also been investigated. A quasi-static model based on angular rotations on the BOP and the LFJ has been presented, and their results have also been compared to directly measured wellhead moment.

The results from the quasi-static approach were not conservative. However, the results shows the promising possibilities from measuring wellhead moment indirectly, and using the results to calculate fatigue damage continuously throughout an operation, to potentially increase fatigue life. The results showed, as previous papers have indicated, that indirect measures based on BOP and LRS angle will give more accurate measures of wellhead moment, than measures based on displacement on the top of the BOP.

13.1 Further Works

Due to time constraints, this report only considers six 1-hour events, chosen from the operational period based on getting a wide range of types of wave environments. Further works could include a consideration of the rest of the data set, to get a wider understanding of the riser behavior.

Local load analysis may also ensue, so that the resulting fatigue damage from oscillating moments can be investigated. Such an analysis could also be used to quantify the difference in fatigue damage calculated from quasi-static approach and model, so that the potential fatigue life extension from such an analysis can be shown.

The quasi-static model may also be improved by adding the effect of dynamic contribution to the wellhead fatigue, and by getting improved measures or approximation of the top tension on the BOP.

Bibliography

[1] URL: https://en.wikipedia.org/wiki/Drilling_riser.

[2] Xavier Arino, Massimiliano Russo, Guttorm Grytør, Jaap de Wilde and Michael Tognarelli. 'FORCED OSCILLATION MODEL TESTS FOR DETERMINATION OF HYDRODYNAMIC COEFFICIENTS OF LARGE SUBSEA BLOWOUT PREVENTERS'. In: *34th International Conference on Ocean, Offshore and Arctic Engineering* (2015).

[3] Kristoffer H. Aronsen, Sergey Kuzmichev, Lorents Reinås, Guttorm Grytøyr, Kathrine Gregersen and Finn Kirkemo. 'ANALYSIS APPROACH FOR ESTIMATING WELLHEAD FATIGUE'. In: *Proceedings of the ASME 2018 37th International Conference on Ocean, Offshore and Arctic Engineering* (2018).

[4] DNV GL. *DNVGL-CG-0129 Fatigue assessment of ship structures*. 2015.

[5] DNV GL. *DNVGL-RP-E104, Wellhead fatigue analysis*. 2019.

[6] O. M. Faltinsen. *SEA LOADS ON SHIPS AND OFFSHORE STRUCTURES*. Cambridge university press, 1998.

[7] Guttorm Grytør, Massimiliano Russo, Halvor Borgen Lindstad and Fredy Coral. 'WELLHEAD FATIGUE DAMAGE BASED ON INDIRECT MEASUREMENTS'. In: *34th International Conference on Ocean, Offshore and Arctic Engineering* (2015).

[8] American Petroleum Institute. 'Geotechnical and Foundational Design Considerations, API RECOMMENDED PRACTICE 2GEO'. In: (2021).

[9] Frank Jahn, Mark Cook and Mark Graham. *Hydrocarbon exploration and production*. Elsevier, 1998.

[10] Massimiliano Russo, Harald Holden, Lorents Reinås and Morten Sæther. 'Fatigue assessment of subsea wells for future and historical operations based on measured riser loads'. In: *31th International Conference on Ocean, Offshore and Arctic Engineering* (2012).

[11] Massimiliano Russo, Erling Myhre, Lasse Eilertsen, Frank Johannsen, Chris Hart and Tore Kalhovd. 'Successful Real Time Instrumentation Of The Conductor And Surface Casing Of An Exploration Subsea Well In The North Sea To Measure The Actual Loads Experienced During Drilling Operation'. In: *2015 Offshore Technology Conference* (2015).

[12] Massimiliano Russo, Urszula Wolak, Erling Myhre and Guttorm Grytør. 'MEASURED WELLHEAD LOADS DURING DRILLING OPERATIONS – PAPER 1 – DATA PROCESSING AND PRELIMINARY RESULTS'. In: *34th International Conference on Ocean, Offshore and Arctic Engineering* (2015).

[13] Massimiliano Russo, Arash Zakeri, Sergey Kuzmichev, Guttorm Grytøyr, Edward Clukey and Elizbar B. Kebadze. 'Integrity Assessment of Offshore Subsea Wells: Evaluation of Wellhead Finite Element Model Against Monitoring Data Using Different Soil Models'. In: *Journal of Offshore Mechanics and Arctic Engineering* (2016).

[14] SINTEF Ocean. *RIFLEX 4.20.2 Theory Manual*. 2021.

[15] SINTEF Ocean. *RIFLEX 4.20.2 User Guide*. 2021.

[16] Charles Sparks. *Fundamentals of marine riser mechanics*. Pennwell, 2007.

[17] Chunguang Wang, Krishnakumar Shankar and Evgeny V Morozov. *Tailored design of top-tensioned composite risers for deep-water applications using three different approaches*. 2017.

Appendix

A A subset of first order motion transfer functions for the semi-submersible rig considered in this report

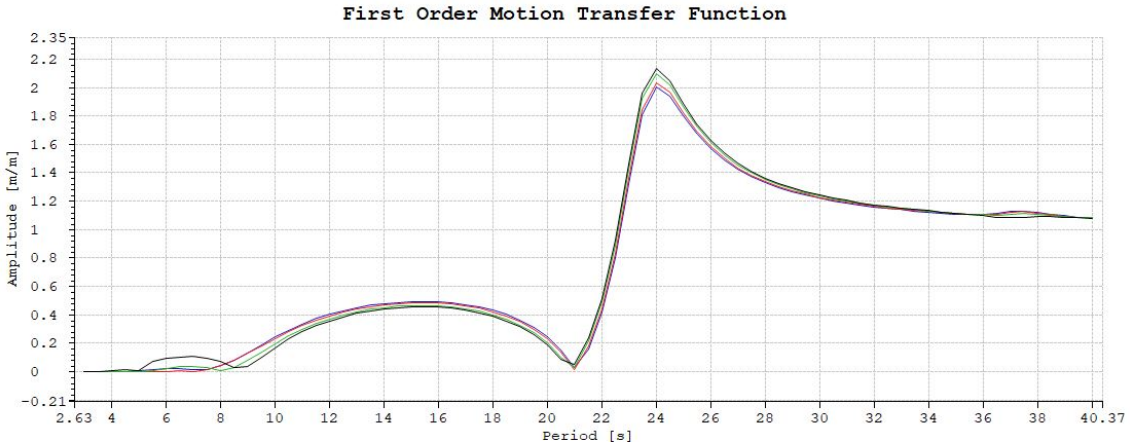

Heave transfer function

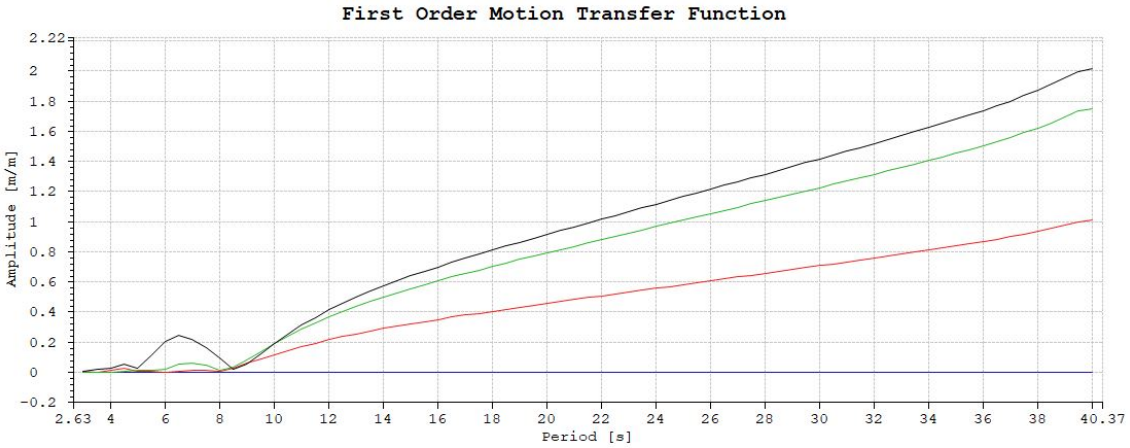

Sway transfer function

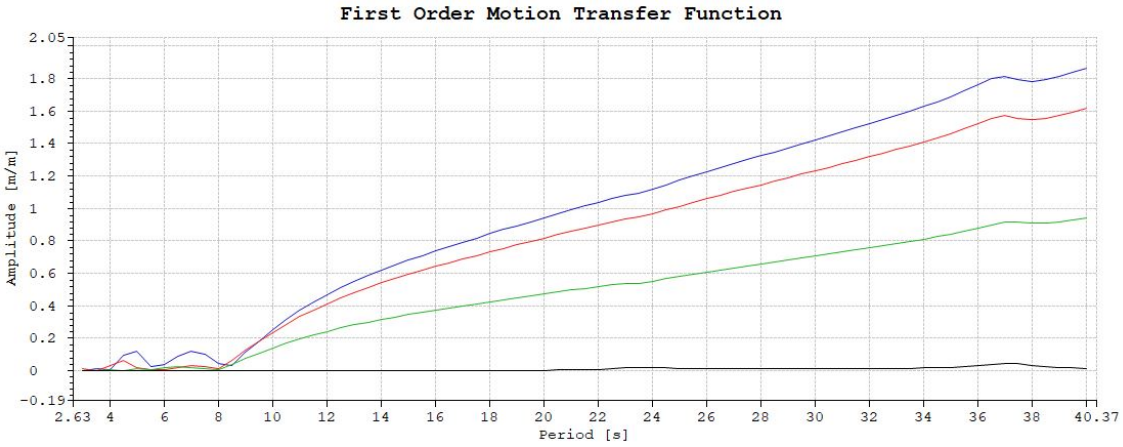

Surge transfer function

Yaw transfer function

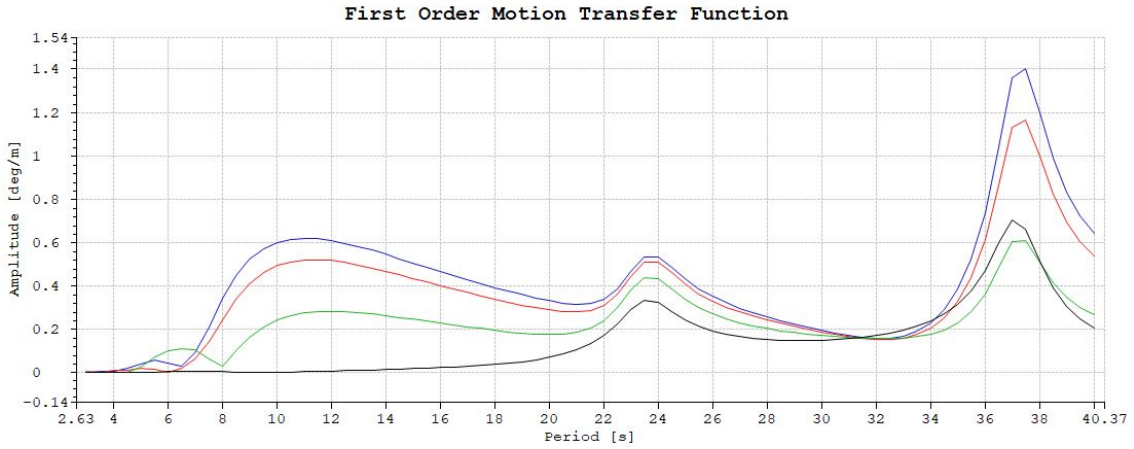

Pitch transfer function

Roll transfer function

Figure 59: First order motion transfer functions for Ocean Vanguard. The blue curves corresponds to waves at 0 degrees, the red curves to 30 degrees, the green curves to 60 degrees and the black curves correspond to waves coming at 90 degrees angle

B Non-linear soil springs

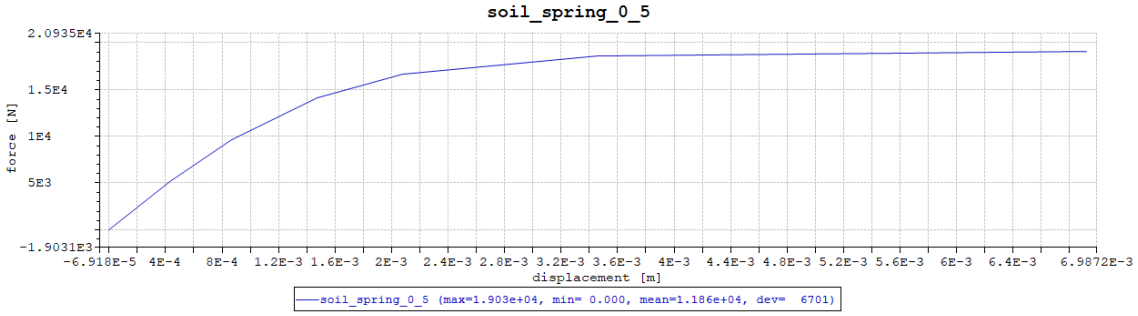

Figure 60: Nonlinear stiffness of spring counteracting movements in XY-plane in the well 0.5 meters below the soil surface

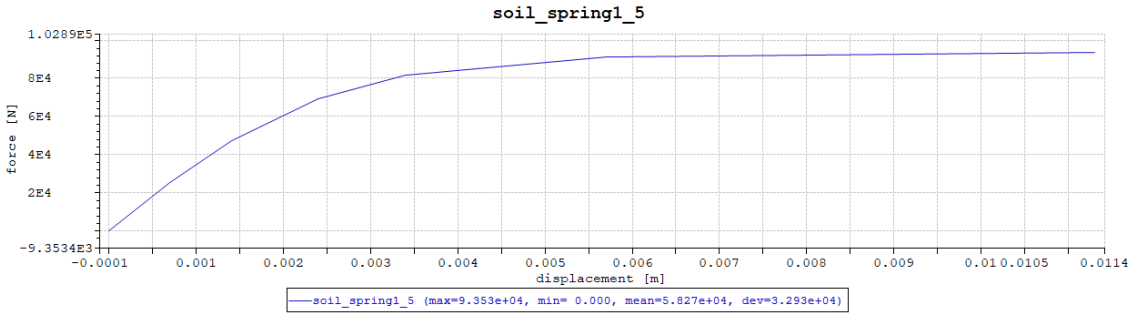

Figure 61: Nonlinear stiffness of spring counteracting movements in XY-plane in the well 1.5 meters below the soil surface

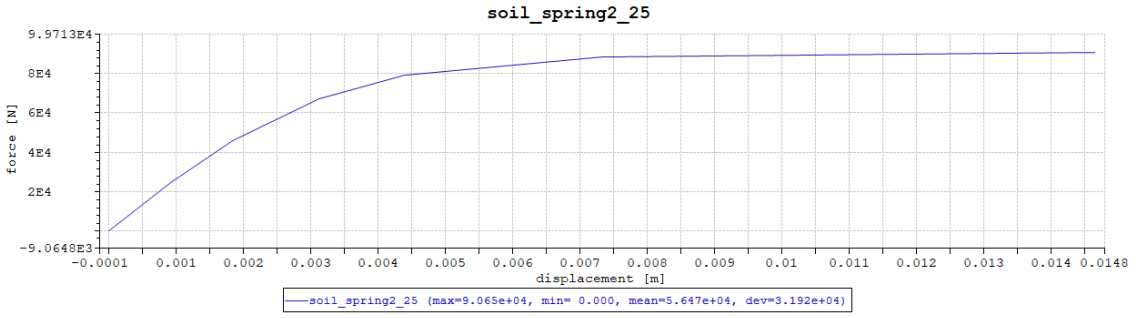

Figure 62: Nonlinear stiffness of spring counteracting movements in XY-plane in the well 2.25 meters below the soil surface

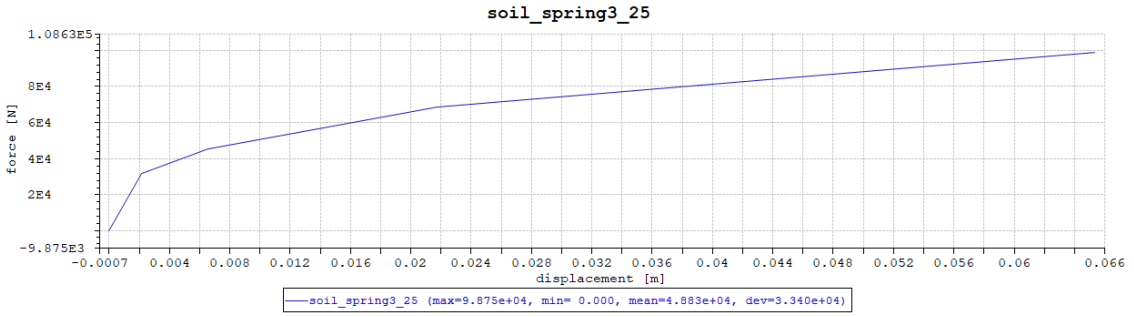

Figure 63: Nonlinear stiffness of spring counteracting movements in XY-plane in the well 3.25 meters below the soil surface

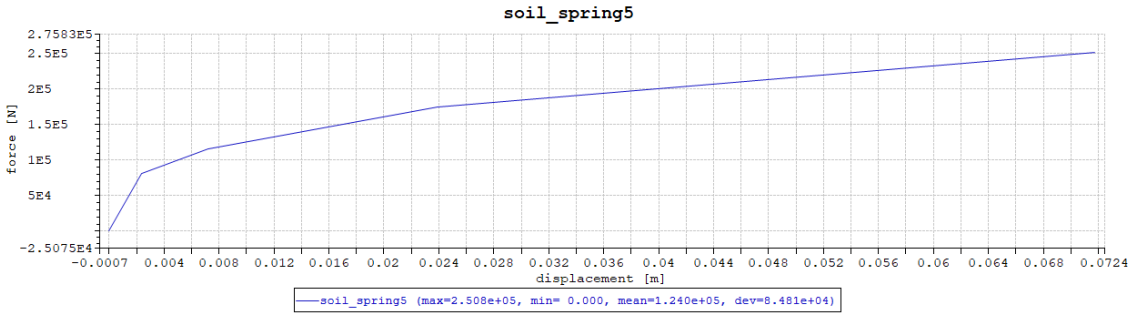

Figure 64: Nonlinear stiffness of spring counteracting movements in XY-plane in the well 5 meters below the soil surface

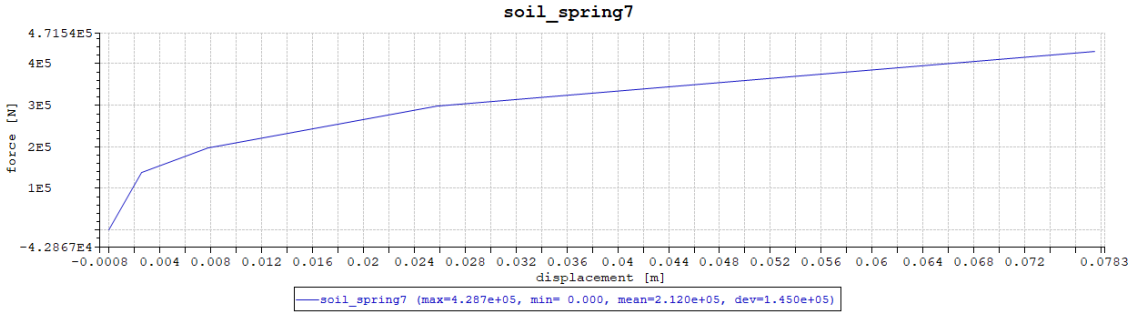

Figure 65: Nonlinear stiffness of spring counteracting movements in XY-plane in the well 7 meters below the soil surface

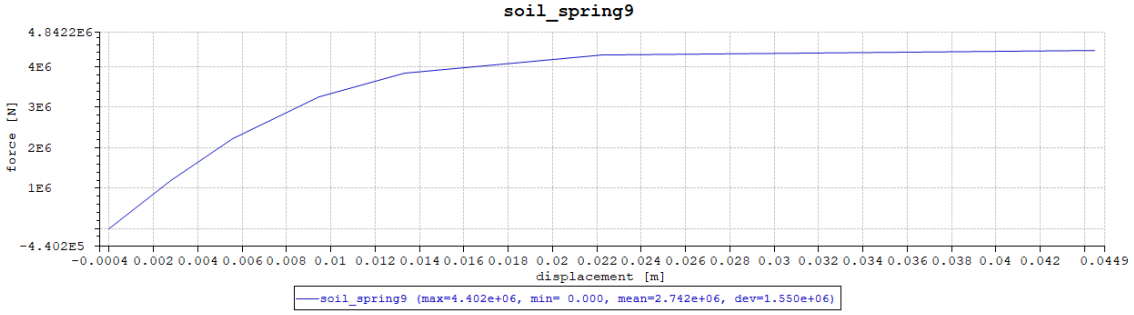

Figure 66: Nonlinear stiffness of spring counteracting movements in XY-plane in the well 9 meters below the soil surface

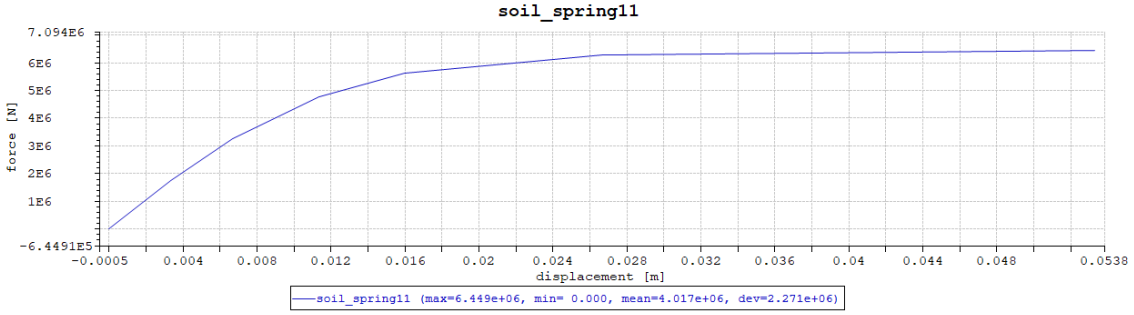

Figure 67: Nonlinear stiffness of spring counteracting movements in XY-plane in the well 11 meters below the soil surface

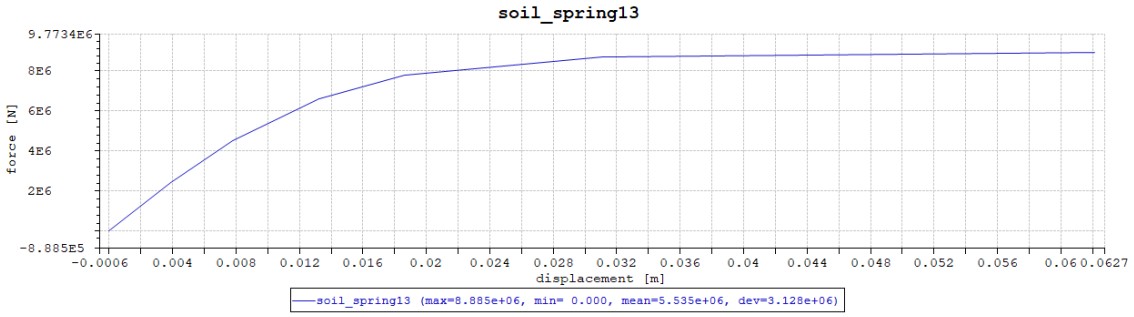

Figure 68: Nonlinear stiffness of spring counteracting movements in XY-plane in the well 13 meters below the soil surface

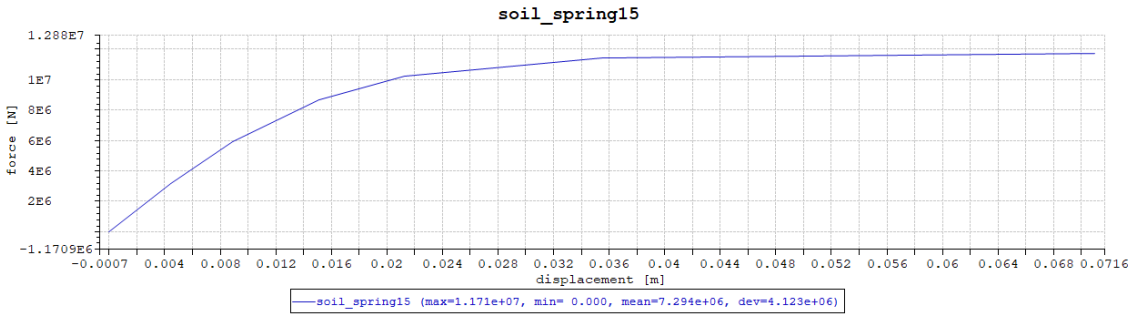

Figure 69: Nonlinear stiffness of spring counteracting movements in XY-plane in the well 15 meters below the soil surface

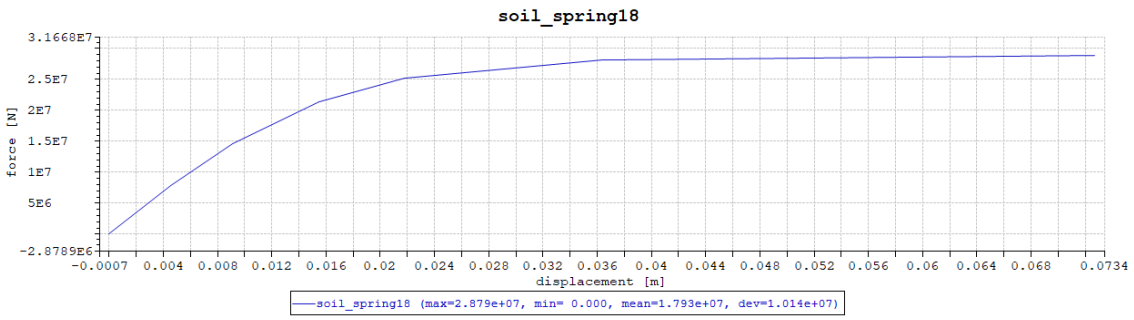

Figure 70: Nonlinear stiffness of spring counteracting movements in XY-plane in the well 18 meters below the soil surface

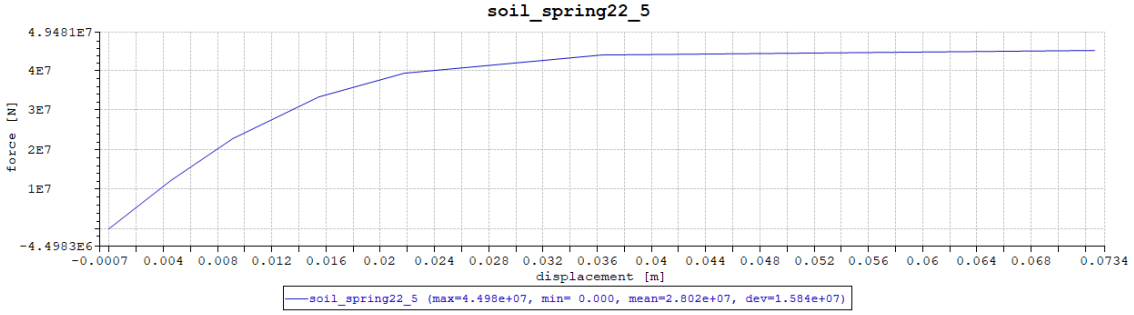

Figure 71: Nonlinear stiffness of spring counteracting movements in XY-plane in the well 22.5 meters below the soil surface

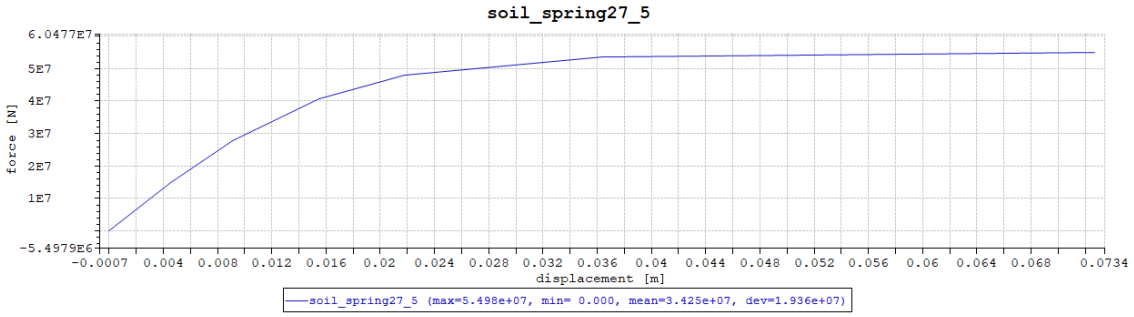

Figure 72: Nonlinear stiffness of spring counteracting movements in XY-plane in the well 27.5 meters below the soil surface

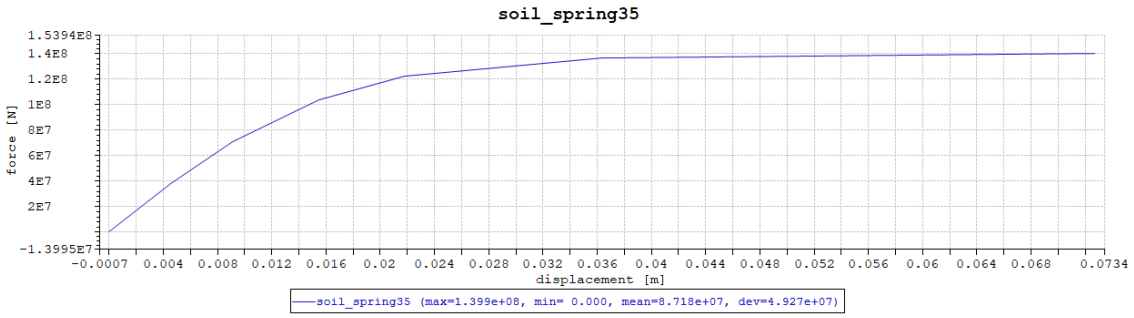

Figure 73: Nonlinear stiffness of spring counteracting movements in XY-plane in the well 35 meters below the soil surface

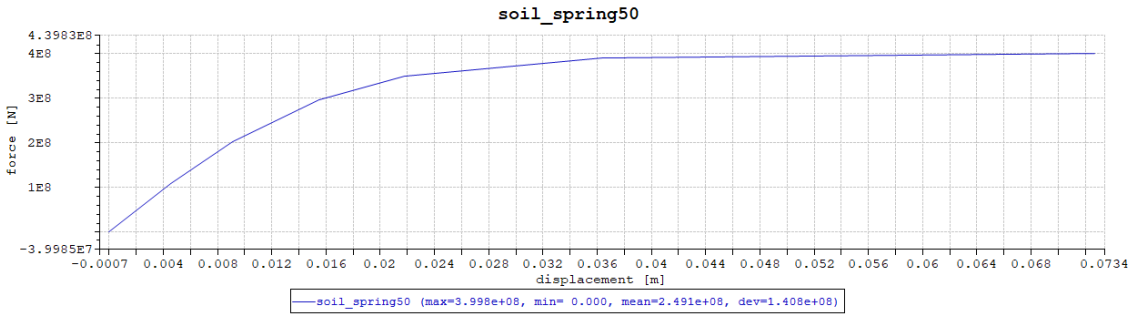

Figure 74: Nonlinear stiffness of spring counteracting movements in XY-plane in the well 50 meters below the soil surface

C 2D wave spectrum for Event 3, Event 4, Event 5 and Event 6

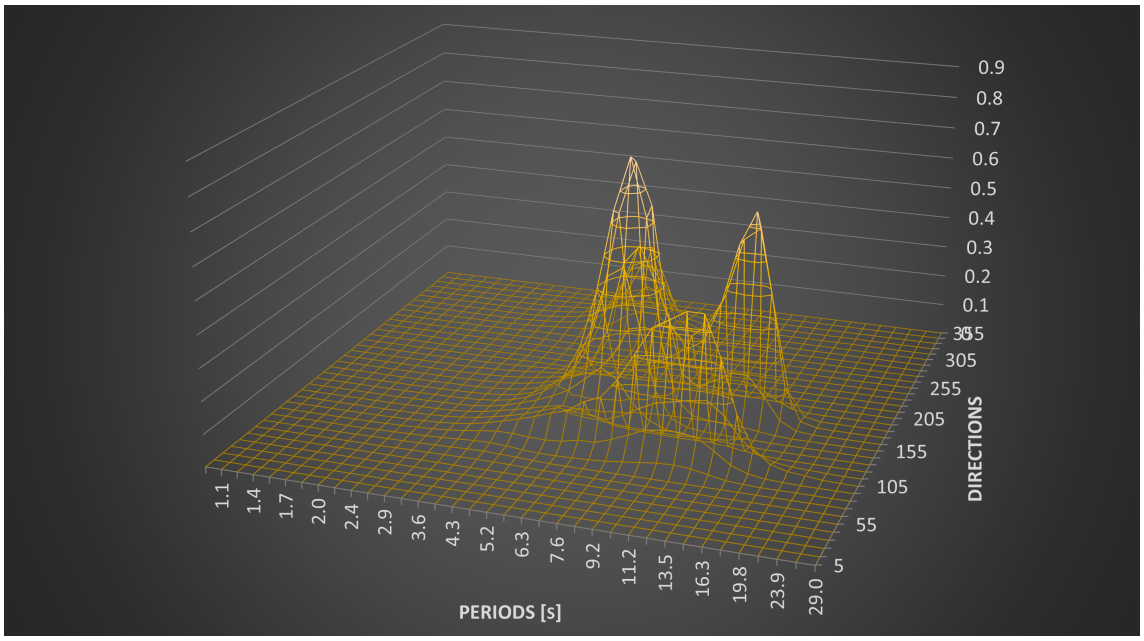

Figure 75: Event 1: 2D-wave spectra

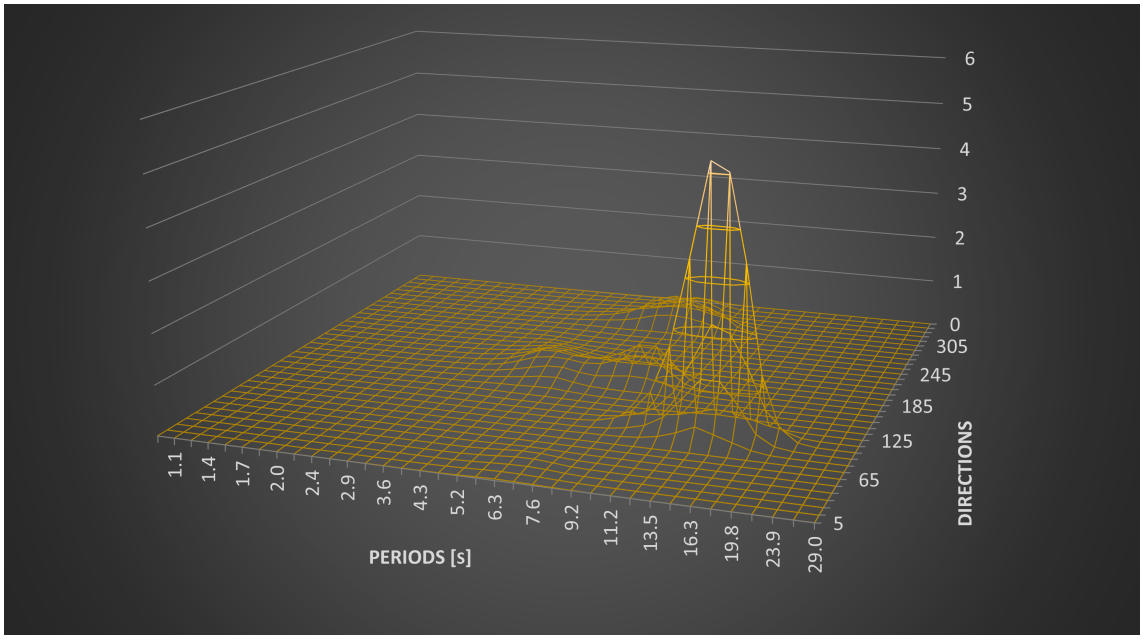

Figure 76: Event 3: 2D-wave spectra

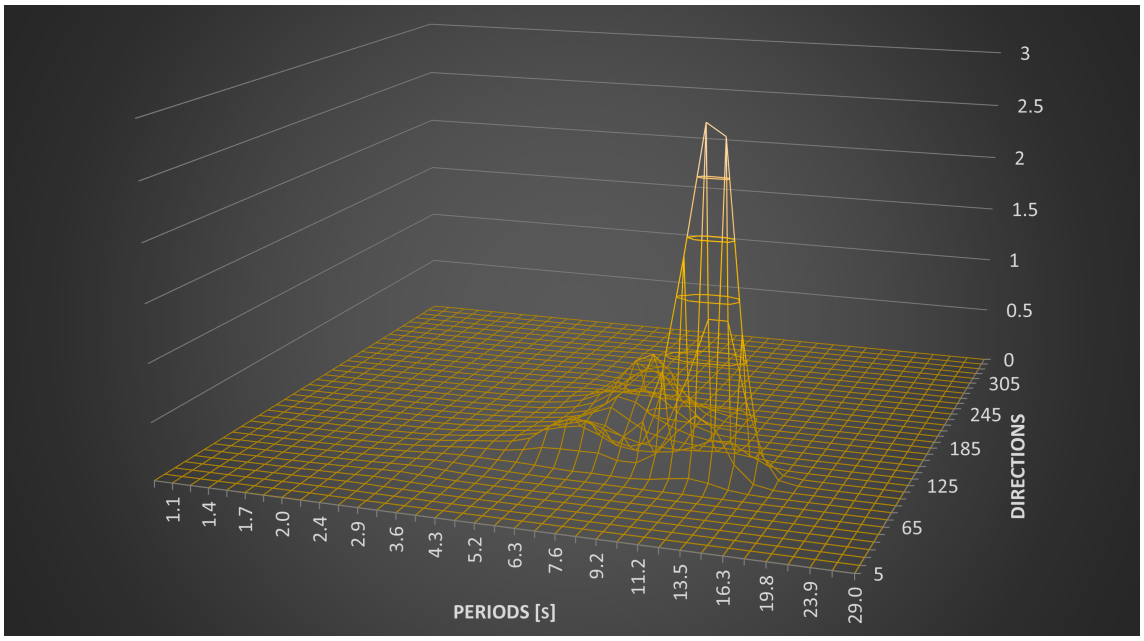

Figure 77: Event 4: 2D-wave spectra

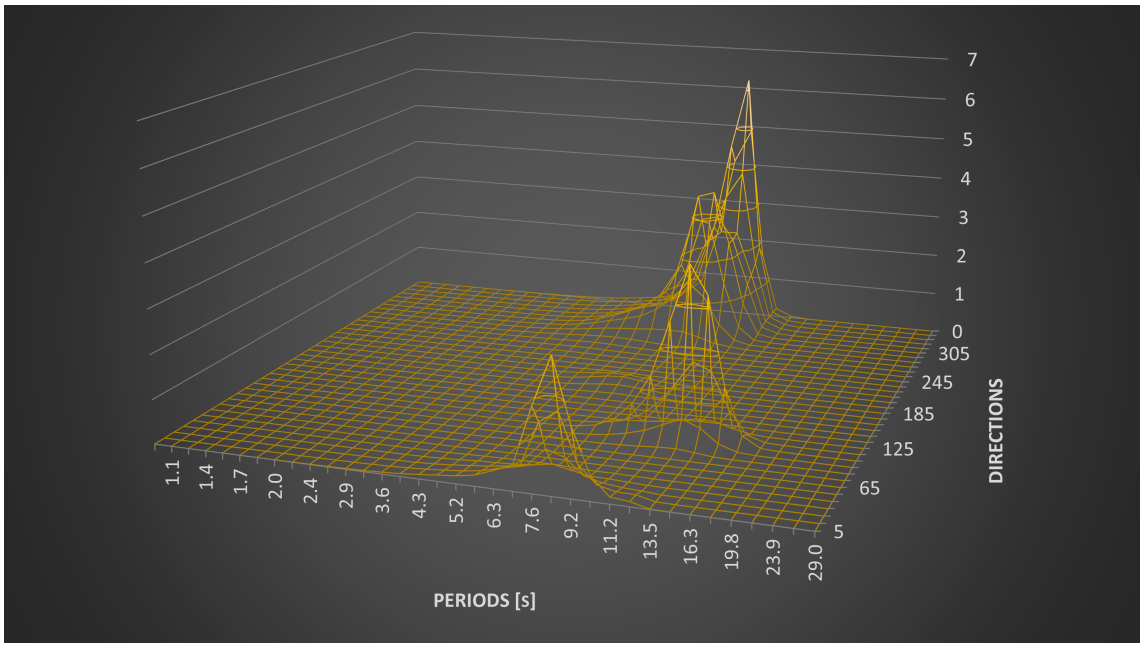

Figure 78: Event 6: 2D-wave spectra

D 1D wave spectrum for the six events

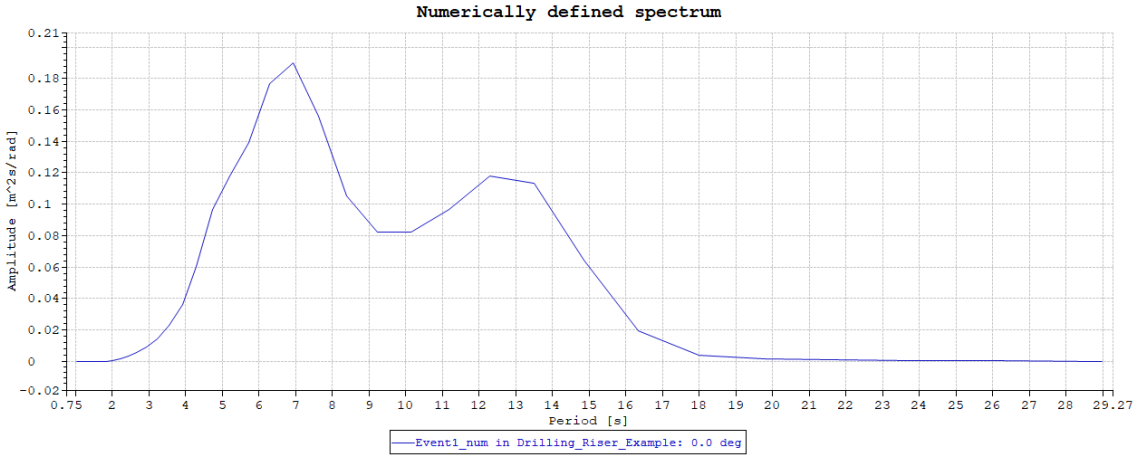

Figure 79: The 1D numerical wave spectra for event 1

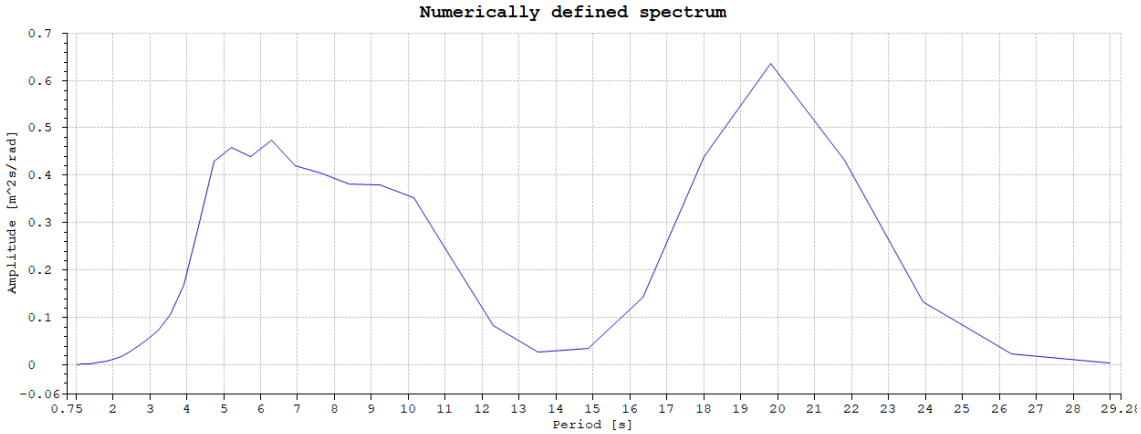

Figure 80: The 1D numerical wave spectra for event 2

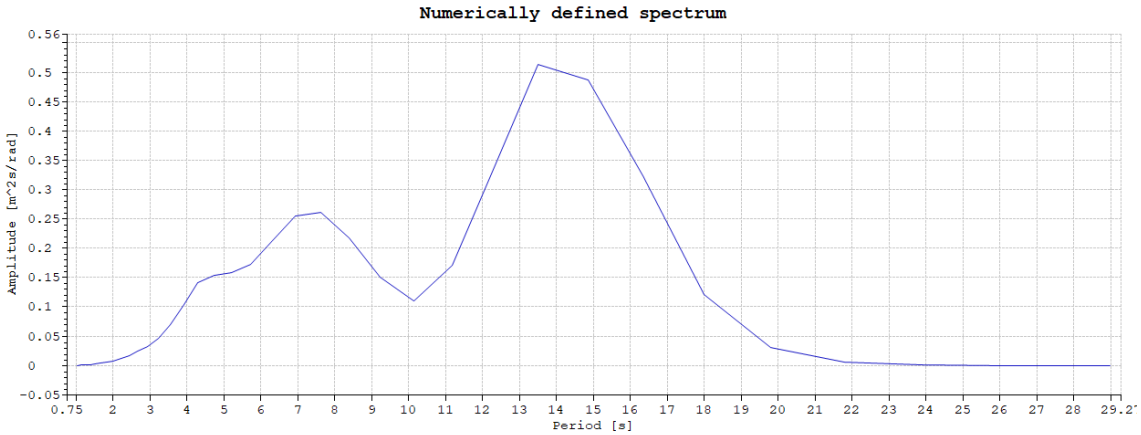

Figure 81: The 1D numerical wave spectra for event 3

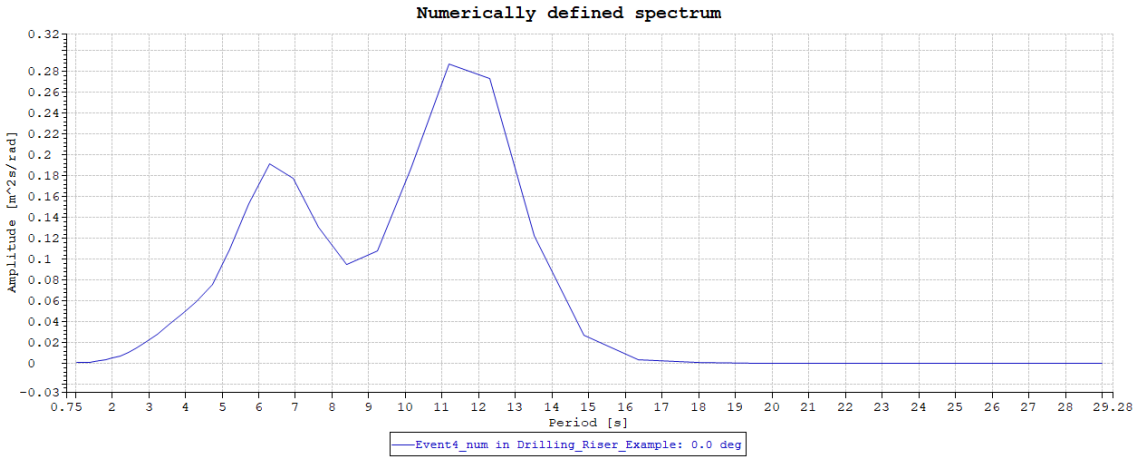

Figure 82: The 1D numerical wave spectra for event 4

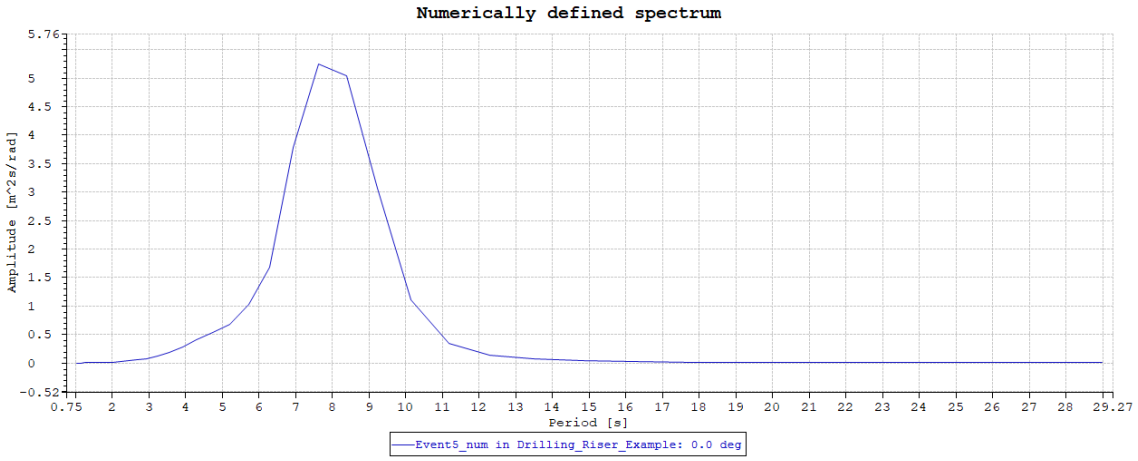

Figure 83: The 1D numerical wave spectra for event 5

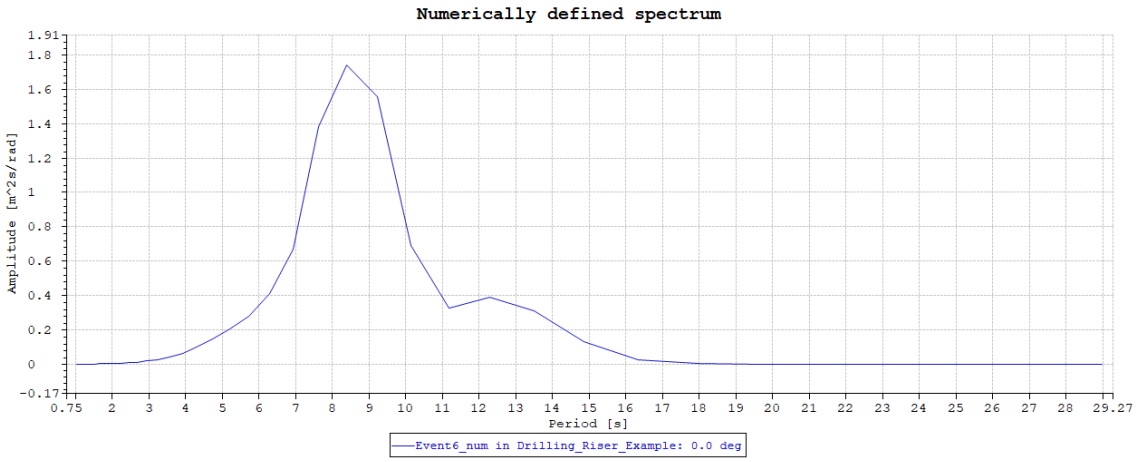

Figure 84: The 1D numerical wave spectra for event 6

E Autospectra for the different types of environments used in Section 10

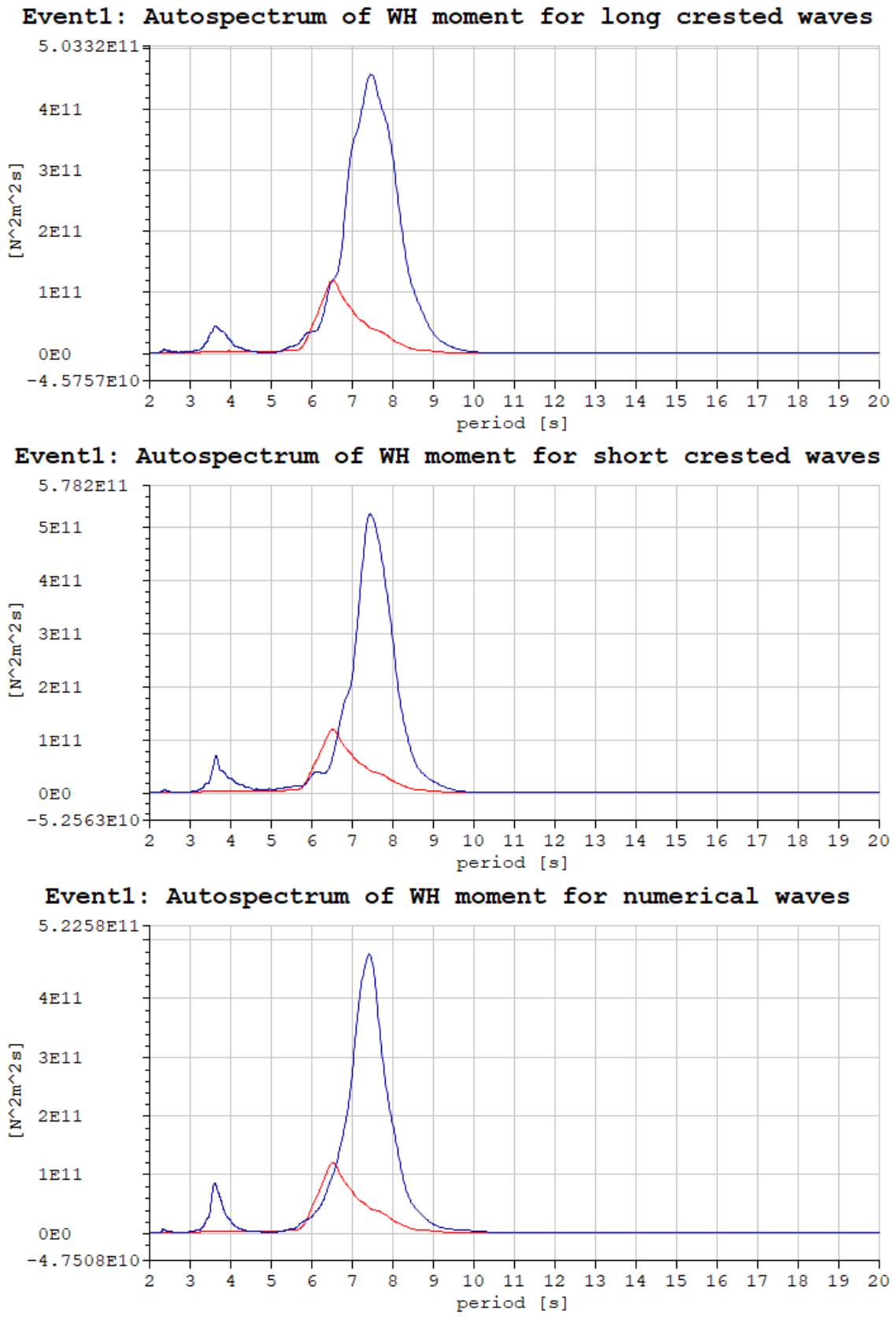

Figure 85: Event 1: Autospectra for different types of environment. The blue graphs is the auto spectra for WH moment in the model for each of the different environments, the red is from measurements

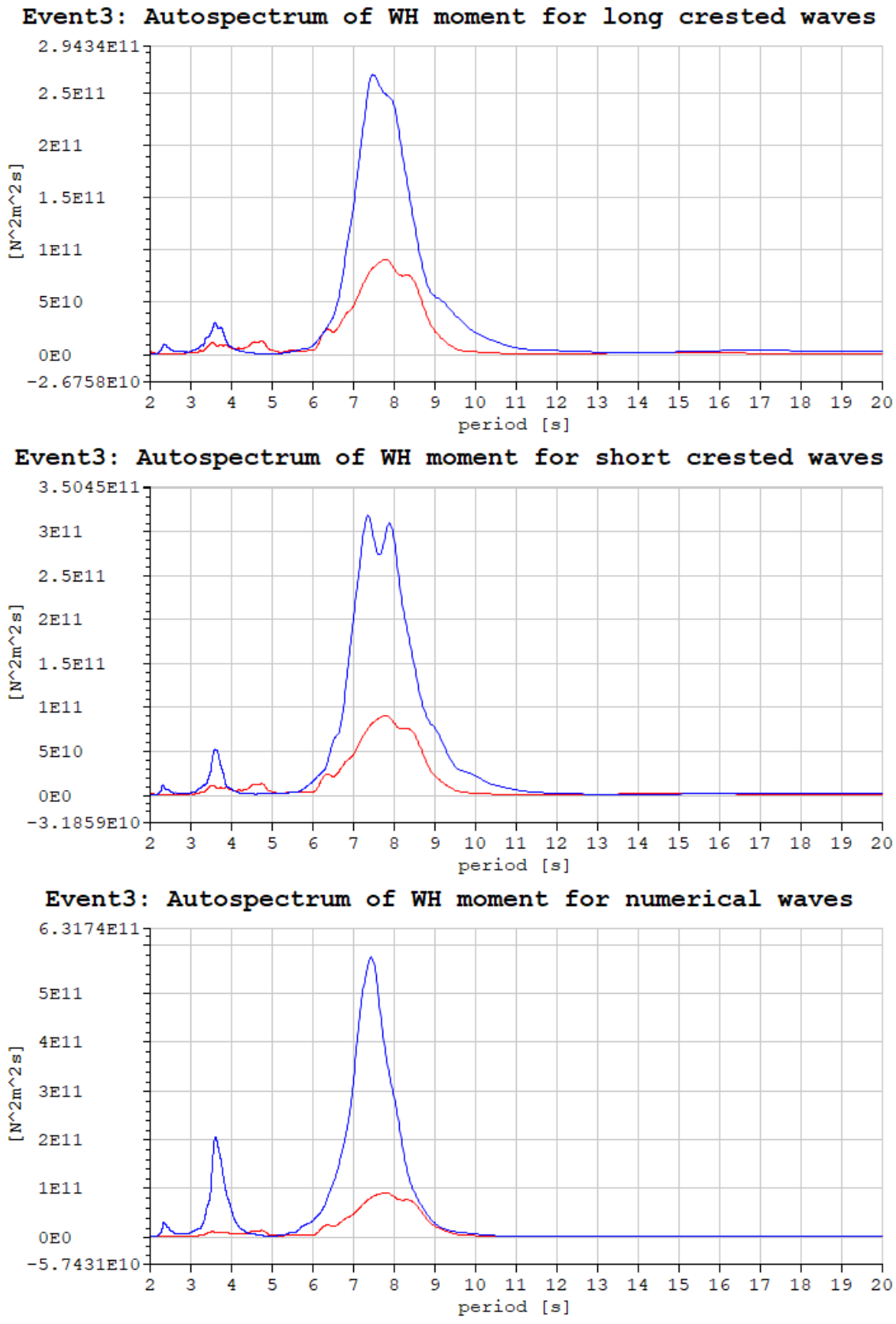

Figure 86: Event 3: Autospectra for different types of environment. The blue graphs is the auto spectra for WH moment in the model for each of the different environments, the red is from measurements

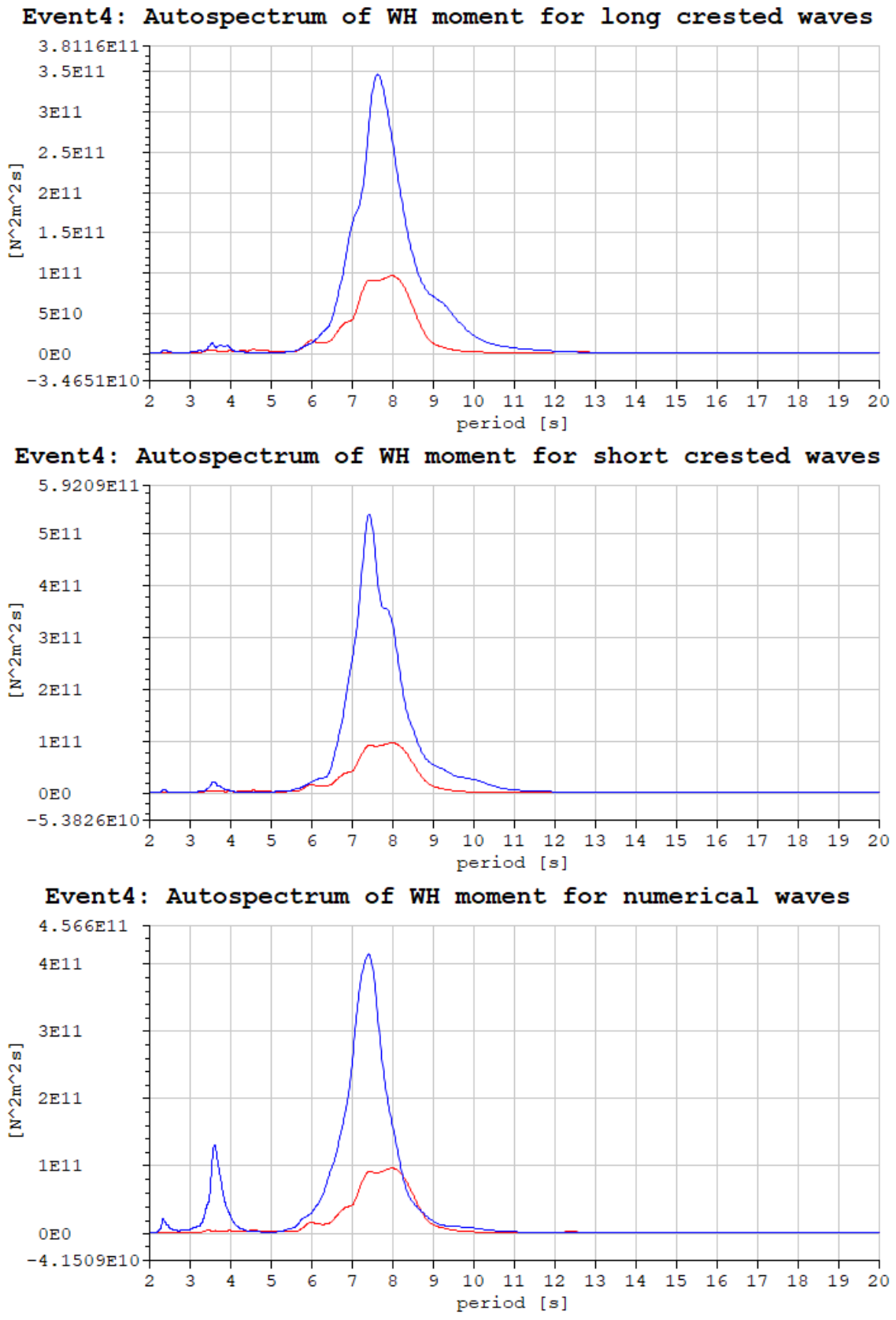

Figure 87: Event 4: Autospectra for different types of environment. The blue graphs is the auto spectra for WH moment in the model for each of the different environments, the red is from measurements

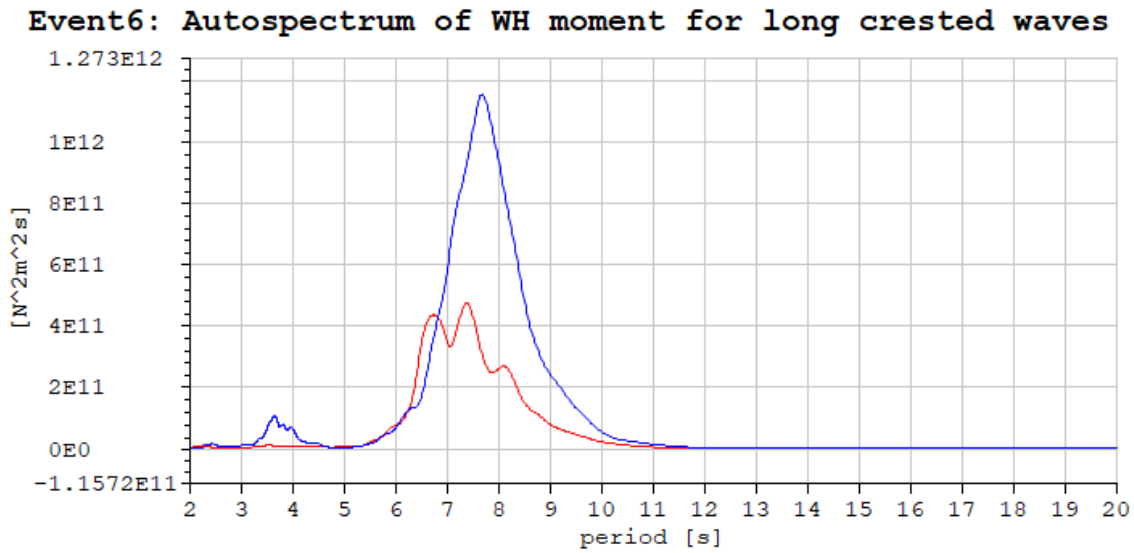

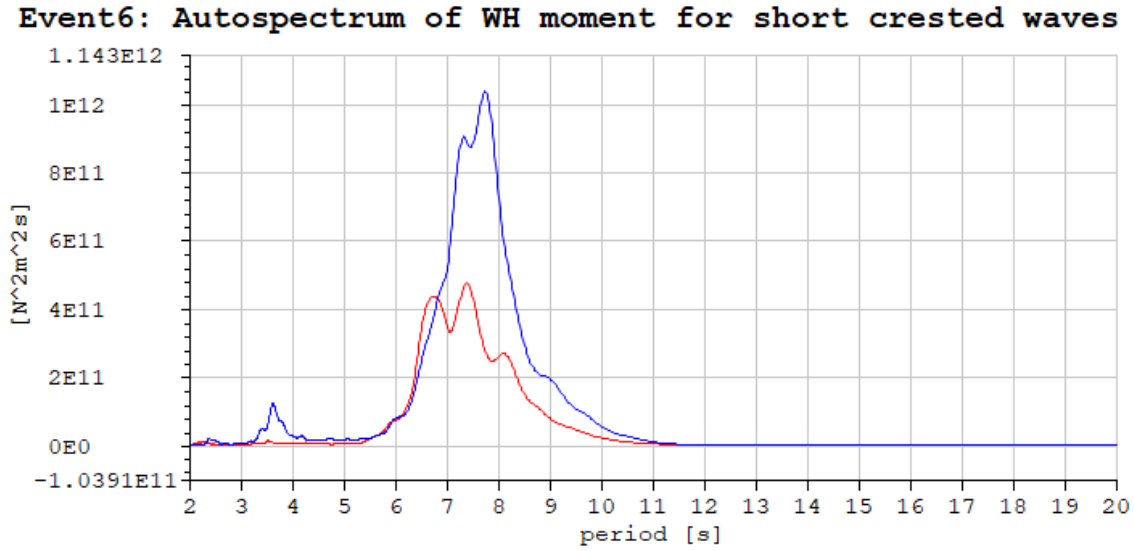

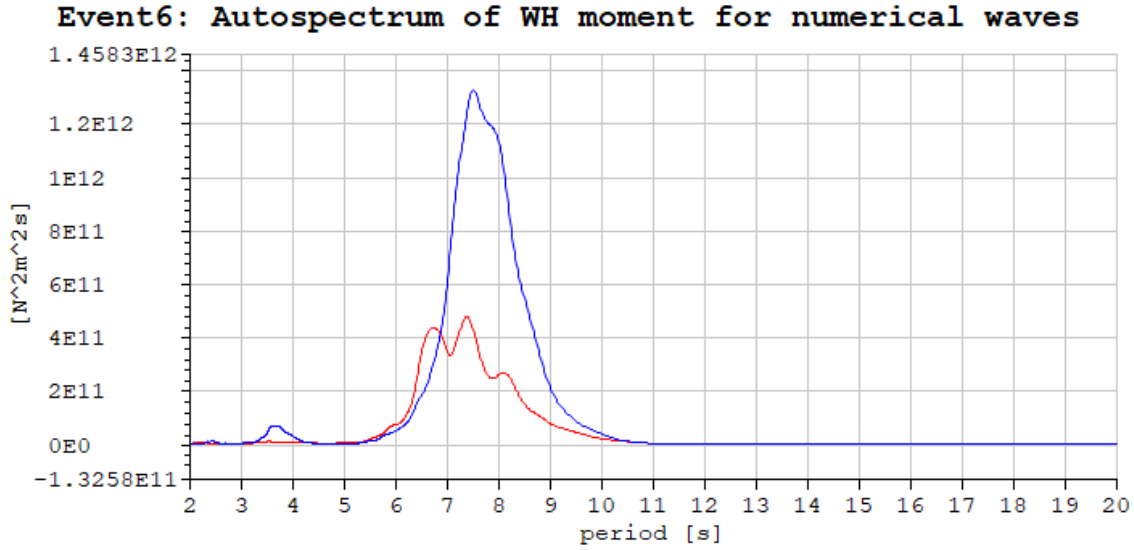

Figure 88: Event 6: Autospectra for different types of environment. The blue graphs is the auto spectra for WH moment in the model for each of the different environments, the red is from measurements

F Autospectrum of Wellhead moment, considering longer periods

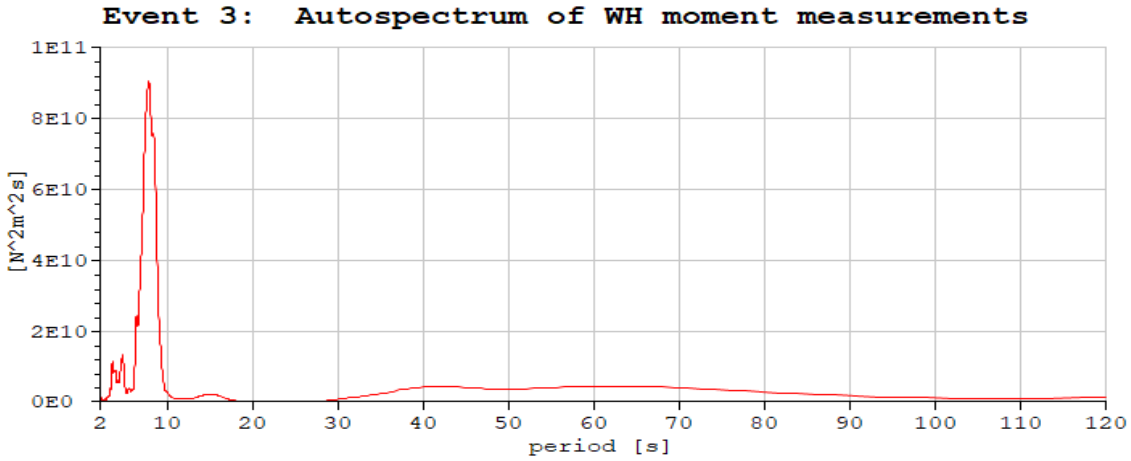

Figure 89: Event 3: Autospectrum of measured WH moment

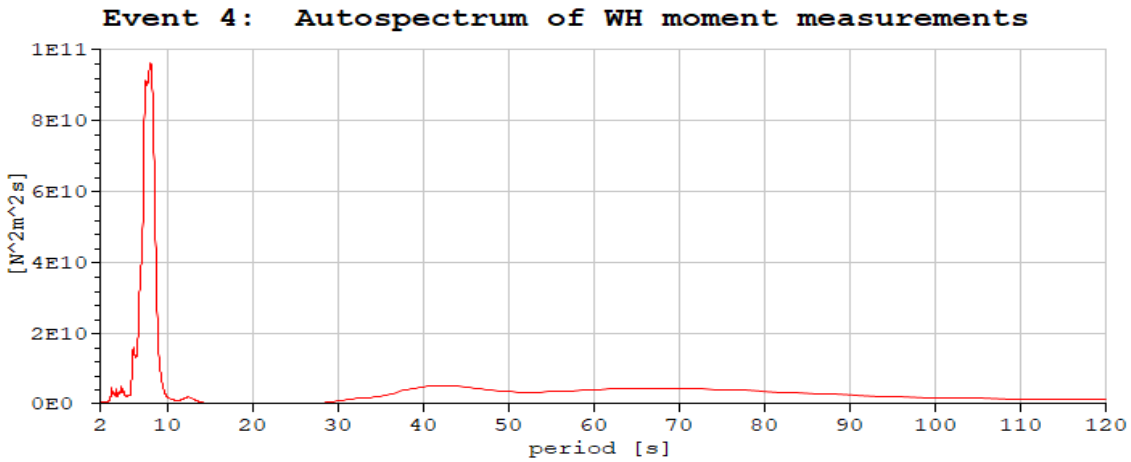

Figure 90: Event 4: Autospectrum of measured WH moment

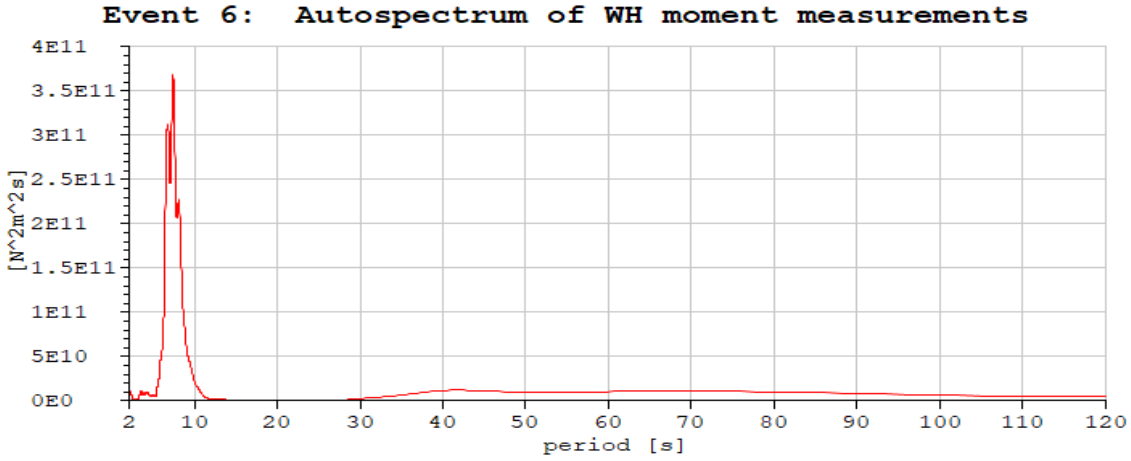

Figure 91: Event 6: Autospectrum of measured WH moment

G Autospectra for WH moment with differing soil_factor

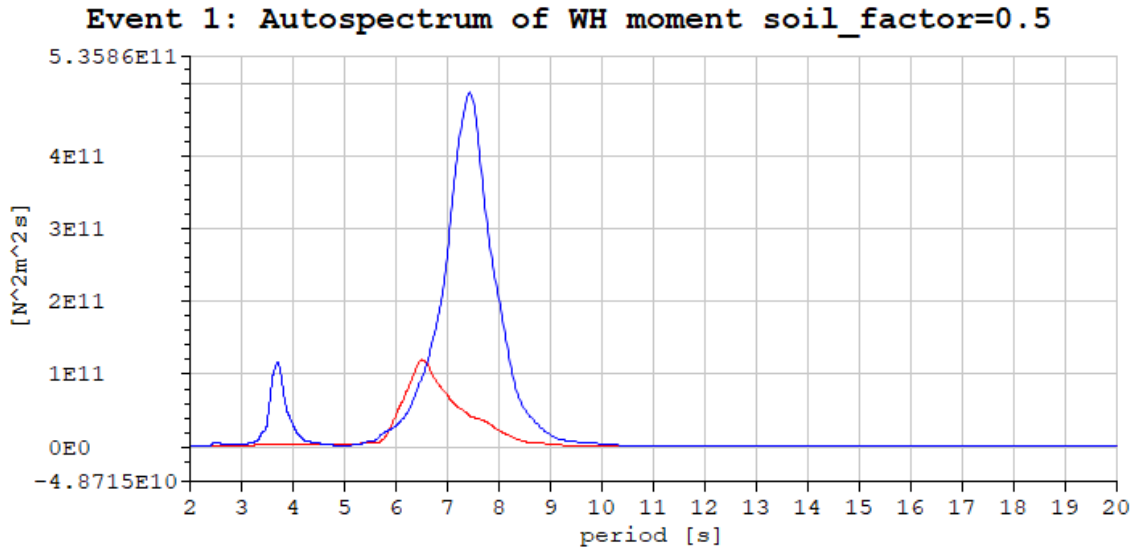

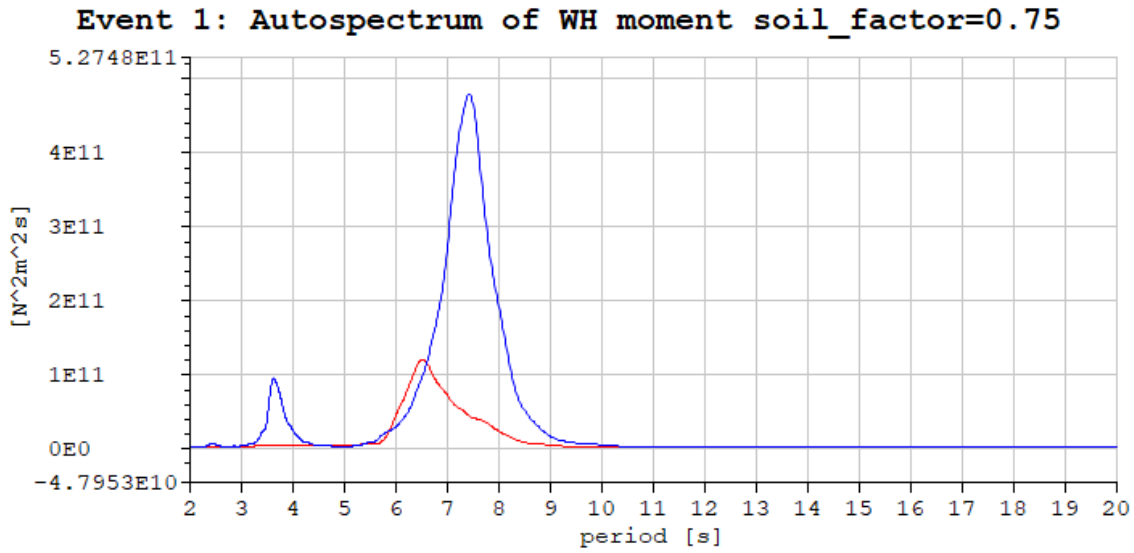

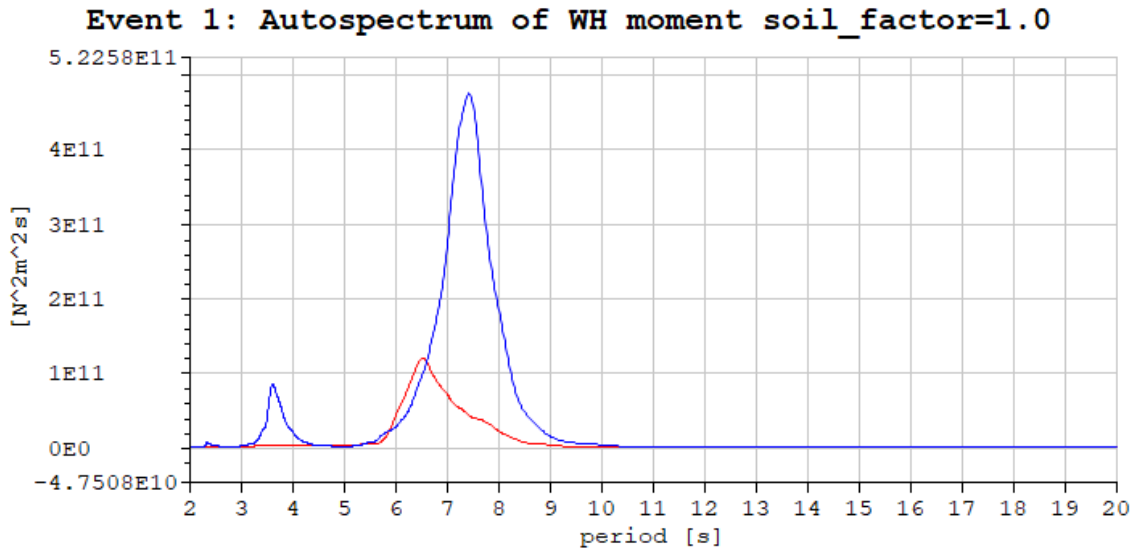

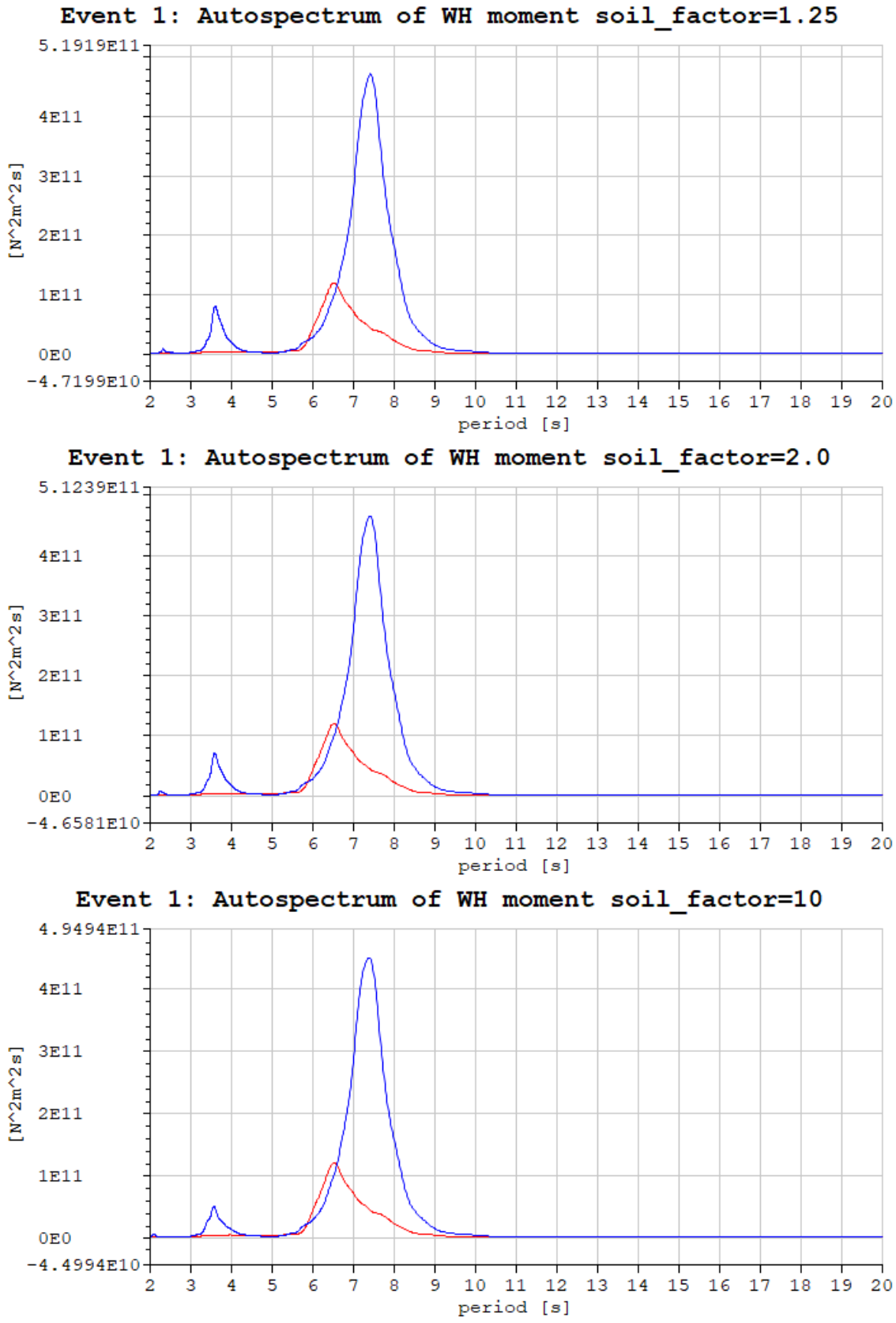

Figure 92: Event 1: The effect of different soil_factor on WH moment. The blue graphs is the auto spectra for WH moment in the model for each of the soil_factor, the red is from measurements

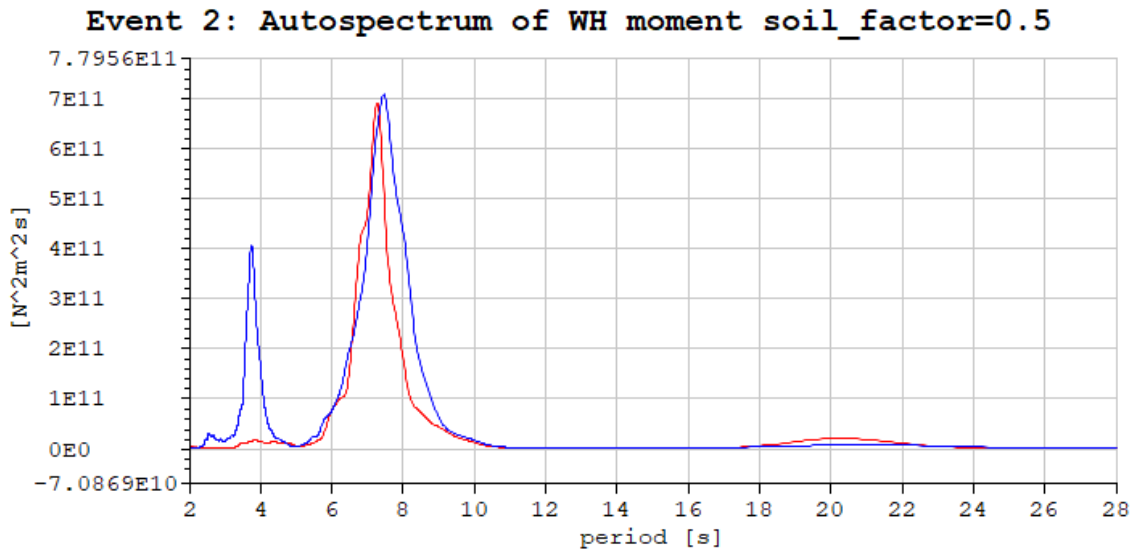
Event 2: Autospectrum of WH moment soil_factor=0.5
7.7956E11
7E11
6E11
5E11
4E11
3E11
2E11
1E11
0E0
-7.0869E10
[N^2m^2s]
2
4
6
8
10
12
14
16
18
20
22
24
26
28
period [s]

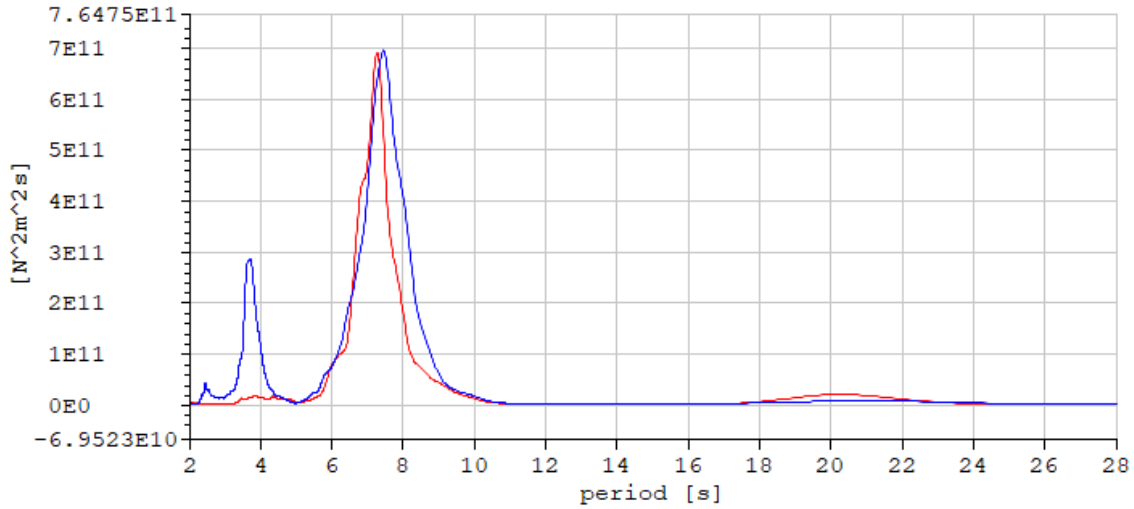
Event 2: Autospectrum of WH moment soil_factor=0.75
7.6475E11
7E11
6E11
5E11
4E11
3E11
2E11
1E11
0E0
-6.9523E10
[N^2m^2s]
2
4
6
8
10
12
14
16
18
20
22
24
26
28
period [s]

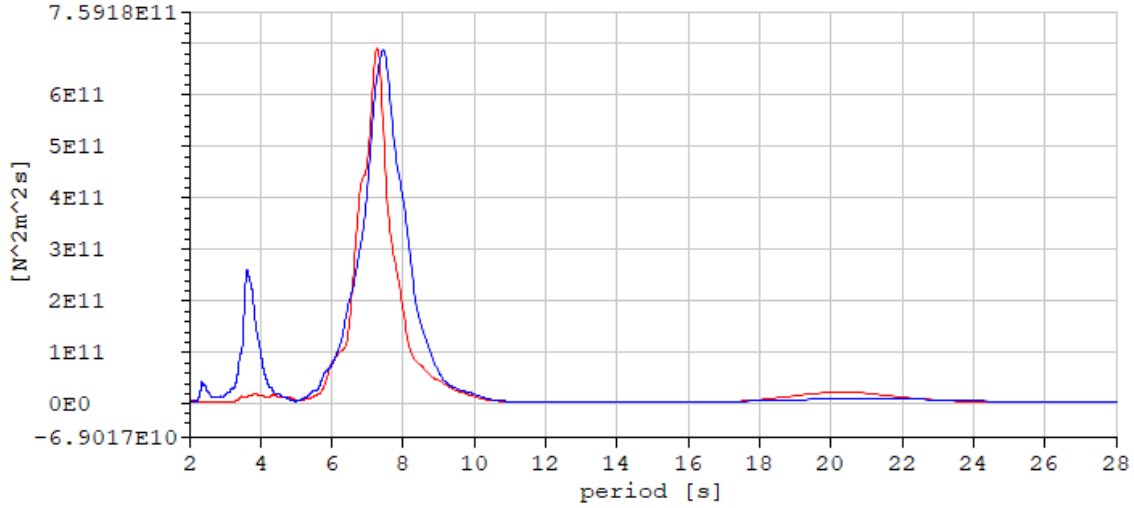
Event 2: Autospectrum of WH moment soil_factor=1.0
7.5918E11
6E11
5E11
4E11
3E11
2E11
1E11
0E0
-6.9017E10
[N^2m^2s]
2
4
6
8
10
12
14
16
18
20
22
24
26
28
period [s]

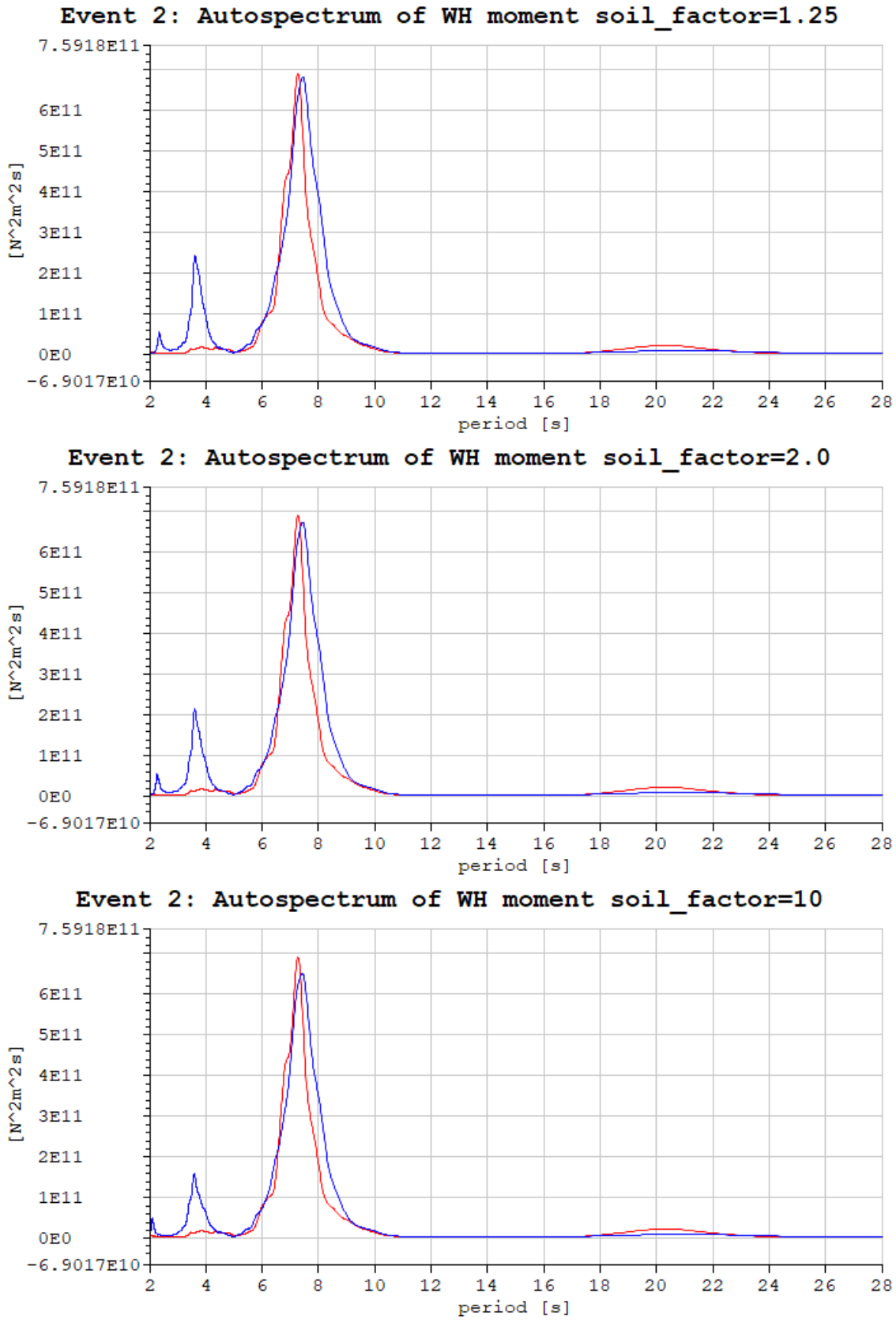

Figure 93: Event 2: The effect of different soil_factor on WH moment. The blue graphs is the auto spectra for WH moment in the model for each of the soil_factor, the red is from measurements

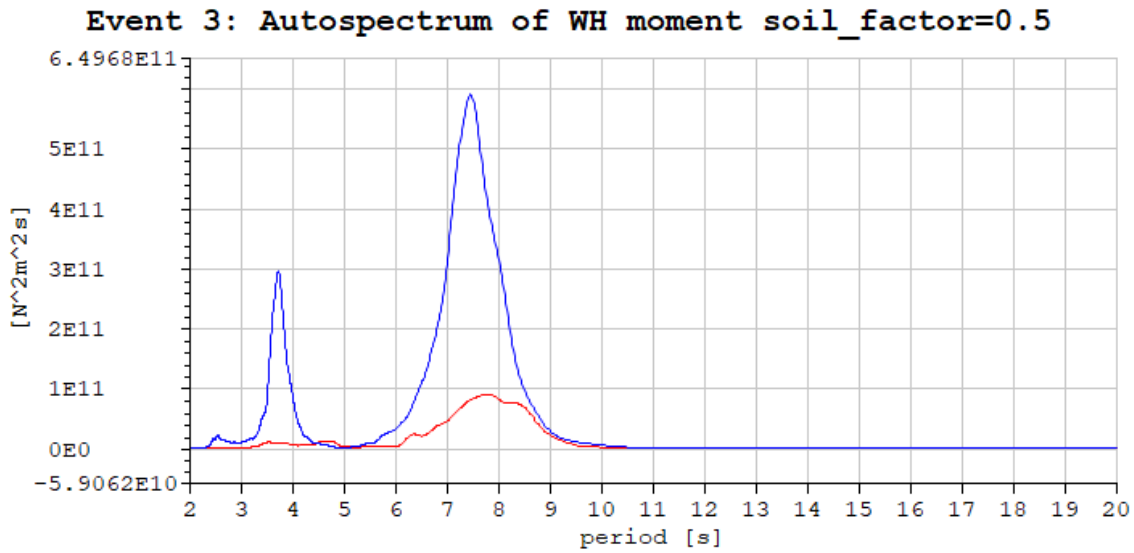
Event 3: Autospectrum of WH moment soil_factor=0.5
6.4968E11
5E11
4E11
3E11
2E11
1E11
0E0
-5.9062E10
[N^2m^2s]
2 3 4 5 6 7 8 9 10 11 12 13 14 15 16 17 18 19 20
period [s]

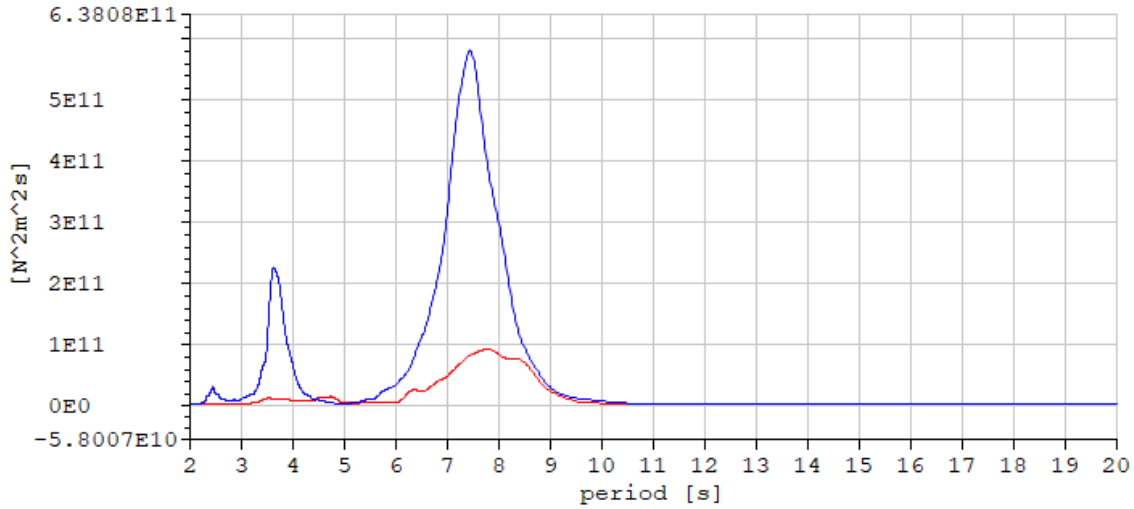
Event 3: Autospectrum of WH moment soil_factor=0.75
6.3808E11
5E11
4E11
3E11
2E11
1E11
0E0
-5.8007E10
[N^2m^2s]
2 3 4 5 6 7 8 9 10 11 12 13 14 15 16 17 18 19 20
period [s]

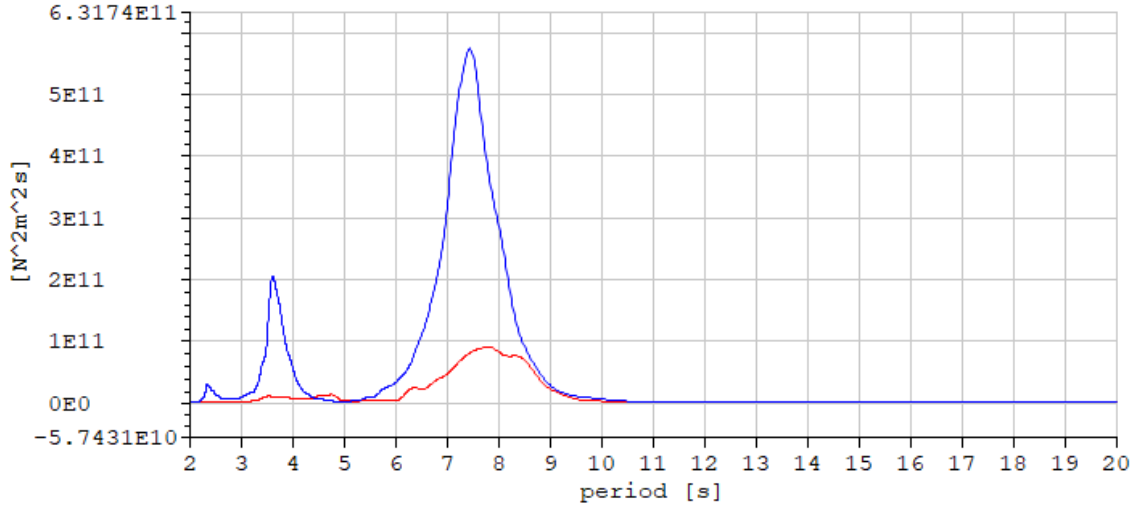
Event 3: Autospectrum of WH moment soil_factor=1.0
6.3174E11
5E11
4E11
3E11
2E11
1E11
0E0
-5.7431E10
[N^2m^2s]
2 3 4 5 6 7 8 9 10 11 12 13 14 15 16 17 18 19 20
period [s]

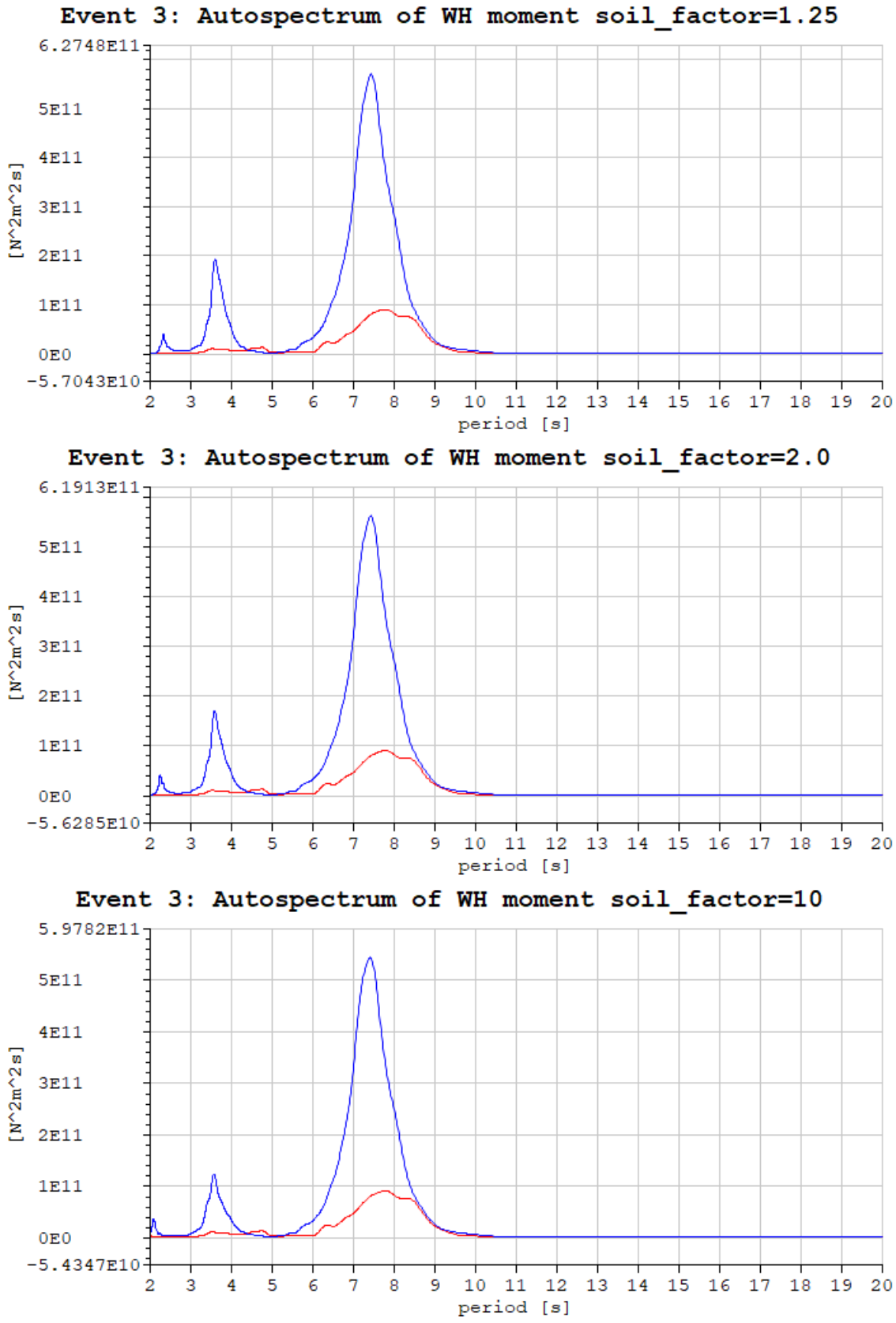

Figure 94: Event 3: The effect of different soil_factor on WH moment. The blue graphs is the auto spectra for WH moment in the model for each of the soil_factor, the red is from measurements

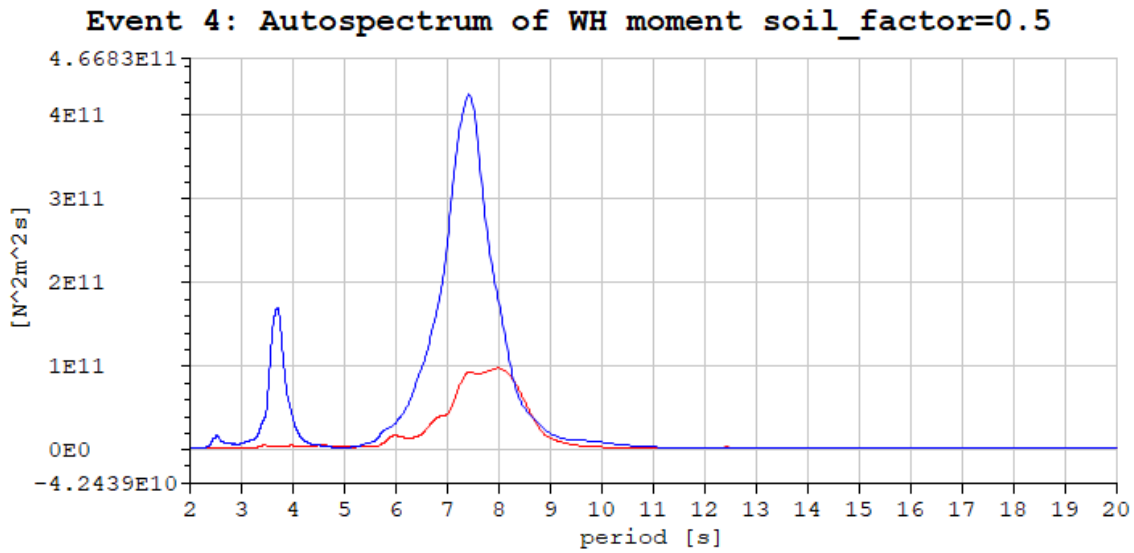
Event 4: Autospectrum of WH moment soil_factor=0.5
4.6683E11
4E11
3E11
2E11
1E11
0E0
-4.2439E10
[N^2m^2s]
2 3 4 5 6 7 8 9 10 11 12 13 14 15 16 17 18 19 20
period [s]

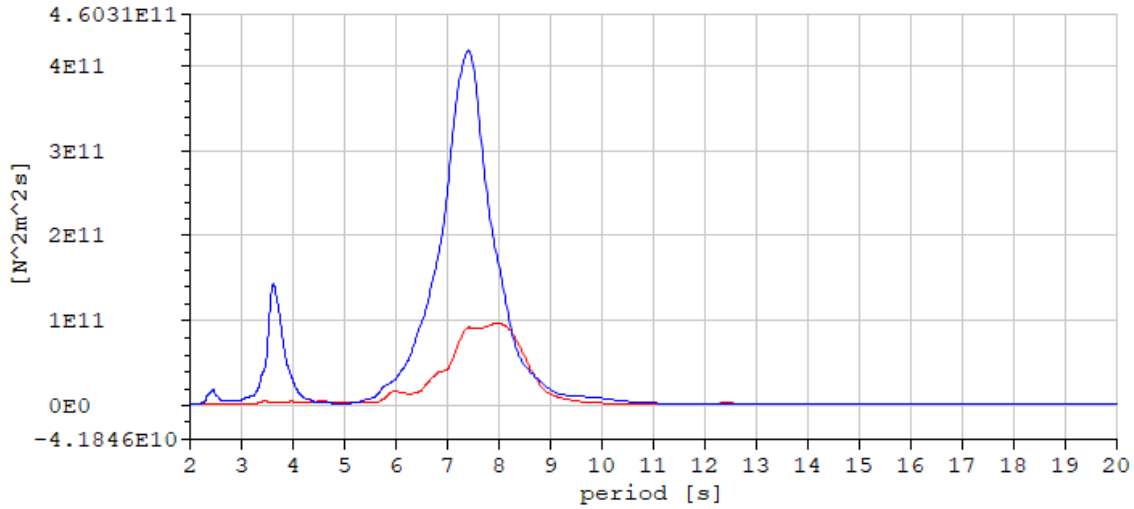
Event 4: Autospectrum of WH moment soil_factor=0.75
4.6031E11
4E11
3E11
2E11
1E11
0E0
-4.1846E10
[N^2m^2s]
2 3 4 5 6 7 8 9 10 11 12 13 14 15 16 17 18 19 20
period [s]

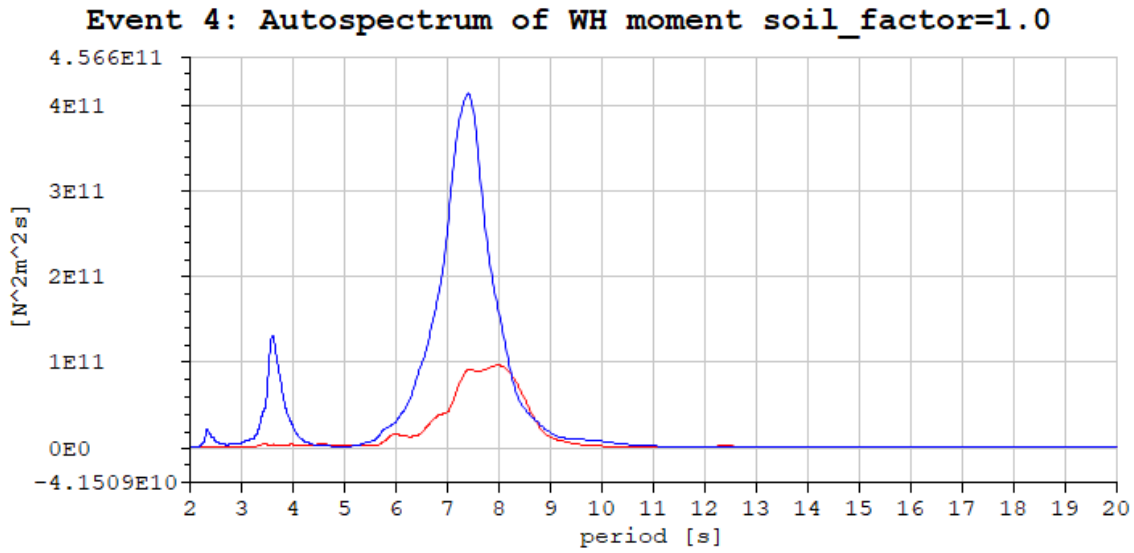
Event 4: Autospectrum of WH moment soil_factor=1.0
4.566E11
4E11
3E11
2E11
1E11
0E0
-4.1509E10
[N^2m^2s]
2 3 4 5 6 7 8 9 10 11 12 13 14 15 16 17 18 19 20
period [s]

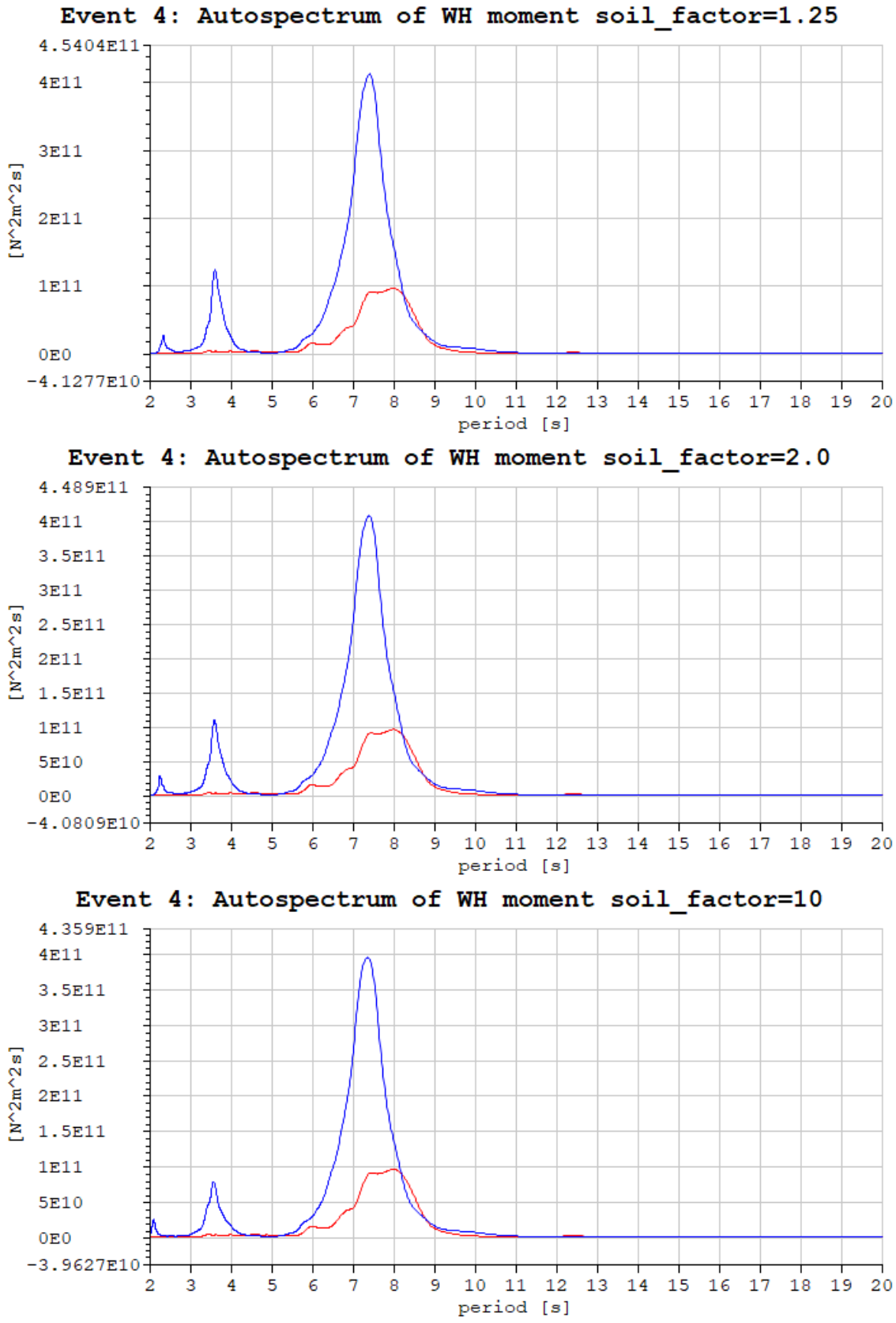

Figure 95: Event 4: The effect of different soil_factor on WH moment. The blue graphs is the auto spectra for WH moment in the model for each of the soil_factor, the red is from measurements

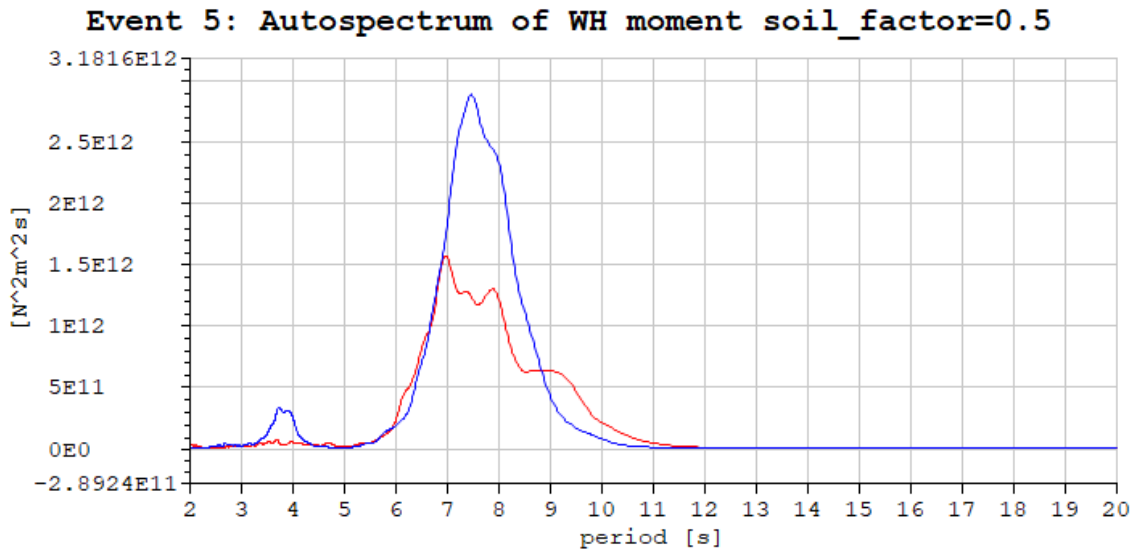
Event 5: Autospectrum of WH moment soil_factor=0.5
3.1816E12
2.5E12
2E12
1.5E12
1E12
5E11
0E0
-2.8924E11
[N^2m^2s]
2 3 4 5 6 7 8 9 10 11 12 13 14 15 16 17 18 19 20
period [s]

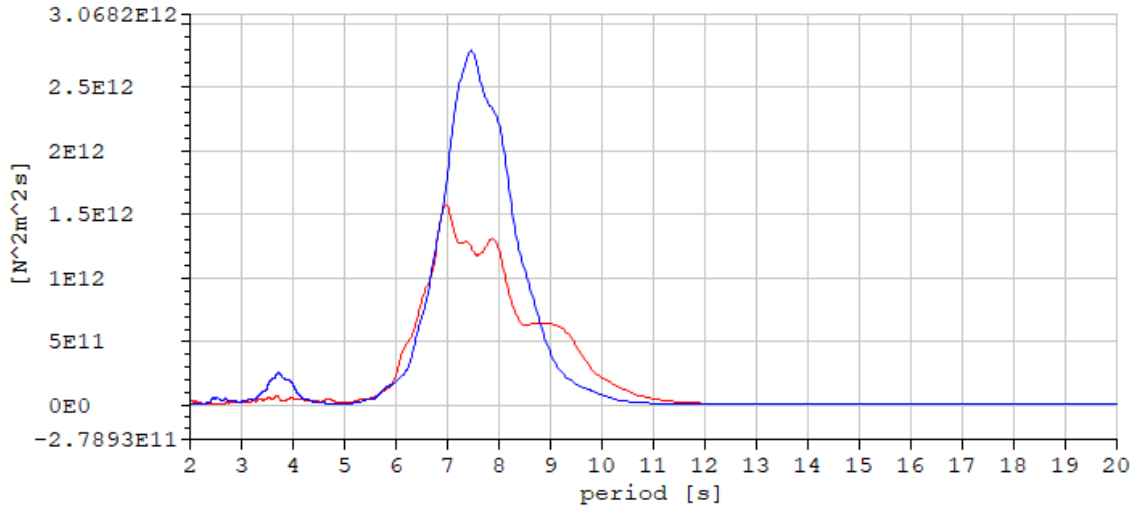
Event 5: Autospectrum of WH moment soil_factor=0.75
3.0682E12
2.5E12
2E12
1.5E12
1E12
5E11
0E0
-2.7893E11
[N^2m^2s]
2 3 4 5 6 7 8 9 10 11 12 13 14 15 16 17 18 19 20
period [s]

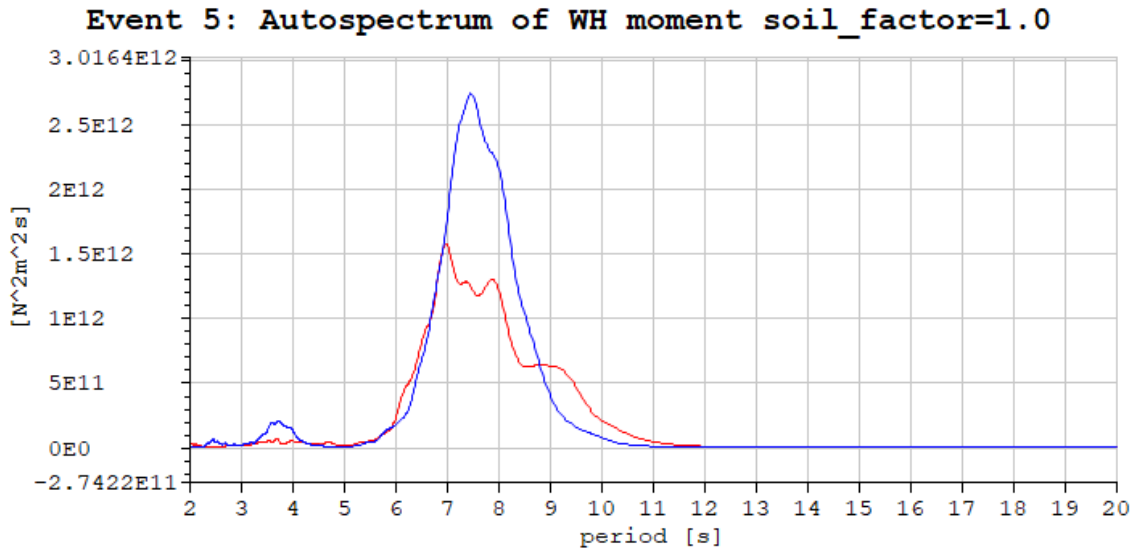
Event 5: Autospectrum of WH moment soil_factor=1.0
3.0164E12
2.5E12
2E12
1.5E12
1E12
5E11
0E0
-2.7422E11
[N^2m^2s]
2 3 4 5 6 7 8 9 10 11 12 13 14 15 16 17 18 19 20
period [s]

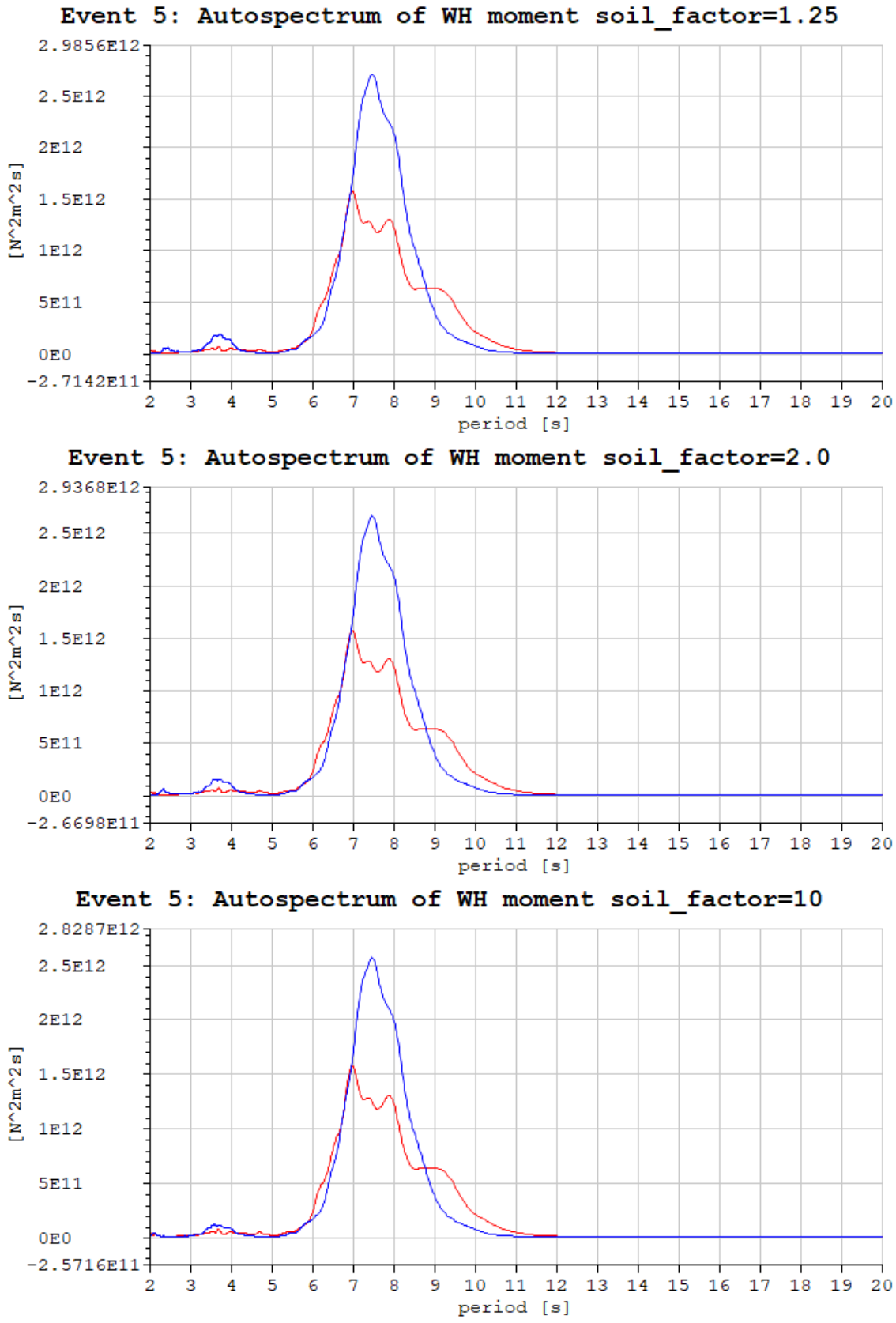

Figure 96: Event 5: The effect of different soil_factor on WH moment. The blue graphs is the auto spectra for WH moment in the model for each of the soil_factor, the red is from measurements

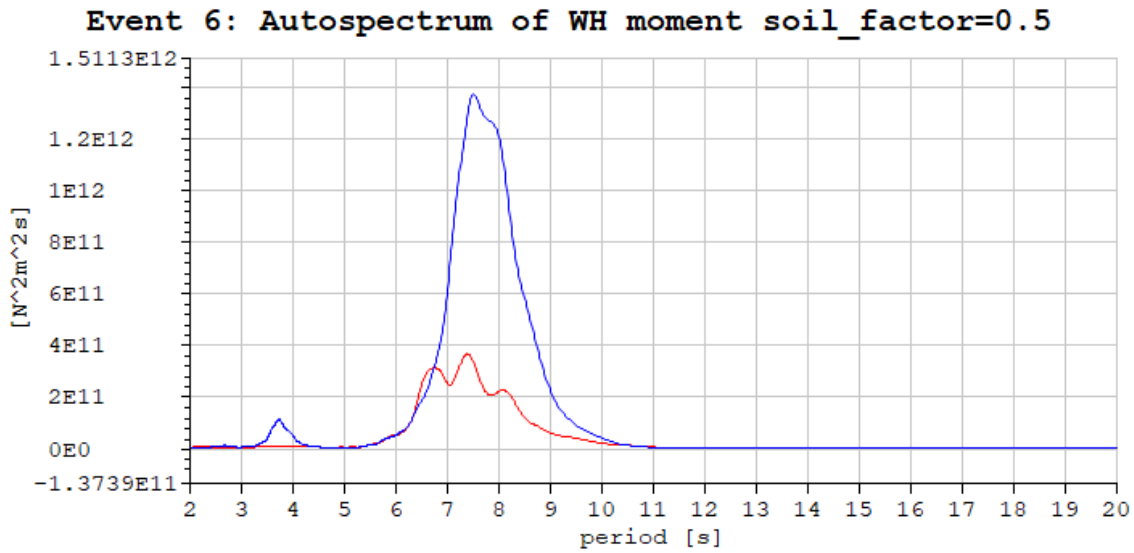
Event 6: Autospectrum of WH moment soil_factor=0.5
1.5113E12
1.2E12
1E12
8E11
6E11
4E11
2E11
0E0
-1.3739E11
[N^2m^2s]
2 3 4 5 6 7 8 9 10 11 12 13 14 15 16 17 18 19 20
period [s]

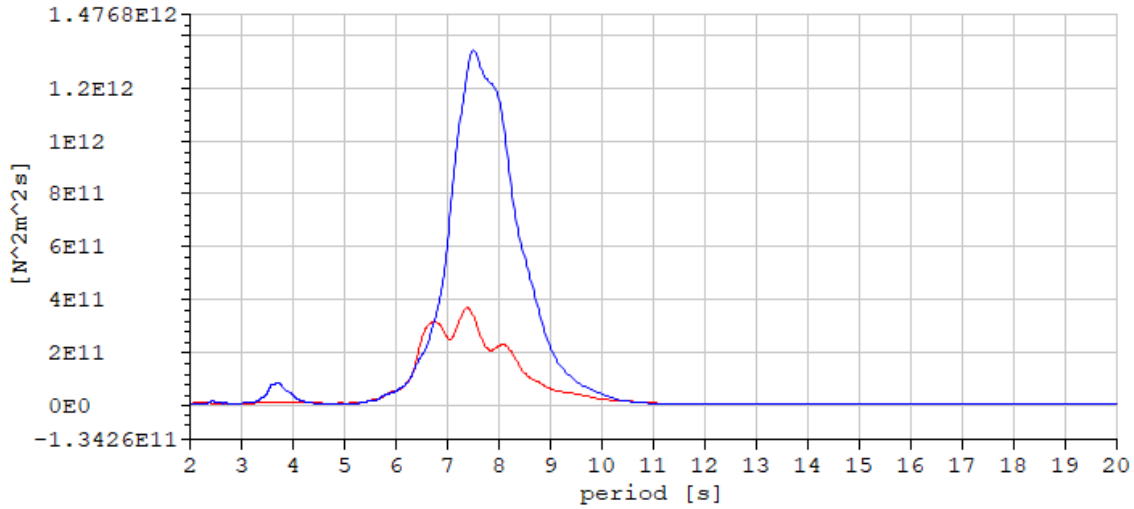
Event 6: Autospectrum of WH moment soil_factor=0.75
1.4768E12
1.2E12
1E12
8E11
6E11
4E11
2E11
0E0
-1.3426E11
[N^2m^2s]
2 3 4 5 6 7 8 9 10 11 12 13 14 15 16 17 18 19 20
period [s]

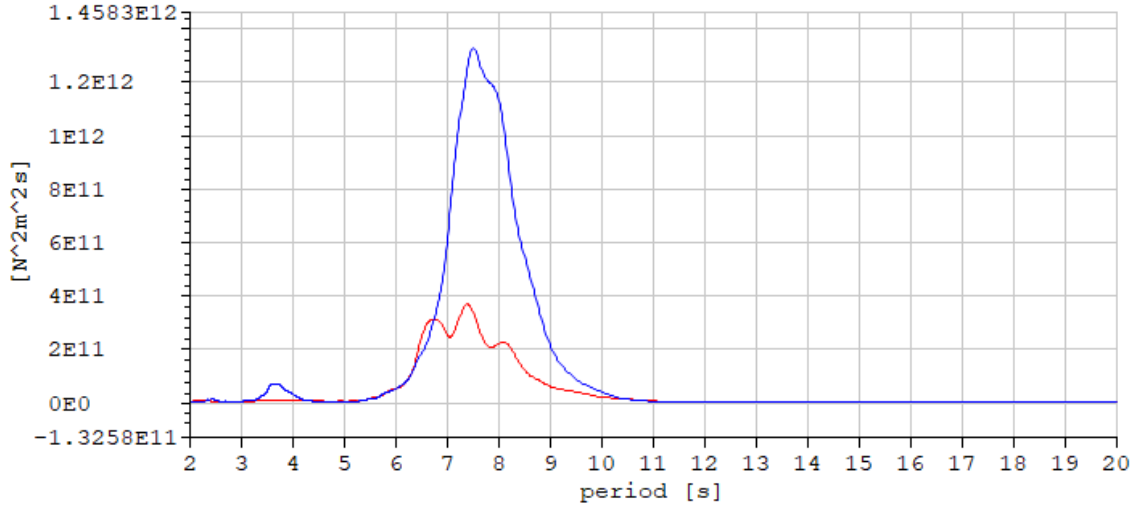
Event 6: Autospectrum of WH moment soil_factor=1.0
1.4583E12
1.2E12
1E12
8E11
6E11
4E11
2E11
0E0
-1.3258E11
[N^2m^2s]
2 3 4 5 6 7 8 9 10 11 12 13 14 15 16 17 18 19 20
period [s]

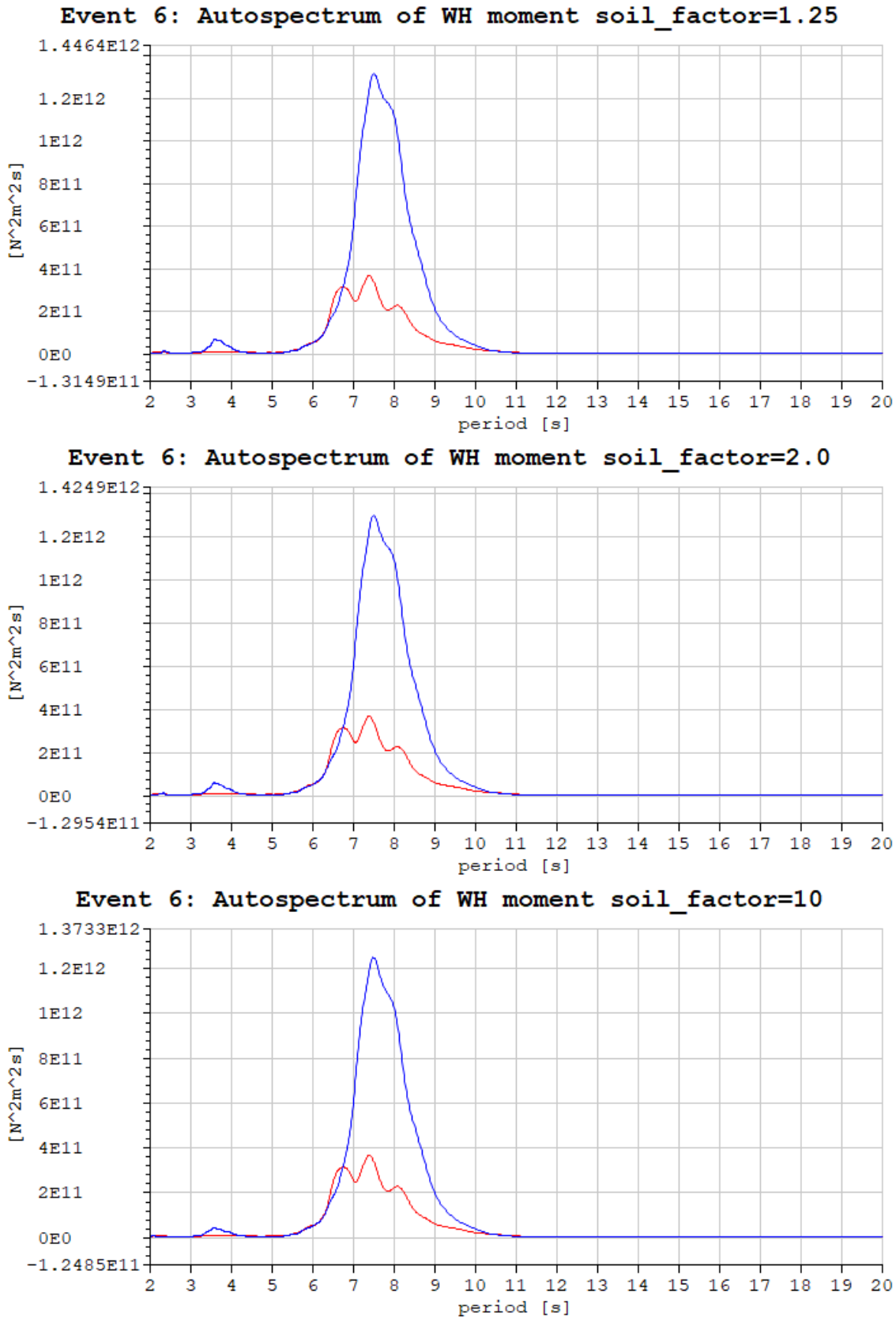

Figure 97: Event 6: The effect of different soil_factor on WH moment. The blue graphs is the auto spectra for WH moment in the model for each of the soil_factor, the red is from measurements

H Autospectra for WH moment with differing top tension

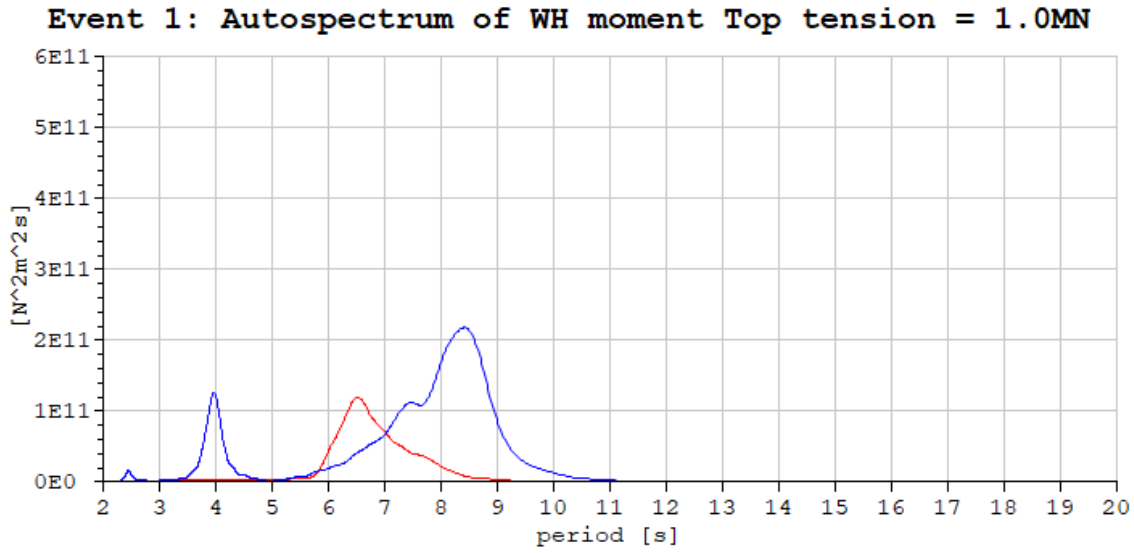

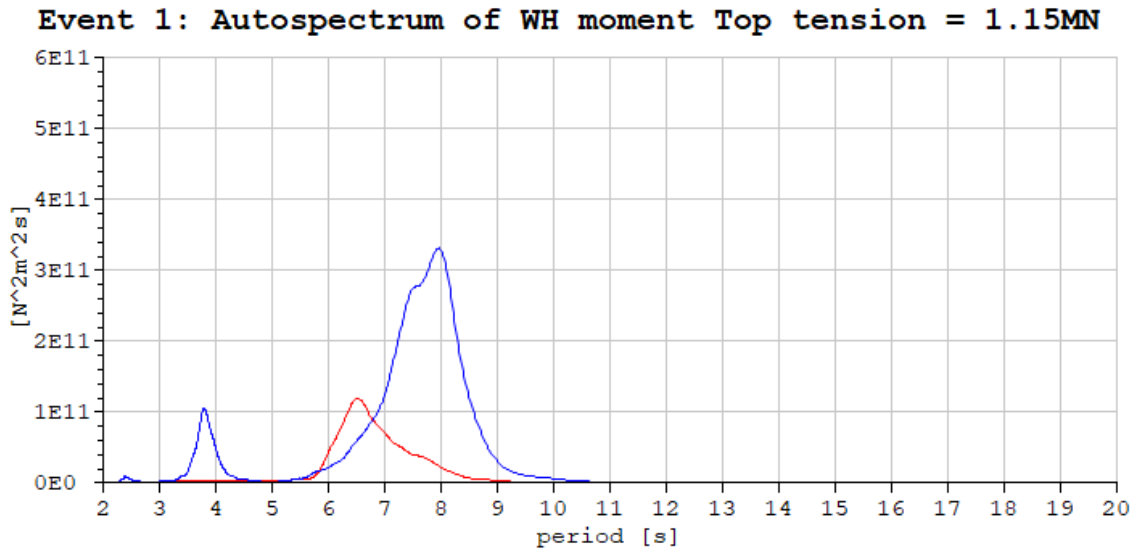

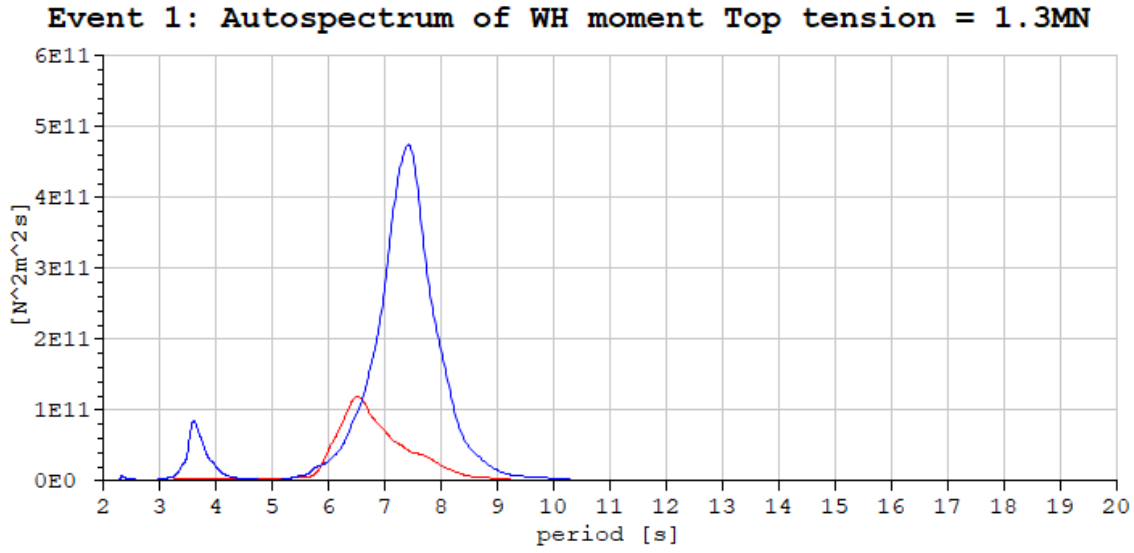

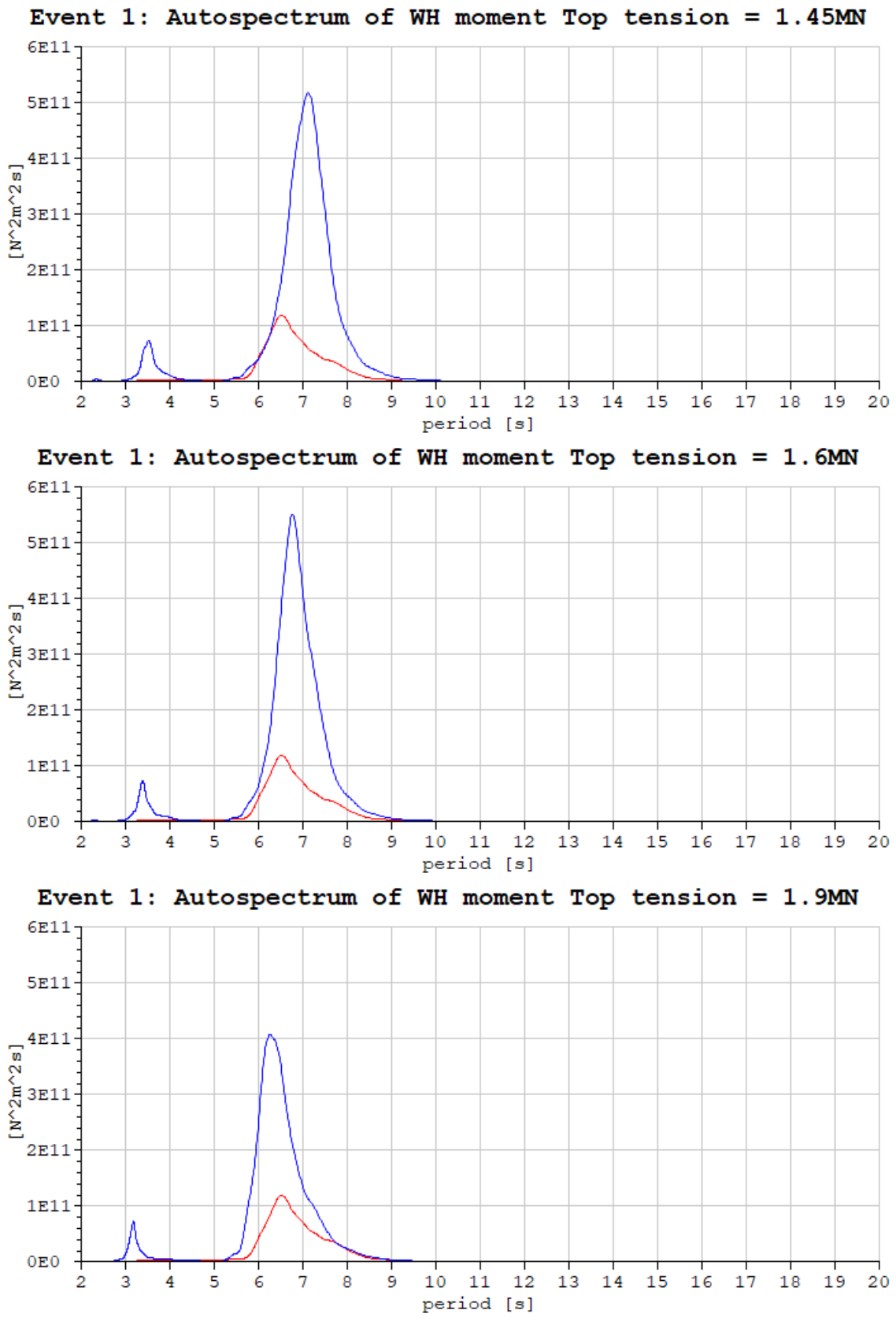

Figure 98: Event 1: The effect of different top tension on WH moment. The blue graphs shows the autospectra for the model with different top tensions, the red graph shows the autospectrum of the measurements

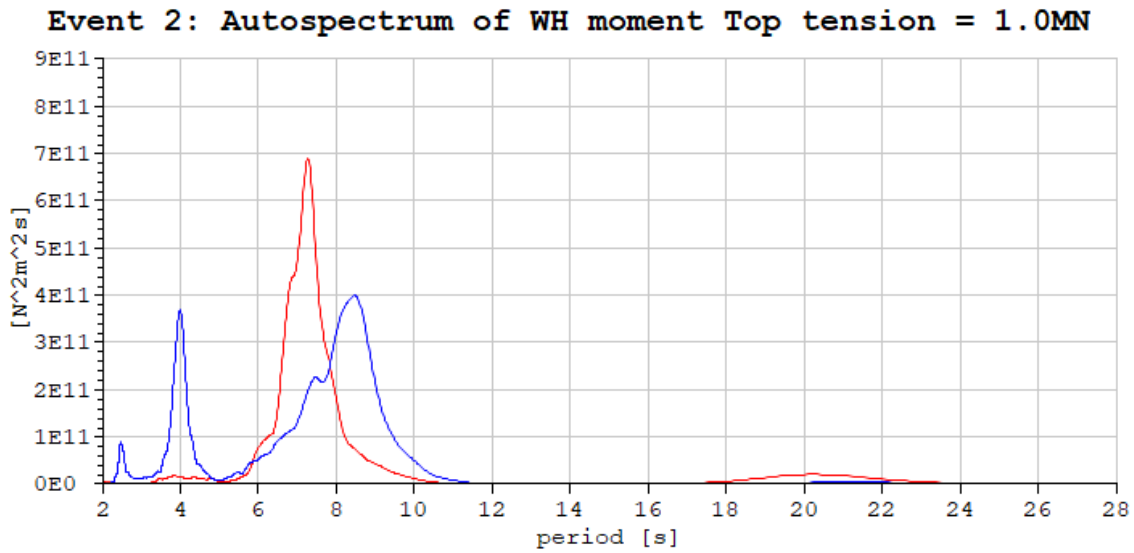
Event 2: Autospectrum of WH moment Top tension = 1.0MN
9E11
8E11
7E11
6E11
5E11
4E11
3E11
2E11
1E11
0E0
[N^2m^2s]
2 4 6 8 10 12 14 16 18 20 22 24 26 28
period [s]

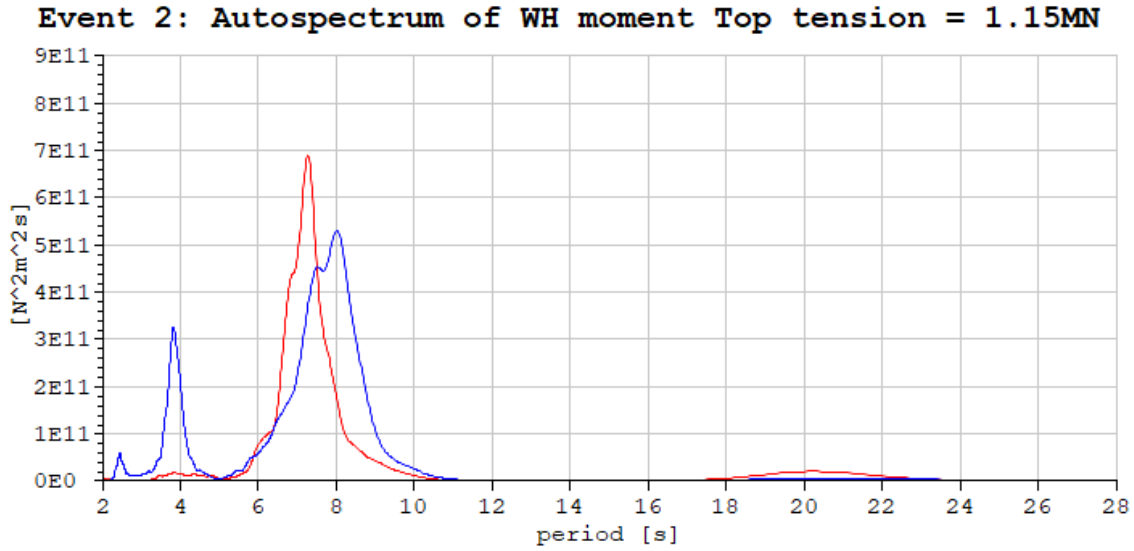
Event 2: Autospectrum of WH moment Top tension = 1.15MN
9E11
8E11
7E11
6E11
5E11
4E11
3E11
2E11
1E11
0E0
[N^2m^2s]
2 4 6 8 10 12 14 16 18 20 22 24 26 28
period [s]

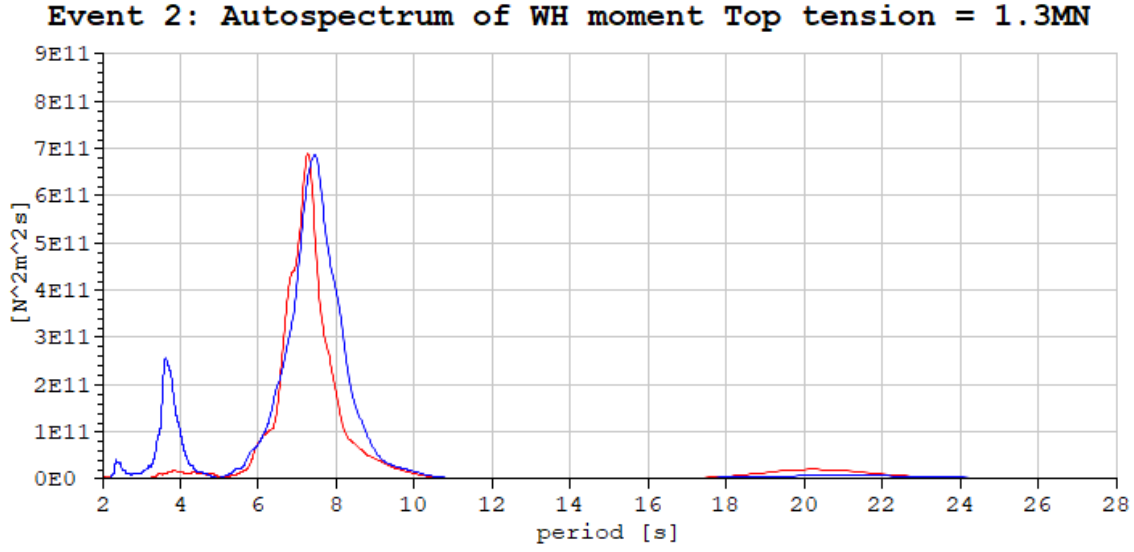
Event 2: Autospectrum of WH moment Top tension = 1.3MN
9E11
8E11
7E11
6E11
5E11
4E11
3E11
2E11
1E11
0E0
[N^2m^2s]
2 4 6 8 10 12 14 16 18 20 22 24 26 28
period [s]

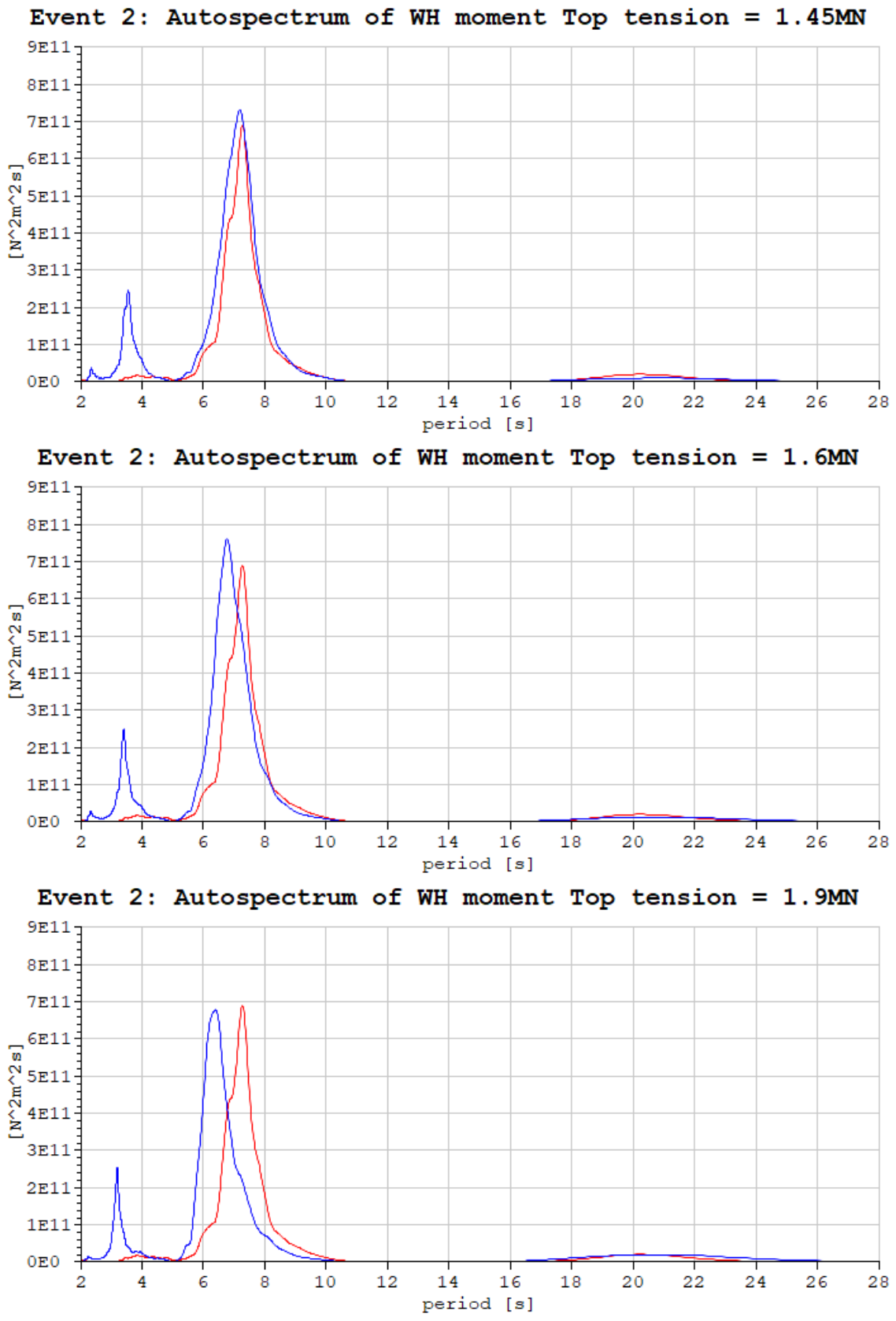

Figure 99: Event 2: The effect of different top tension on WH moment. The blue graphs shows the autospectra for the model with different top tensions, the red graph shows the autospectrum of the measurements

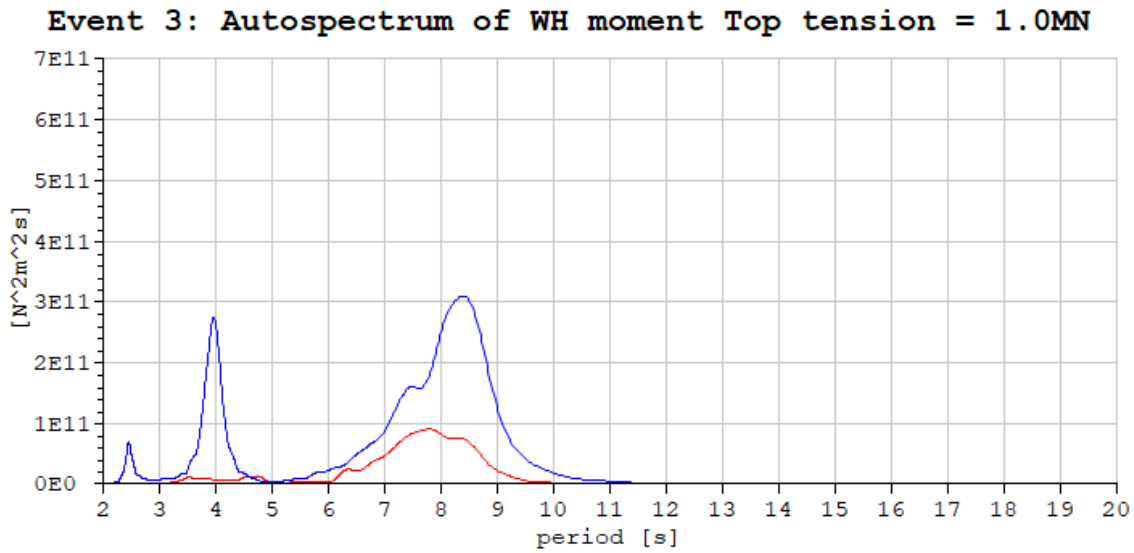
Event 3: Autospectrum of WH moment Top tension = 1.0MN
7E11
6E11
5E11
4E11
3E11
2E11
1E11
0E0
[N^2m^2s]
2 3 4 5 6 7 8 9 10 11 12 13 14 15 16 17 18 19 20
period [s]

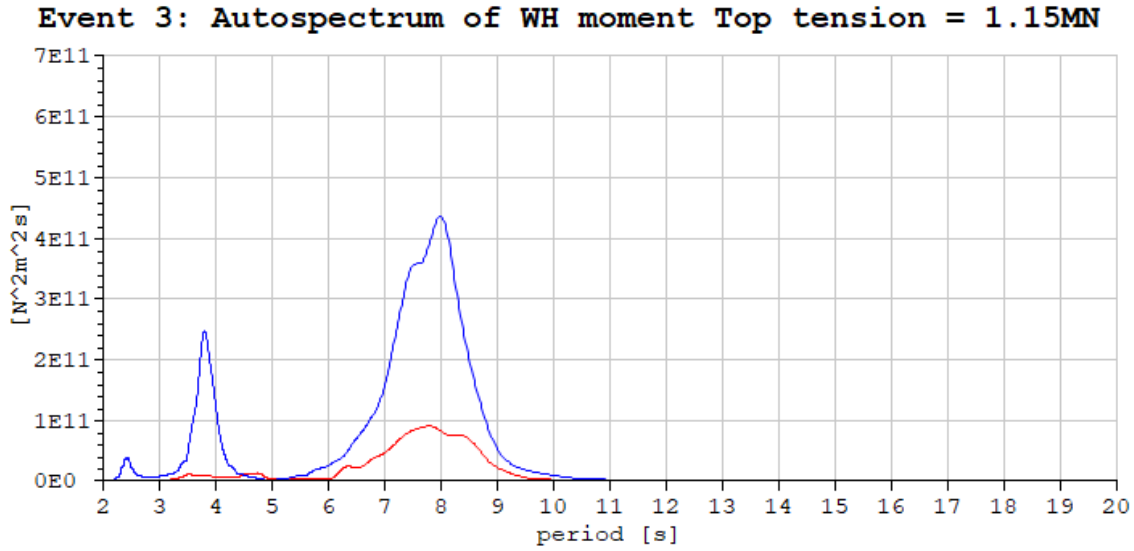
Event 3: Autospectrum of WH moment Top tension = 1.15MN
7E11
6E11
5E11
4E11
3E11
2E11
1E11
0E0
[N^2m^2s]
2 3 4 5 6 7 8 9 10 11 12 13 14 15 16 17 18 19 20
period [s]

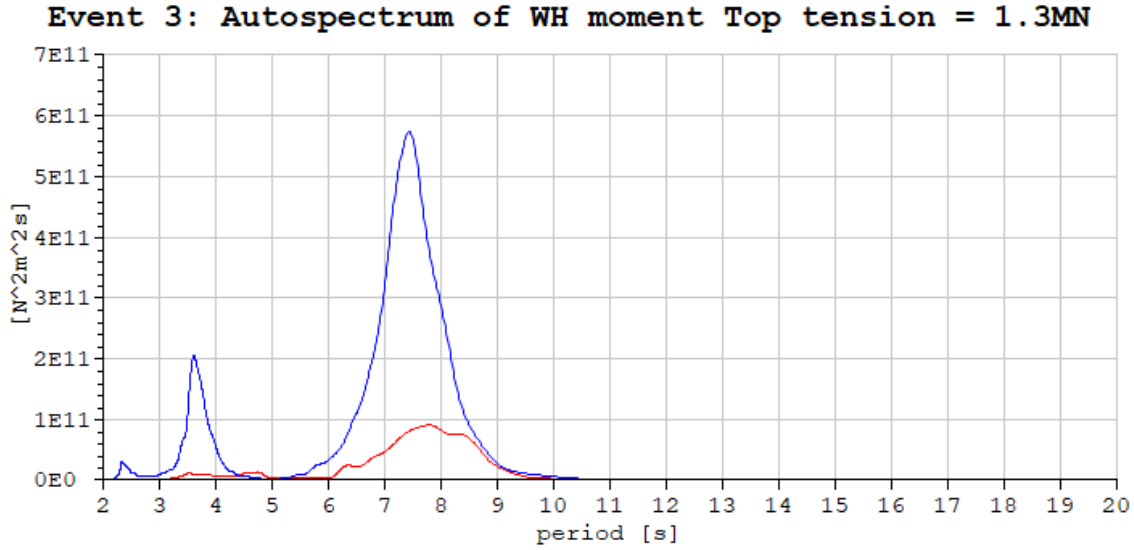
Event 3: Autospectrum of WH moment Top tension = 1.3MN
7E11
6E11
5E11
4E11
3E11
2E11
1E11
0E0
[N^2m^2s]
2 3 4 5 6 7 8 9 10 11 12 13 14 15 16 17 18 19 20
period [s]

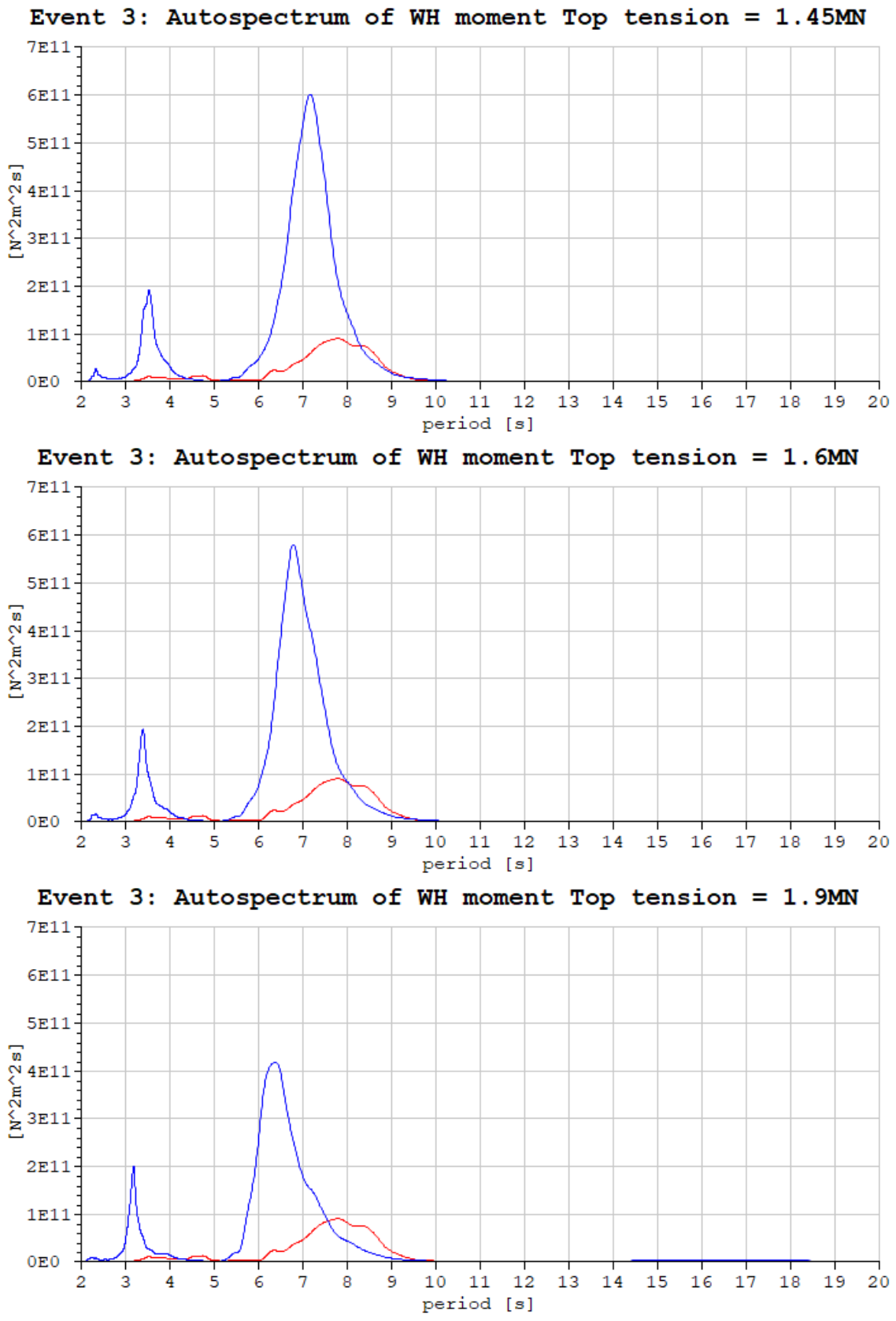

Figure 100: Event 3: The effect of different top tension on WH moment. The blue graphs shows the autospectra for the model with different top tensions, the red graph shows the autospectrum of the measurements

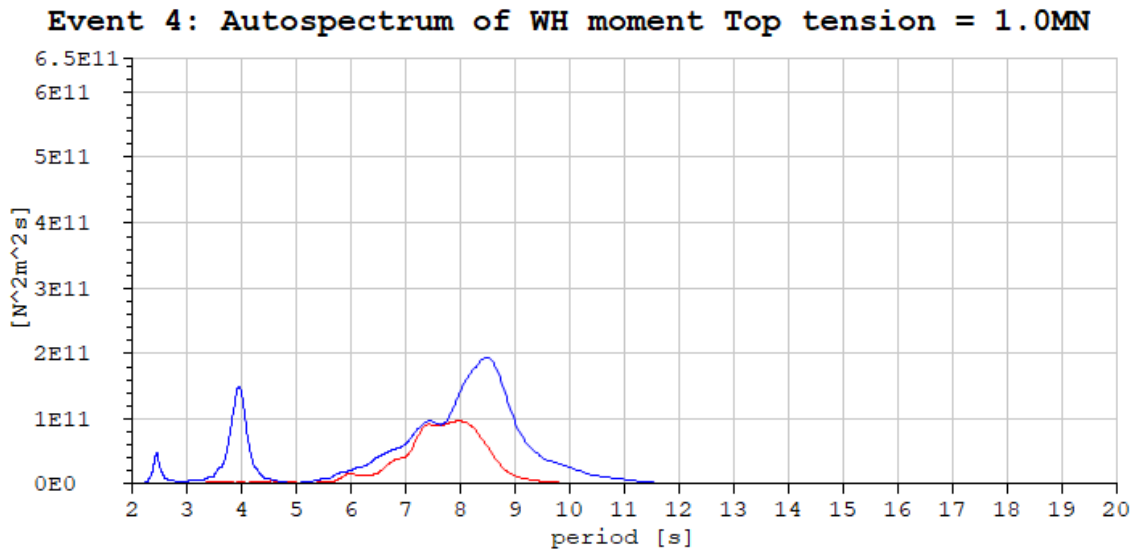
Event 4: Autospectrum of WH moment Top tension = 1.0MN
6.5E11
6E11
5E11
4E11
3E11
2E11
1E11
0E0
[N^2m^2s]
2 3 4 5 6 7 8 9 10 11 12 13 14 15 16 17 18 19 20
period [s]

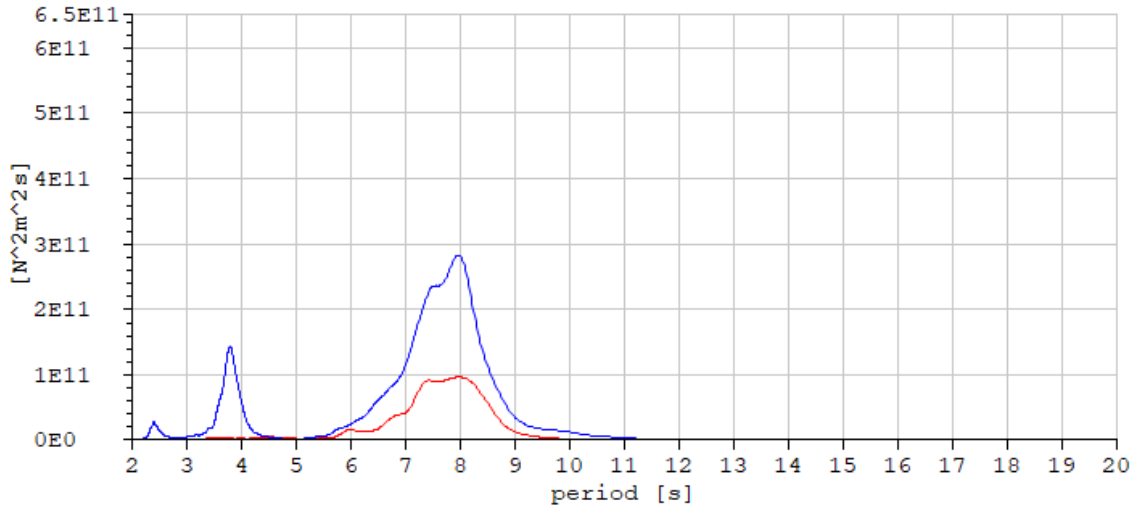
Event 4: Autospectrum of WH moment Top tension = 1.15MN
6.5E11
6E11
5E11
4E11
3E11
2E11
1E11
0E0
[N^2m^2s]
2 3 4 5 6 7 8 9 10 11 12 13 14 15 16 17 18 19 20
period [s]

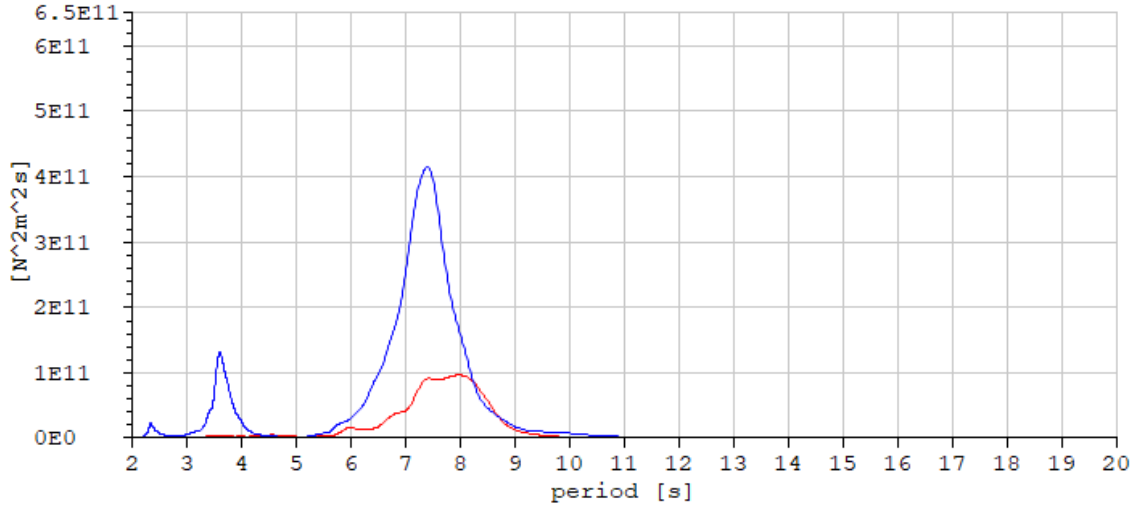
Event 4: Autospectrum of WH moment Top tension = 1.3MN
6.5E11
6E11
5E11
4E11
3E11
2E11
1E11
0E0
[N^2m^2s]
2 3 4 5 6 7 8 9 10 11 12 13 14 15 16 17 18 19 20
period [s]

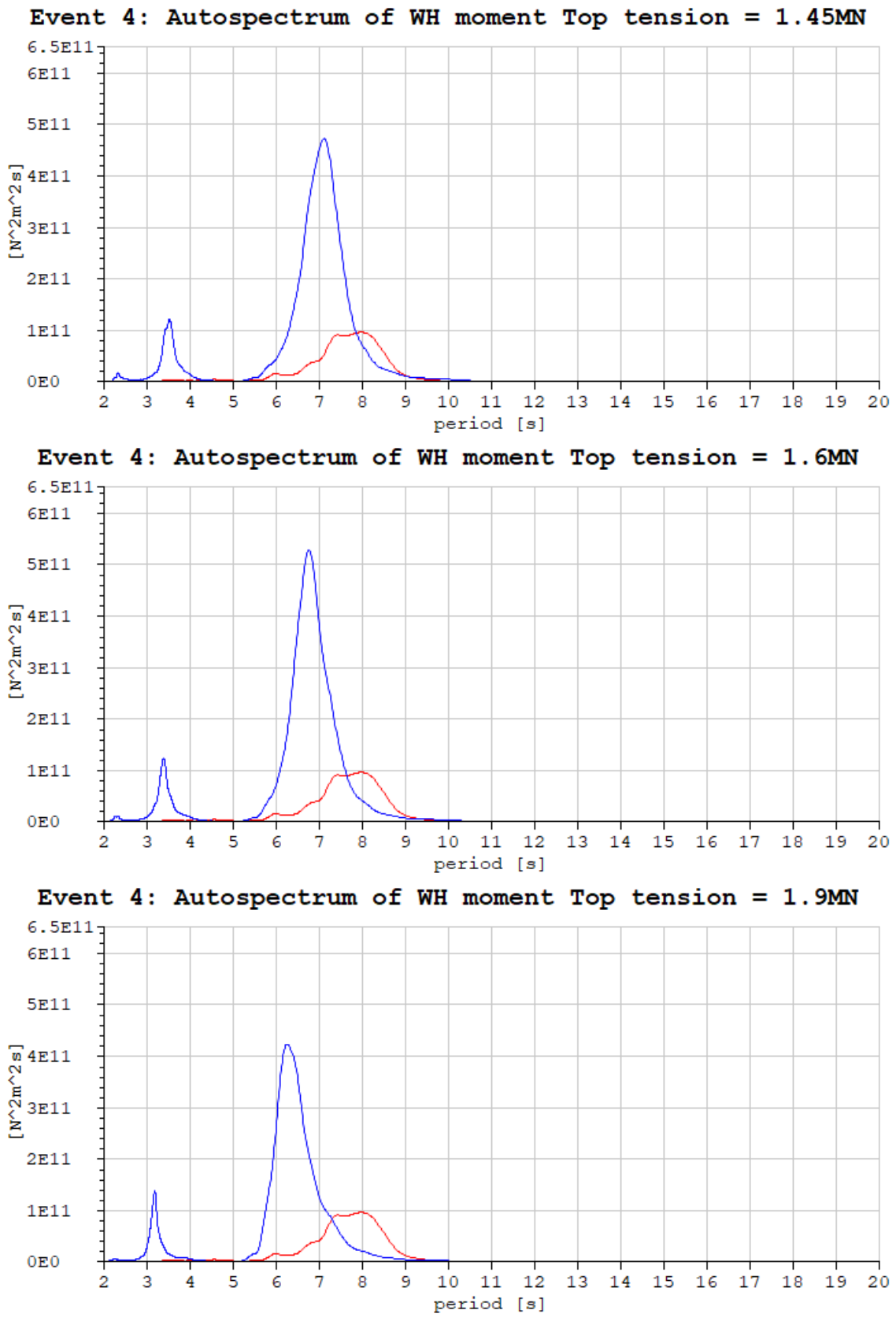

Figure 101: Event 4: The effect of different top tension on WH moment. The blue graphs shows the autospectra for the model with different top tensions, the red graph shows the autospectrum of the measurements

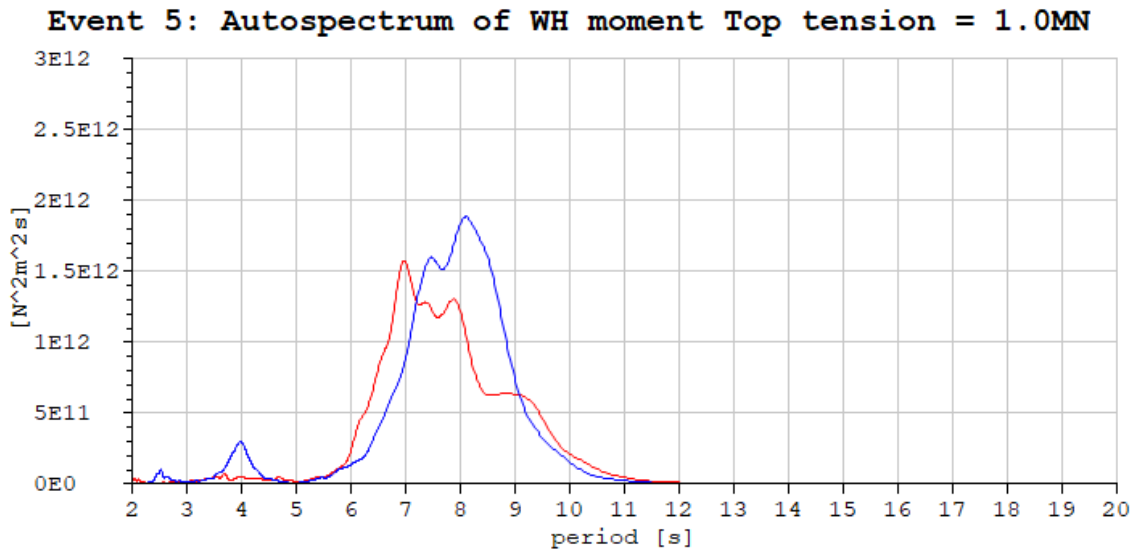
Event 5: Autospectrum of WH moment Top tension = 1.0MN
3E12
2.5E12
2E12
1.5E12
1E12
5E11
0E0
[N^2m^2s]
2 3 4 5 6 7 8 9 10 11 12 13 14 15 16 17 18 19 20
period [s]

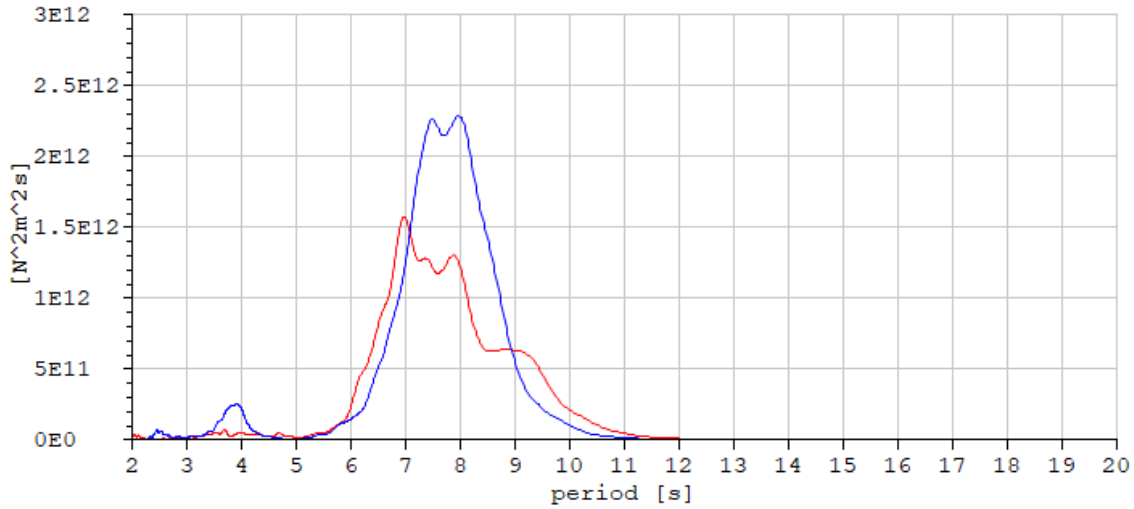
Event 5: Autospectrum of WH moment Top tension = 1.15MN
3E12
2.5E12
2E12
1.5E12
1E12
5E11
0E0
[N^2m^2s]
2 3 4 5 6 7 8 9 10 11 12 13 14 15 16 17 18 19 20
period [s]

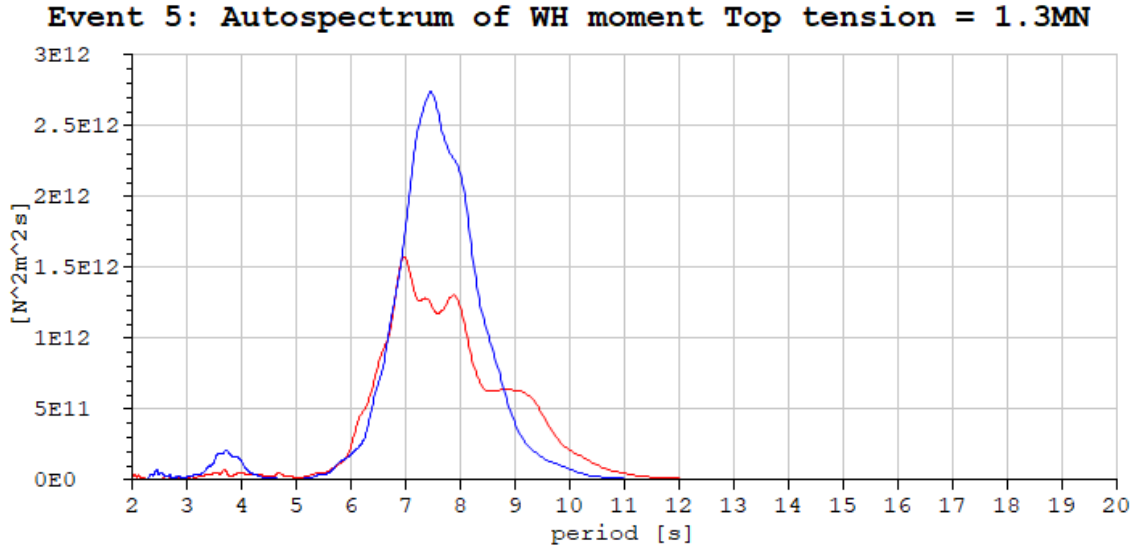
Event 5: Autospectrum of WH moment Top tension = 1.3MN
3E12
2.5E12
2E12
1.5E12
1E12
5E11
0E0
[N^2m^2s]
2 3 4 5 6 7 8 9 10 11 12 13 14 15 16 17 18 19 20
period [s]

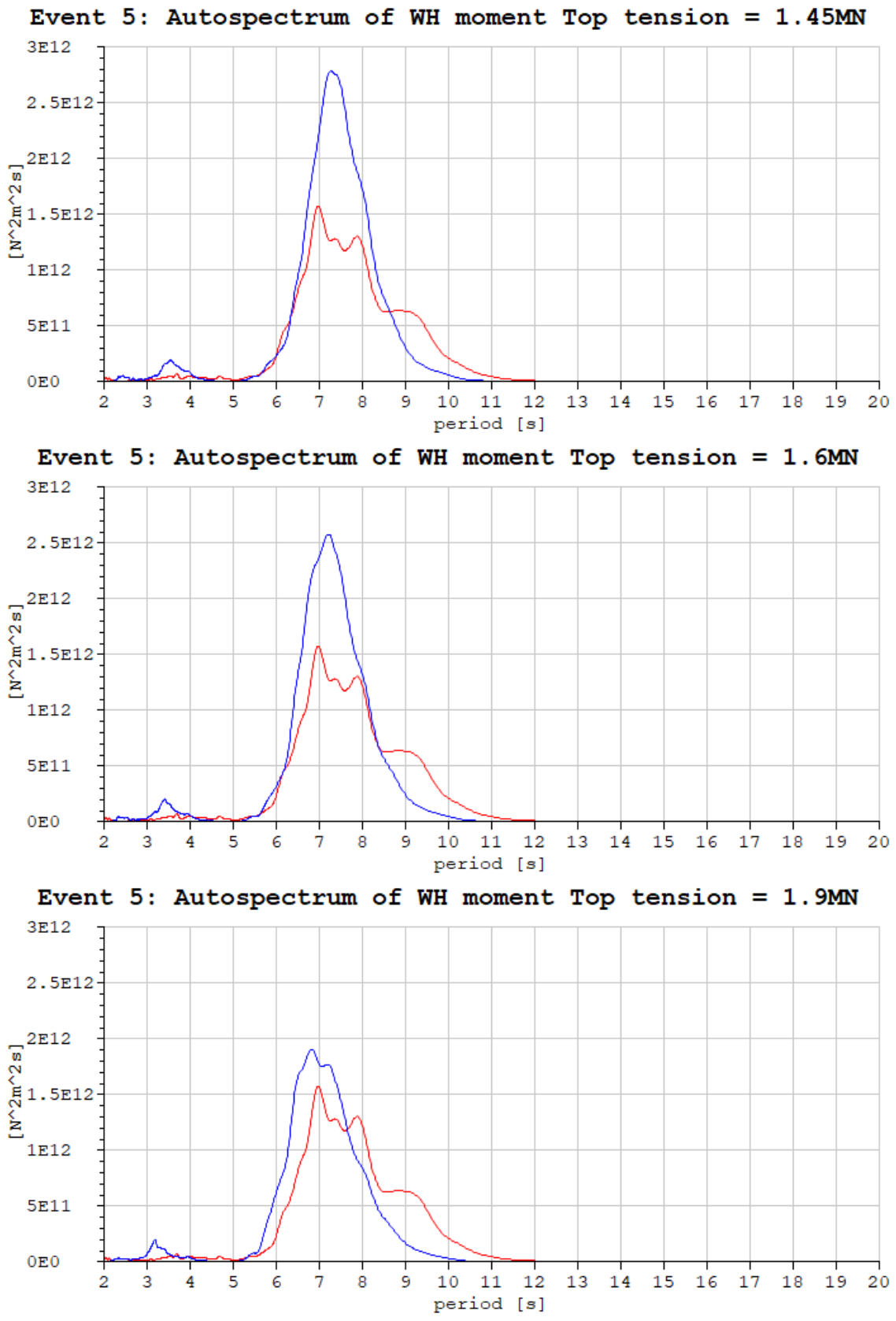

Figure 102: Event 5: The effect of different top tension on WH moment. The blue graphs shows the autospectra for the model with different top tensions, the red graph shows the autospectrum of the measurements

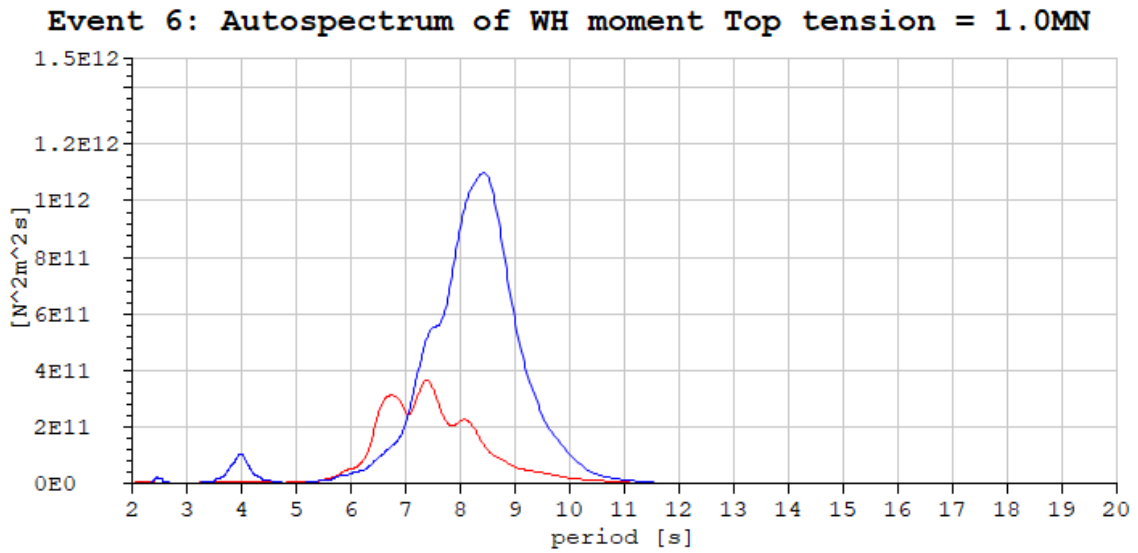
Event 6: Autospectrum of WH moment Top tension = 1.0MN
1.5E12
1.2E12
1E12
8E11
6E11
4E11
2E11
0E0
[N^2m^2s]
2 3 4 5 6 7 8 9 10 11 12 13 14 15 16 17 18 19 20
period [s]

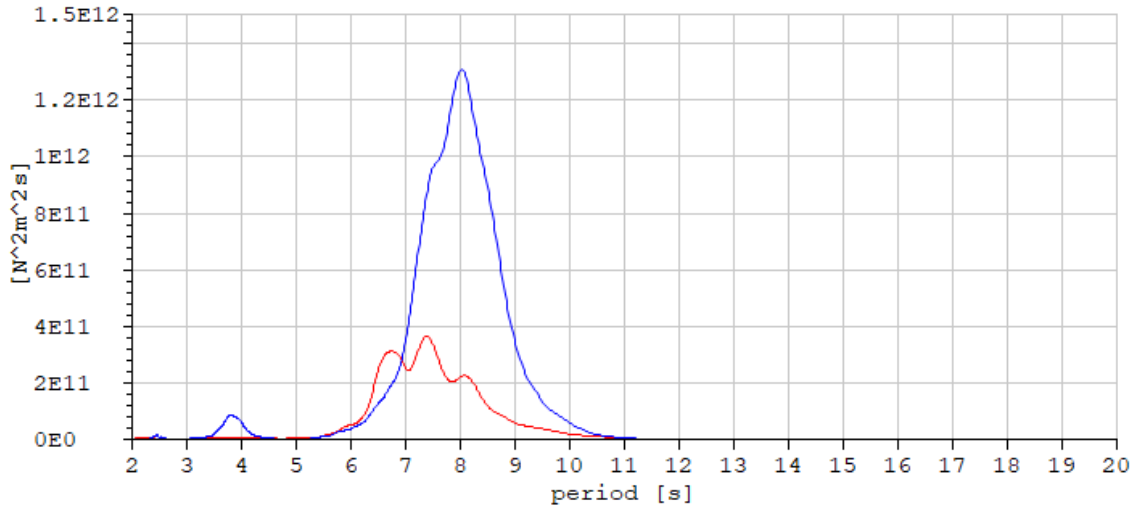
Event 6: Autospectrum of WH moment Top tension = 1.15MN
1.5E12
1.2E12
1E12
8E11
6E11
4E11
2E11
0E0
[N^2m^2s]
2 3 4 5 6 7 8 9 10 11 12 13 14 15 16 17 18 19 20
period [s]

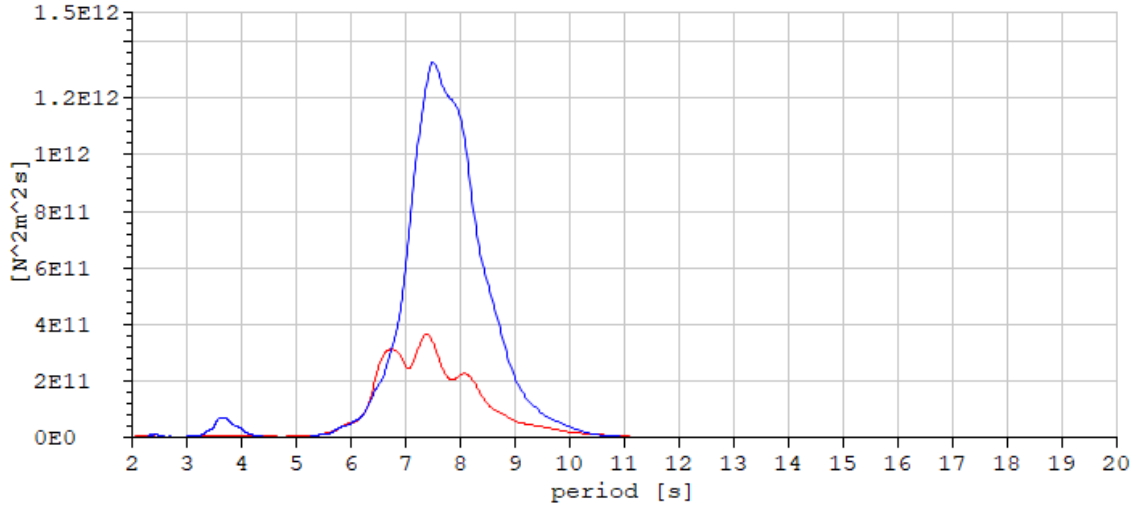
Event 6: Autospectrum of WH moment Top tension = 1.3MN
1.5E12
1.2E12
1E12
8E11
6E11
4E11
2E11
0E0
[N^2m^2s]
2 3 4 5 6 7 8 9 10 11 12 13 14 15 16 17 18 19 20
period [s]

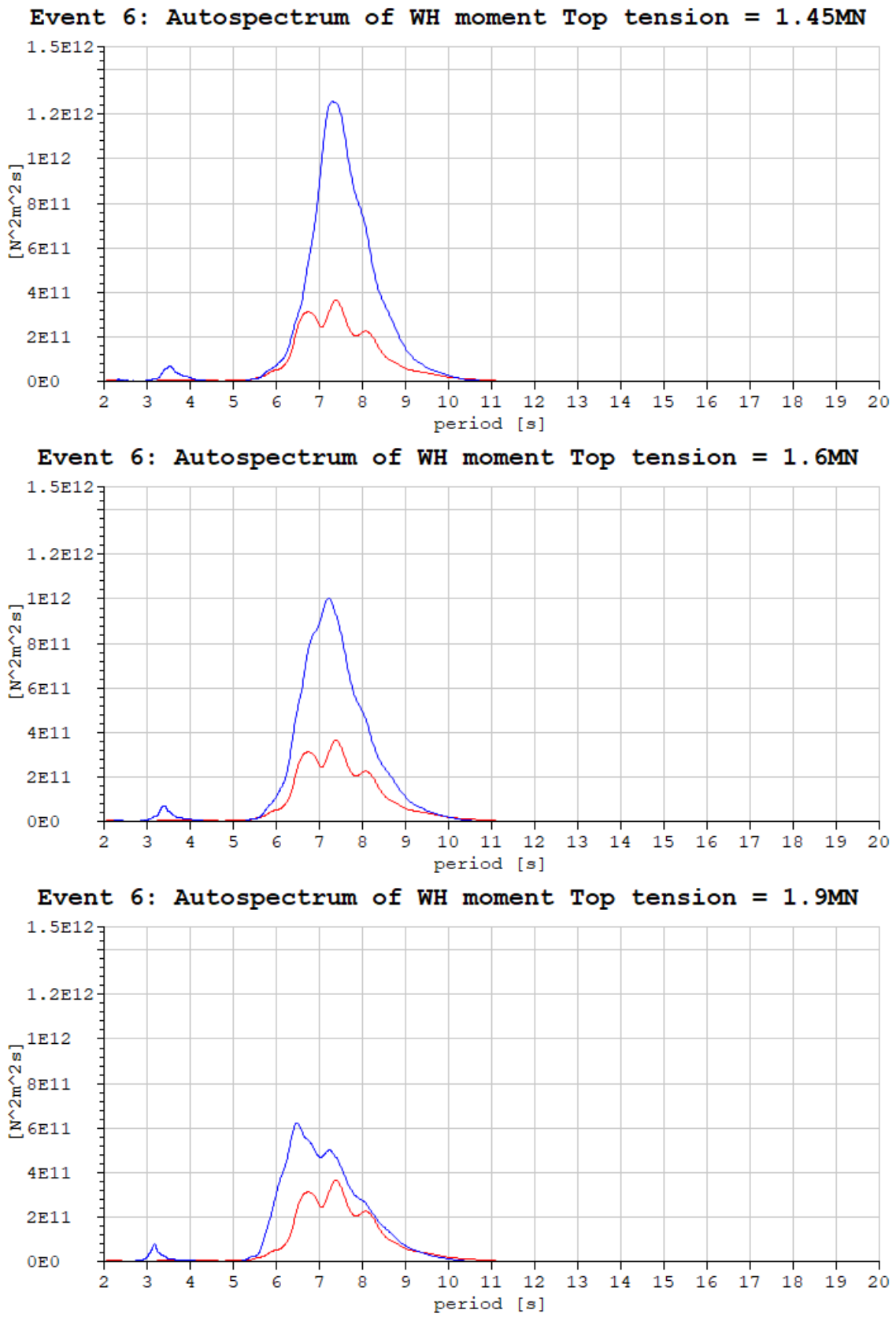

Figure 103: Event 6: The effect of different top tension on WH moment. The blue graphs shows the autospectra for the model with different top tensions, the red graph shows the autospectrum of the measurements

I WH moment with different types of Rayleigh damping

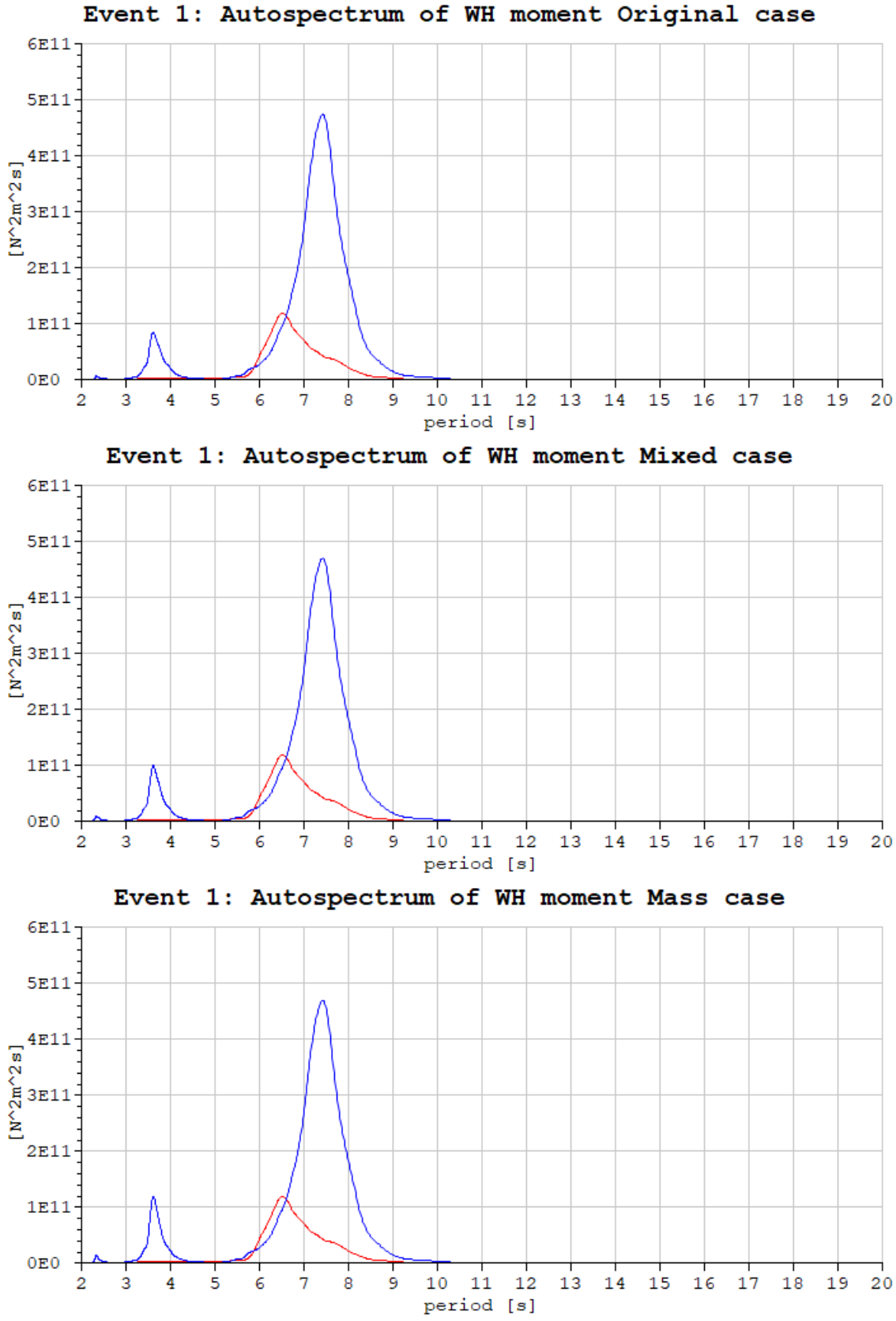

Figure 104: Event1: Autospectra for different types of Rayleigh damping. The blue graphs is the autospectra for WH moment in the model for each of the different damping cases described in Section 11.3.1, the red is from measurements

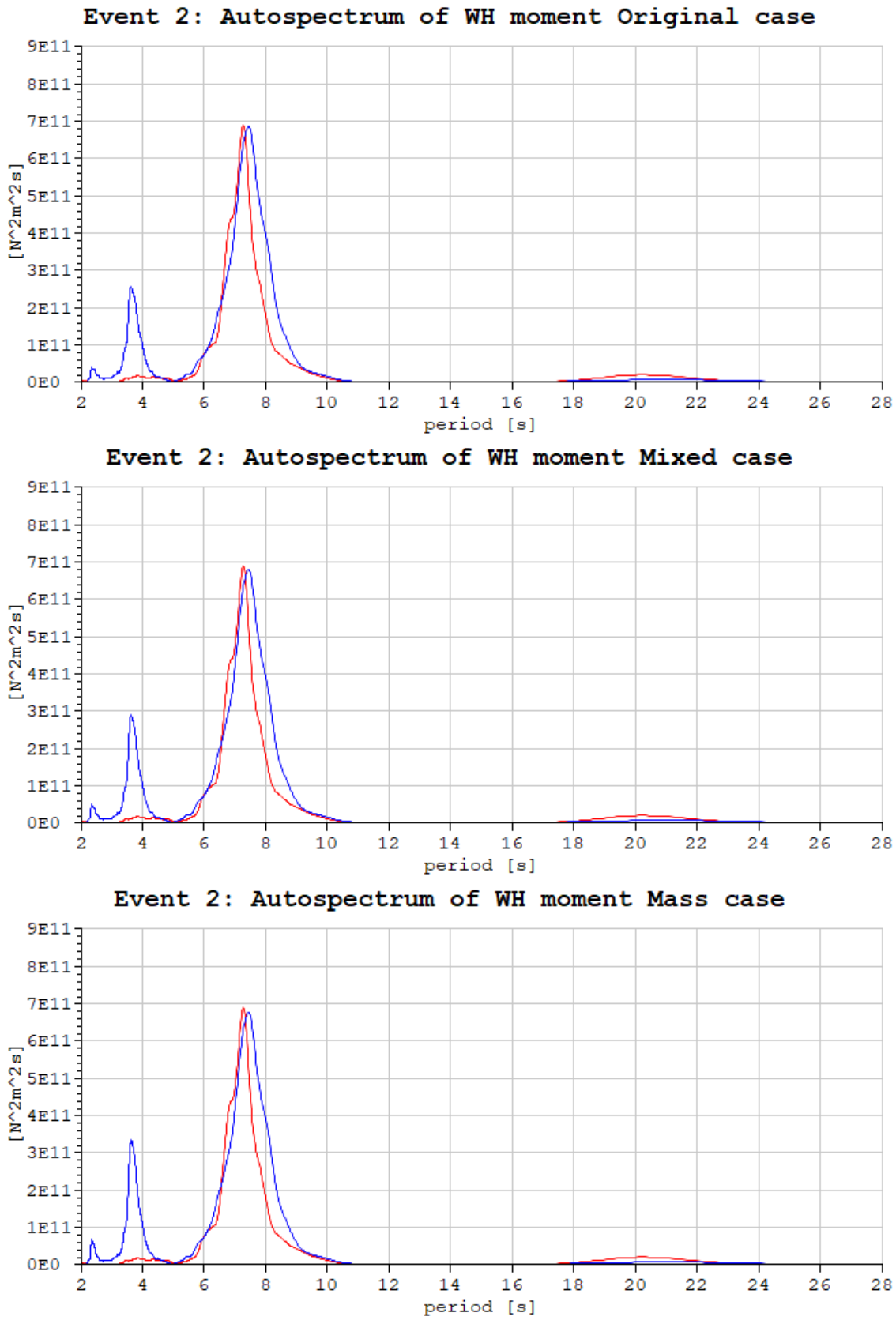

Figure 105: Event2: Autospectra for different types of Rayleigh damping. The blue graphs is the autospectra for WH moment in the model for each of the different damping cases described in Section 11.3.1, the red is from measurements

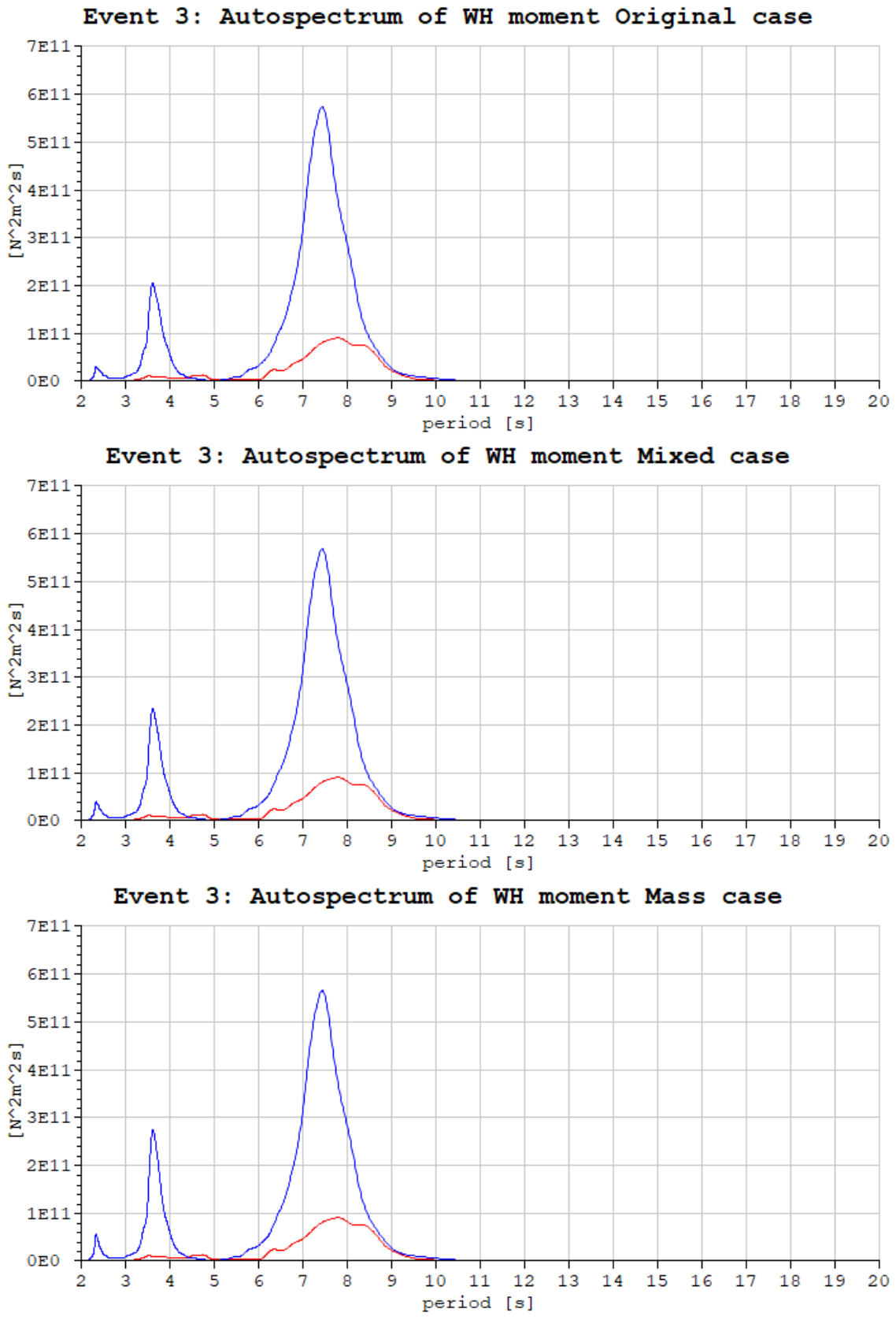

Figure 106: Event3: Autospectra for different types of Rayleigh damping. The blue graphs is the autospectra for WH moment in the model for each of the different damping cases described in Section 11.3.1, the red is from measurements

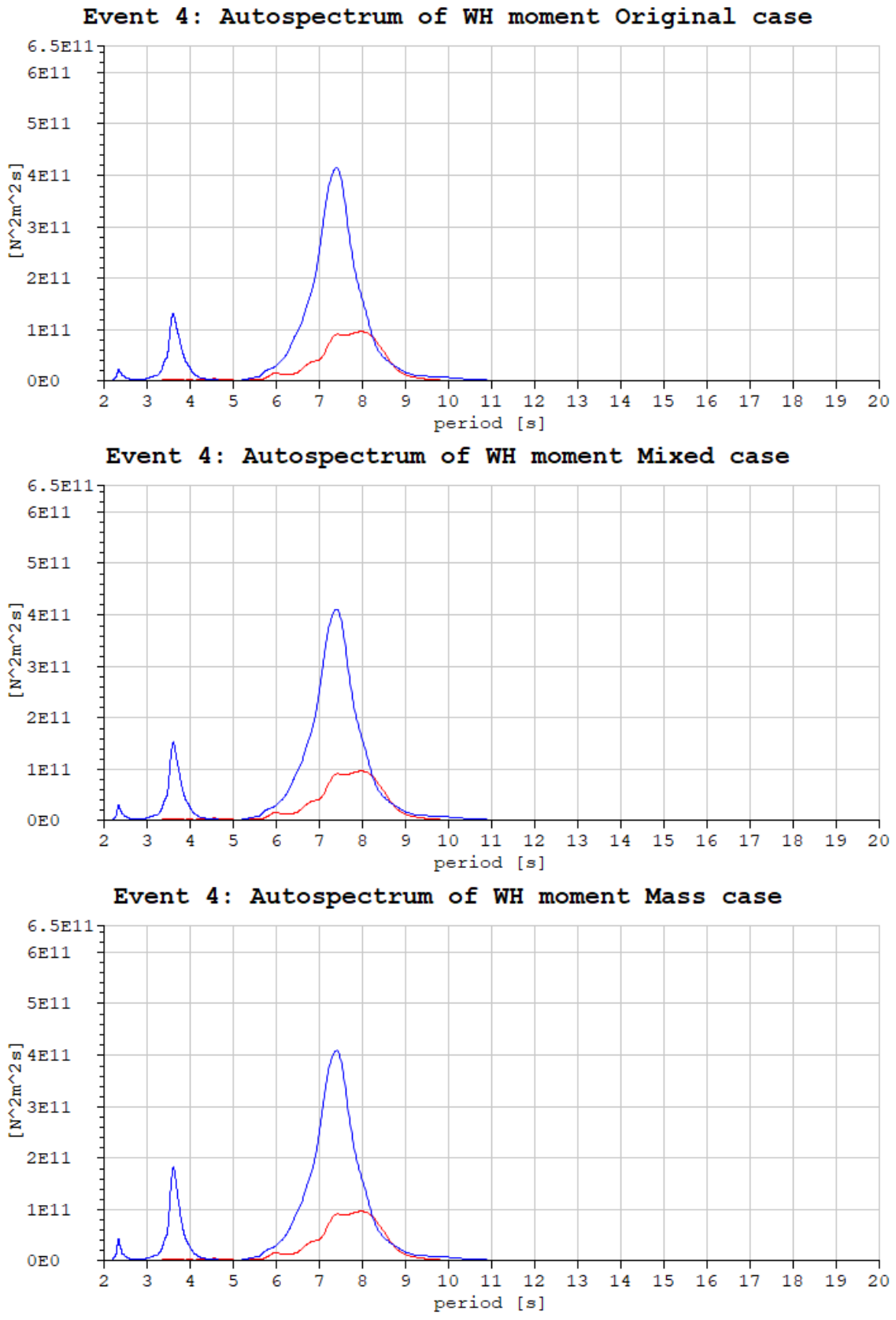

Figure 107: Event4: Autospectra for different types of Rayleigh damping. The blue graphs is the autospectra for WH moment in the model for each of the different damping cases described in Section 11.3.1, the red is from measurements

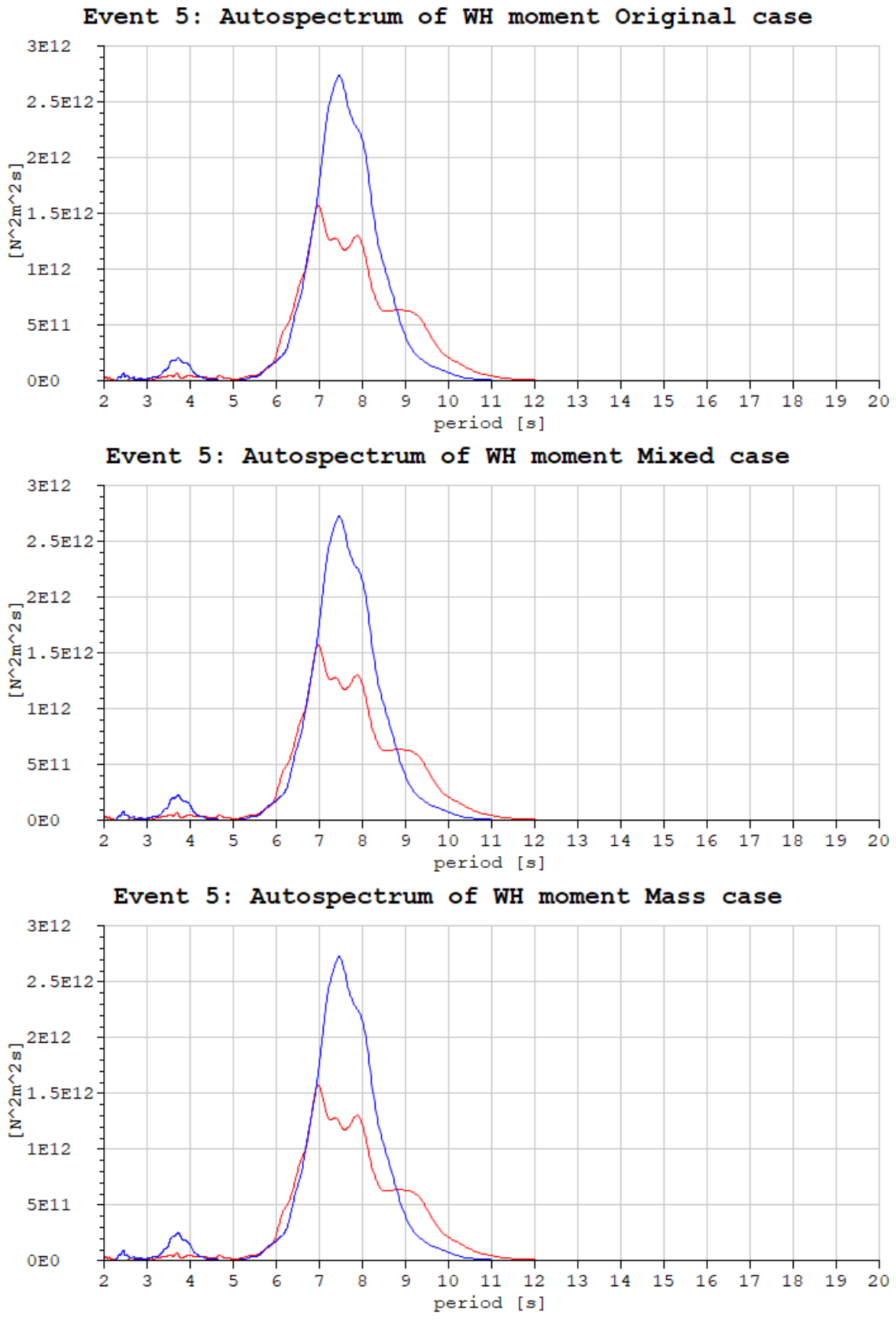

Figure 108: Event5: Autospectra for different types of Rayleigh damping. The blue graphs is the autospectra for WH moment in the model for each of the different damping cases described in Section 11.3.1, the red is from measurements

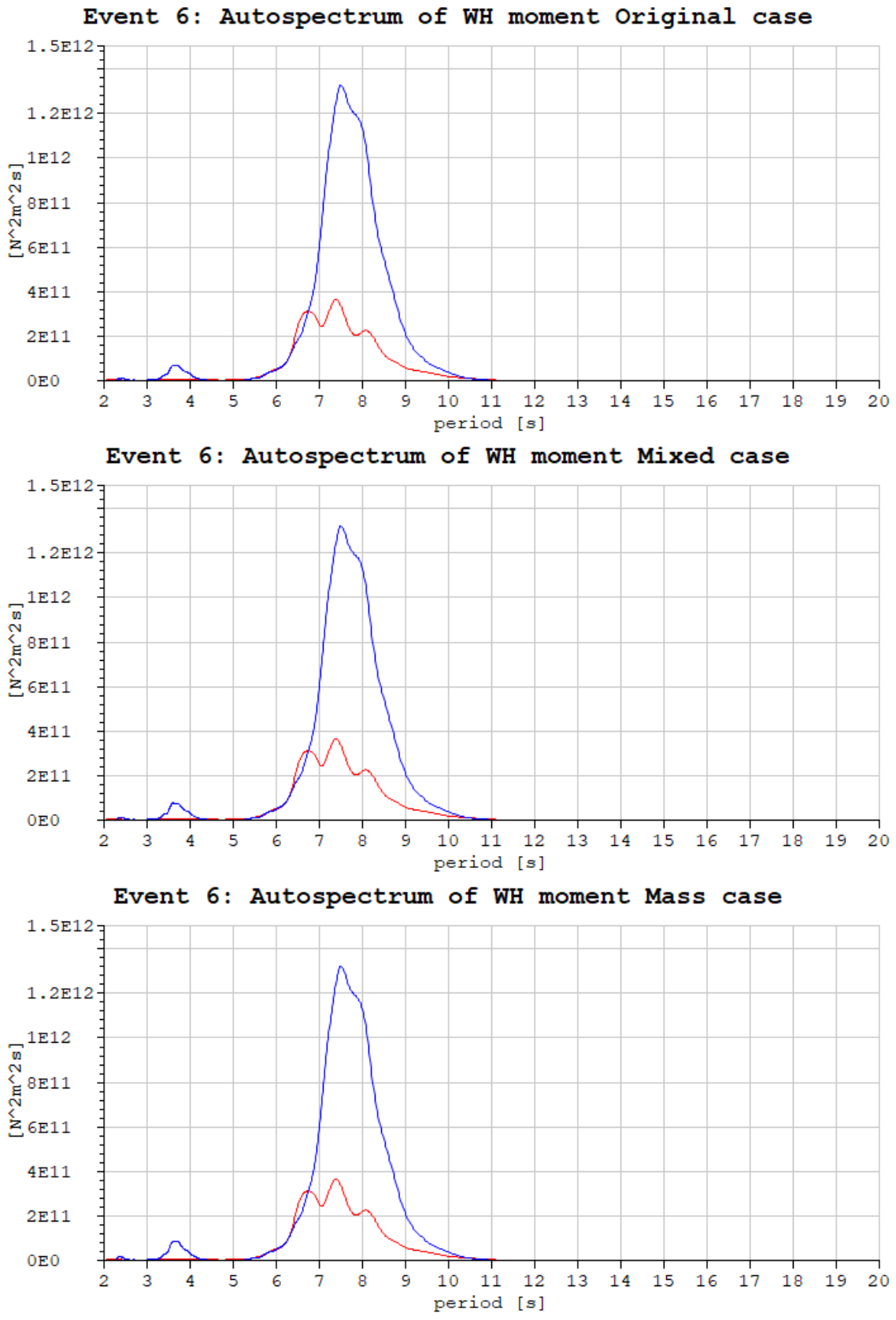

Figure 109: Event6: Autospectra for different types of Rayleigh damping. The blue graphs is the autospectra for WH moment in the model for each of the different damping cases described in Section 11.3.1, the red is from measurements

J WH moment with different critical damping ratios

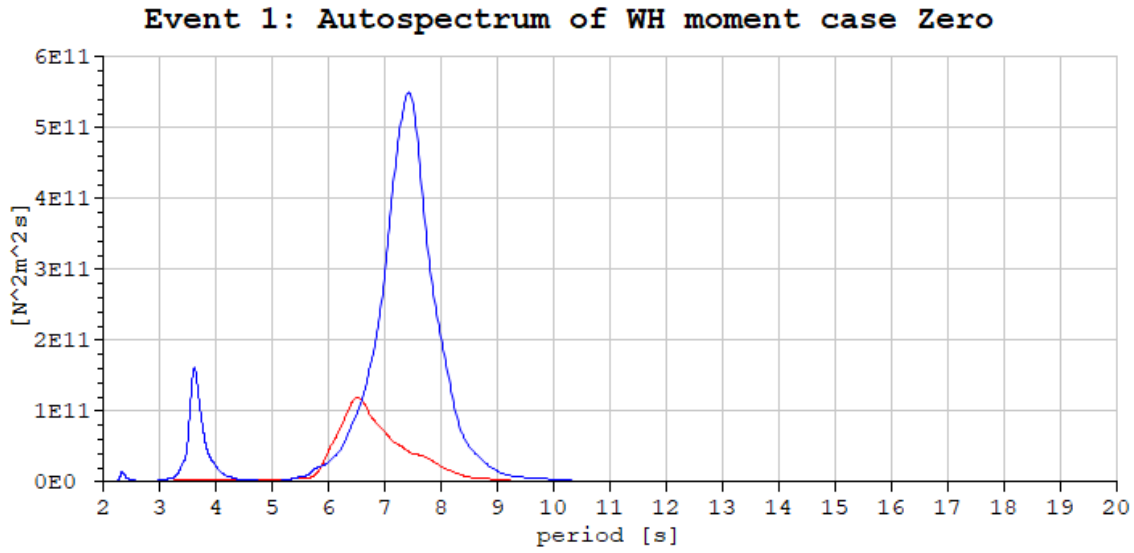

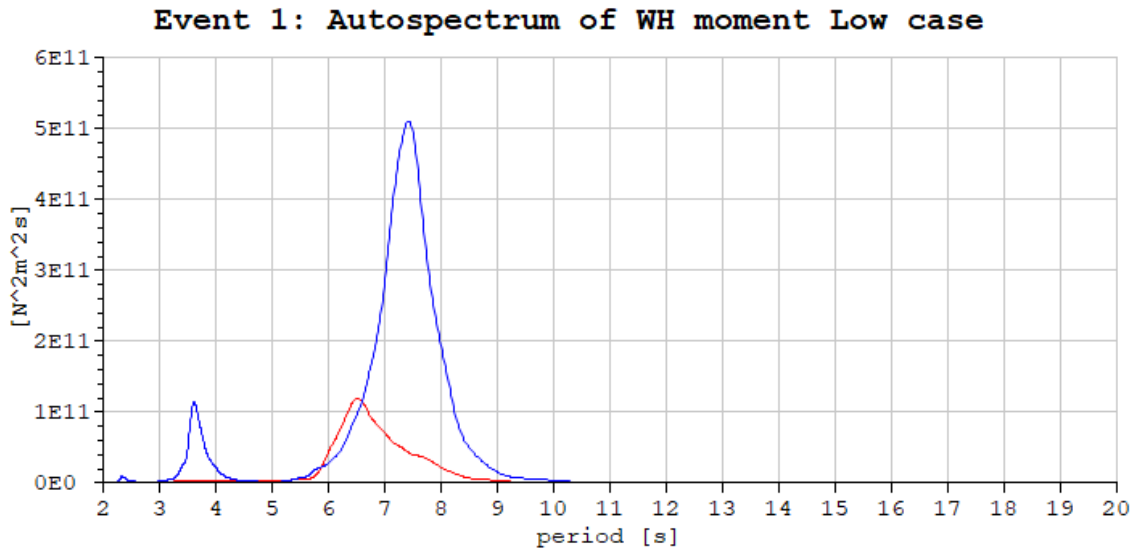

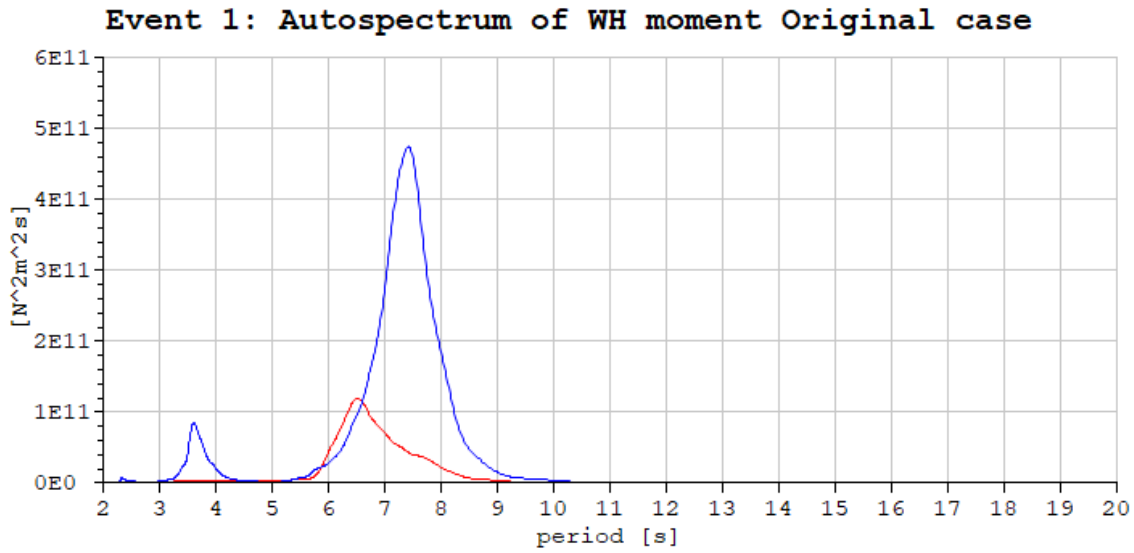

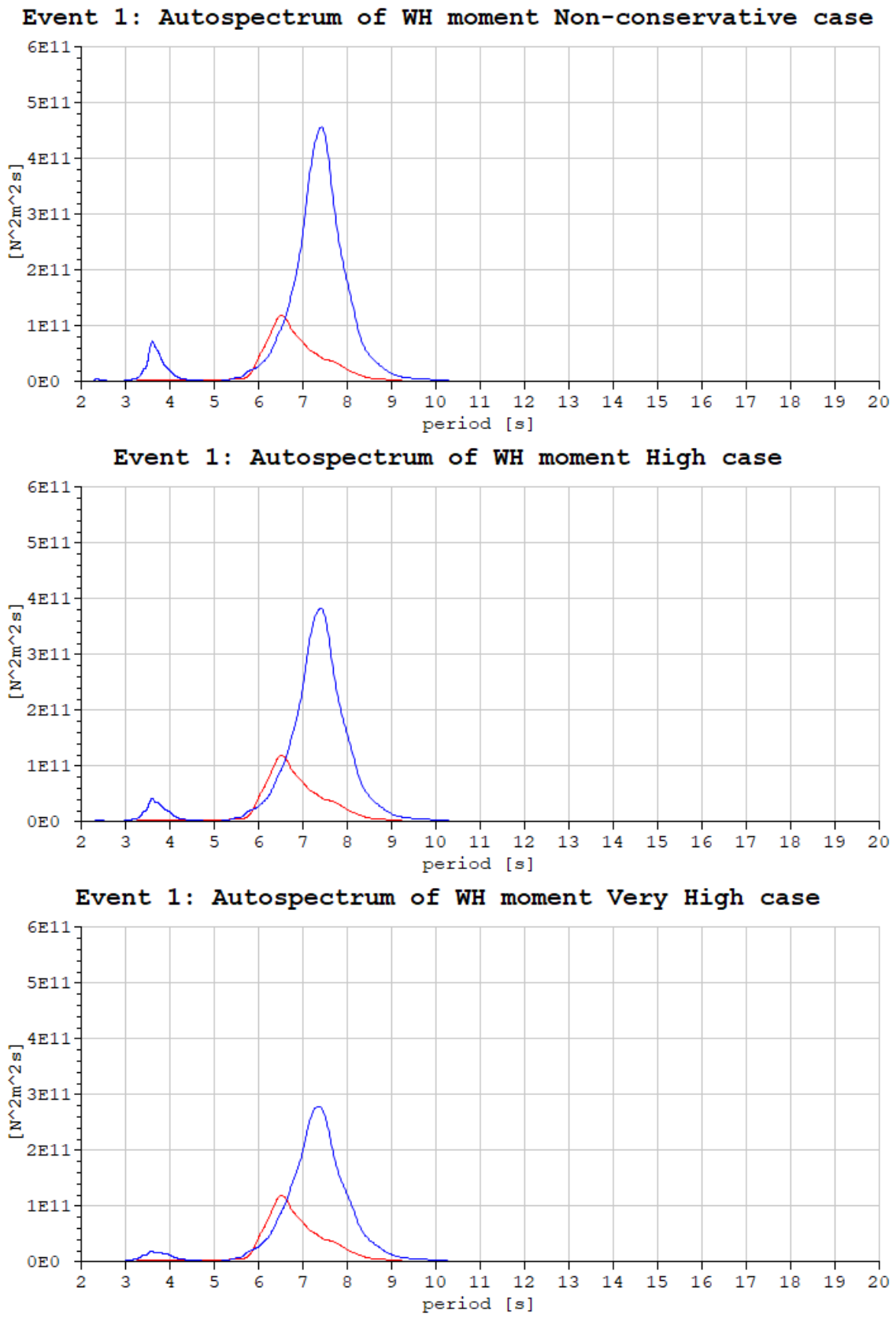

Figure 110: Event 1: The effect of different critical damping ratio on WH moment autospectrum. The blue graphs is the autospectra for WH moment in the model for each of the different damping ratios described in Table 19, the red is from measurements

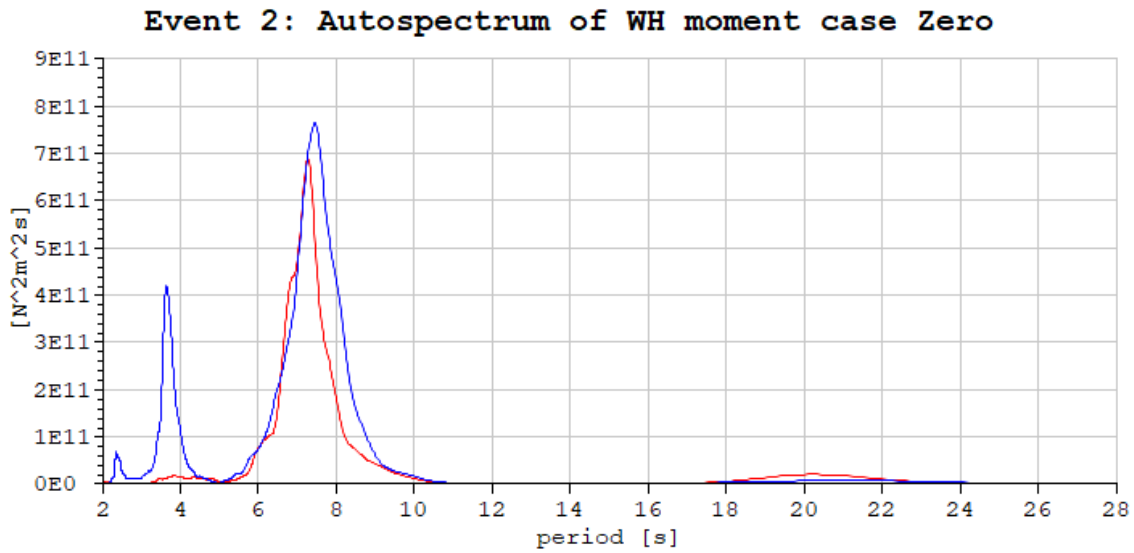
Event 2: Autospectrum of WH moment case Zero
9E11
8E11
7E11
6E11
5E11
4E11
3E11
2E11
1E11
0E0
[N^2m^2s]
2
4
6
8
10
12
14
16
18
20
22
24
26
28
period [s]

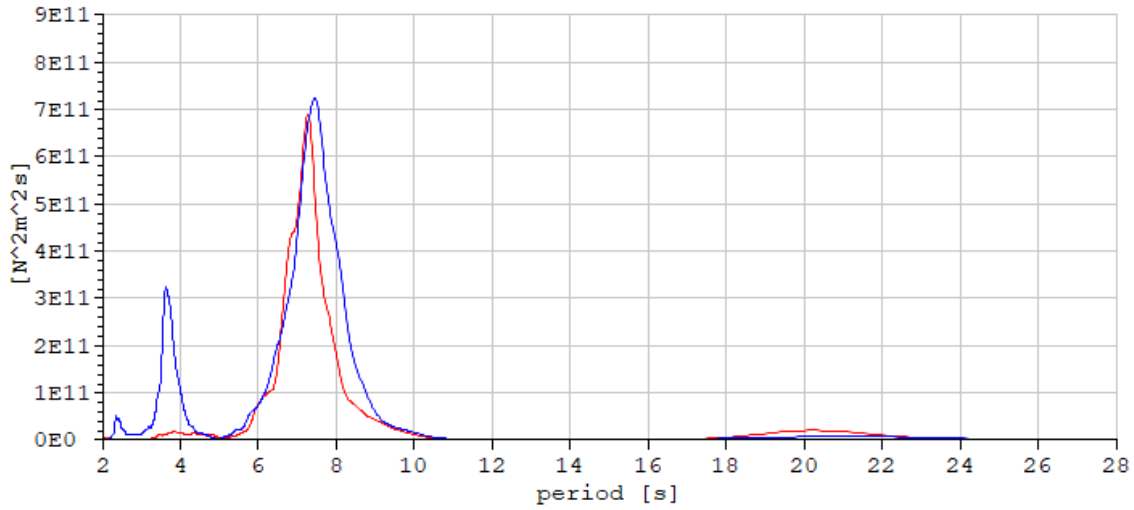
Event 2: Autospectrum of WH moment Low case
9E11
8E11
7E11
6E11
5E11
4E11
3E11
2E11
1E11
0E0
[N^2m^2s]
2
4
6
8
10
12
14
16
18
20
22
24
26
28
period [s]

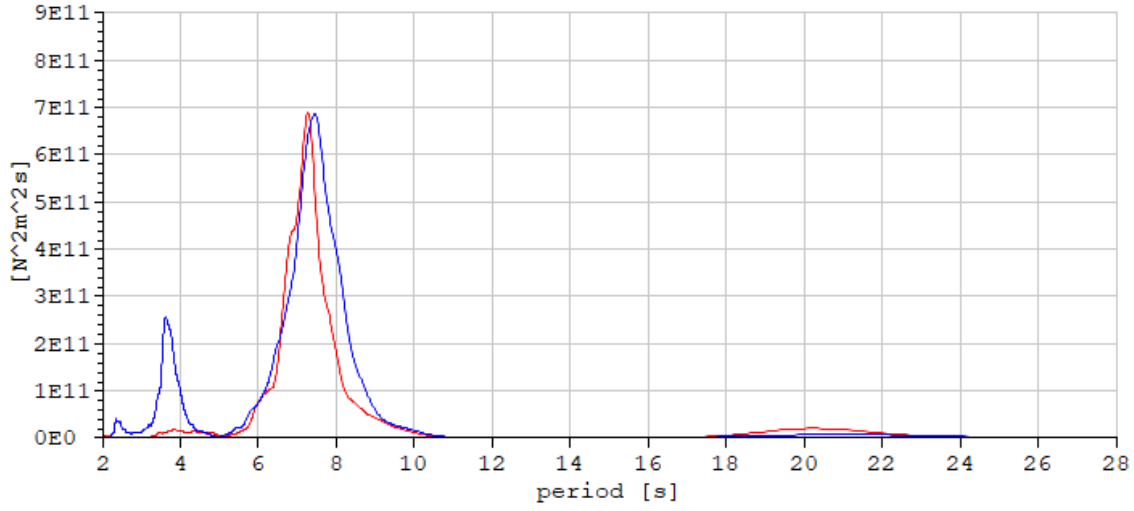
Event 2: Autospectrum of WH moment Original case
9E11
8E11
7E11
6E11
5E11
4E11
3E11
2E11
1E11
0E0
[N^2m^2s]
2
4
6
8
10
12
14
16
18
20
22
24
26
28
period [s]

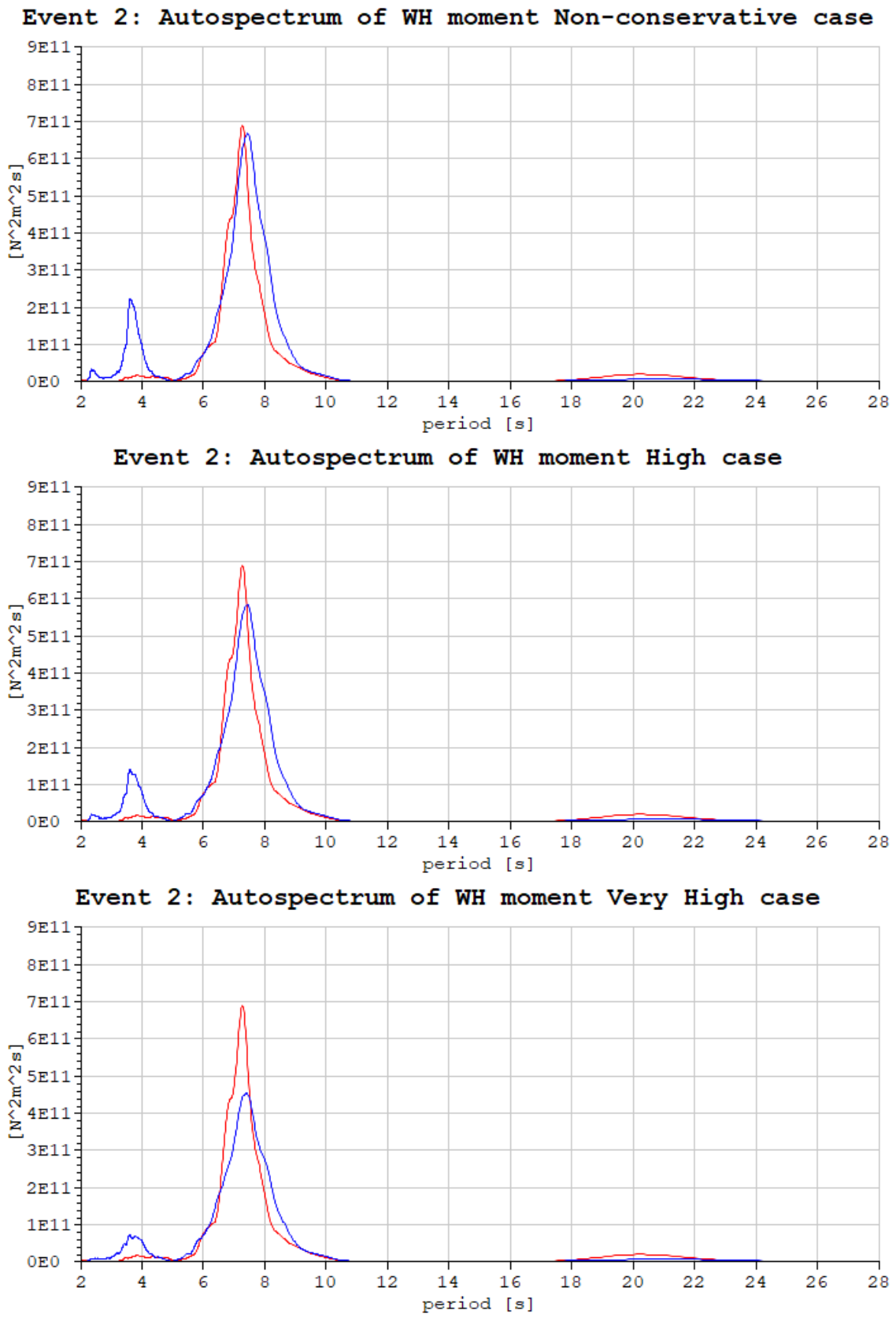

Figure 111: Event 2: The effect of different critical damping ratio on WH moment autospectrum. The blue graphs is the autospectra for WH moment in the model for each of the different damping ratios described in Table 19, the red is from measurements

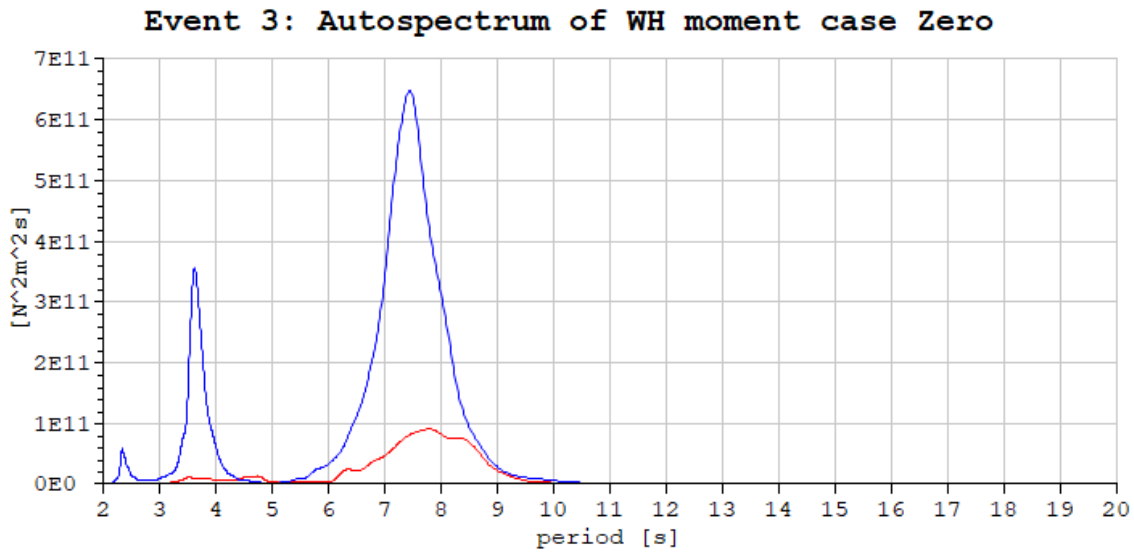
Event 3: Autospectrum of WH moment case Zero
7E11
6E11
5E11
4E11
3E11
2E11
1E11
0E0
[N^2m^2s]
2 3 4 5 6 7 8 9 10 11 12 13 14 15 16 17 18 19 20
period [s]

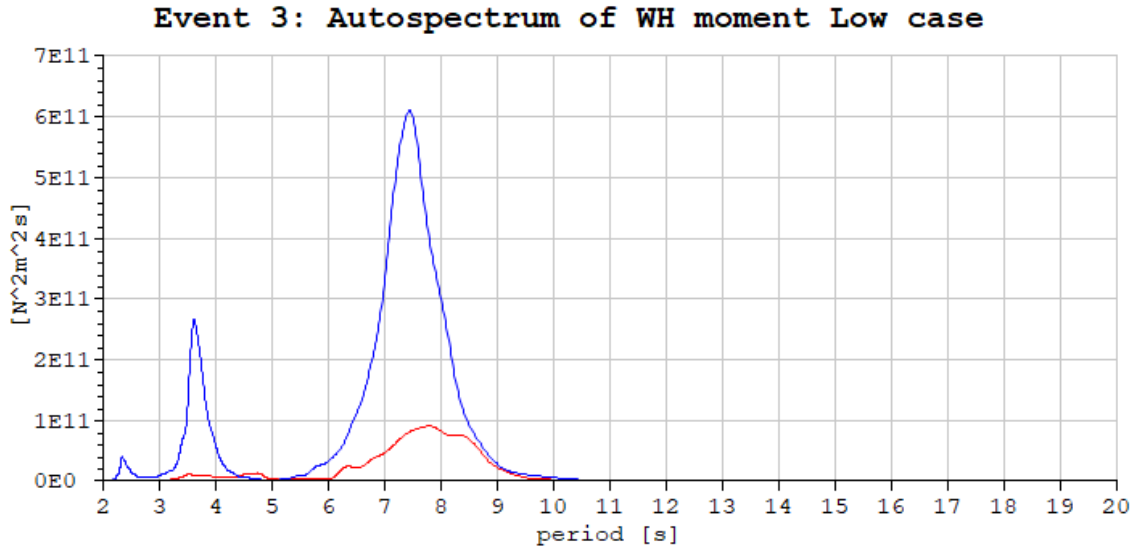
Event 3: Autospectrum of WH moment Low case
7E11
6E11
5E11
4E11
3E11
2E11
1E11
0E0
[N^2m^2s]
2 3 4 5 6 7 8 9 10 11 12 13 14 15 16 17 18 19 20
period [s]

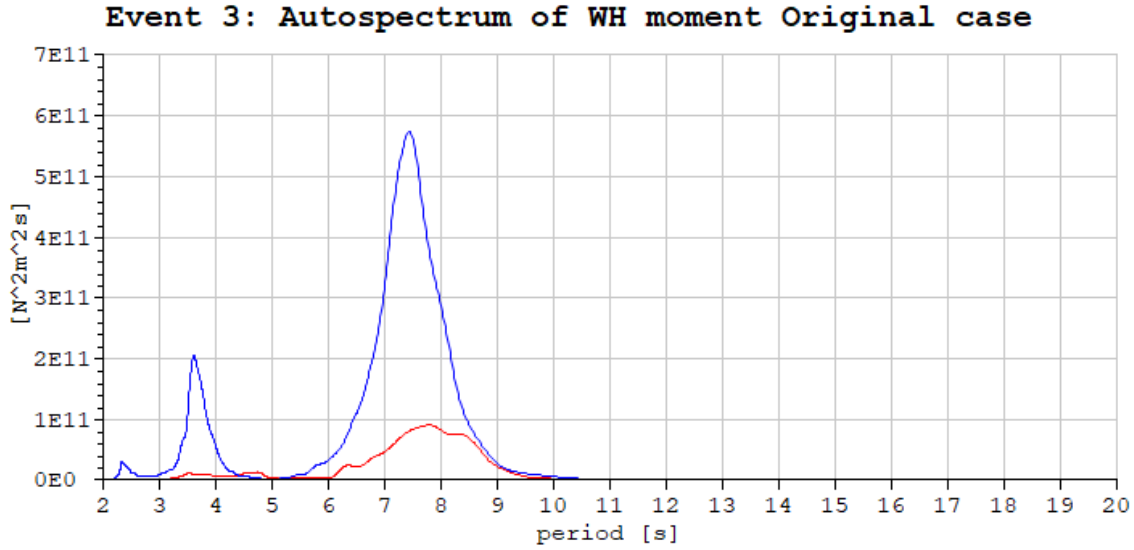
Event 3: Autospectrum of WH moment Original case
7E11
6E11
5E11
4E11
3E11
2E11
1E11
0E0
[N^2m^2s]
2 3 4 5 6 7 8 9 10 11 12 13 14 15 16 17 18 19 20
period [s]

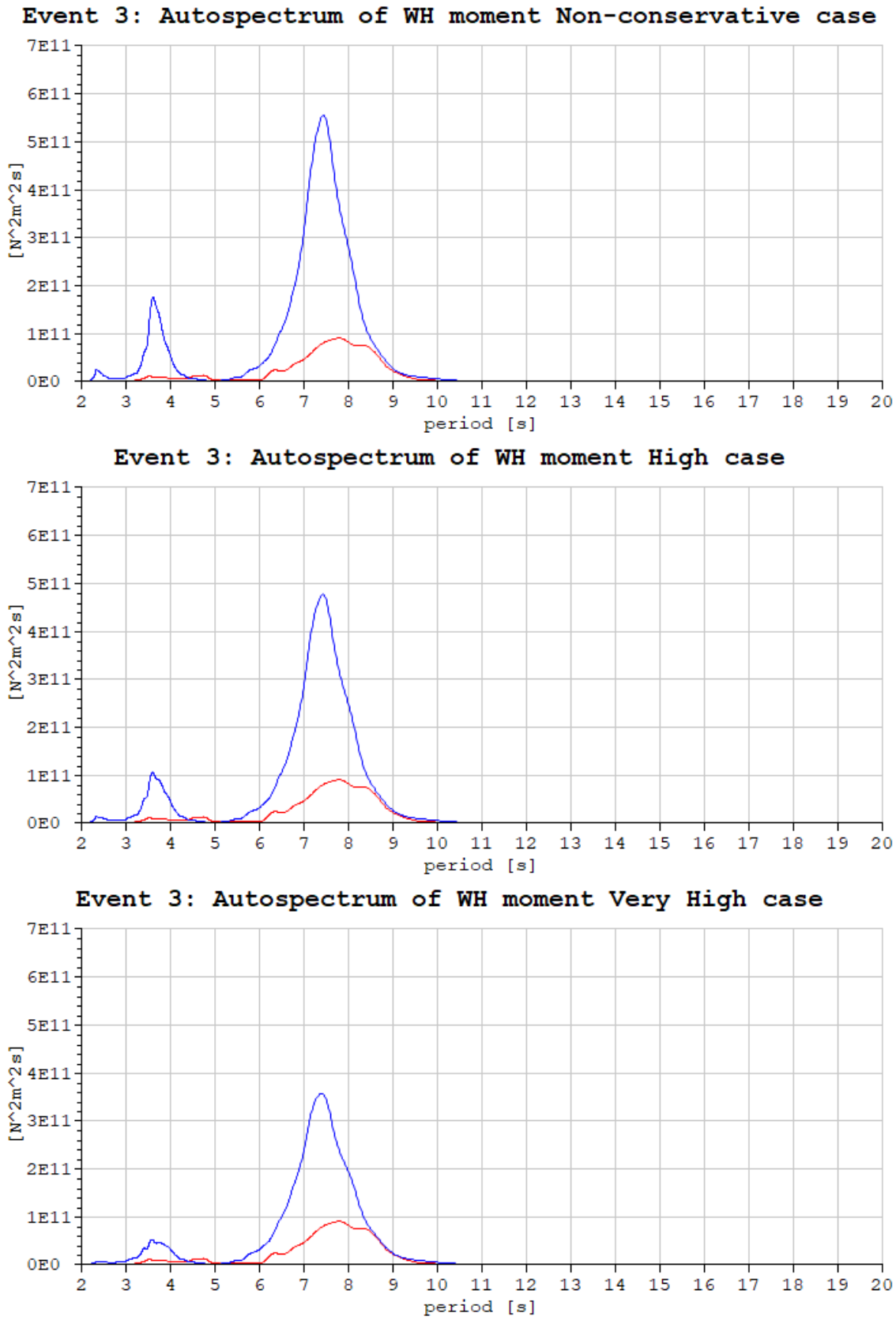

Figure 112: Event 3: The effect of different critical damping ratio on WH moment autospectrum. The blue graphs is the autospectra for WH moment in the model for each of the different damping ratios described in Table 19, the red is from measurements

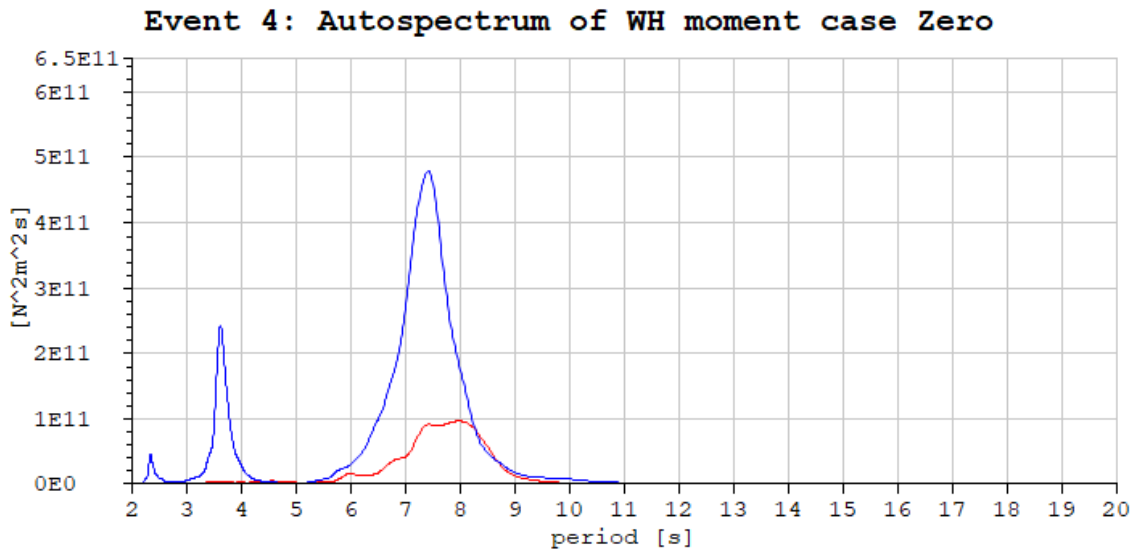
Event 4: Autospectrum of WH moment case Zero
6.5E11
6E11
5E11
4E11
3E11
2E11
1E11
0E0
[N^2m^2s]
2 3 4 5 6 7 8 9 10 11 12 13 14 15 16 17 18 19 20
period [s]

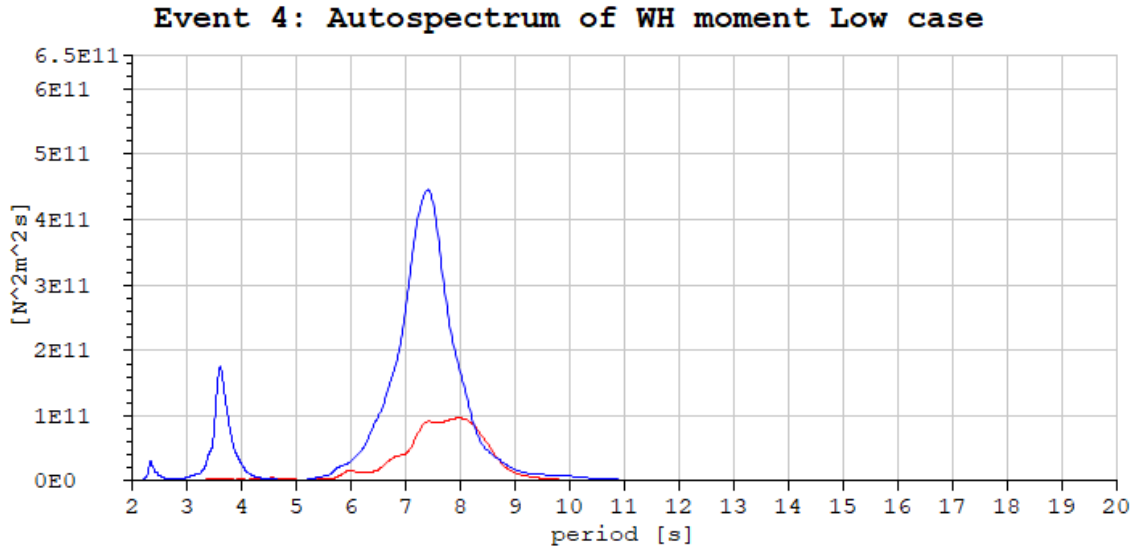
Event 4: Autospectrum of WH moment Low case
6.5E11
6E11
5E11
4E11
3E11
2E11
1E11
0E0
[N^2m^2s]
2 3 4 5 6 7 8 9 10 11 12 13 14 15 16 17 18 19 20
period [s]

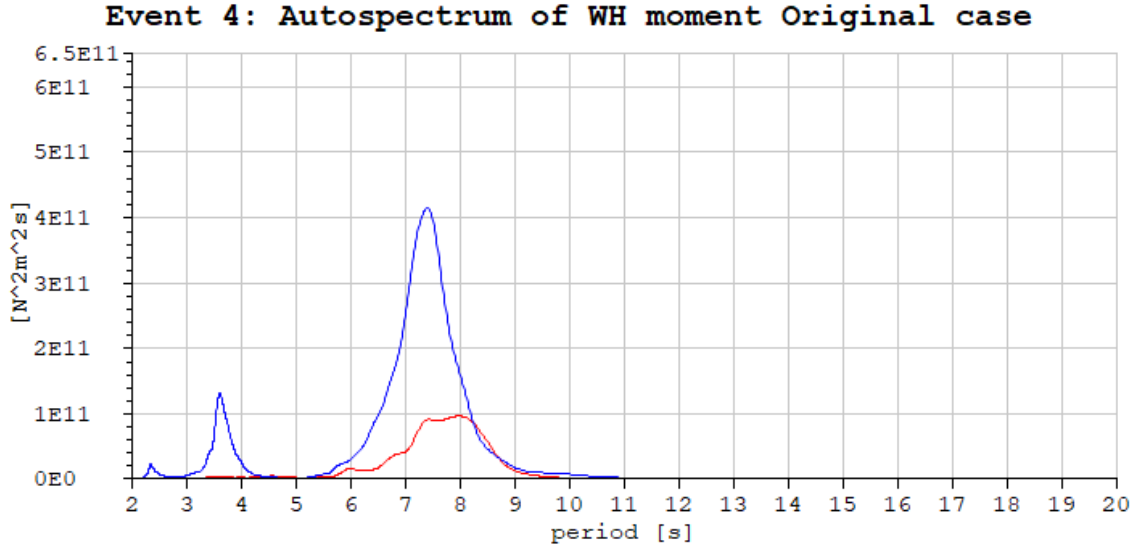
Event 4: Autospectrum of WH moment Original case
6.5E11
6E11
5E11
4E11
3E11
2E11
1E11
0E0
[N^2m^2s]
2 3 4 5 6 7 8 9 10 11 12 13 14 15 16 17 18 19 20
period [s]

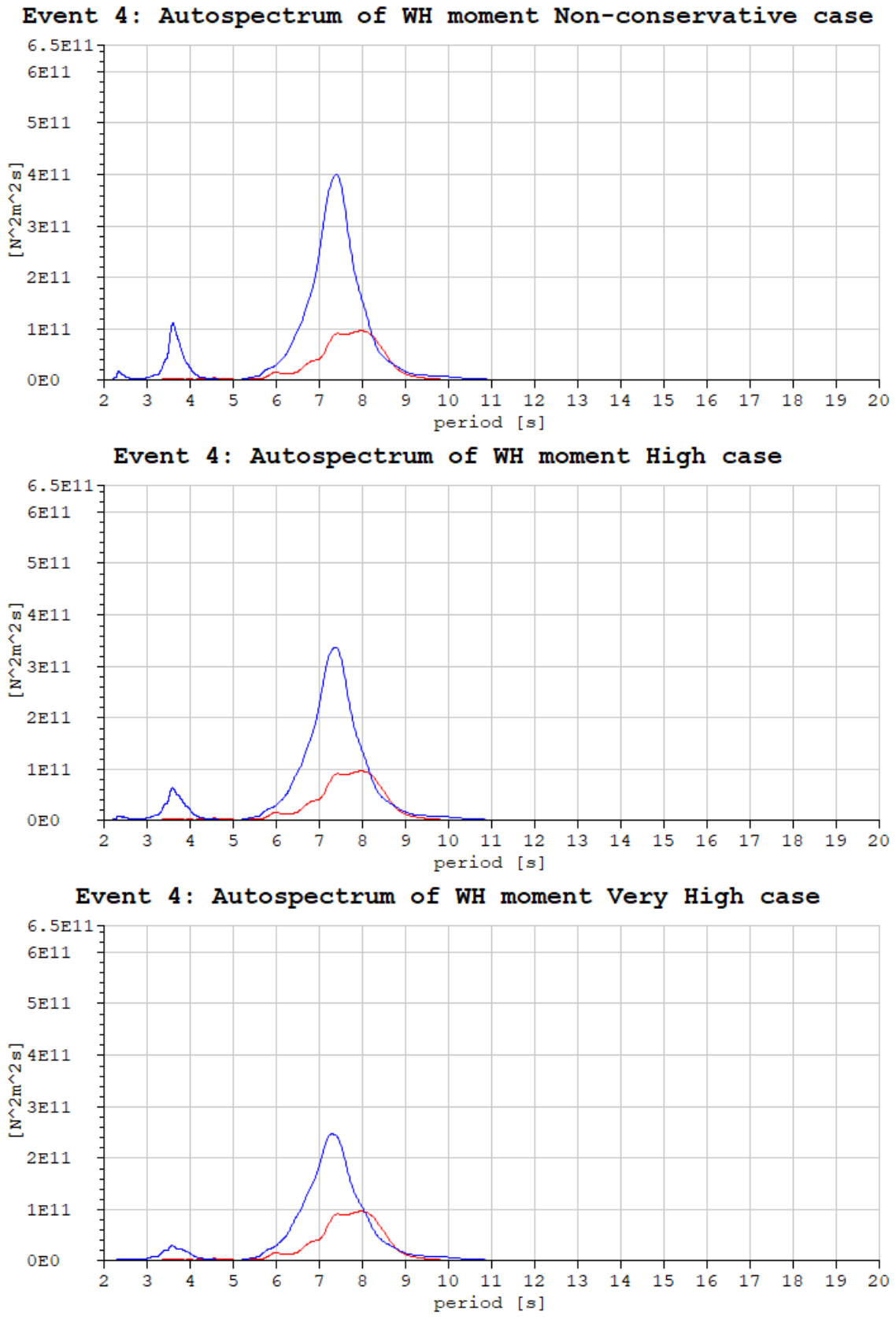

Figure 113: Event 4: The effect of different critical damping ratio on WH moment autospectrum. The blue graphs is the autospectra for WH moment in the model for each of the different damping ratios described in Table 19, the red is from measurements

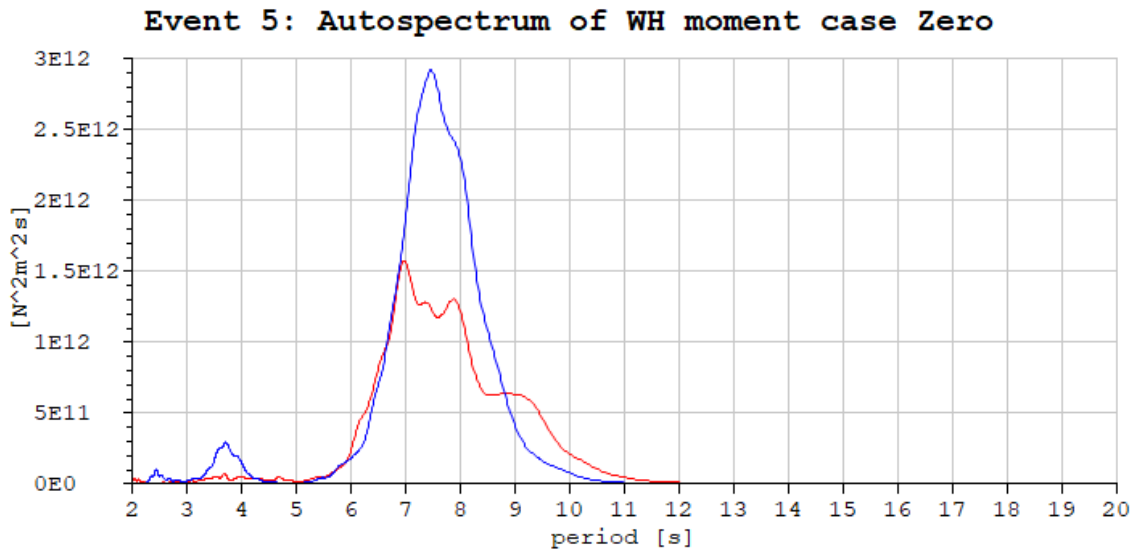
Event 5: Autospectrum of WH moment case Zero
3E12
2.5E12
2E12
1.5E12
1E12
5E11
0E0
[N^2m^2s]
2 3 4 5 6 7 8 9 10 11 12 13 14 15 16 17 18 19 20
period [s]

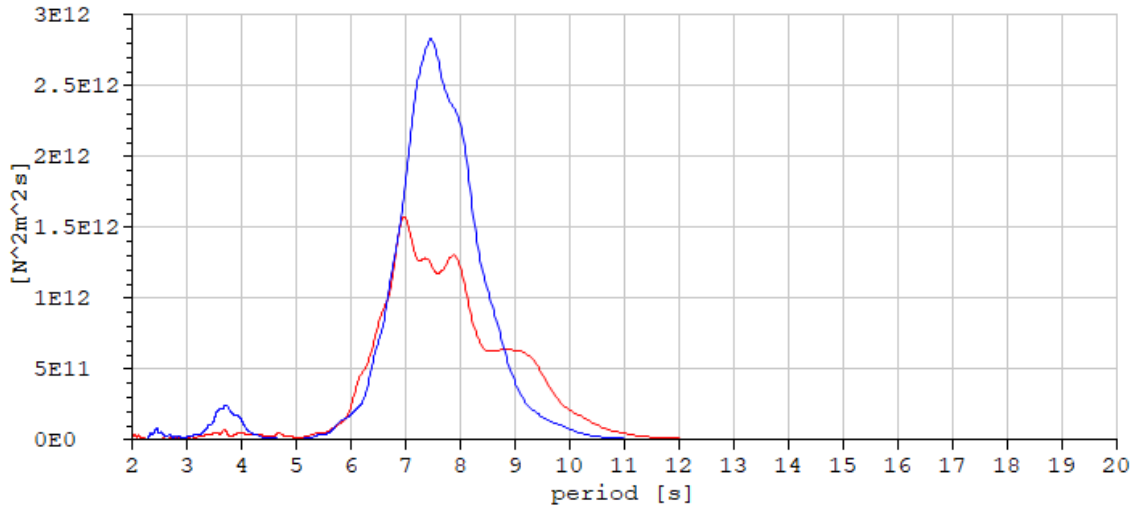
Event 5: Autospectrum of WH moment Low case
3E12
2.5E12
2E12
1.5E12
1E12
5E11
0E0
[N^2m^2s]
2 3 4 5 6 7 8 9 10 11 12 13 14 15 16 17 18 19 20
period [s]

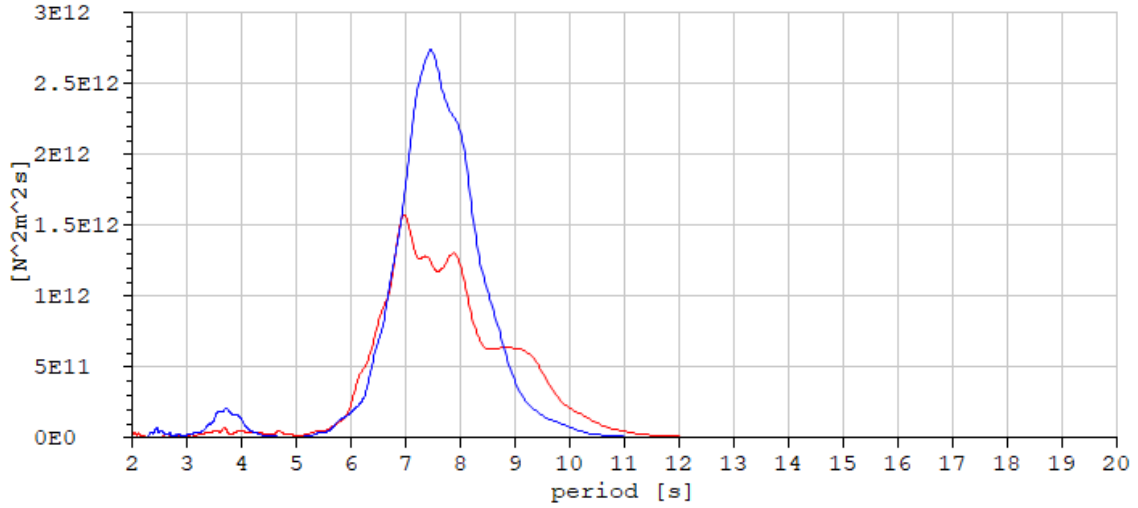
Event 5: Autospectrum of WH moment Original case
3E12
2.5E12
2E12
1.5E12
1E12
5E11
0E0
[N^2m^2s]
2 3 4 5 6 7 8 9 10 11 12 13 14 15 16 17 18 19 20
period [s]

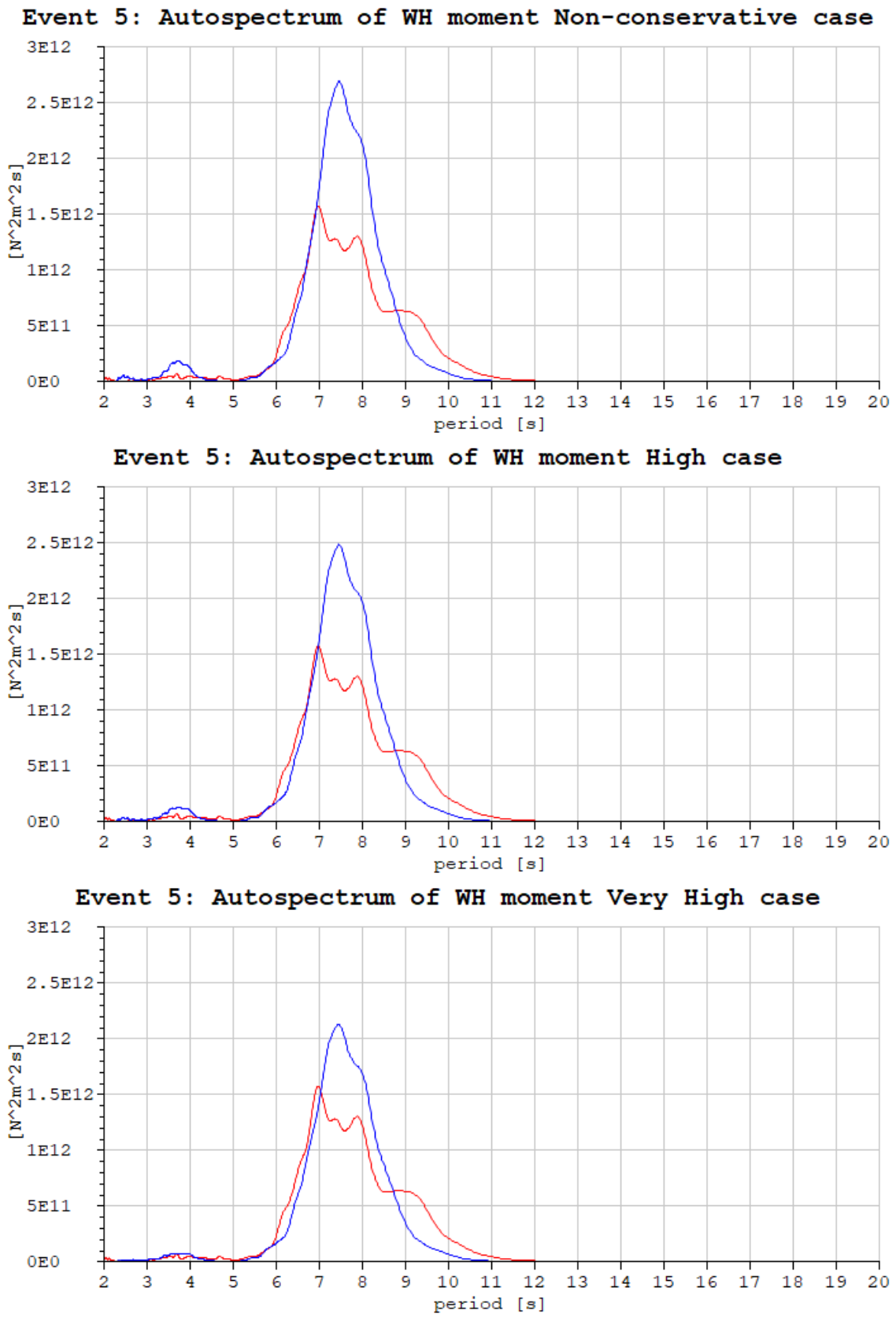

Figure 114: Event 5: The effect of different critical damping ratio on WH moment autospectrum. The blue graphs is the autospectra for WH moment in the model for each of the different damping ratios described in Table 19, the red is from measurements

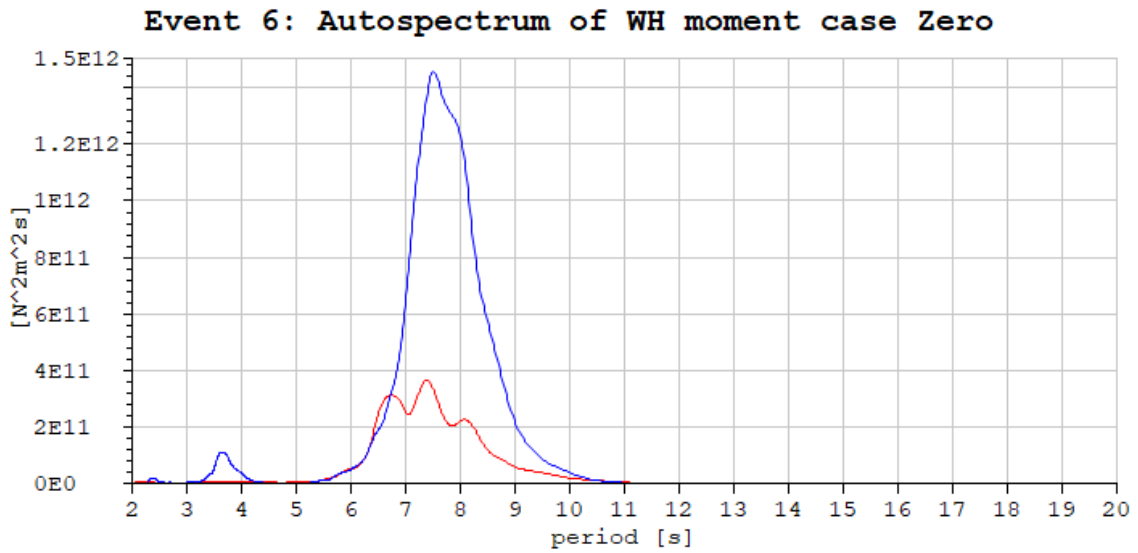
Event 6: Autospectrum of WH moment case Zero
1.5E12
1.2E12
1E12
8E11
6E11
4E11
2E11
0E0
[N^2m^2s]
2 3 4 5 6 7 8 9 10 11 12 13 14 15 16 17 18 19 20
period [s]

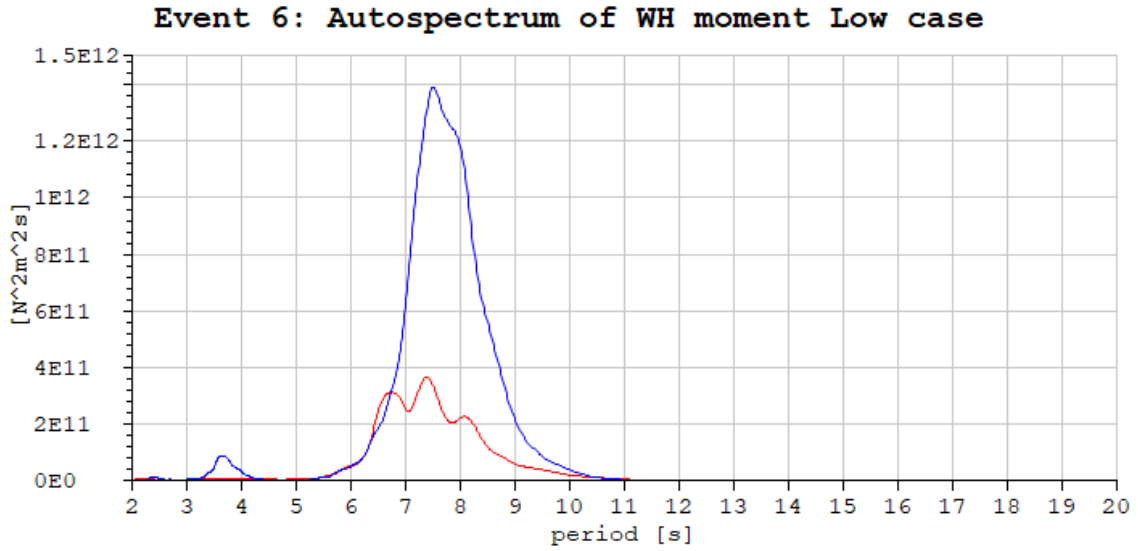
Event 6: Autospectrum of WH moment Low case
1.5E12
1.2E12
1E12
8E11
6E11
4E11
2E11
0E0
[N^2m^2s]
2 3 4 5 6 7 8 9 10 11 12 13 14 15 16 17 18 19 20
period [s]

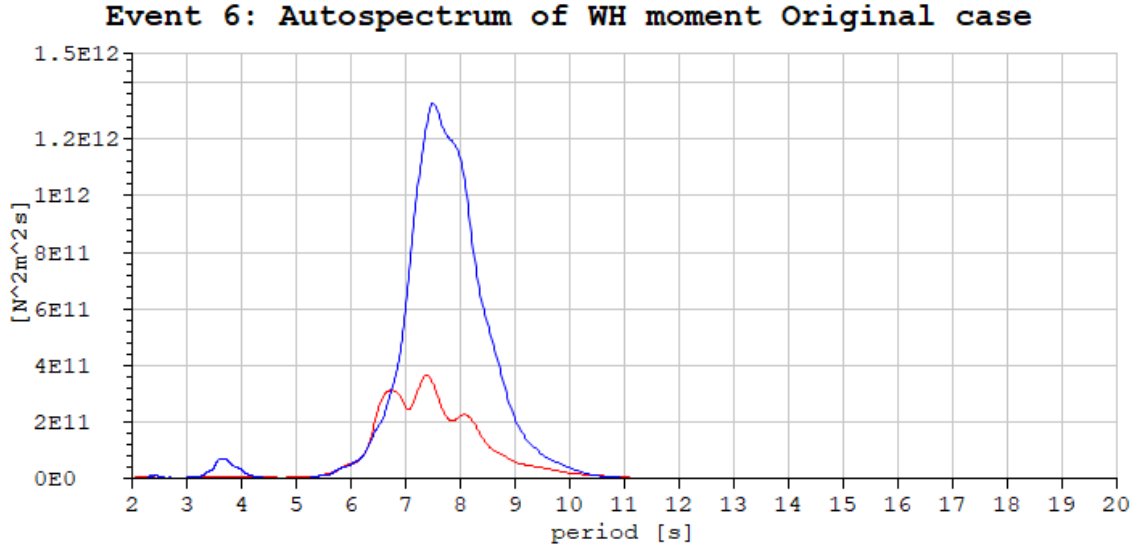
Event 6: Autospectrum of WH moment Original case
1.5E12
1.2E12
1E12
8E11
6E11
4E11
2E11
0E0
[N^2m^2s]
2 3 4 5 6 7 8 9 10 11 12 13 14 15 16 17 18 19 20
period [s]

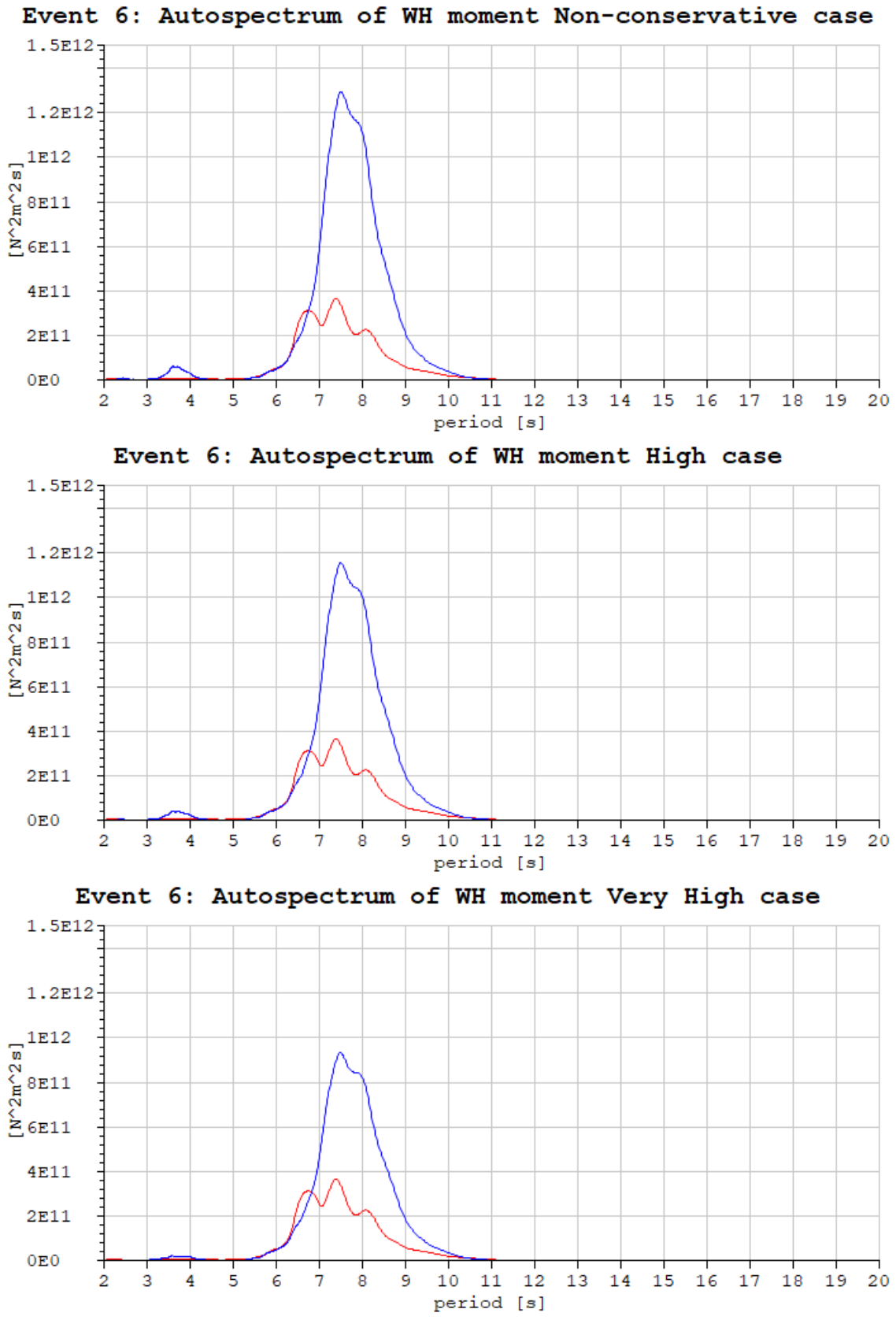

Figure 115: Event 6: The effect of different critical damping ratio on WH moment autospectrum. The blue graphs is the autospectra for WH moment in the model for each of the different damping ratios described in Table 19, the red is from measurements

K Matlab script for quasi-static method

```
%MX0 and MY0 corresponds to the wellhead moment calculated from strain gauges



flex_momentX=zeros(length(LRS_angY),1);
flex_momentY=zeros(length(LRS_angY),1);

for i=1:length(LRS_angY)
    flex_momentX(i)=moment_from_angle(LRS_angX(i)-BOP_angX(i));
    flex_momentY(i)=moment_from_angle(LRS_angY(i)-BOP_angY(i));
end



%Calculating moment from the top tension:
TT=1200; %1600; %kN
WH_dist=12.54;% m
BOP_wet_weight=181.437;%tons

TT_H_X=TT*(LRS_angX*3.14/180); %kN
TT_H_Y=TT*(LRS_angY*3.14/180);

TT_H_moment_X=TT_H_X*WH_dist; %kNm
TT_H_moment_Y=TT_H_Y*WH_dist;

TT_V_moment_X=TT*WH_dist*(BOP_angX*3.14/180); %kNm
TT_V_moment_Y=TT*WH_dist*(BOP_angY*3.14/180);


%Calculating moment from weight
weight_moment_X=BOP_wet_weight*9.81*(BOP_angX*3.14/180)*WH_dist; %kNm
weight_moment_Y=BOP_wet_weight*9.81*(BOP_angY*3.14/180)*WH_dist;




%Calculating inertia moment
% delta_t=time(2)-time(1);
%
% dry_mass_BOP=211; %tons
%added_massBOP=1.025*1.1*3.14*1.118^2/4*WH_dist; %tons
% Inert=dry_mass_BOP*WH_dist^2/4; %1000*kg*m^2
%
% BOP_ang_acc_x=zeros(length(BOP_angY),1);
% BOP_ang_acc_y=zeros(length(BOP_angY),1);
% for i=2:(length(BOP_angY)-1)
%     BOP_ang_acc_x(i)=(BOP_angX(i-1)-2*BOP_angX(i) + BOP_angX(i+1))/delta_t^2;
%     BOP_ang_acc_y(i)=(BOP_angY(i-1)-2*BOP_angY(i) + BOP_angY(i+1))/delta_t^2;
% end

%inertia_moment_x=Inert*BOP_ang_acc_x*3.14/180; %1000*kg*m^2* 1/s^2 =kNm
%inertia_moment_y=Inert*BOP_ang_acc_y*3.14/180;
```

```
%Calculatring total moment
total_moment_X=flex_momentX + TT_H_moment_X - TT_V_moment_X + weight_moment_X;% -
↪  inertia_moment_x;
total_moment_Y=flex_momentY + TT_H_moment_Y - TT_V_moment_Y + weight_moment_Y;% -
↪  inertia_moment_y;

moment_from_ang=sqrt(total_moment_X.^2 + total_moment_Y.^2);
SRSS_mea=sqrt(MX0.^2 + MY0.^2);

% figure
% scatter(moment_from_ang,SRSS_mea,1,'filled')
% title('moment from angle to moment form sg')
% set(gca,'FontSize',40)



fprintf('SRSS of STD \n')
sqrt(std(total_moment_X)^2 + std(total_moment_Y)^2)
sqrt(std(MX0)^2 + std(MY0)^2)


% plot_autocorr_comp(MX0,MY0, total_moment_X,total_moment_Y,time)
```

L Results from Quasi-static approach

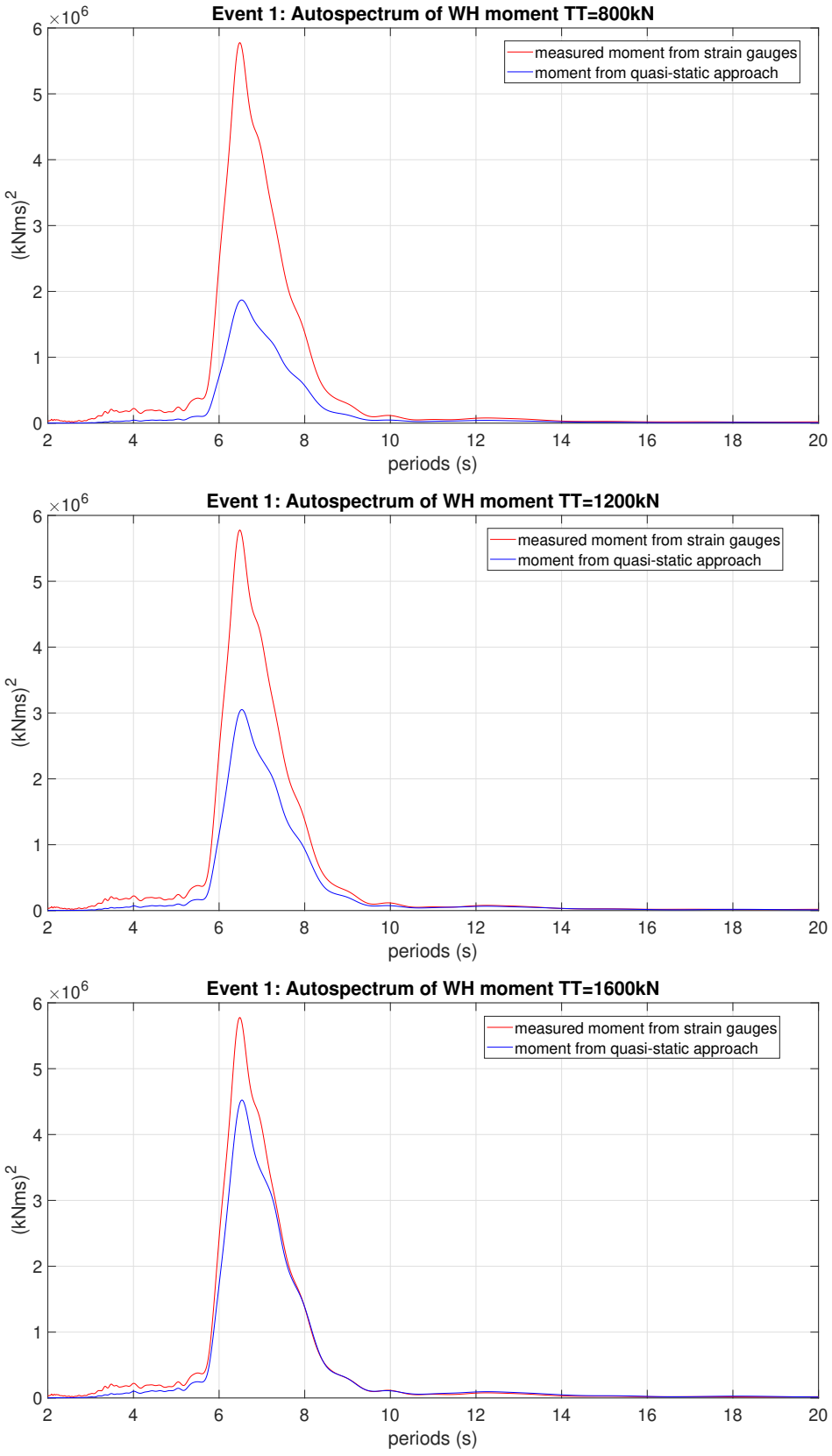

Figure 116: Event 1: Autospectra from quasi-static approach with differing top tension on BOP

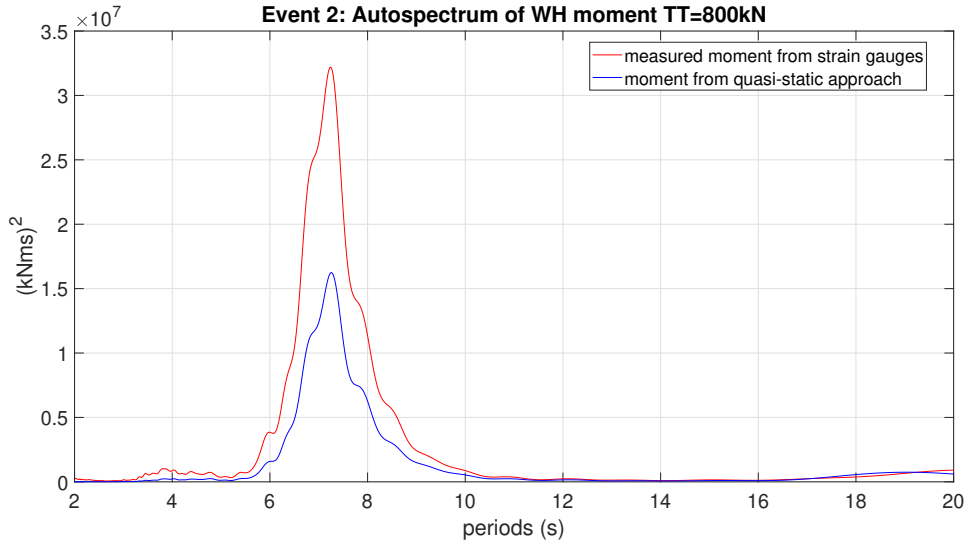

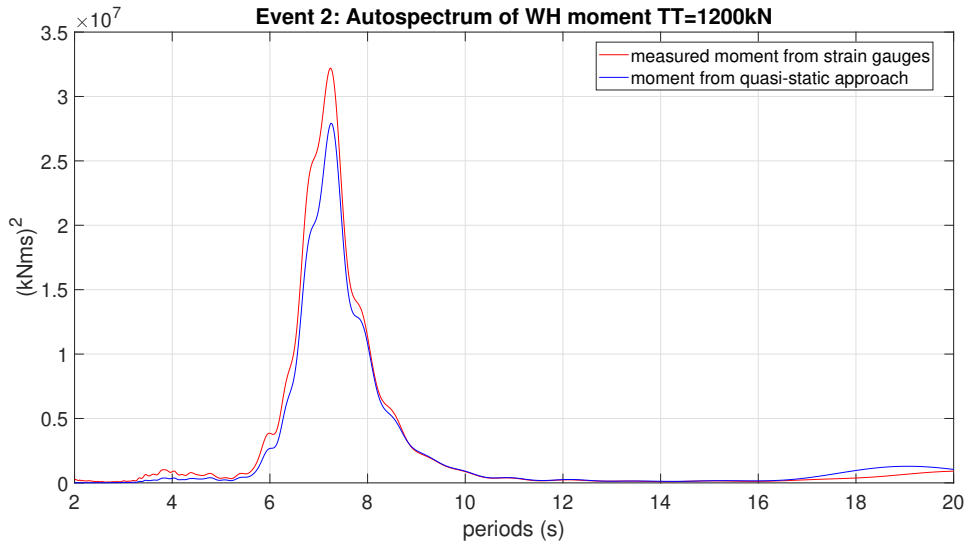

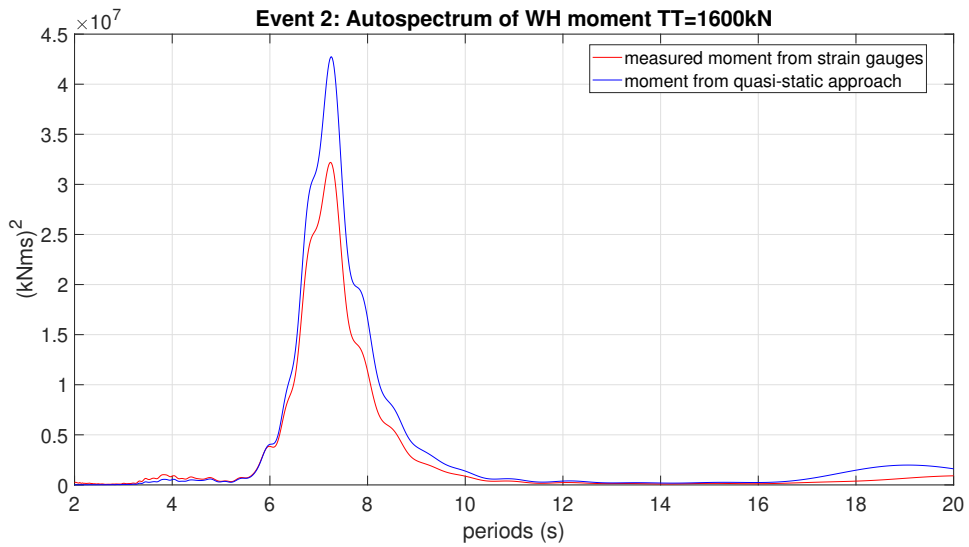

Figure 117: Event 2: Autospectra from quasi-static approach with differing top tension on BOP

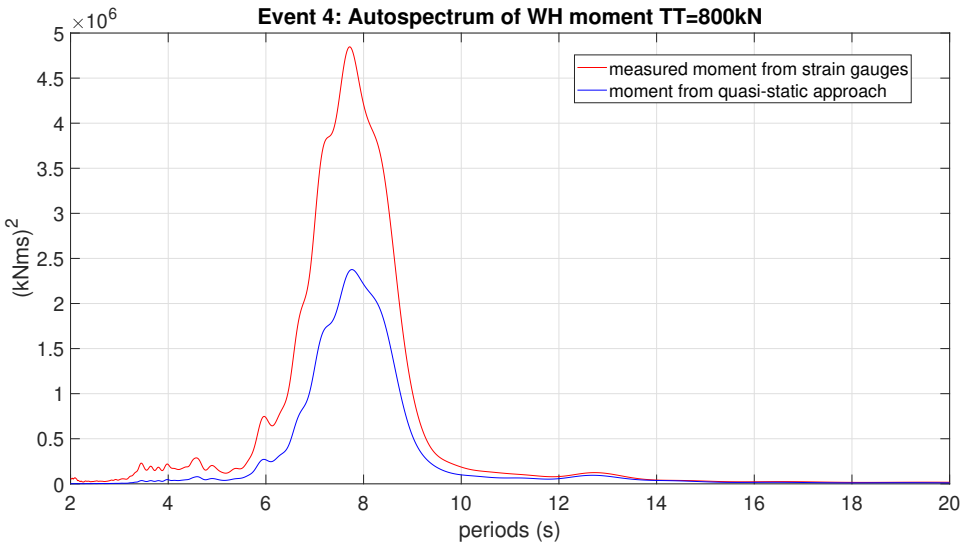

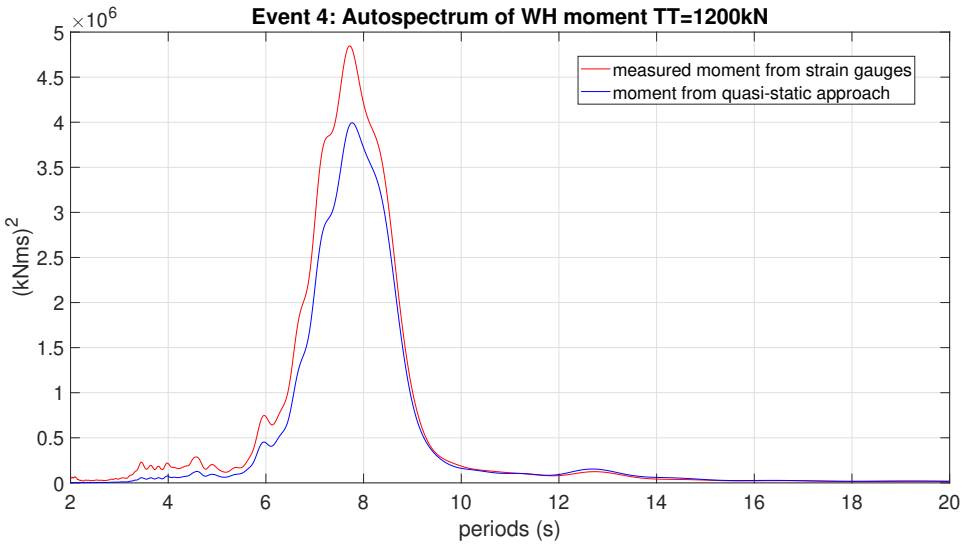

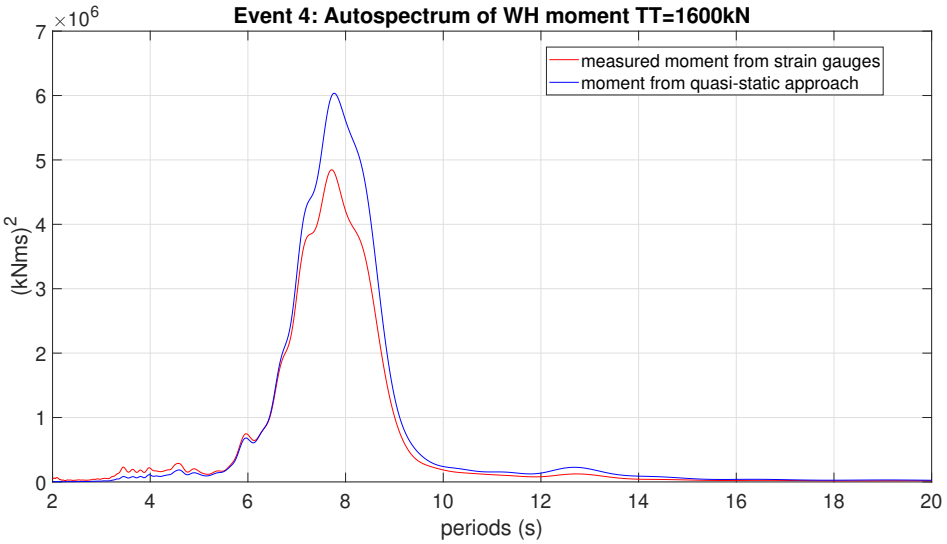

Figure 118: Event 4: Autospectra from quasi-static approach with differing top tension on BOP

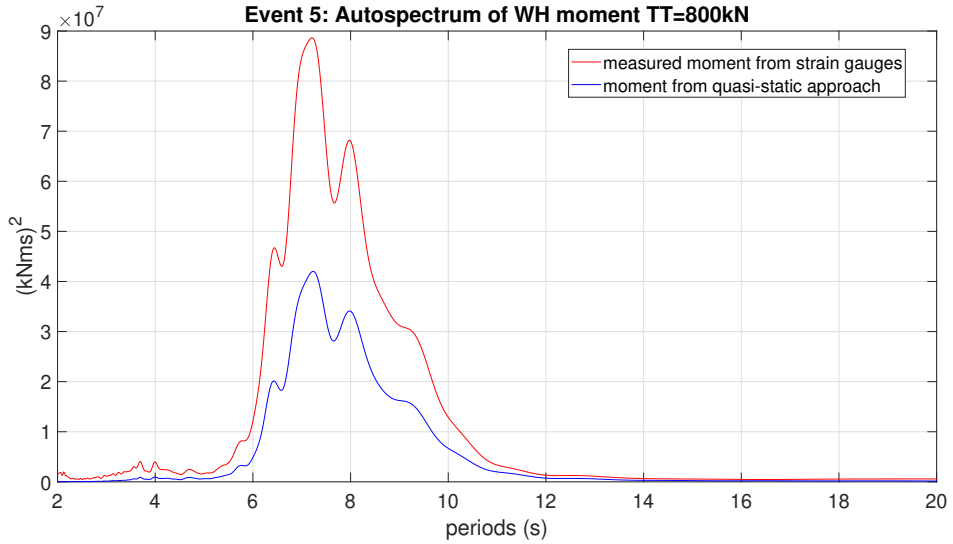

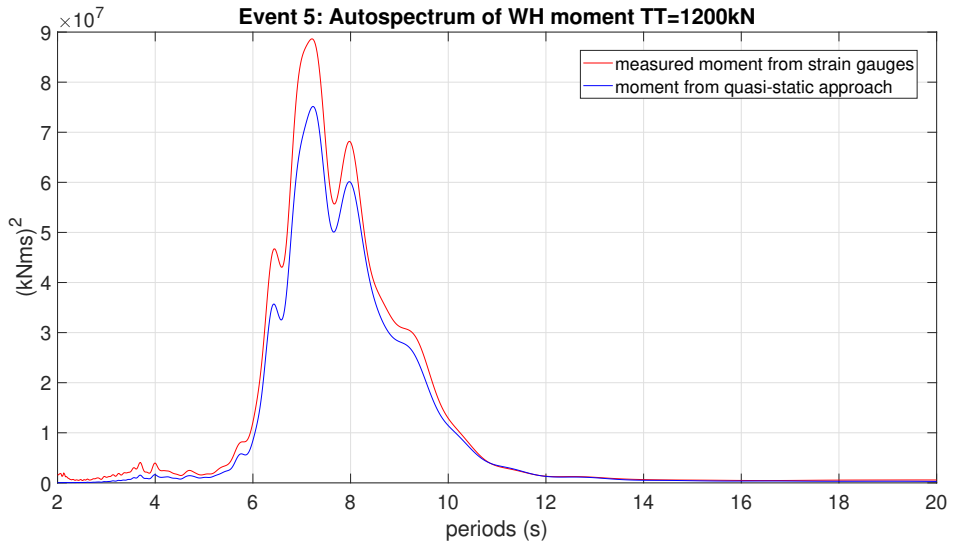

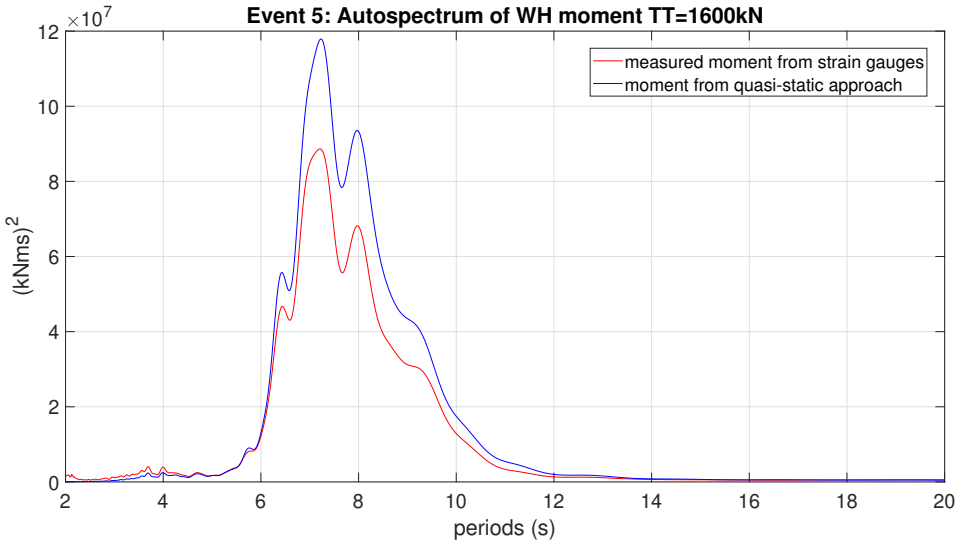

Figure 119: Event 5: Autospectra from quasi-static approach with differing top tension on BOP

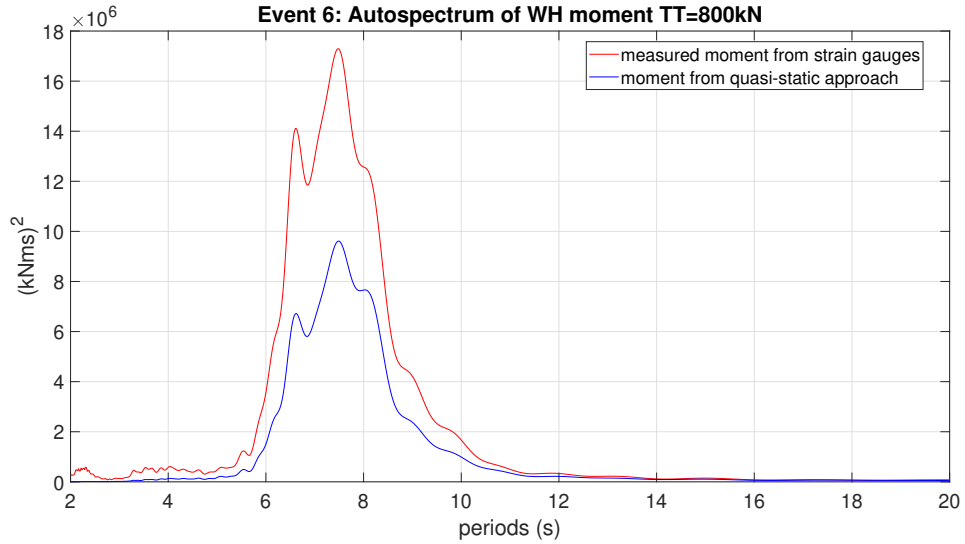

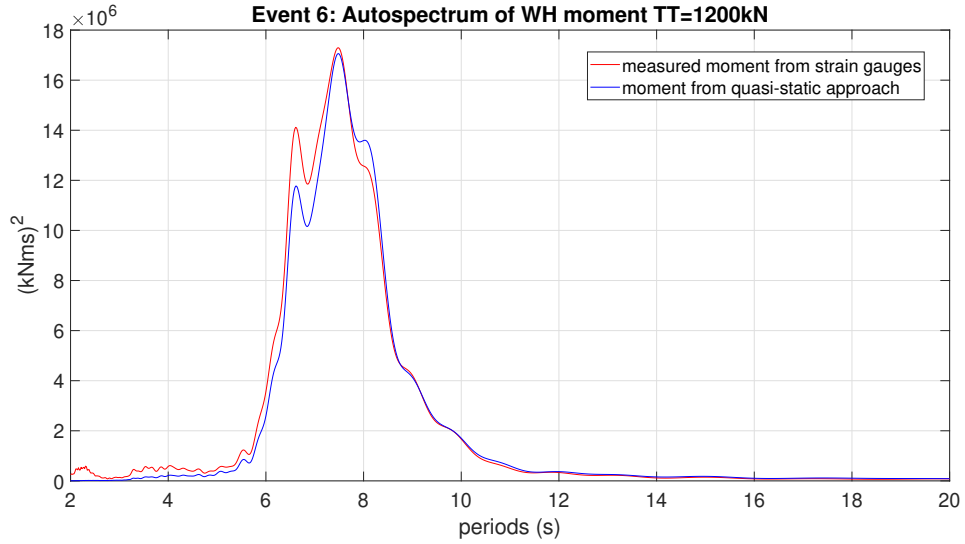

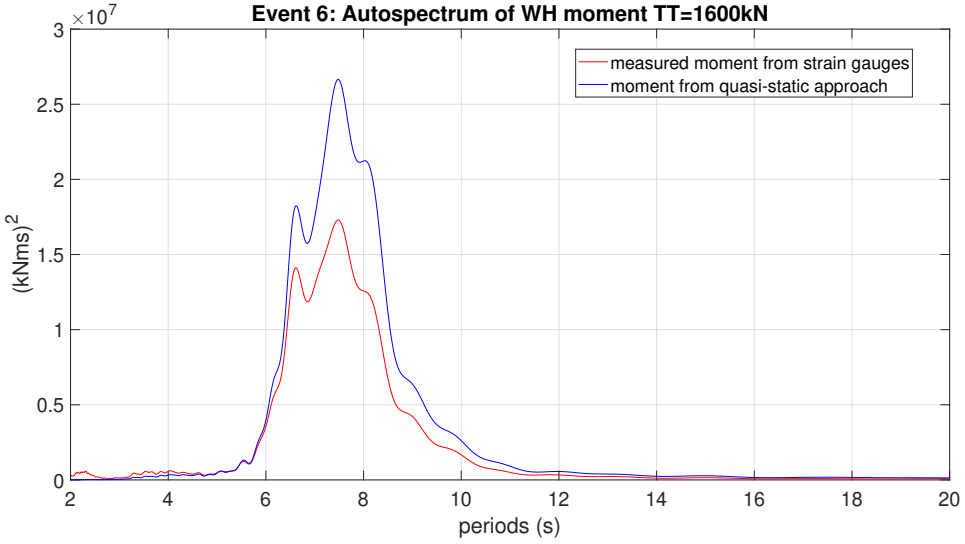

Figure 120: Event 6: Autospectra from quasi-static approach with differing top tension on BOP

M Correlation between WH moment and other measurement parameters

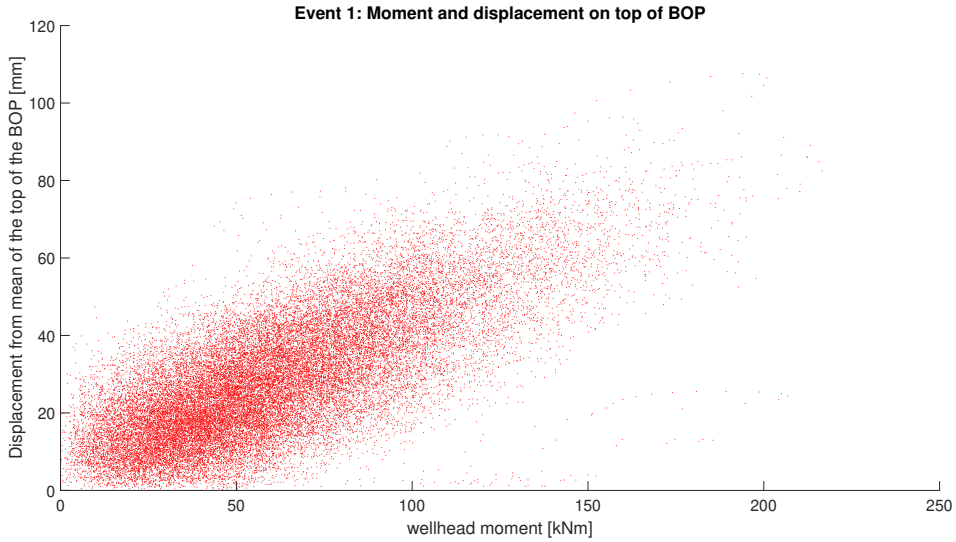

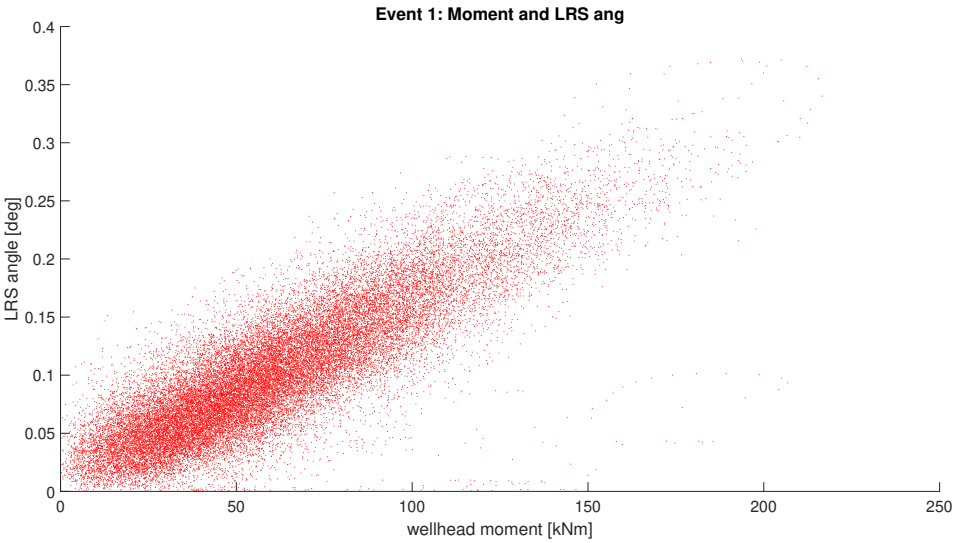

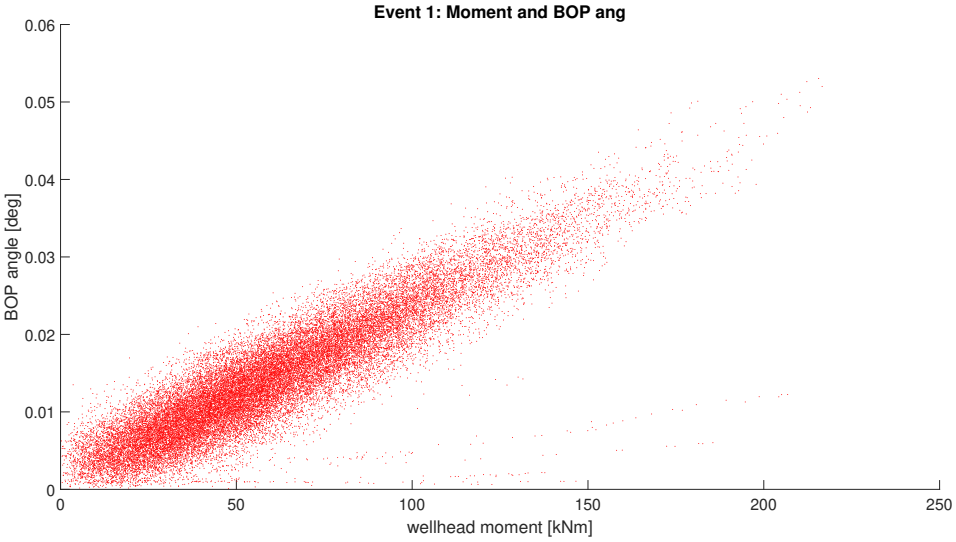

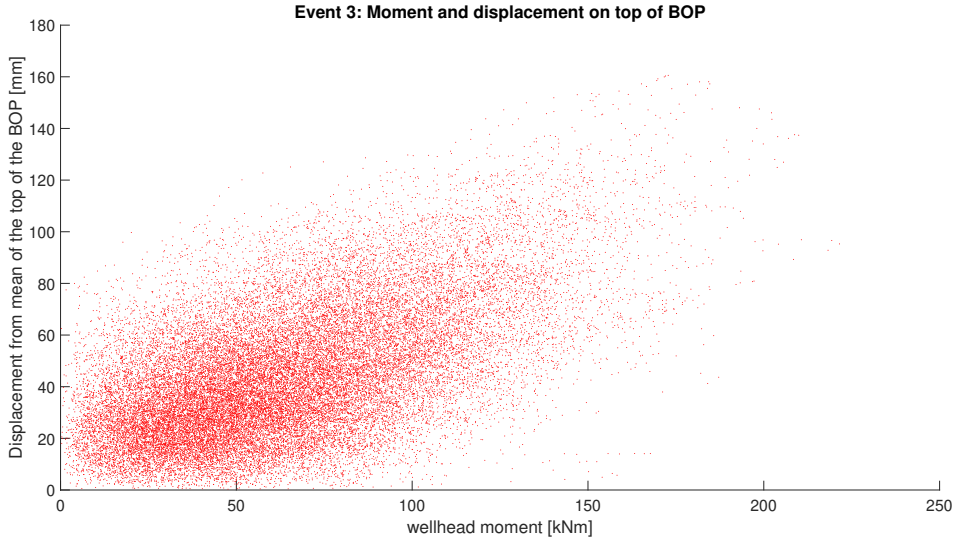
Event 3: Moment and displacement on top of BOP
Displacement from mean of the top of the BOP [mm]
wellhead moment [kNm]
0
20
40
60
80
100
120
140
160
180
0
50
100
150
200
250

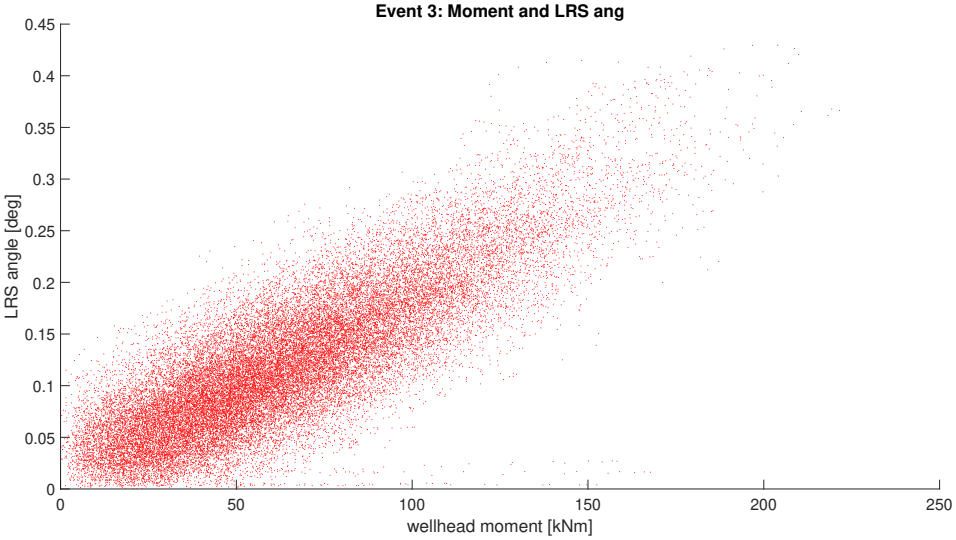
Event 3: Moment and LRS ang
LRS angle [deg]
wellhead moment [kNm]
0
0.05
0.1
0.15
0.2
0.25
0.3
0.35
0.4
0.45
0
50
100
150
200
250

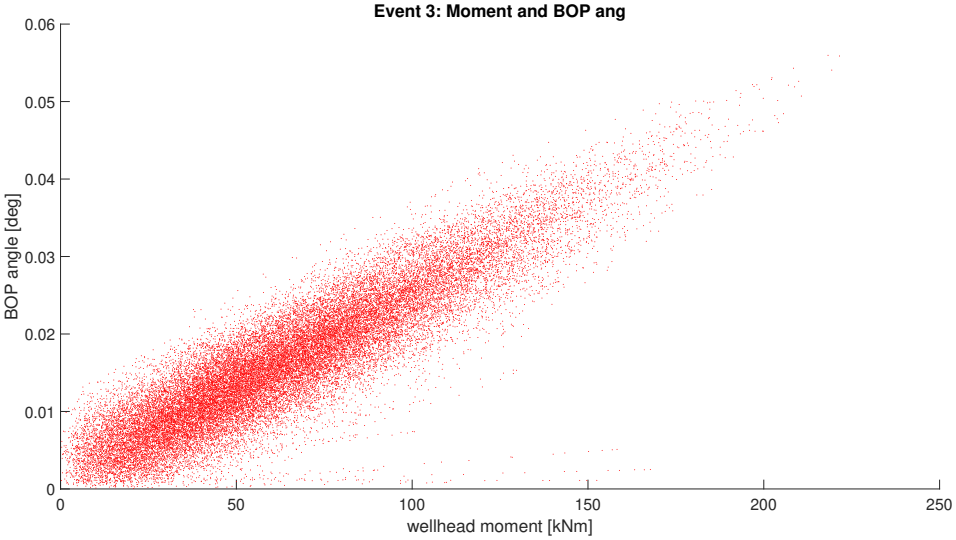
Event 3: Moment and BOP ang
BOP angle [deg]
wellhead moment [kNm]
0
0.01
0.02
0.03
0.04
0.05
0.06
0
50
100
150
200
250

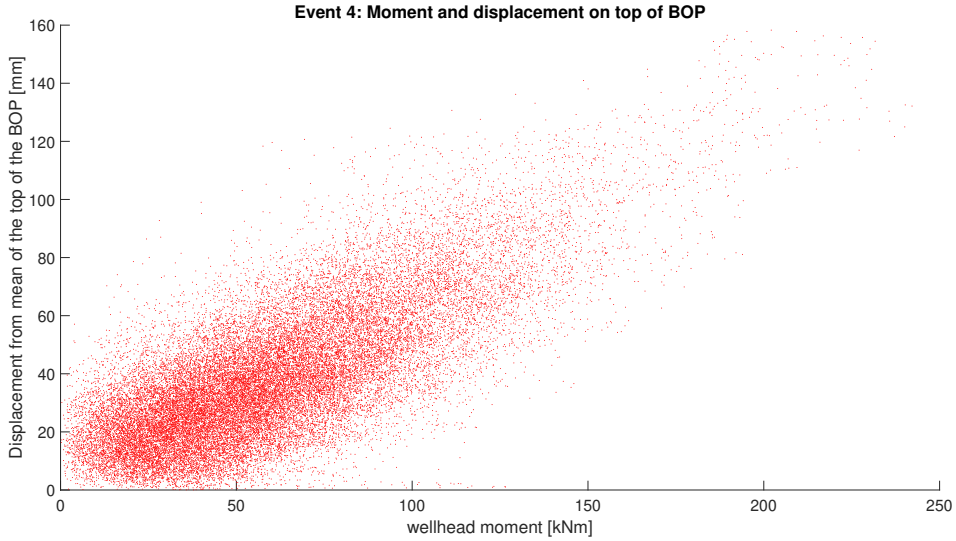
Event 4: Moment and displacement on top of BOP
Displacement from mean of the top of the BOP [mm]
wellhead moment [kNm]
0
20
40
60
80
100
120
140
160
0
50
100
150
200
250

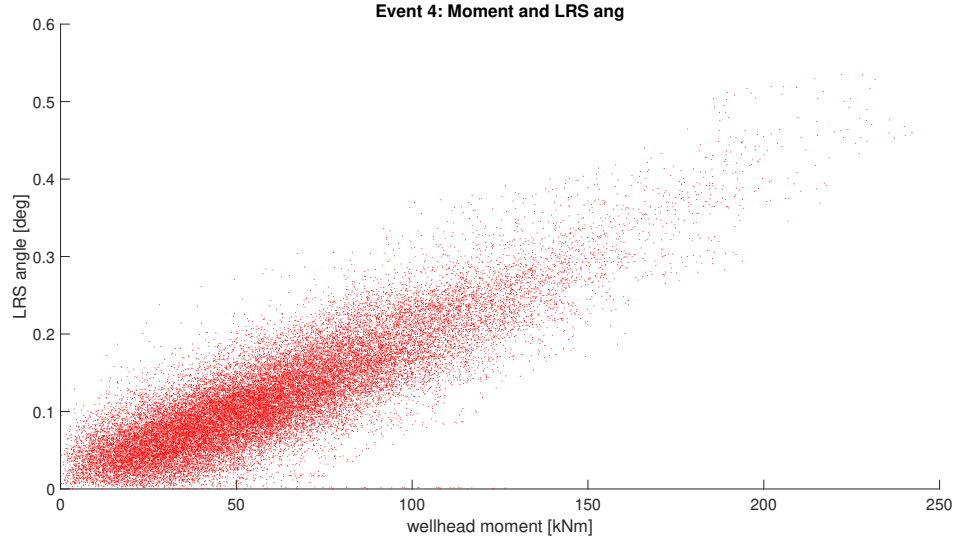
Event 4: Moment and LRS ang
LRS angle [deg]
wellhead moment [kNm]
0
0.1
0.2
0.3
0.4
0.5
0.6
0
50
100
150
200
250

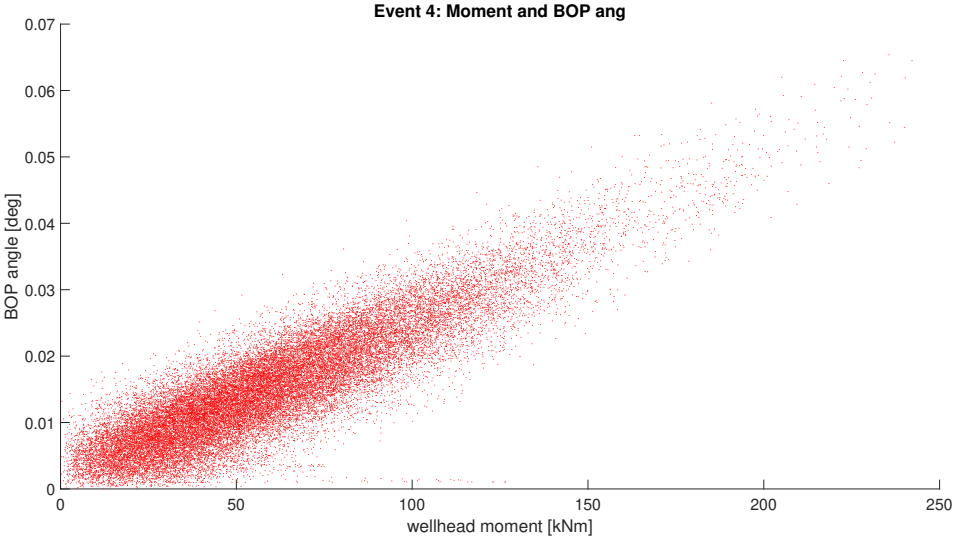
Event 4: Moment and BOP ang
BOP angle [deg]
wellhead moment [kNm]
0
0.01
0.02
0.03
0.04
0.05
0.06
0.07
0
50
100
150
200
250

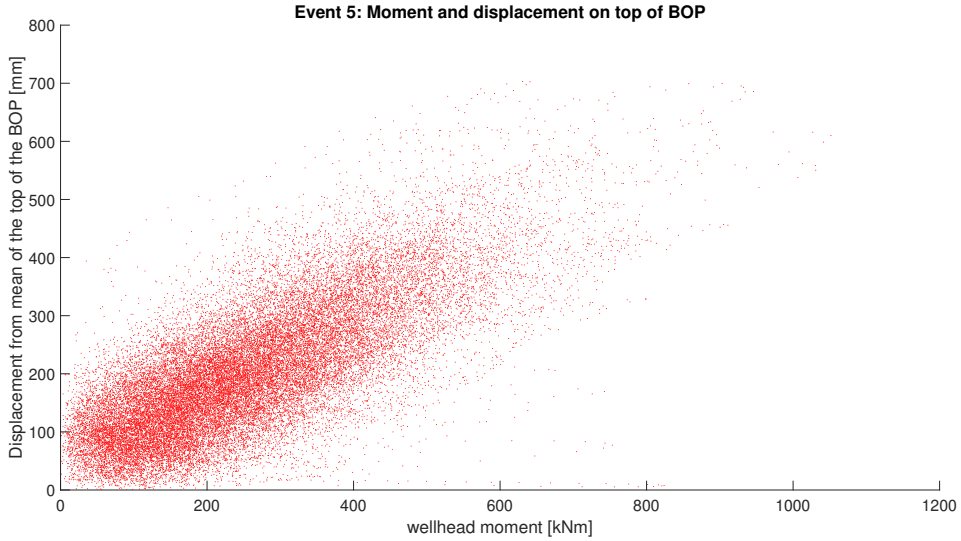
Event 5: Moment and displacement on top of BOP
Displacement from mean of the top of the BOP [mm]
wellhead moment [kNm]
0
100
200
300
400
500
600
700
800
0
200
400
600
800
1000
1200

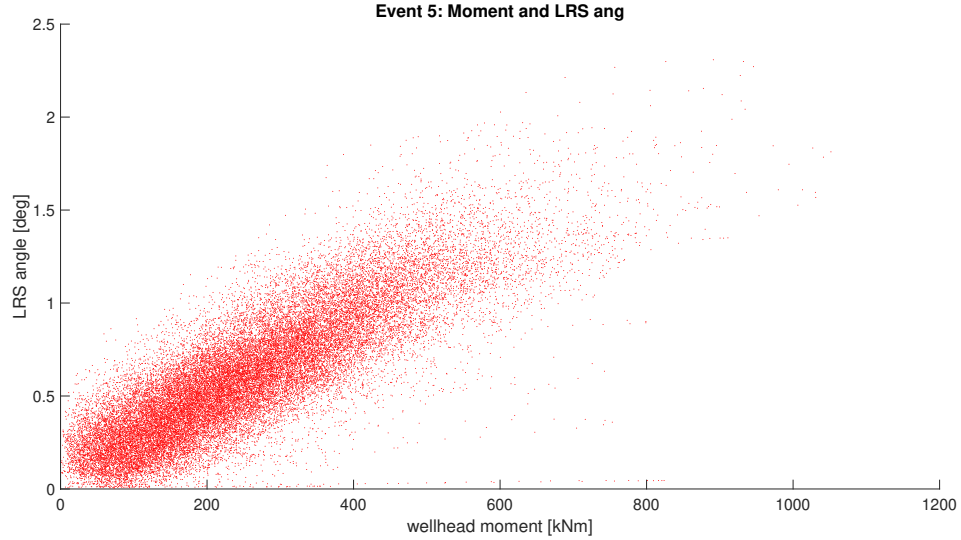
Event 5: Moment and LRS ang
LRS angle [deg]
wellhead moment [kNm]
0
0.5
1
1.5
2
2.5
0
200
400
600
800
1000
1200

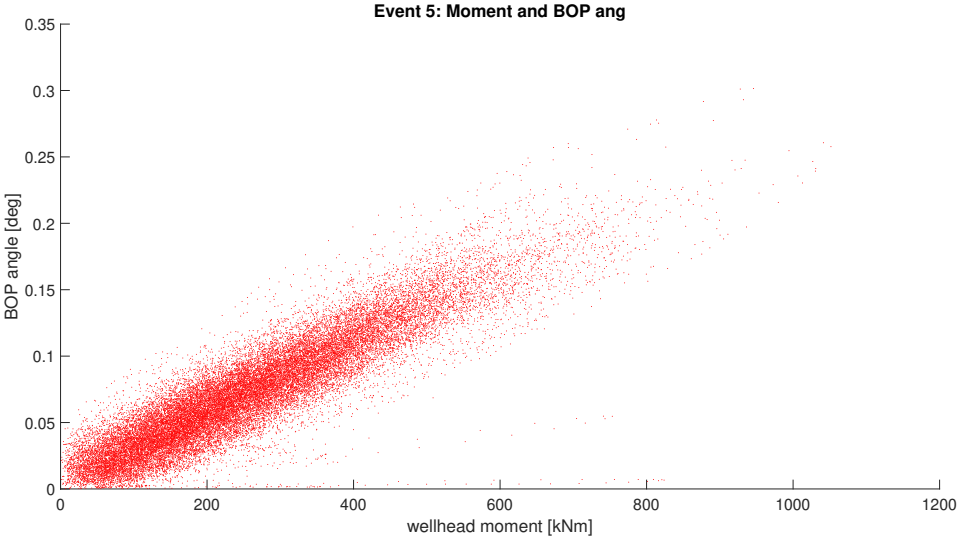
Event 5: Moment and BOP ang
BOP angle [deg]
wellhead moment [kNm]
0
0.05
0.1
0.15
0.2
0.25
0.3
0.35
0
200
400
600
800
1000
1200

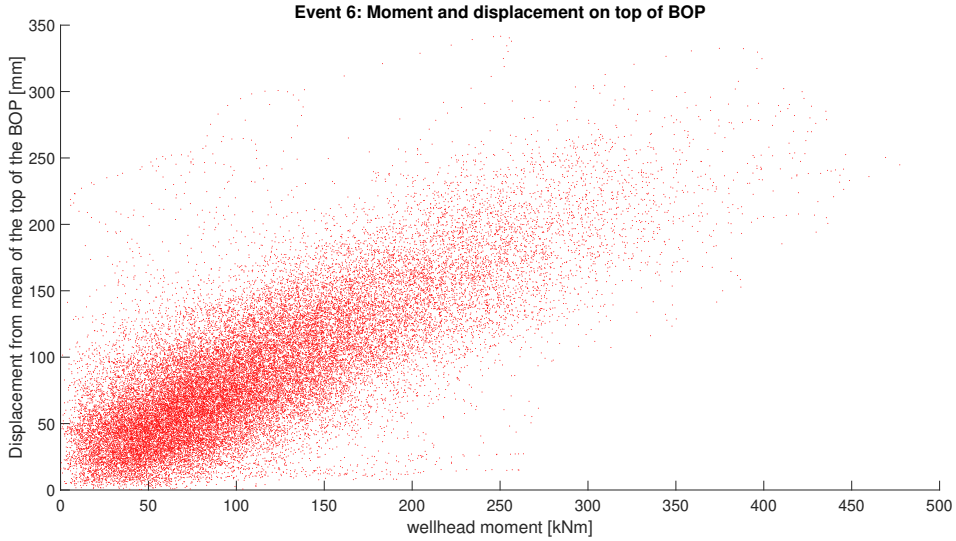
Event 6: Moment and displacement on top of BOP
Displacement from mean of the top of the BOP [mm]
wellhead moment [kNm]
0
50
100
150
200
250
300
350
400
450
500

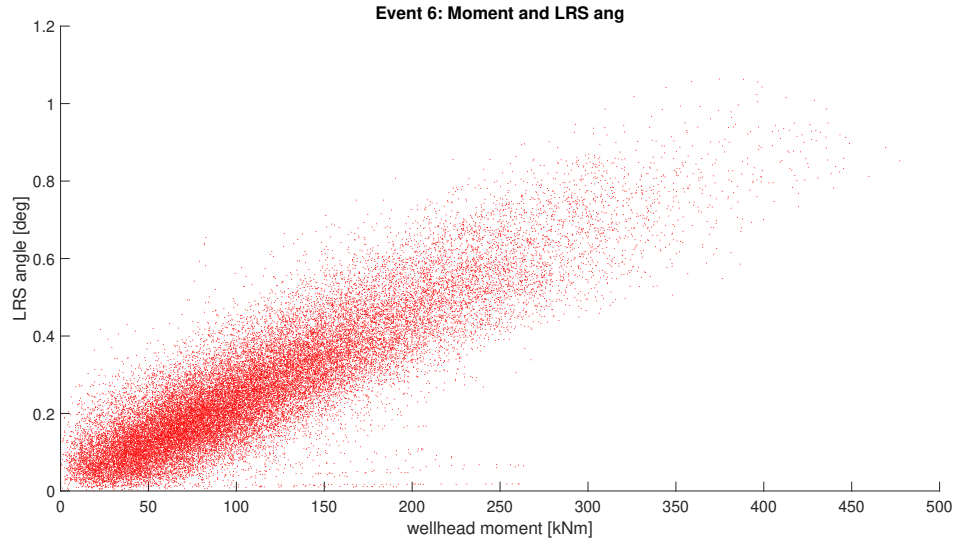
Event 6: Moment and LRS ang
LRS angle [deg]
wellhead moment [kNm]
0
0.2
0.4
0.6
0.8
1
1.2
50
100
150
200
250
300
350
400
450
500

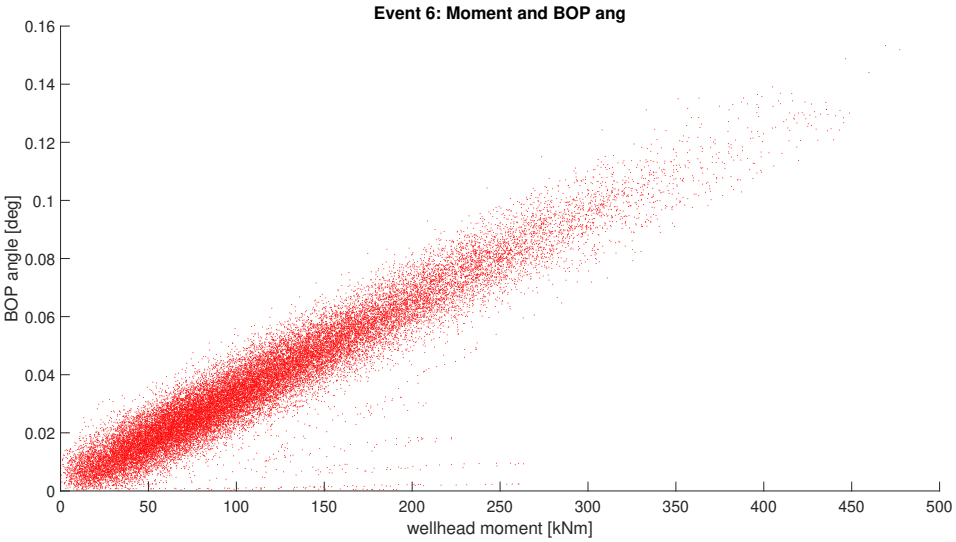
Event 6: Moment and BOP ang
BOP angle [deg]
wellhead moment [kNm]
0
0.02
0.04
0.06
0.08
0.1
0.12
0.14
0.16
50
100
150
200
250
300
350
400
450
500